

NATIONAL AERONAUTICS AND SPACE ADMINISTRATION

Space Programs Summary No. 37-40, Volume III

for the period May 1, 1966 to June 30, 1966

The Deep Space Network

jpl

JET PROPULSION LABORATORY
CALIFORNIA INSTITUTE OF TECHNOLOGY
PASADENA, CALIFORNIA

July 31, 1966

GPO PRICE \$ _____

CFSTI PRICE(S) \$ _____

Hard copy (HC) \$ 3.00

Microfiche (MF) 1.00

7 653 July 65

N66 38546	N66 38572
(ACCESSION NUMBER)	(THRU)
127	1
(PAGES)	(CODE)
CR-78436	07
(NASA CR OR TMX OR AD NUMBER)	(CATEGORY)

NATIONAL AERONAUTICS AND SPACE ADMINISTRATION

Space Programs Summary No. 37-40, Volume III

for the period May 1, 1966 to June 30, 1966

The Deep Space Network

JET PROPULSION LABORATORY
CALIFORNIA INSTITUTE OF TECHNOLOGY
PASADENA, CALIFORNIA

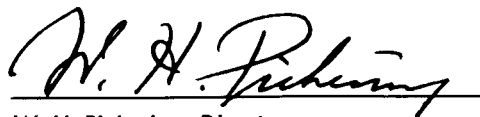
July 31, 1966

Preface

The *Space Programs Summary* is a six-volume, bimonthly publication that documents the current project activities and supporting research and advanced development efforts conducted or managed by JPL for the NASA space exploration programs. The titles of all volumes of the *Space Programs Summary* are:

- Vol. I. The Lunar Program (Confidential)
- Vol. II. The Planetary-Interplanetary Program (Confidential)
- Vol. III. The Deep Space Network (Unclassified)
- Vol. IV. Supporting Research and Advanced Development (Unclassified)
- Vol. V. Supporting Research and Advanced Development (Confidential)
- Vol. VI. Space Exploration Programs and Space Sciences (Unclassified)

The *Space Programs Summary*, Vol. VI consists of an unclassified digest of appropriate material from Vols. I, II, and III; an original presentation of technical supporting activities, including engineering development of environmental-test facilities, and quality assurance and reliability; and a reprint of the space science instrumentation studies of Vols. I and II.



W. H. Pickering, Director
Jet Propulsion Laboratory

Space Programs Summary No. 37-40, Volume III

Copyright © 1966, Jet Propulsion Laboratory, California Institute of Technology
Prepared under Contract No. NAS 7-100, National Aeronautics & Space Administration

Contents

I. Introduction	1
II. Communications Research and Development	3
A. Digital Module Development: Clock Pulse Shaper	3 ✓
<i>P. D. Herrin</i>	
B. Information Systems: A Program for Finite Fourier Transforms	6 ✓
<i>L. R. Welch</i>	
C. Information Systems: A Double Error-Correction Program for DSN Teletype	8 ✓
<i>H. Fredricksen</i>	
D. New Scientific Data Systems (SDS) Digital Computer Programs	11 ✓
<i>F. B. Leppa, G. B. Bigler, C. McNeal, and M. Dyson</i>	
E. Wide-Band Receiver System Development: Wide-Band Power Multiplier	13 ✓
<i>K. D. Schreder and G. Lutes</i>	
F. Efficient Antenna Systems: A Stepped-Mode Transducer Using Homogeneous Waveguides	21 ✓
<i>D. A. Bathker</i>	
G. High-Power Continuous-Wave (CW) S-Band Traveling Wave Resonator	24 ✓
<i>R. B. Kolbly</i>	
H. Frequency Stability Determination for Two Hydrogen Masers	26 ✓
<i>R. L. Sydnor</i>	
I. Frequency Generation and Control: Properties of a Hydrogen Maser Frequency Standard	29 ✓
<i>W. H. Higa</i>	
J. Improved RF Calibration Techniques: DC Potentiometer Microwave Insertion-Loss Test Set	30 ✓
<i>C. T. Stelzried and D. Mullen</i>	
References	33
III. Communications Development Engineering	35
A. Frequency Generation and Control: Comparison of Frequency Synthesizers	35 ✓
<i>W. F. Gillmore</i>	
B. S- and X-Band Central Frequency Synthesizer at the Venus Deep Space Station	57 ✓
<i>G. U. Barbani</i>	
C. Experimental S-Band Receiver at the Mars Deep Space Station	62 ✓
<i>D. W. Brown</i>	
D. Operational System Temperature at Mars Deep Space Station During Solar Occultation of <i>Mariner IV</i>	67 ✓
<i>D. W. Brown</i>	
E. Equipment for RF Carrier Acquisition Using the MSFN S-Band Receiver/Exciter	69 ✓
<i>M. H. Brockman and R. E. Weller</i>	
F. Efficient Antenna Systems: Advanced Antenna System Patterns Obtained Using the <i>Surveyor I</i> Spacecraft	75 ✓
<i>D. Bathker</i>	
G. Advanced Development of Microwave Antenna Subsystems	80 ✓
<i>R. W. Hartop</i>	
H. High-Power Transmitter Development	80 ✓
<i>E. J. Finnegan</i>	

Contents (Cont'd)

I. A Manual Gain Control Remote-Control Subsystem for the Mars Deep Space Station Receiver	84	✓
<i>C. F. Foster</i>		
J. Redesign of Mod II and Mod III Stored Program Controllers	86	✓
<i>J. W. Newton</i>		
K. Microwave Maser Development: Traveling Wave Maser for the Venus Deep Space Station	90	✓
<i>R. Clauss</i>		
L. Venus Deep Space Station R&D Cone Calibration	93	✓
<i>T. Otoshi and C. T. Stelzreid</i>		
References	100	
IV. Deep Space Station Engineering and Operations	101	
A. Flight Project Support	101	✓
<i>J. Orbison</i>		
B. Facility Construction and Equipment Installation	103	✓
<i>J. Orbison</i>		
C. Venus DSS Operations	106	✓
<i>E. B. Jackson, M. A. Gregg, A. L. Price, and R. M. Gosline</i>		
D. On-Site Prediction Generation at DSS 72, DSS 61, and DSS 42 During the <i>Atlas/Centaur 8</i> Mission	108	✓
<i>A. L. Berman</i>		

I. Introduction

The Deep Space Network (DSN), established by the NASA Office of Tracking and Data Acquisition, is under the system management and technical direction of JPL. The DSN is responsible for two-way communications with unmanned spacecraft travelling from approximately 10,000 miles from Earth to interplanetary distances. Tracking and data-handling equipment to support these missions is provided. Present facilities permit simultaneous control of a newly launched spacecraft and a second one already in flight. In preparation for the increased number of U.S. activities in space, a capability is being developed for simultaneous control of either two newly launched spacecraft plus two in flight, or four spacecraft in flight. Advanced communications techniques are being implemented to make possible obtaining data from, and tracking spacecraft to, planets as far out in space as Jupiter.

The DSN is distinct from other NASA networks such as the Scientific Satellite Tracking and Data Acquisition Network (STADAN), which tracks Earth-orbiting scientific and communication satellites, and the Manned Space

Flight Network (MSFN), which tracks the manned spacecraft of the *Gemini* and *Apollo* programs.

The DSN supports, or has supported, the following NASA space exploration projects: (1) *Ranger*, *Surveyor*, *Mariner*, and *Voyager* Projects of JPL; (2) *Lunar Orbiter* Project of the Langley Research Center; (3) *Pioneer* Project of the Ames Research Center, and (4) *Apollo* Project of the Manned Spacecraft Center (as backup to the Manned Space Flight Network). The main elements of the network are: the Deep Space Instrumentation Facility (DSIF), with space communications and tracking stations located around the world; the Ground Communications System (GCS), which provides communications between all elements of the DSN; and the JPL Space Flight Operations Facility (SFOF), the command and control center.

The DSIF tracking stations are situated such that three stations may be selected approximately 120 deg apart in longitude in order that a spacecraft in or near the ecliptic

plane is always within the field of view of at least one of the selected ground antennas. The DSIF stations are:

Deep Space Communication Complex (DSCC)	Deep Space Station (DSS)	DSS serial designation ¹
Goldstone	Pioneer	11
	Echo	12
	Venus	13
	Mars	14
Canberra ²	Woomera	41
	Tidbinbilla	42
	Booroomba ³	43
	Johannesburg	51
Madrid ²	Robledo	61
	Cebreros ⁴	62
	Rio Cofio ³	63
	Cape Kennedy (Spacecraft Monitoring)	71
	Ascension Island ⁴ (Spacecraft Guidance and Command)	72

¹As of June 1966, DSIF serial designations (e.g., DSIF-11) are no longer used.
²Planned.
³Station not yet authorized.
⁴Station not yet operational.

JPL operates the U.S. stations, and will operate the Ascension Island Station. The overseas stations are normally staffed and operated by government agencies of the respective countries, with the assistance of U.S. support personnel.

The Cape Kennedy Station supports spacecraft final checkout prior to launch, verifies compatibility between the DSN and the flight spacecraft, measures spacecraft frequencies during countdown, and provides telemetry reception from lift-off to local horizon. The other DSIF stations obtain angular position, velocity (doppler), and distance (range) data for the spacecraft, and provide command control to (up-link), and data reception from (down-link), the spacecraft. Large antennas, low noise phase-lock receiving systems, and high-power transmitters are utilized. The 85-ft diameter antennas have gains of 53 db at 2300 MHz, with a system temperature of 55°K, making possible the receipt of significant data rates at distances as far as the planet Mars. To improve the data rate and distance capability, a 210-ft diameter antenna has been built at the Goldstone Mars Station, and two additional antennas of this size are planned for installation at overseas stations.

In their present configuration, all stations with the exception of Johannesburg, are full S-band stations. The Johannesburg receiver has the capability for L- to S-band

conversion. The Ascension Island Station will be basically full S-band when it becomes operational.

It is the policy of the DSN to continuously conduct research and development of new components and systems and to engineer them into the network to maintain a state-of-the-art capability. Therefore, the Goldstone stations are also used for extensive investigation of space tracking and telecommunications techniques, establishment of DSIF/spacecraft compatibility, and development of new DSIF hardware and software. New DSIF-system equipment is installed and tested at the Goldstone facilities before being accepted for system-wide integration into the DSIF. After acceptance for general use, it is classed as Goldstone Duplicate Standard (GSDS) equipment, thus standardizing the design and operation of identical items throughout the system.

The GCS consists of voice, teletype, and high-speed data circuits provided by the NASA World-Wide Communications Network between each overseas station, the Cape Kennedy Station, and the SFOF. Voice, teletype, high-speed data, and video circuits between the SFOF and the Goldstone stations are provided by a DSN microwave link. The NASA Communications Network is a global network consisting of more than 100,000 route mi and 450,000 circuit mi, interconnecting 89 stations of which 34 are overseas in 18 foreign countries. It is entirely operationally oriented and comprises those circuits, terminals, and switching equipments interconnecting tracking and data acquisition stations with, for example, mission control, project control, and computing centers. Circuits used exclusively for administrative purposes are not included.

During the support of a spacecraft, the entire DSN operation is controlled by the SFOF. All spacecraft command, data processing, and data analysis can be accomplished within this facility. The SFOF, located in a three-story building at JPL, utilizes operations control consoles, status and operations displays, computers, and data-processing equipment for the analysis of spacecraft performance and space science experiments, and communications facilities to control space flight operations. This control is accomplished by generating trajectories and orbits, command and control data from tracking and telemetry data received from the DSIF in near-real time. The SFOF also reduces the telemetry, tracking, command, and station performance data recorded by the DSIF into engineering and scientific information for analysis and use by scientific experimenters and spacecraft engineers.

N66 38547

II. Communications Research and Development

A. Digital Module Development: Clock Pulse Shaper

P. D. Herrin

1. Introduction

A clock pulse shaper has been developed for use as a standard digital module in the clocked logic systems of the Telecommunications Division. The circuit transforms sinusoidal waveforms from the clock generator into clock pulses that satisfy the triggering requirements of the digital flip-flop module. Tests show that the clock pulse shaper circuit more than meets the requirements imposed by the Division design standards.

2. Initial Design Specifications

The design of the shaper circuit was controlled by system requirements as well as by specifications previously established as standards for the module program. The circuit is required to operate reliably while being subjected to the following conditions: (1) A temperature range of 0°C to 110°C. (2) An input amplitude of 0.5 V to 1.5 V RMS. (3) An input frequency of 50 Hz to 3.5 MHz. (4) A $\pm 10\%$ variation of supply voltages. (5) A

5% variation of resistor values, and a 15% variation of capacitance about their nominal values. (6) Each transistor to have a minimum H_{FE} of 10.

The circuit should tolerate a substantial amount of ground noise superimposed upon its input. A common mode noise rejection of ± 4 V was established to insure reliability of circuit operation. Circuit specifications for normal operation are shown in Table 1.

Table 1. Circuit specifications—normal operation

Temperature	=	25°C
Source impedance	=	50 Ω
Input waveform	=	sinusoidal
Input amplitude	=	1.0 V RMS
Frequency range	=	1.0 kHz to 3.0 MHz
Power supply voltages	=	± 12.0 V DC
Power consumption	=	87 ma at +12.0 V 66 ma at -12.0 V
Total power dissipation	=	1.84 watts
Output waveform parameters		
Amplitude	=	+12V to 0 pulse
Rise time	=	8 nsec maximum
Fall time	=	10 nsec maximum
Pulse width	=	167 nsec nominal
Width adjustment	=	from 145 to 185 nsec

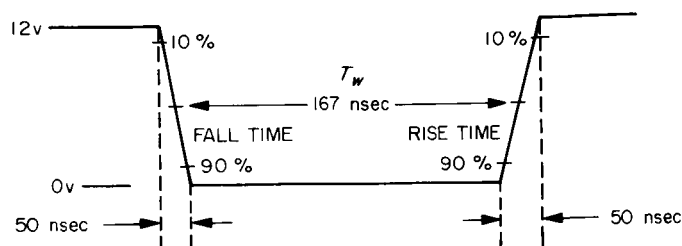


Fig. 1. Output waveform from clock pulse shaper

The required output parameters under worst-case conditions are as follows: Rise and fall times of the output pulse must not exceed 50 nsec. Pulse width at 50% amplitude is required to be 167 nsec $\pm 10\%$, as shown in Fig. 1. The circuit must produce the desired rise and fall times and pulse width while simultaneously subjected to all specified worst-case conditions listed in Table 2.

Table 2. Specifications—worst case operation

Temperature range	=	0°C to 110°C
Source impedance	=	50 Ω
Input amplitude	=	0.5 V to 1.5 V RMS
Frequency range	=	50 Hz to 3.5 MHz
Power supply voltages ($\pm 10\%$ variation)	=	± 10.8 V minimum ± 13.2 V maximum
Power consumption	=	78 ma at +10.8 V 60 ma at -10.8 V 95 ma at +13.2 V 72 ma at -13.2 V
Total power dissipation	=	at ± 10.8 V, 1.65 watts at ± 13.2 V, 2.0 watts
Resistor tolerance	=	5%
Capacitor tolerance	=	15%
Minimum transistor beta	=	10
Output waveform parameters		
Rise and fall times between 10% and 90% levels	=	less than 50 nsec
Pulse width at 50% pts	=	167 nsec, $\pm 10\%$

3. Circuit Description

The block diagram of Fig. 2 shows the circuits of the clock pulse shaper. Fig. 3 gives the circuit details.

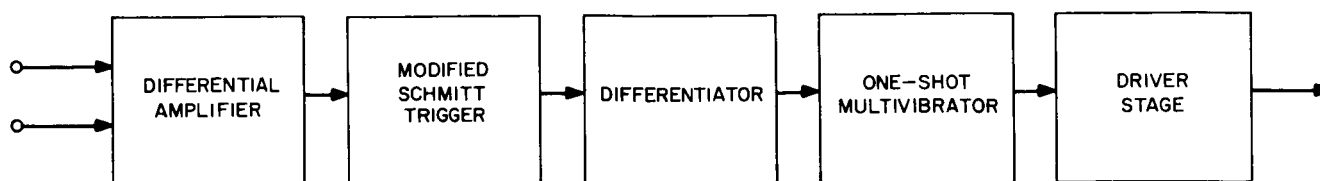


Fig. 2. Clock pulse shaper block diagram

a. The differential amplifier. The differential amplifier was selected primarily because of its ability to provide rejection of system ground noise. The amplifier transistors are used as nonsaturating current-switching devices which convert the input signal voltage into an output current that is sufficient to trigger the Schmitt circuit reliably.

The shield of the input cable serves as the input to the base of the second transistor in order to reduce the effect of system ground noise on circuit operation. Emitter currents to the differential transistors come from a constant-current source circuit which improves amplifier stability by reducing the effects of voltage variation. The amplifier requires a minimum difference-voltage swing of ± 0.3 V at the inputs for the following Schmitt trigger circuit to operate properly.

b. The modified Schmitt trigger. One function of the Schmitt trigger is to reduce the effect of low-level spurious noise on circuit operation. The other function is to modify the input waveform into an acceptable square wave with amplitude and switching characteristics sufficient to trigger the one-shot multivibrator reliably through the differentiator. This circuit is a modified version of the conventional Schmitt trigger. Biasing techniques using Zener diode voltage regulation produce an extremely stable and reliable circuit. The transistors of the trigger circuit operate in a nonsaturating mode to allow for faster switching times as well as to hold the output impedance fairly constant during switching.

c. The differentiator. A typical clamped RC differentiator is used to convert the square wave output of the Schmitt into a negative-going pulse sufficient to trigger the one-shot multivibrator under the worst-case conditions.

d. The one-shot multivibrator. The function of the one-shot multivibrator is to produce a positive-going pulse of a specified width that must remain within tolerance while subjected to worst-case operation. Since the output pulse width changes considerably with variations of supply voltages, a Zener diode was placed in the timing network to stabilize the width. To prevent the possibility of

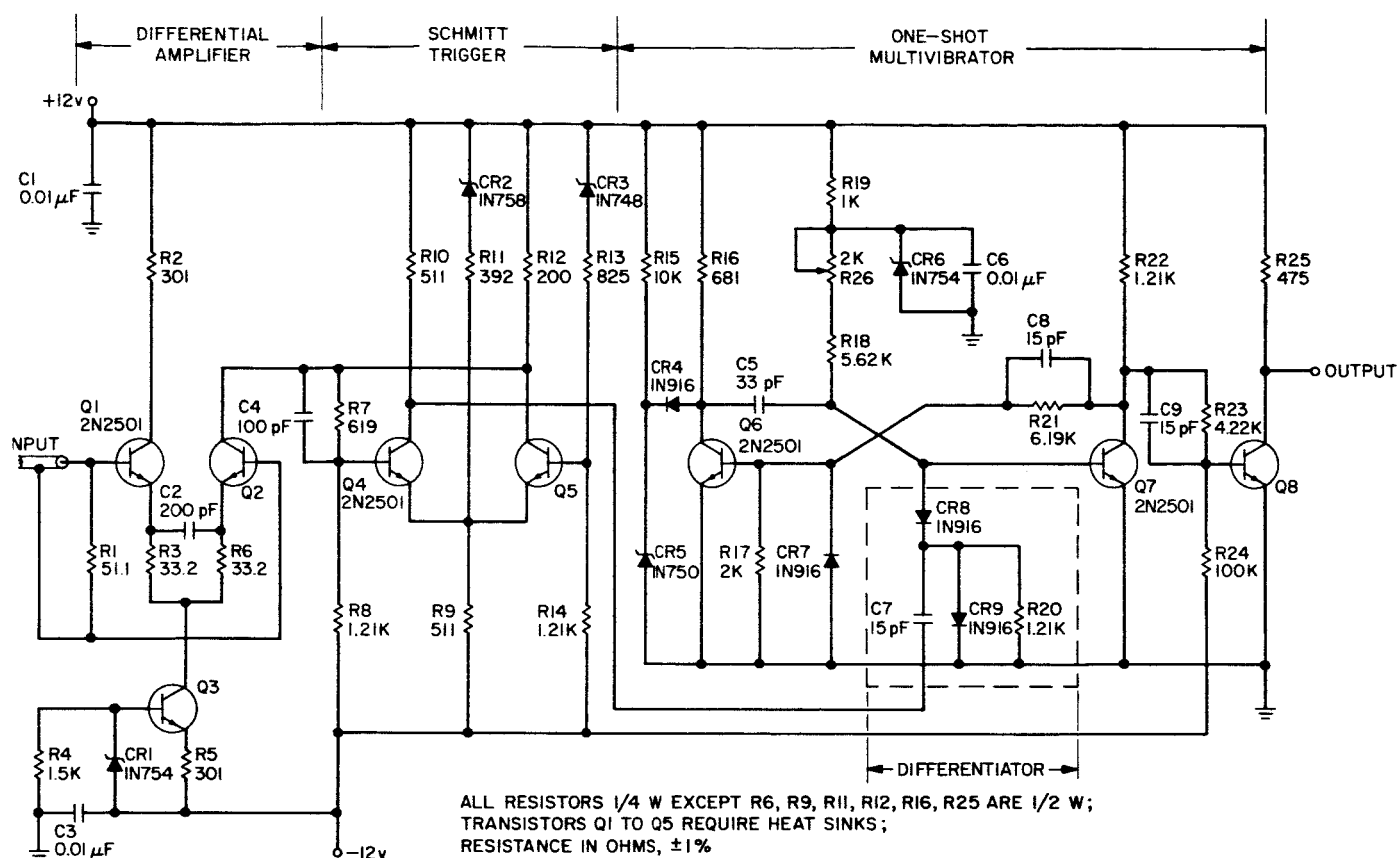


Fig. 3. Clock pulse shaper circuit

circuit oscillation, the Zener was bypassed to lower its impedance at higher frequencies.

In order to prevent reverse base-emitter breakdown in transistor Q7, a Zener voltage clamp was placed in the collector circuit of Q6. This reduces the voltage swing at the base of Q7. Reliability considerations warranted the addition of a diode on the base of Q8 to prevent base voltage from exceeding the emitter-to-base breakdown voltage.

4. Circuit Design Considerations

Division standards for circuit design require that a circuit be designed to function normally and reliably while simultaneously subjected to all specified worst-case conditions.

Each circuit of the clock pulse shaper has been worst-case designed to accommodate the various restrictive conditions. Through careful design, it was possible to develop a reliable circuit that exceeds the limitations imposed by worst-case requirements.

To insure a high amount of noise immunity, the shaper was designed to tolerate up to ± 4 V of common mode noise.

Each transistor was derated to improve reliability. For example, at maximum supply voltage levels during worst-case operation, each transistor is functioning below 35% of its total rated power dissipation, below 25% of its maximum current capability, and below 50% of its voltage ratings.

The basic shaper circuits have been designed to be relatively insensitive to beta change. Any 2N2501 transistor with a minimum beta of 10 may be used in any part of the total circuit without appreciably affecting its normal operating capabilities. Within a broad range of beta, noise rejection will not vary more than $\pm 10\%$.

Every circuit component has been derated adequately for long-term operation and reliability. Resistor tolerance may be 5% and capacitor tolerance may be 20% without affecting normal operation. Resistors operate at less than

50% of their power rating, and capacitors at less than 10% of their maximum voltage rating.

5. Test Results

Output parameters were recorded as the circuit was simultaneously subjected to all specified worst-case conditions. Rise and fall times were measured between the 10% and 90% levels of the pulse, and width was measured at 50% amplitude. All final data were compiled from laboratory tests measuring pulse width and rise and fall times versus temperature, input amplitude, frequency, and supply voltage variation.

Results of the test experiments are given in Table 3. The maximum rise time of 8 nsec and the maximum fall time of 13 nsec were considerably less than the required 50 nsec limitation.

Table 3. Test results

Parameter	Time, nsec		
	Min.	Typ.	Max.
Temperature 25°C			
Rise time	—	8.0	—
Fall time	9	10.5	12
Pulse width	165	167	176
Temperature 0°C			
Rise time	7	7.5	8
Fall time	8	9.5	11
Pulse width	165	167	174
Temperature 110°C			
Rise time	—	8.0	—
Fall time	12	12.5	13
Pulse width	163	167	173
Test conditions			
Input amplitude	0.5 V to 1.5 V		
Frequency range	50 Hz to 3.5 MHz		
Supply voltages	±10.8; ±12.0; ±13.2 V		

B. Information Systems: A Program for Finite Fourier Transforms

L. R. Welch¹

1. Introduction

In SPS 37-37, Vol. IV, pp. 295-297, an algorithm was described for computing Fourier transforms over finite abelian groups. This algorithm, which was specialized to ordinary Fourier transforms, has been previously published by Cooley and Tukey (Ref. 1) but is not well known among computer users. In order to determine the usefulness of the algorithm for computing spectra in the DSN,

a machine language, Fortran callable subroutine has been written for the SDS 930 computer. This program computes the sine and cosine sums for an integer-valued function defined on N points, where N is a power of 2.

2. Program Description

The computation proceeds by a recursive construction of arrays, the last of which contains the cosine-sine sums (see SPS 37-37). Special use is made of the facts that the functions are real valued and that each multiplication is used in more than one term. The following system of equations is the basis of computation. In these equations, $N_k = 2^k$, $M_k = N/N_k$ and C_k and S_k are matrices of dimension $N_k/2$ by M_k .

$$\begin{aligned}
 C_2(0,j) &= f(j) + f\left(j + \frac{N}{2}\right) + f\left(j + \frac{N}{4}\right) + f\left(j + \frac{3N}{4}\right) \\
 C_2(2,j) &= f(j) + f\left(j + \frac{N}{2}\right) - f\left(j + \frac{N}{4}\right) - f\left(j + \frac{3N}{4}\right) \\
 C_2(1,j) &= f(j) - f\left(j + \frac{N}{2}\right) \\
 S_2(1,j) &= f\left(j + \frac{N}{4}\right) - f\left(j + \frac{3N}{4}\right) \quad \text{for } j = 0, \dots, M_k - 1
 \end{aligned} \tag{1a}$$

¹Consultant, Electrical Engineering Department, University of Southern California, Los Angeles.

$$C_k(0,j) = C_{k-1}(0,j) + C_{k-1}(0,j + M_k) \quad (1b-i)$$

$$C_k\left(\frac{N_k}{2}, j\right) = C_{k-1}(0,j) - C_{k-1}(0,j + M_k) \quad (1b-ii)$$

$$C_k\left(\frac{N_k}{4}, j\right) = C_{k-1}\left(\frac{N_{k-1}}{2}, j\right) \quad (1b-iii)$$

$$S_k\left(\frac{N_k}{4}, j\right) = C_{k-1}\left(\frac{N_{k-1}}{2}, j + M_k\right)$$

$$C_k(m,j) = C_{k-1}(m,j) + \left(\cos \frac{2\pi m M_k}{N}\right) C_{k-1}(m,j + M_k) - \left(\sin \frac{2\pi m M_k}{N}\right) S_{k-1}(m,j + M_k) \quad (1b-iv)$$

$$S_k(m,j) = S_{k-1}(m,j) + \left(\cos \frac{2\pi m M_k}{N}\right) S_{k-1}(m,j + M_k) + \left(\sin \frac{2\pi m M_k}{N}\right) C_{k-1}(m,j + M_k)$$

$$C_k\left(\frac{N_k}{2} - m, j\right) = C_{k-1}(m,j) - \left(\cos \frac{2\pi m M_k}{N}\right) C_{k-1}(m,j + M_k) + \left(\sin \frac{2\pi m M_k}{N}\right) S_{k-1}(m,j + M_k) \quad (1b-v)$$

$$S_k\left(\frac{N_k}{2} - m, j\right) = -S_{k-1}(m,j) + \left(\cos \frac{2\pi m M_k}{N}\right) S_{k-1}(m,j + M_k) + \left(\sin \frac{2\pi m M_k}{N}\right) C_{k-1}(m,j + M_k)$$

The index j ranges from 0 to M_{k-1} , and, in Items (1b-iv) and (1b-v), m ranges from 0 to $N_k/4 - 1$. Undefined array components are not used in further computation and need not be computed.

3. Program Usage

Program specifications are as follows:

- (a) Name and parameter sequence:
Fouriers (IF, IOUT, ISIN, LOGN, Iscratch)
- (b) N , the number of points in the domain, must be a power of 2 and LOGN is the logarithm of N to the base 2.
- (c) $\{IF(I), I = 0 \text{ to } N - 1\}$ is the function to be transformed (integer valued)

(d) Iscratch is a work array of length N

(e) $ISIN(k) = (2^{23} - 1) * \sin 2\pi k/N, k = 0 \text{ to } N/4$

(f) $Iout(0) = N * \sum IF(I)$,
 $\{Iout(I), I = 1, N/2\}$ are the cosine sums,
 $\{Iout(I), I = N/2 + 1, N - 1\}$ are the sine sums.

4. Results

From the form of the program it can be concluded that the time of execution can be written as the following function of N :

$$T_N = a \cdot N \cdot \log_2 N + b \cdot N + c \cdot \log_2 N + d. \quad (2)$$

The subroutine was executed repeatedly for N equal to each of the powers of 2 from 8 to 1024. The elapsed times

were used to obtain the parameters in Eq. (2). The result is that the time of execution on the SDS 930 is approximately

$$T_N \simeq (31 \cdot N \cdot \log_2 N - 23 \cdot N + 320 \cdot \log_2 N) \mu\text{sec}. \quad (3)$$

Some measured times are as follows (1 part per 100 error):

$$\begin{aligned} T_{64} &= 12.3 \text{ msec} \\ T_{128} &= 27.0 \text{ msec} \\ T_{256} &= 60.2 \text{ msec} \\ T_{512} &= 0.134 \text{ sec} \\ T_{1024} &= 0.297 \text{ sec} \end{aligned} \quad (4)$$

Since single precision arithmetic was used, the program was executed with a variety of inputs in order to determine what types of errors in the output spectral coefficients could be expected. It was found that, for each N , the maximum absolute error was about $N/4$, independent of the amplitude of the spectrum. This occurred when the input was a cosine wave whose frequency was an odd multiple of $1/N$ and whose amplitude ranged from 10 to 8000. The error was insensitive to amplitude in the above range but fell off to zero as the amplitude went progressively through the integers 5, 3, 2, 1, 0. The major errors occurred at the sines and cosines of the input frequency and its third harmonic. Errors at other frequencies seemed normally distributed with $0.5N^{1/2}$ as standard deviation, again insensitive to amplitude.

5. Conclusions

The program reported here can serve as a high-speed medium accuracy Fourier transform routine. Since the errors are insensitive to amplitude, the input function should have as large an amplitude as possible without causing overflow. For example, if $N = 1024$ and the output terms are on the order of 10^6 then the maximum relative error would be 0.25×10^{-3} .

The maximum errors are probably systematic errors caused by the truncation of the results of multiplication as opposed to rounding to the nearest integer. It is conjectured that incorporating roundoff after multiplication would increase running time about 25% but reduce all errors to about $0.5N^{1/2}$. Incorporating double precision would contribute a factor of 2^{-23} to the size of errors but would increase the execution time by a factor of from 4 to 8.

C. Information Systems: A Double-Error-Correction Program for DSN Teletype

H. Fredricksen

1. Introduction

The teletype communications system employed in the DSN is discussed in SPS 37-34, Vol. III, pp. 64-68. The error characteristics of that system were investigated and reported on in that *Summary*. The feasibility of an error-correction scheme was considered, and a code providing a high degree of communications reliability was proposed. The error-correction was to be carried out in the Communications Processor—an SDS 910 digital computer. The error-correction program for encoding and decoding blocks of data has now been completed and successfully demonstrated in the laboratory. The capabilities of the code chosen were discussed in SPS 37-37, Vol. III, pp. 49-50. In this *Summary*, we report on the program which implements the code.

2. The Program

As implemented, the program takes a block of 8 symbols (32 binary bits) and encodes them into a word of 15 symbols (75 binary bits). Each symbol is constrained to have even parity to make messages compatible with accepted communication practices. The 15 symbols are broken into classes of 8 information symbols, 6 check symbols and 1 synchronization symbol. The distance between code words in the code is 7, so 3 errors can be corrected. The full error-correction capability is not used; only 2 errors are corrected, but up to 4 errors are then detected. The synchronization symbol is employed to guard against errors introduced by the insertion or deletion of symbols during transmission. The program as implemented in the 910 requires (2600) storage locations.

3. Encoding

The encoding program is located in memory locations 2400 to 2750 with access at 2400. As in most coding schemes, the encoding phase is almost trivial. Eight information symbols (elements of the 16 element field) are typed into the computer along with the (fixed) synchronization symbol, the sync symbol being inserted first. Six check symbols are computed by the recursion $x^9 = c_8 x^8 + c_7 x^7 + \dots + c_0 x^0$, where the x vector (x^8, x^7, \dots, x^0) is the vector of information and sync symbols (x^0 the sync symbol), and the c vector is ($\beta^3, \beta^{13}, \beta^{10}, \beta^{10}, \beta^{14}, \beta^7, \beta^3, \beta, \beta^0$) where

β satisfies $y^4 = y + 1$. The powers of β are stored in memory locations 2126 to 2144, and the c_i are stored in memory locations 2552 to 2562. After the check symbols have been computed, a permutation $(a_1 a_2 \cdots a_7 a_0 a_8 \cdots a_{14})$ is performed on the encoded word which moves the sync symbol into the middle of the word. This permutation is performed so that a deletion of a symbol from a word of the form $SSabc \cdots k l S$ followed by another word of the same form, where S is the sync symbol and a, b, c , etc. are any symbol, will be detected. After the message is encoded, it can be transmitted by any method desired. The encoding requires only milliseconds to complete.

4. Decoding

This phase of the program is the most interesting and most complex, requiring most of the storage and most of the time. The decoding of correctly synchronized words containing two errors, which is the worst case attempted, requires approximately 0.05 sec. This compares with the transmission time of about 2.5 sec for a 15 symbol word so that real-time decoding is assured. In the event of zero or one error the decoding is done in approximately half the time for the two error case. In the event of a sync error or more than two errors, a repeat transmission request will be initiated. The detection of 3 or more errors requires about the same time as the correction in the 2-error case, whereas the detection of a sync error is done immediately and requires only milliseconds.

The error-correction routine follows very closely the method outlined in Ref. 2. The received message is stored in two locations in memory (2206 to 2224 and 640 to 656). This is done so that when corrections are made to the copy in locations 2206 to 2224 the uncorrected version is still available for examination. The entry to the decoding program is located at 600, and to about 700 the program is involved with reading in the received message. The test for sync error is performed at 705. If a sync error has occurred, the repeat request is made. If not, then the error-correction phase is initiated at location 713.

Locations 713 to 760 and 200 to 246 are used to compute the S_j discussed in Ref. 2. The S_j are given by the Reed formula

$$S_j = \sum a_i \beta^{ij}$$

where the a_i are the received symbols, and the β 's are defined above. Addition is, of course, done term-wise modulo 2. Locations 200 to 246 contain a subroutine to compute the product ij (modulo 15) for numbers i, j in the range 0 to 15. (A *multiply* command is not available on

the 910.) Initially only S_1 , S_2 , and S_3 are computed before the test for a single error is performed. If it is found that more than one error has occurred, S_4 and S_5 are computed to test for a double error. The test for single and double errors is essentially to see if certain determinants are zero.

The test for zero errors is performed in 762 to 1004 with entry at 1001. The test for a single error as well as its correction is performed in locations 100 to 162 with entry at location 100. If the test for single errors indicates that multiple errors have occurred, the test for double errors is begun. This routine is entered from the single-error routine at location 1004, and the test for double errors and their correction requires the contents of memory locations 1004 to 1305 and 2266 to 2357.

In the event 0, 1, or 2 errors have been made in transmission and after they have been corrected, the corrected version of the received message is outputted. In the laboratory, this is done on the typewriter. When the Communications Processor is installed at the remote sites, all transmissions to the station will be intercepted, interpreted, corrected if necessary, and routed to the proper location. In the laboratory edition of the CP, the output routine is located in locations 300 to 453 with entry at 410. Both the received and corrected messages are outputted with the received version appearing first. Also, the form of the output message differs from the input in two respects. Firstly, the sync symbol is reinstalled in the first position of the sequence. Secondly, whereas the received message is interpreted as 15 symbols from a 16 element field and characterized by a character from the keyboard of the typewriter, the output version of the message regards the symbols as 4-tuples of 0's and 1's. This difference is not major, but should be noted.

5. Output

Table 4 gives some samples of the output of the program. Each group consists of the information symbols, the encoded word, the received version of the transmitted word, and the received and corrected versions of the message in the form of binary 4-tuples. As explained above, a synchronization symbol and 8 information symbols serve as the input to the encoding program. All input and output appears at the typewriter, and the first line of Table 4 is the input to the encoding program. In the encoder, the 6 check symbols are computed, the permutation of the symbols is performed, and the encoded word is the output which appears in the second line of the table. Notice the sync symbol which was the first symbol of the

Table 4. Output of program

a. No error			b. Double error (Cont'd)		
Information and sync symbols 00000001 181:53 00000000 181:53 00000000 181:53 1. 0000 0000 Sync symbol 2. 0000 0000 3. 0000 0000 4. 0000 0000 Received and corrected versions 5. 0000 0000 6. 0000 0000 No errors 7. 0000 0000 8. 0000 0000 9. 0001 0001 10. 1000 1000 11. 0001 0001 12. 1101 1101 13. 0101 0101 14. 0011 0011 15. 1010 1010			10. 1101 0100 Corrected errors 11. 1101 0100 12. 1101 1101 13. 0000 0000 14. 0001 0001 15. 1000 1000		
b. Double error			c. Sync error		
Information and sync symbols 01928476 : 44: 018 1928476 0 : : : 018 1928476 0 : : : 018 1. 0000 0000 Sync symbol 2. 0001 0001 3. 1001 1001 4. 0010 0010 5. 1000 1000 6. 0100 0100 7. 0111 0111 8. 0110 0110 9. 1101 1101			099887766 9988776 0 6 = > 80 ✓ 9987760 6 = > 80 ✓ 2 Sync		
d. Single error					
Information and sync symbols 099887766 9988776 0 6 = > 80 ✓ 0988776 0 6 = > 80 ✓ 1. 0000 0000 Sync symbol 2. 0000 1001 Corrected error 3. 1001 1001 4. 1000 1000 5. 1000 1000 6. 0111 0111 7. 0111 0111 8. 0110 0110 9. 0110 0110 10. 1011 1011 11. 1110 1110 12. 1000 1000 13. 0000 0000 14. 1111 1111 15. 1010 1010					

input line has been permuted to the middle of the encoded word. The third line is the input to the decoder. In actual operation, this will be a received message and when read into the program will be examined for errors. Again the sync symbol appears as the 8th symbol of the word. If it does not, a "sync error" has occurred and a retransmission is requested. If no sync error is observed, the test for additive errors is performed; if a correctible error has occurred, the correction is made and the received and corrected versions of the message are typed out on the next 15 lines (as 4-tuples). The sync symbol has been repositioned as the first symbol of the message with the 2nd through 9th being the information symbols.

In particular, in the first example, the zero symbol (0 = 0000) is taken as the sync symbol and the eight information symbols are 00000001. These are mapped into the 15-tuple 00000000181:53—by the encoder. The

last symbol is 1010 in the SDS typewriter code. This is a space, hence, it appears as a blank. The encoded and received versions of the message are identical; no errors have occurred in transmission. Therefore, in the next 15 lines there are no difference in the two columns.

The second example is like the first, but the received message has two errors. The tenth and eleventh symbols should be 4(= 0100), but were received as : (= 1101). However, all patterns of two errors are correctible. Therefore, in lines ten and eleven the two columns differ, the first column being the received (incorrect) version of the message and the second column the corrected version.

In the third example, the symbol appearing in the position of the sync symbol is not the sync symbol (0). Thus a sync error has occurred and retransmission is requested. Note that either the 3rd or 4th symbol has been deleted

in transmission. Furthermore, the 1st symbol from the next word has become the 15th symbol of this word. When resynchronization has occurred, the 15th symbol will be the blank symbol (1010) as it should be.

The fourth example is similar to the second, but with a single error in the 2nd symbol. The incorrect and corrected versions are given.

Experiments will be performed to demonstrate this code, using the Teletype Interface Console that has been installed for use with the SDS 910. The NASCOM has assigned the call letters JGUS for the experimental teletype station set up at JPL in Bldg. 238-432 for this purpose.

D. New Scientific Data Systems (SDS) Digital Computer Programs

F. B. Leppa, G. B. Bigler, C. McNeal, and M. Dyson

The following computer programs have been written by the Systems Data Analysis Group for Scientific Data Systems (SDS) Digital Computers. Three programs have been completed since the last reporting period. They are presented as abstracts identified by their DSIF Program Library Numbers.

1. External Display Test Program: DSIF Library No. DOI-5034-TP

G. B. Bigler

The purpose of this program is to test two external display panels associated with the Digital Instrumentation Subsystem. These panels are located in the station manager's console and in the receiver subsystem console.

In order to test all bit configurations possible, a set of ten numbers is generated. These numbers are then displayed with the four possible color combinations at a reasonably slow rate such that the operator may observe the displays.

This program will operate in the SDS 910 or 920 and takes approximately 2 min 15 sec to run a complete test.

2. Symbolic Paper Tape Editor: DSIF Library No. DOI-5022-OP

G. B. Bigler

This computer program is a modified version of the standard SDS Symbolic Paper Tape Editor. The original SDS version was not a complete self-loading relocatable program and was impossible to use under certain circumstances. Therefore, the program was rewritten using Symbolic language and provided with a relocatable bootstrap loader.

This program provides the following capabilities:

- (1) Reproduction of paper tapes.
- (2) Listing of paper tapes.
- (3) Generation of paper tapes from the keyboard console.
- (4) The insertion and deletion of specific records on a paper tape. The various options are controlled through use of the breakpoint switches and input control messages.

3. Real Time Star Track: DSIF Library No. DOI-5000-OP

C. McNeal

The Real Time Star Track Program (RTST) computes data which can be used to compute coefficients for antenna systematic pointing error functions that describe Local Hour Angle and Declination pointing errors.

This is accomplished by tracking an optical star or a radio source and comparing observed Local Hour Angle and Declination values with predicted values. The differences (residuals) between observed and predicted values over a range of declinations from +40 deg to -40 deg for full tracks (270° to 90° Local Hour Angle) are punched on teletype tape.

If antenna systematic pointing error coefficients have previously been computed by another program, RTST uses them to compare observed and calculated residuals and every hour on the hour lists an RMS value of the differences during the hour.

The program utilizes interrupts to pick up the observed values of GMT, Local Hour Angle and Declination from the Tracking Data Handling Subsystem (TDH).

Star position calculation is carried out as follows: Star coordinates referred to the current epoch are reduced to the apparent place for each instant of time picked up from the TDH.

The apparent place of a star is its position at a certain date on the celestial sphere and referred to the actual

equator and equinox of date. The apparent place on a certain date is obtained from the mean place at the beginning of the year by applying corrections for precession, nutation, aberration (using independent day numbers on mag tape) and proper motions for the fractions of the year.

The position of the star is calculated for a given instant of time. This is done by computing the GMT of local meridian crossing. This is simple because at the instant of

local meridian crossing the local sidereal time is equal to the right ascension of the source. Using the sidereal rate, the coordinates for any point in time are then computed. The inverse of refraction correction is then added to the computed points. The computed star position is then subtracted from the observed point to form the residual.

A teletype tape is punched by utilizing a communications buffer and end-of-transmission interrupts. Infor-

STA	GMT	HAO	HAO-HAC	ELHA	DECO	DECO-DECC	EDEC	DAY
11	03 55 01	65.423	-0.032	0.000	343.379	-0.024	0.000	127
11	03 56 01	65.647	-0.057	0.000	343.379	-0.025	0.000	127
11	03 57 01	65.927	-0.025	0.000	343.379	-0.027	0.000	127
11	03 58 01	66.159	-0.042	0.000	343.379	-0.029	0.000	127
11	03 59 01	66.405	-0.044	0.000	343.379	-0.031	0.000	127
11	04 00 01	66.651	-0.046	0.000	343.379	-0.032	0.000	127
11	04 01 01	66.905	-0.040	0.000	343.379	-0.034	0.000	127
11	04 02 01	67.151	-0.042	0.000	343.379	-0.036	0.000	127
11	04 03 01	67.399	-0.042	0.000	343.385	-0.032	0.000	127
11	04 04 01	67.651	-0.038	0.000	343.389	-0.030	0.000	127
11	04 05 01	67.899	-0.038	0.000	343.389	-0.032	0.000	127
11	04 06 01	68.141	-0.044	0.000	343.389	-0.035	0.000	127
11	04 07 01	68.377	-0.055	0.000	343.395	-0.031	0.000	127
11	04 08 01	68.641	-0.038	0.000	343.395	-0.033	0.000	127
11	04 09 01	68.899	-0.028	0.000	343.395	-0.036	0.000	127
11	04 10 01	69.135	-0.039	0.000	343.395	-0.038	0.000	127
11	04 11 01	69.377	-0.044	0.000	343.401	-0.035	0.000	127
11	04 12 01	69.627	-0.041	0.000	343.401	-0.037	0.000	127
11	04 13 01	69.879	-0.035	0.000	343.401	-0.040	0.000	127
11	04 14 01	70.127	-0.034	0.000	343.407	-0.037	0.000	127
11	04 15 01	70.377	-0.030	0.000	343.407	-0.040	0.000	127
11	04 16 01	70.629	-0.025	0.000	343.415	-0.035	0.000	127
11	04 17 01	70.873	-0.027	0.000	343.415	-0.039	0.000	127
11	04 18 01	71.113	-0.032	0.000	343.413	-0.044	0.000	127
11	04 19 01	71.361	-0.030	0.000	343.421	-0.040	0.000	127
11	04 20 01	71.613	-0.023	0.000	343.421	-0.044	0.000	127
11	04 21 01	71.863	-0.018	0.000	343.421	-0.048	0.000	127

HEADER EXPLANATIONS:

STA	IS THE DSIF STATION NUMBER
GMT	IS GREENWICH MEAN TIME
HAO	IS OBSERVED LOCAL HOUR ANGLE
HAO-HAC	IS OBSERVED LOCAL HOUR ANGLE MINUS PREDICTED LOCAL HOUR ANGLE
ELHA	IS (HAO-HAC) MINUS THE PREDICTED VALUE OF (HAO-HAC)
DECO	IS OBSERVED DECLINATION
DECO-DECC	IS OBSERVED DECLINATION MINUS CALCULATED DECLINATION
EDEC	IS (DECO-DECC) MINUS THE PREDICTED VALUE OF (DECO-DECC)
DAY	IS DAY NUMBER CORRESPONDING TO GMT TIME

Fig. 4. Typical output of Real-Time Star Track Computer Program DOI-5000-OP

mation contained on the teletype tape is as follows: Station number, GMT, hour angle observed, hour angle residual, difference between observed hour angle residual and computed residual, observed declination residual, difference between observed declination residual and computed residual, and the day number. If angular correction coefficients representing the previous history of station pointing error are not available, ELHA and EDEC in Fig. 4 are output as zeroes.

4. Reformatting TTY Predicts to Magnetic Tape: DSIF Library No. DOI-5004-OP

M. Dyson

The purpose of this program is to read Tracking Data Predict Tapes (TTY), check for transmission errors—correcting or deleting data accordingly, and reformatting the information for output to magnetic tape/or paper tape.

Since the program must work at remote DSIF stations where teletype input tapes can be garbled, an elaborate search and check operation must be performed to save as much of the data as possible. The program has several input parameters which allow the operator to control use of the various check routines.

The magnetic tape output contains time-labeled angle and doppler data which can be used by tracking data monitor programs. The paper tape output consists of time-labeled angle data and can be used as a drive tape for antenna pointing.

The program will operate in an 8K SDS 920 Computer and at present will not fit into an SDS 910 with the same amount of memory. The programming language used is Fortran II with Symbol subroutines to read and convert the Baudot coded teletype tapes.

E. Wide-Band Receiver System Development: Wide-Band Power Multiplier

K. Schreder and G. Lutes

1. Introduction

The Wide-Band Receiver System (WBRS) is an S-Band system which is suitable for operating over the Deep Space Network (DSN) and the Manned Space Flight Net-

work (MSFN) frequency bands. As reported in SPS 37-30, Vol. III, pp. 86-92, the WBRS is to cover this frequency range with no tuning adjustments. For this wide tuning range to be possible, the critical modules in the exciter chain of the transmitter section and the local oscillator chain of the receiver section must be broadband modules. (The block diagram and the section description of the WBRS are reported in SPS 37-33, Vol. III, pp. 96-107.)

One of the wide bandwidth modules will be discussed in this report. The module is the $\times 32$ Frequency Multiplier which is used in both the exciter and local oscillator sections. The module has been separated into two sections. A $\times 8$ portion which is part of the Goldstone Duplicate Standard (GSDS) Block III system configuration and a $\times 4$ power amplifier portion. The $\times 4$ part is the Wideband Power Multiplier (WPM) which will be discussed in this report.

2. Circuit Description

The WPM consists of two chassis. The chassis are machined, gold-plated cavity type conforming to the two standard DSN module configurations. Fig. 5 shows the chassis and components of the two doublers through the power splitter. Fig. 6 shows the chassis and components of the last three power amplifiers and the strip line.

Design goals for the module are: (1) output center frequency of 280 MHz, (2) 13 MHz output bandwidth, (3) 2 watts CW output power, and (4) no indication of instability within the -40 db bandwidth. The final circuit configuration is shown in Figs. 7 and 8. Due to system constraints the bandwidth, power and stability were the parameters which were maximized. The bandwidth was maximized by using wide bandwidth circuits and untuned output stages. The power was maximized by building power amplifier stages following the multiplier stages. The stability was maximized through conservative design of simple circuits and extreme caution with impedance matching and decoupling networks. A description of the WPM circuit will follow.

The input circuit is used to provide a low input voltage standing wave ratio (VSWR) over the -1 db bandwidth. The first stage, Q1, is a standard amplifier stage. It provides isolation between the $\times 2$ multiplier (doubler) and the input. It also limits hard, to produce a constant voltage to the multiplier. The doubler is a very broadband, full-wave circuit. The diodes are matched pairs to suppress the fundamental frequency. The doubler circuit produces harmonic frequencies of the doubled frequency

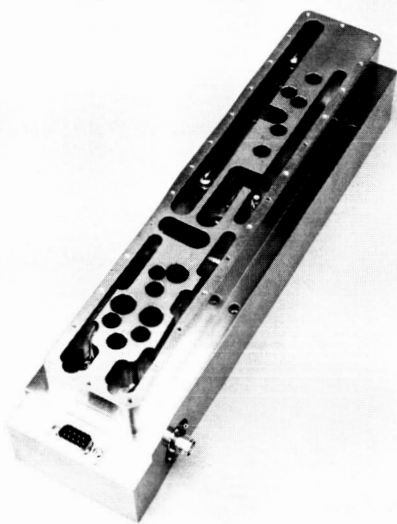
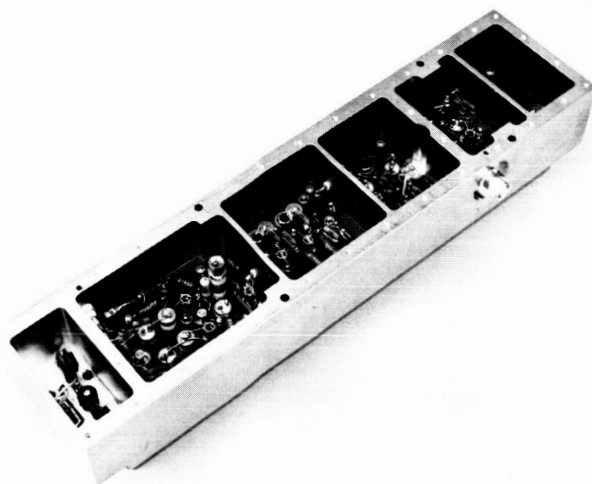
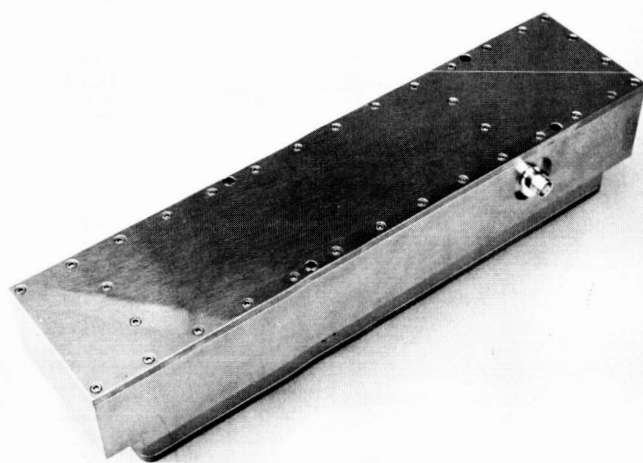


Fig. 5. Completed chassis, top view, and bottom view of $\times 4$ frequency multiplier of WPM

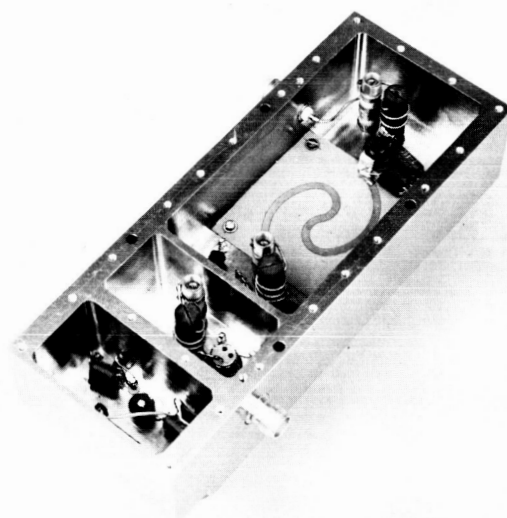
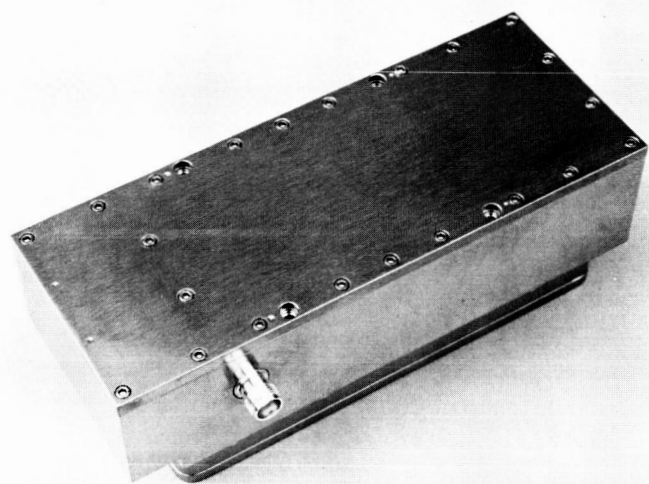


Fig. 6. Completed chassis and top view of power amplifier of WPM

such as the 4th, 6th, 8th, etc. Therefore, a broad passband coaxial filter is required to reduce the undesired harmonics and to suppress the fundamental frequency further than can be achieved by the matching diodes. The next stage consisting of Q2 and Q3 again are standard amplifier stages. As in the first stage, these stages provide isolation between doublers, and voltage limits. This limiting maintains a constant voltage at the input to the second doubler. (It is important to keep a constant voltage at the input to the doubler since the overall efficiency and carrier suppression are optimized for a small range of voltages.) The second doubler uses the same circuit as the first doubler. The matched diodes are more important in the second doubler than the first due to the higher fundamental frequency.

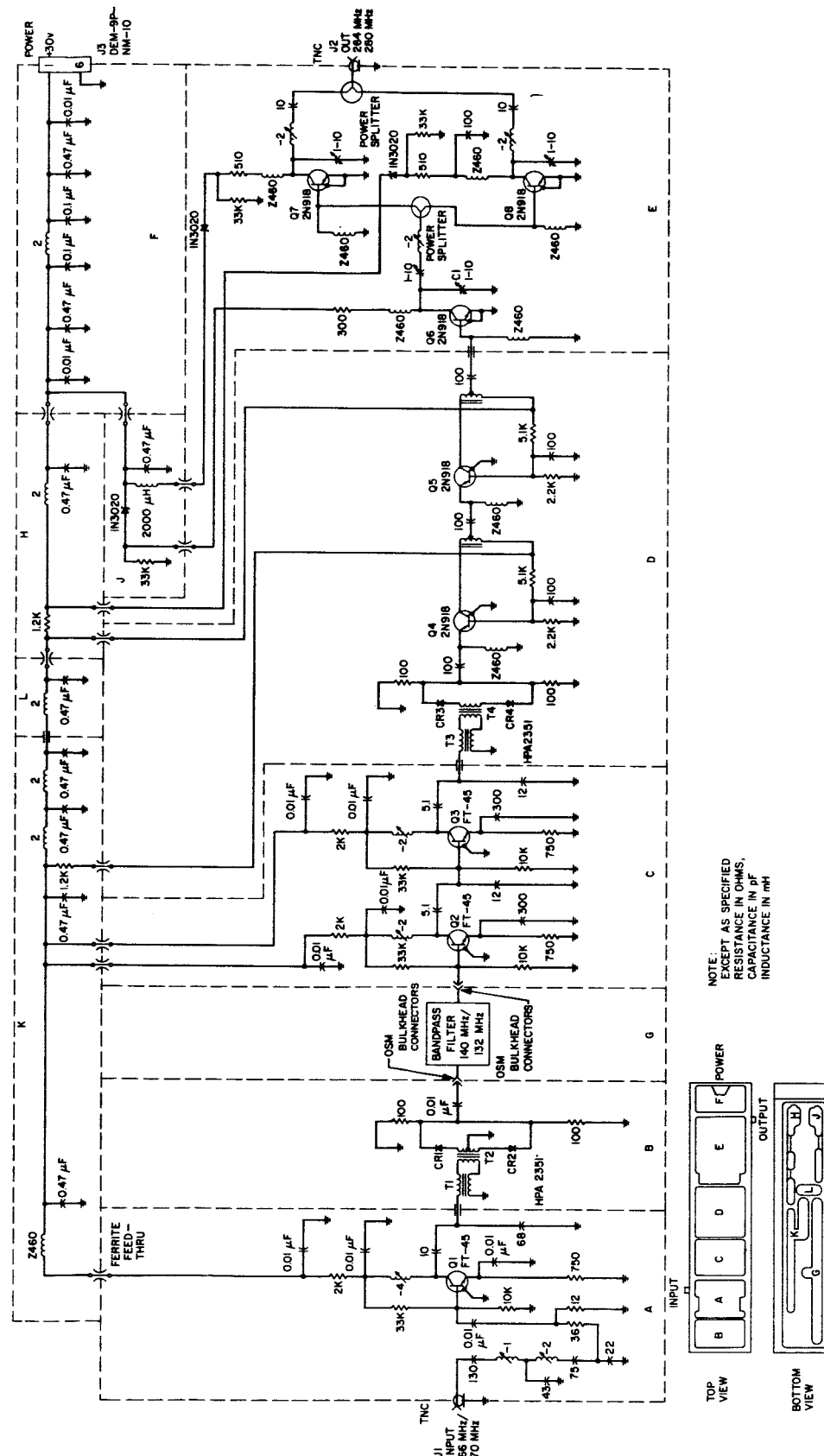


Fig. 7. Schematic of X 4 frequency multiplier of WPM

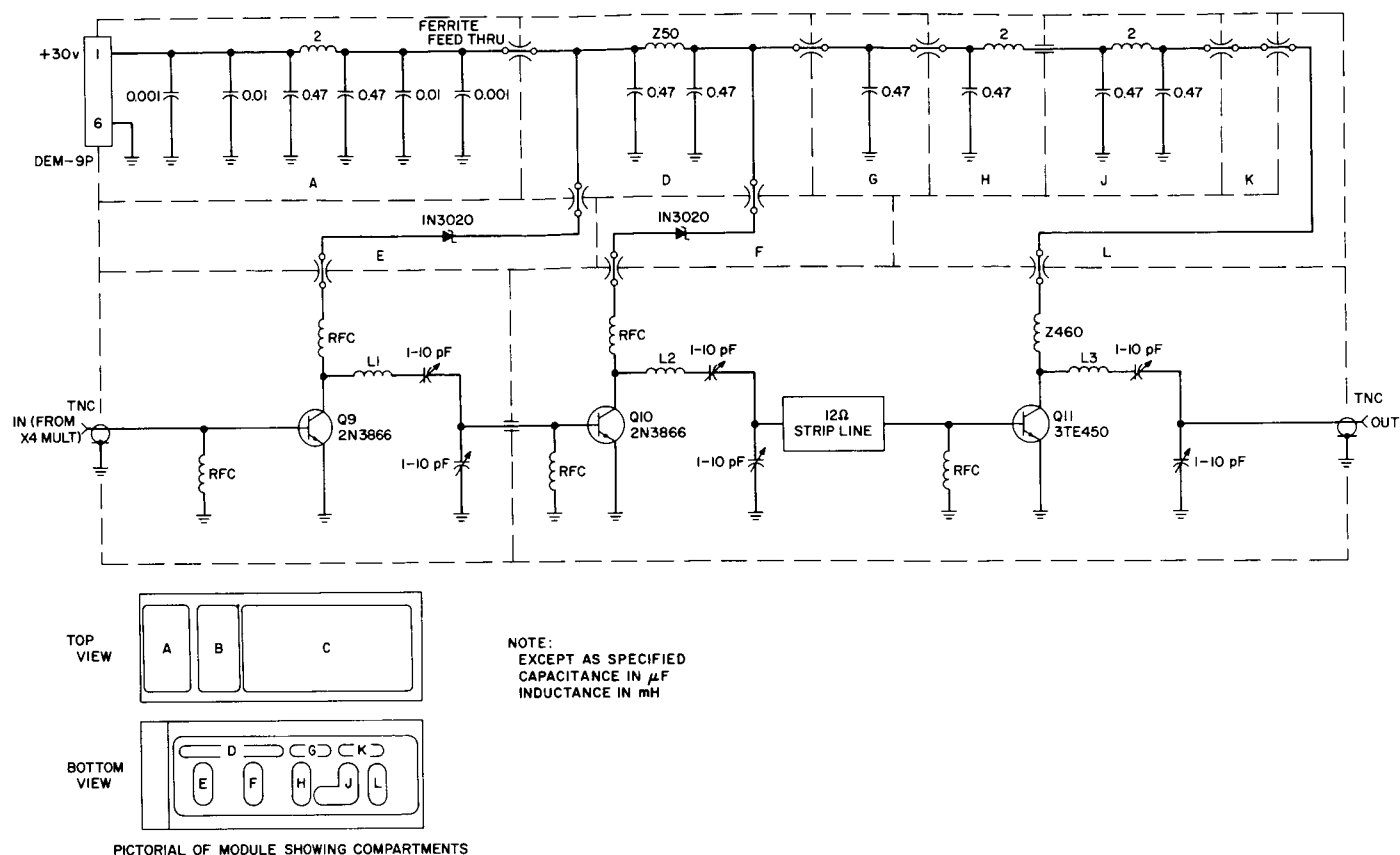


Fig. 8. Schematic of power amplifier of WPM

Following the second doubler is the power amplifier stage. Two extremely broadband amplifiers, Q4 and Q5, are first. The gain of each amplifier is determined by the impedance transformation only. The broadband impedance transformation is achieved by using a balun. A driver amplifier, Q6, was required to drive the power splitter. (The 2N918 transistor was found to be very stable at 280 MHz). The power splitter approach was used to achieve greater than 90 mv of output power out of the power adder without any loss in stability. The parallel amplifiers, Q7 and Q8, each produce half of the output power and can therefore be operated safely within the transistor power rating. The amplifiers were not stagger tuned as sufficient bandwidth was achieved using the standard technique of tuning for maximum power.

The final three amplifiers, Q9, Q10 and Q11, in the power amplifier stage are standard designed amplifiers. A quarter-wave impedance transformation network (strip line) is required to match the output impedance of Q10 to the input impedance of Q11. (The input resistance of Q11 is nominally 3 to 4 ohms.)

3. Performance Characteristics

The basic design criterion which was adhered to throughout the WPM design was simple, stable circuits with a minimum number of tuning adjustments. From Figs. 7 and 8 the number of tuning elements is 17 with a total of 11 transistor amplifiers. The final power amplifiers require two tuning elements to be able to adjust for center frequency and power match. The simple circuits and relatively few tuning elements allow the WPM to be tuned in successive order when using full input power (+13 dbm) and rated voltage (+30 V DC). The stability of the circuit allows for this type of tuning since there are no parasitic oscillations. Fig. 9 shows the spectrum of the output power of the WPM between the -40 db bandwidth points. (The multi-exposed pictures were taken by superimposing the carrier.) The output load may also be removed with full input power without damaging any transistors. Rated output power was achieved again when the load was replaced. A spectrum picture of the output voltage with no load is shown in Fig. 10. (This picture was taken the same way the picture of Fig. 9 was taken.) Only one point of instability (parasitic oscillation) was

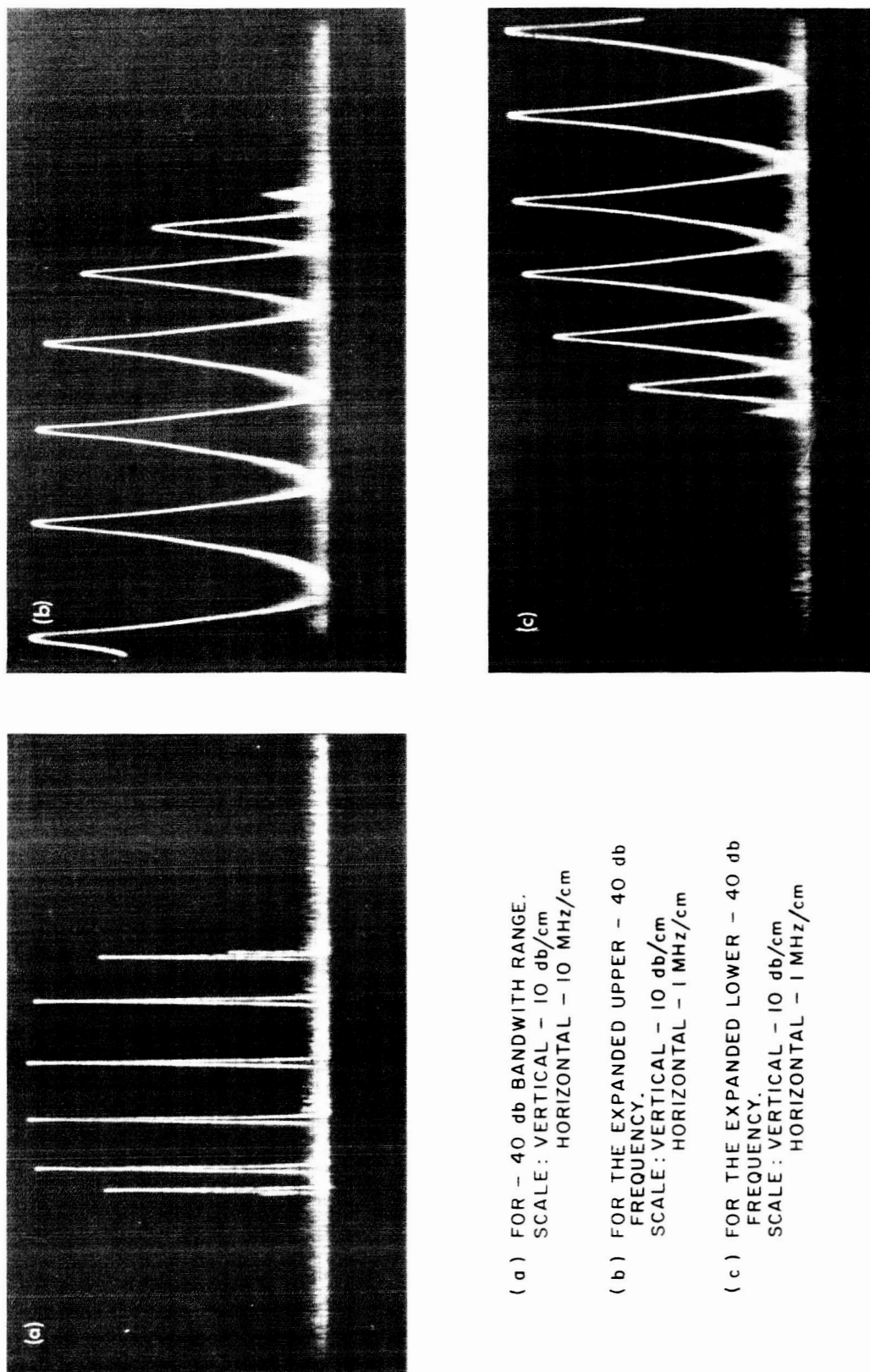


Fig. 9. Power spectrum of a superimposed carrier

SCALE: VERTICAL - 10 db/cm
HORIZONTAL - 10 MHz/cm

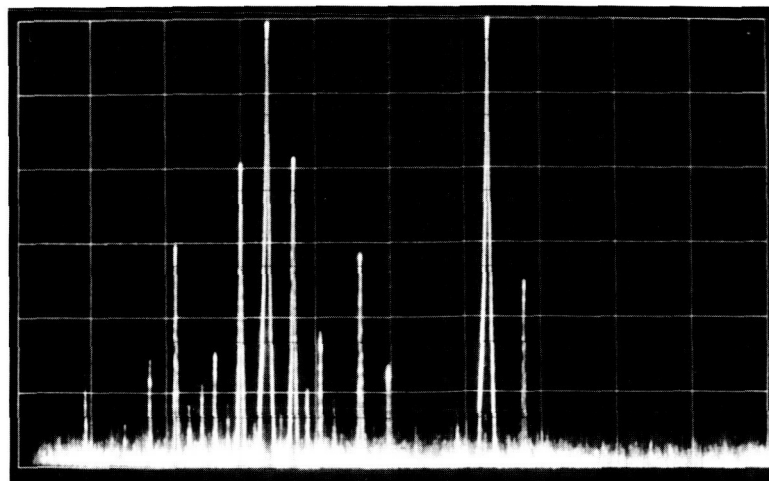


Fig. 10. Voltage spectrum of a superimposed carrier with no load

SCALE: VERTICAL - SHOWN
HORIZONTAL - 4 MHz/cm

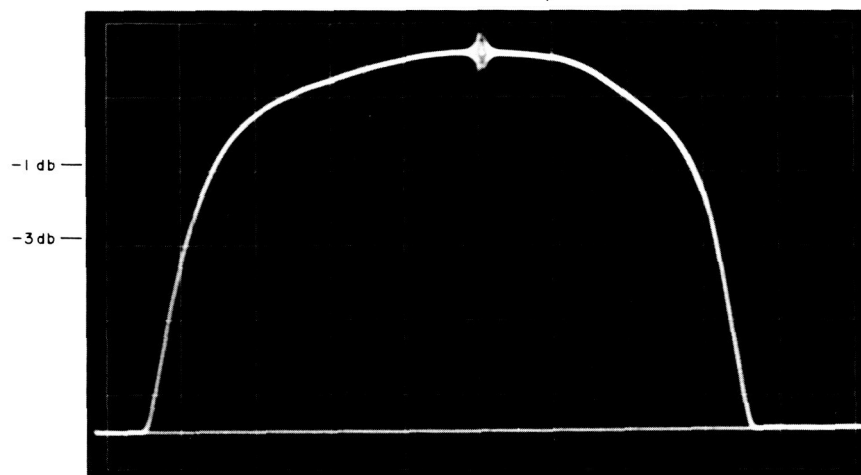


Fig. 11. Bandwidth of WPM with marker at 280 MHz

found over a 100-MHz bandwidth about the center frequency which is shown in Fig. 10.

The bandwidth of the WPM with 3 watts of output power and +13 dbm input power is shown in Fig. 11. The symmetrical -1 db bandwidth is 16 MHz and the symmetrical -3 db bandwidth is 24 MHz.

The input VSWR is less than 1.10 over the entire -3 db bandwidth for input power variations from +7 to +19 dbm. The harmonic distortion is shown in Fig. 12 with no filter on the output of the WPM. Since there is no filter

after the second doubler, the higher harmonic frequencies such as the 4th and 6th and the fundamental frequency are not totally suppressed. With a coaxial filter on the output of the WPM, the harmonic distortion is less than 40 db below the center frequency carrier throughout the -1 db bandwidth range which is shown in Fig. 13.

The limiting curve of the WPM is shown in Fig. 14. The sharp cutoff in output power is due to the class C operation of the last three amplifiers, for there must be a minimum input power to turn the amplifiers on.

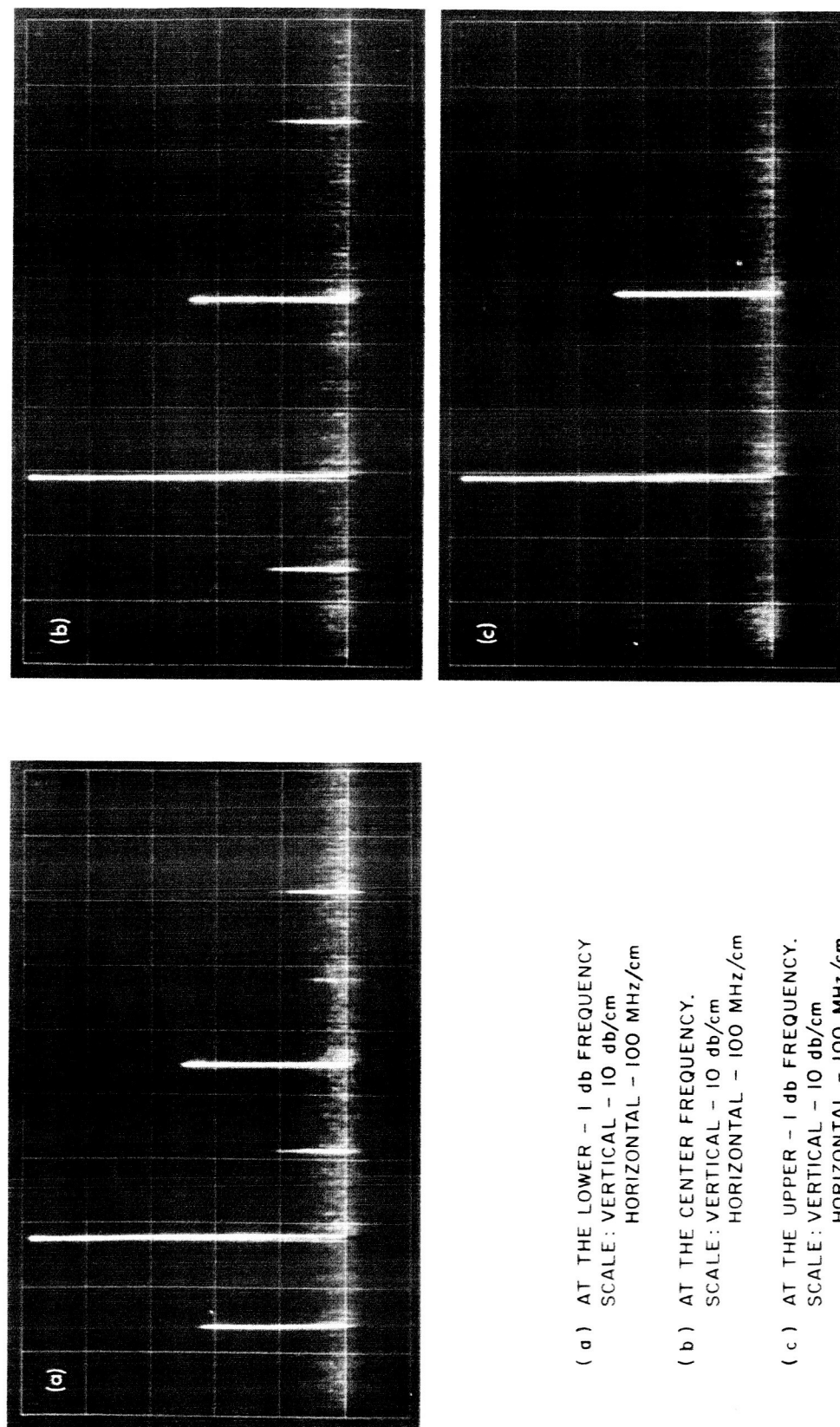
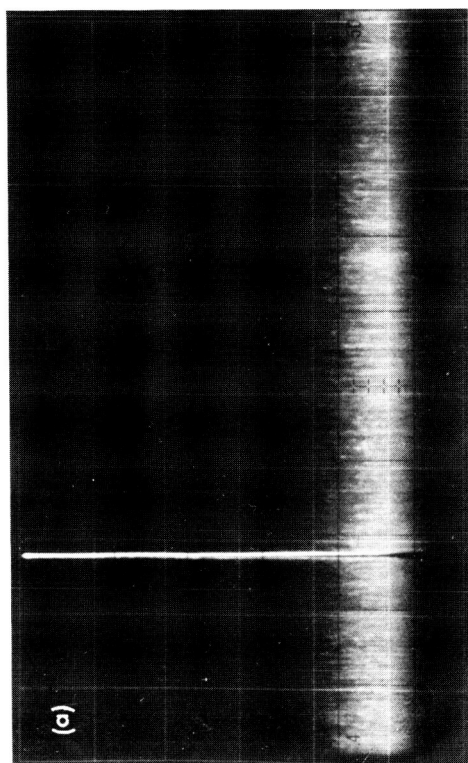
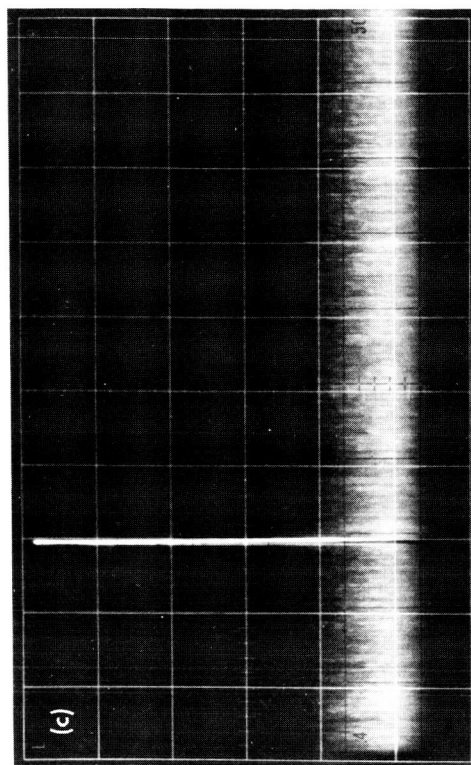
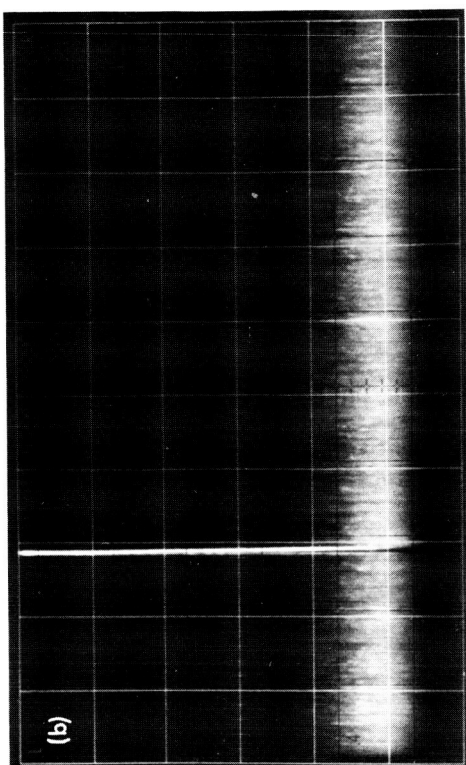


Fig. 12. Output harmonic distortion with no filter



(a) AT THE LOWER - 1 db FREQUENCY.
SCALE: VERTICAL - 10 db/cm
HORIZONTAL - 100 MHz/cm

(b) AT THE CENTER FREQUENCY.
SCALE: VERTICAL - 10 db/cm
HORIZONTAL - 100 MHz/cm

(c) AT THE UPPER - 1 db FREQUENCY.
SCALE: VERTICAL - 10 db/cm
HORIZONTAL - 100 MHz/cm

Fig. 13. Output harmonic distortion with coaxial filter

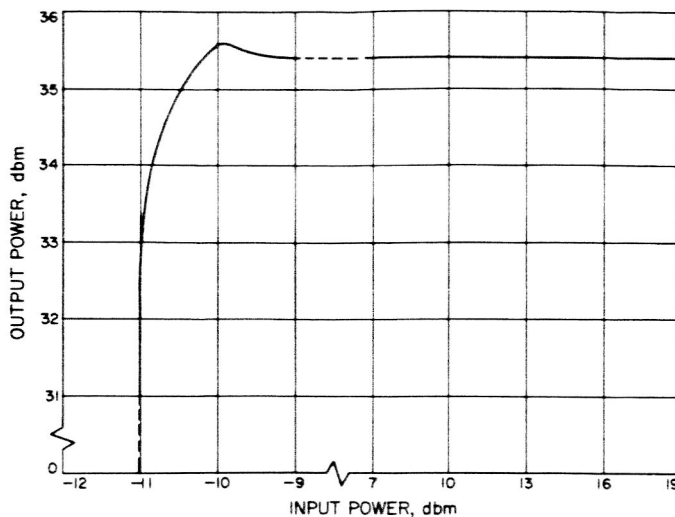


Fig. 14. Limiting curve of the WPM

The nominal power required for the WPM is 400 ma from a +30 V DC power supply. The output power for B+ variations is shown in Fig. 15. The output power varies less than 3 db for a $\pm 10\%$ variation in B+ voltage. The power amplifiers are saturated, so that linear increases in the B+ do not cause a linear increase in output power.

The WPM has exceeded all the target goals set and will be used as part of the $\times 32$ frequency multiplier modules of the WBRs.

F. Efficient Antenna Systems: A Stepped-Mode Transducer Using Homogeneous Waveguides

D. A. Bathker

1. Summary

A rectangular-to-cylindrical waveguide transducer is described which couples the dominant rectangular (TE_{10}) and dominant cylindrical (TE_{11}^0) modes. The maximum voltage reflection coefficient remains less than 0.025 over the design bandwidth. Symmetry considerations substantiated by moding tests show the transducer to be higher-order mode free. Previous work is reviewed, the design method discussed, and experimental data shown. The transducer is expected to find a variety of uses for broadband feeds as well as laboratory equipment such as compact rotary vane attenuators.

2. Theory

During the development of the interchangeable Research and Development Feedcone (SPS 37-28, Vol. IV), a need existed for a broadband low-reflection transducer between a dominant-mode rectangular and a dominant-mode cylindrical waveguide. Frequently, such transducers are realized by the construction of a taper section several wavelengths in size. As a result of a recent study

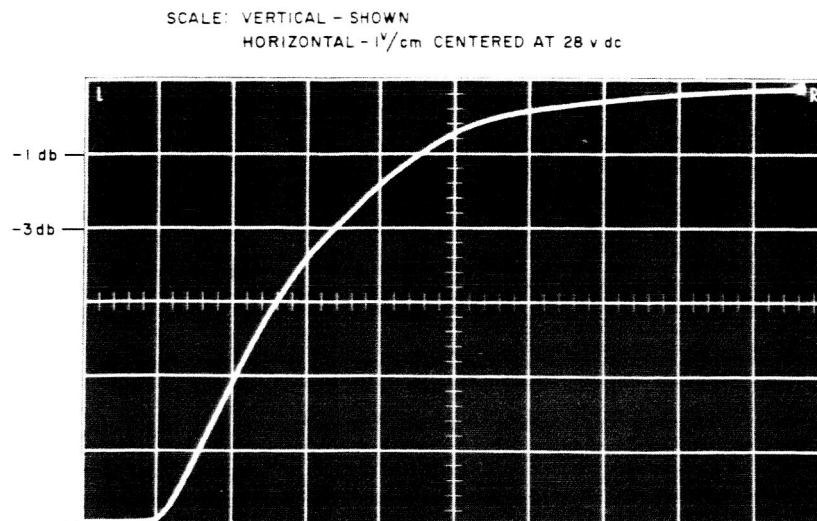


Fig. 15. Output power as a function of B+ variation

of the dominant-mode cutoff wavelengths of truncated cross-section cylindrical waveguide, Pyle (Ref. 3) has shown the conditions necessary to realize a transition of variable cross section but constant cutoff wavelength between the above waveguides. Pyle's conditions may be applied to the tapered line approach; the resulting structure would be classed homogeneous since the guide wavelength would be independent of position along the direction of propagation.

Stuchly and Kraszewski (Ref. 4) have recently reported a stepped transducer based on a series of *E*-plane truncated cylindrical waveguide quarter-wave sections with a single *H*-plane step to rectangular cross section. The design basis was equality of cylindrical and rectangular waveguide cutoff wavelengths yielding an overall frequency-independent impedance transformation ratio. Because the cutoff wavelength of *E*-plane truncated cross section cylindrical waveguide depends upon the degree of truncation (Ref. 5), quarter-wave sections of this type introduce frequency-dependent impedance ratios thereby causing this structure to be classed inhomogeneous.

A completely homogeneous stepped solution is possible by retaining the cutoff wavelength equality between the cylindrical and rectangular waveguides as well as among the quarter-wave transformer sections by applying Pyle's conditions for constant cutoff wavelength at selected impedance levels. Pyle's conditions lead to simultaneous *E*- and *H*-plane truncations of the cylindrical waveguide; this approach not only avoids possible problems of frequency-dependent impedance ratios but also distributes the *H*-plane step among the junctions.

Avoiding the question of a consistent solution for the characteristic impedance of *E*- and *H*-plane truncated

cylindrical waveguide, it was assumed, since λc is constant for all sections, that characteristic impedance

$$Z_0 \propto 2 \frac{b}{a} \quad (1)$$

where a , b are defined in Fig. 16. Note that, in the limits, $b/a = 1/2$, $b = a = 2r$, (1) is rigorously consistent with the power-voltage definitions of characteristic impedance for dominant moded rectangular and cylindrical waveguides (Ref. 6). The approximation made here is that (1) applies for the intermediate *E*- and *H*-plane truncated sections, $1/2 < b/a < 1$.

Young's tables for homogeneous quarter-wave transformers (Ref. 7) were used to obtain characteristic impedance levels for a selected bandwidth $w = 0.80$ and an impedance transformation ratio of 2.000 with $N = 4$

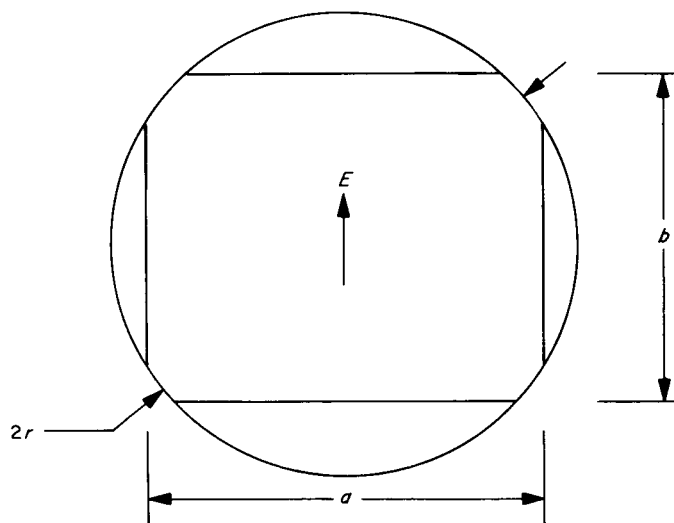


Fig. 16. *E*- and *H*-plane truncated cylindrical waveguide

Table 5. Impedance levels, cross sections and lengths for 1700 to 2600 MHz transducer

Section	Normalized characteristic impedance	Type	b , in.	a , in.	Capacitive junction correction, in.	Inductive junction correction, in.	Weighted length, in. $\frac{\lambda_{g0}}{4} = 1.844$ in.
Z_0	1.00000	Rectangular	2.150	4.300	—	—	—
Z_1	1.06726	Rectangular	2.295	4.300	-0.073	0.000	1.771
Z_2	1.26420	Rectangular	2.720	4.303	-0.112	+0.027	1.732
Z_3	1.58203	Truncated, $2r = 5.040$ in.	3.468	4.384	-0.091	+0.078	1.781
Z_4	1.87396	Truncated, $2r = 5.040$ in.	4.346	4.638	-0.003	+0.029	1.841
Z_5	2.00000	Cylindrical, $2r = 5.040$ in.	5.040	5.040	—	—	—

sections. Table 5 lists the impedance levels and b/a ratios which simultaneously satisfy (1) and the cutoff wavelength conditions (Ref. 3). Junction susceptance length corrections were obtained for the E - and H -planes independently similar to Young's outline (Ref. 8) and are shown in Table 5.

3. Test Results

The completed transducer is shown in Fig. 17. In order to test the design assumptions under controlled conditions and to insure a high degree of symmetry, tolerances better than $10^{-3}\lambda_0$ were held.

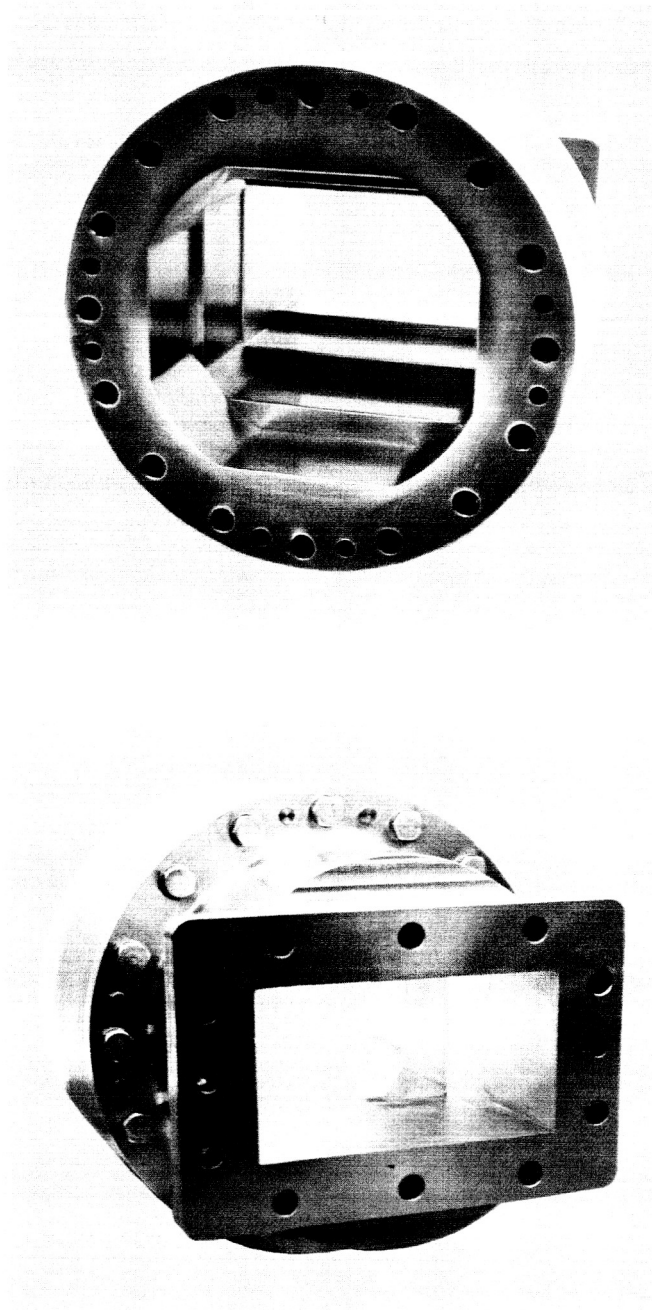


Fig. 17. Homogeneous waveguide transducer, showing cylindrical and rectangular ends

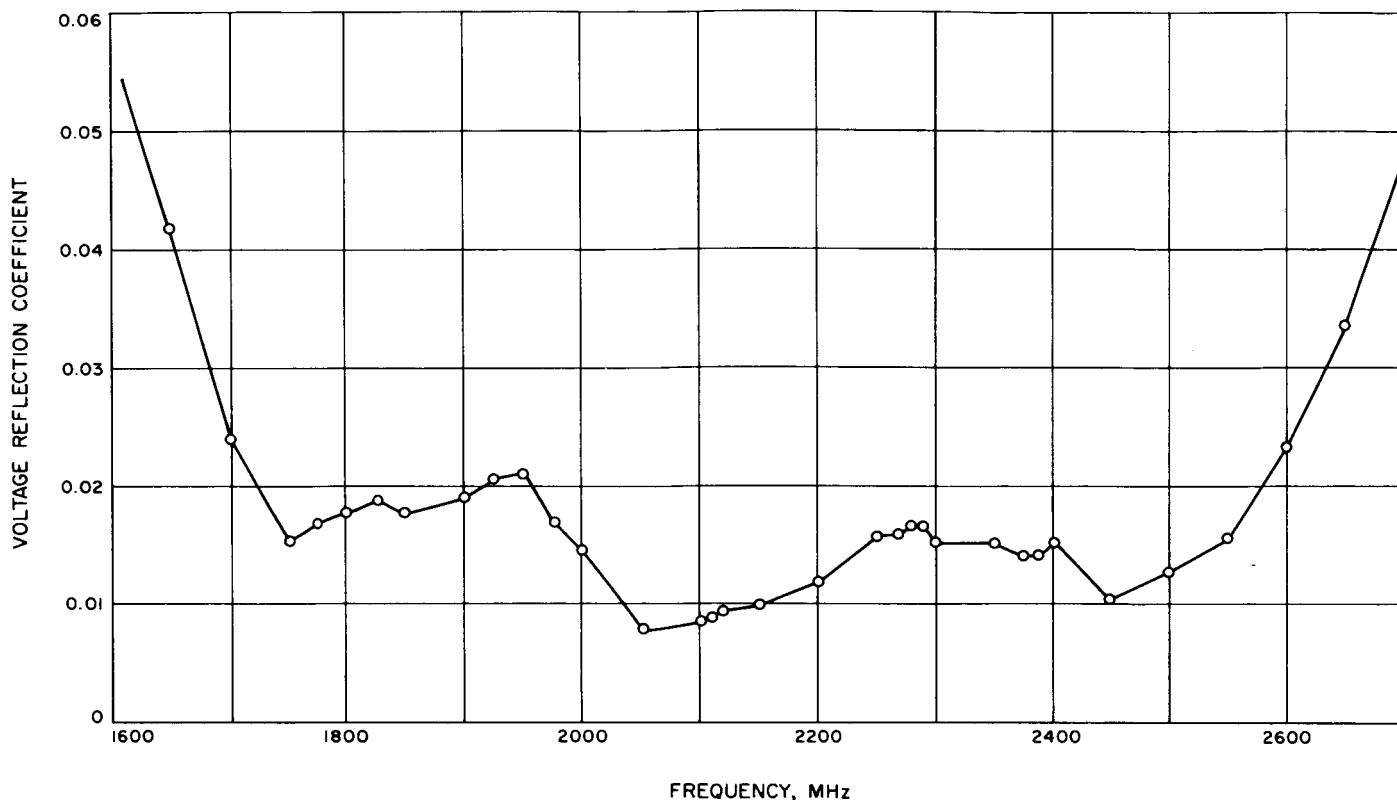


Fig. 18. Reflection coefficient of WR-430 to 5.040-in.-diameter transducer

Transducer VSWR was obtained in WR-430 slotted section and sliding cylindrical termination with spot checks using a high-accuracy tuned reflectometer. Three experiments were run to assess optimum junction susceptance length corrections. The first run used length corrections consisting of the algebraic sum of the *E*- and *H*-plane length corrections listed in Table 5. A final run consisted of *E*-plane length corrections only. An intermediate run, based on weighting the length corrections according to *E*- and *H*-plane susceptance magnitudes gave best performance. The weighted lengths are listed in Table 5 and the results shown in Fig. 18. Predicted performance based on absence of frequency dependent junction susceptances is a Chebyshev ripple voltage reflection coefficient maximum of 0.008 over 1680 to 2620 MHz. The results show a mean reflection coefficient approximately twice theoretical with slight bandwidth compression.

No evidence of possible TM_{01}^o or TE_{21}^o moding was detected with the transducer exciting a mode sensitive suppressed sidelobe conical feedhorn. The moding detector was the space radiation patterns of the feedhorn.

G. High-Power Continuous Wave (CW) S-Band Traveling Wave Resonator

R. B. Kolbly

1. Summary

In the past, there have been several experimental setups (Refs. 9 and 10) to test low-loss high-power microwave components by use of a traveling wave resonator (TWR), sometimes called a "resonant ring."

The Microwave Test Facility (MTF) personnel at Goldstone (GSCS) have been engaged in the design and development of a TWR capable of obtaining up to 500 kw at 2113 MHz. An overall picture of the complete TWR is shown in Fig. 19, and a block diagram is shown in Fig. 20.

RF power is generated at 2113 MHz by a 5KM70SI klystron, which is part of the high-power test laboratory located at the MTF. After passing through the usual

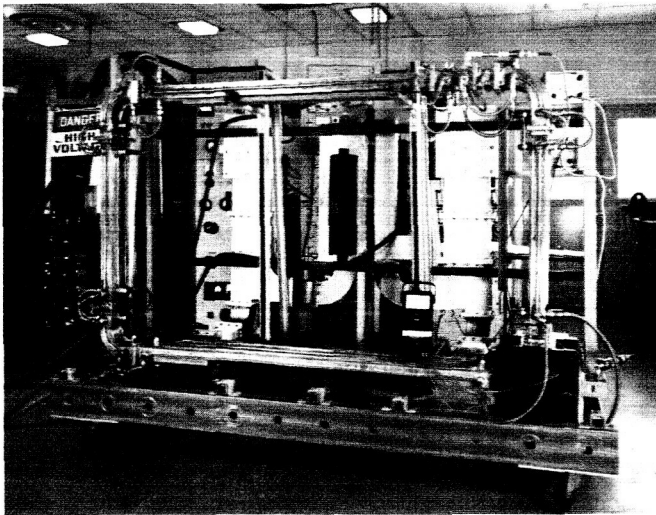


Fig. 19. Photograph of 500-kW S-band TWR

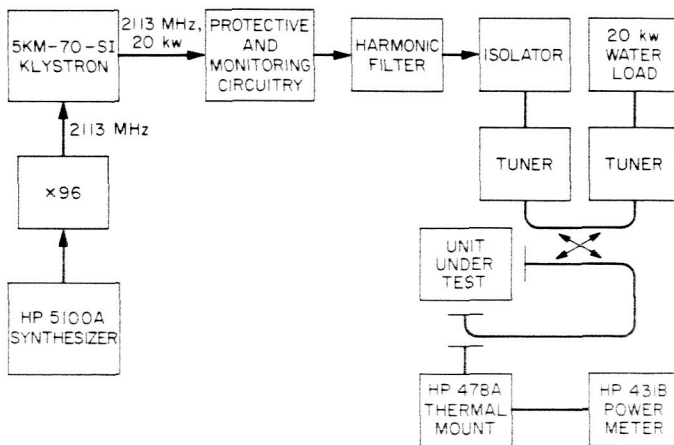


Fig. 20. Block diagram of 500-kW S-band TWR

protective and monitoring circuitry, the signal is applied to the input tuner of the TWR through a high-power isolator. The input tuner and output tuners, which are identical, were developed for this application; each consists of a short-slot hybrid and two sliding shorts. A tuner of this type gives independent control of both reflection coefficient and phase over a wide range.

The high-power directional coupler was designed and built by MTF personnel and is a multi-hole side-wall coupler with 21 db nominal coupling. Since the ring was used over a narrow range of frequencies, a binominal coefficient taper was used in the design of this coupler. The output of the coupler is connected through an output tuner to a 20-kw water load. The resonant structure is

33λ long and is constructed of WR-430 waveguide made with OFHC copper.

Power circulating in the resonator is monitored with a resistive loop directional coupler. Due to the high circulating power, it is necessary to attenuate the output of the coupler to a power level acceptable to a coaxial thermistor mount. Details of the power-monitoring coupler and water cooling lines are shown in Fig. 21.

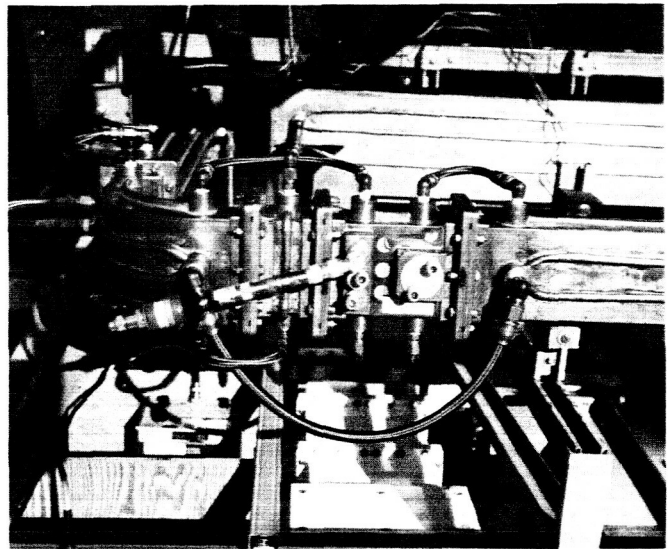


Fig. 21. Circulating power monitoring and water cooling lines

2. Operation

When the resonator is operating properly, there is no power delivered to the 20-kw water load so the resonator must dissipate the total power input, which at full capability is approximately 20 kw. It was found necessary to solder six lines of $\frac{3}{8}$ -in. copper tubing to the resonator waveguide and pass cooling water through them. Even with the additional cooling, it is necessary to bring the resonator up in power slowly and to adjust the input frequency to maintain resonance as the resonator waveguide expands due to heating. As a standard DSIF VCO does not have a sufficient tuning range, and a signal generator is not sufficiently stable, the output of a frequency synthesizer was multiplied by a factor of 96 and amplified by the klystron to supply the 20 kw, 2113 MHz drive. The resonator showed a temperature rise of 8°F at a stabilized cooling water temperature of 138°F. The operating Q of the resonator is approximately 15,000 with a circulating power of 475 kw.

3. Results

The TWR was used to test the isolation and power-handling capability of two waveguide switches, a RAM-256 and a RP-A09, SN001. Fig. 22 shows one of these switches installed in the resonator. A Model 652 thermistor thermometer adapter for a Model 260 VOM was used to monitor temperatures. In Fig. 22, the insulated covers for the thermistor probes have been removed. The RP-A09 SN001 switch was operated for a period of 1.8 hr at 475 kw. At the end of this period, the switch isolation was measured at >90 db. (The isolation of the switch at ambient temperature was approximately 80 db; as the switch heated, the isolation increased to greater than 90 db.) The rotor temperature stabilized at 225°F , and the stator temperature was stabilized at 196°F , at a power level of 475 kw. Immediately after removal of power, the switch was switched several times in a satisfactory manner.

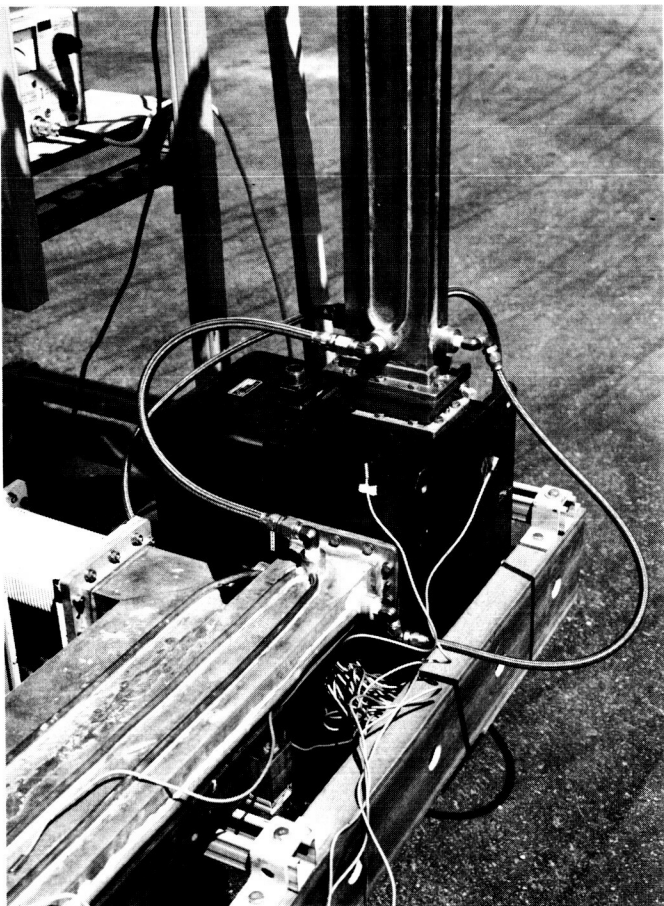


Fig. 22. Temperature monitoring of component under test

The RAM 256 switch was tested at 400 kw for 1 hr. After this time, the switch had reached a stator temperature of 225°F and an isolation of 98.8 db. At this power, the switch arced at the gap between the rotor and stator, which caused the klystron amplifier to shut down. An attempt was made to switch the switch, but the rotor had frozen in position. Later, disassembly of the switch showed scoring of the rotor and stator; it also showed arc burns.

4. Conclusions

The TWR is useful as a device to test low-loss high-power microwave components. Powers in excess of 450 kw at 2113 MHz can be obtained. The use of this resonator will allow the testing of microwave components such as switches, directional couplers, and filters at very high CW power levels.

H. Frequency Stability Determination for Two Hydrogen Masers

R. L. Sydnor

The two hydrogen masers recently purchased from Varian Associates, Quantum Electronics Division (SPS 37-35, Vol. IV, pp. 259-261; SPS 37-36, Vol. IV, p. 249) have been operating since their arrival at JPL. A test system (on loan from Varian) is being used to monitor the frequency difference between the two units and thus to obtain data on their stability. A block diagram of this test system is shown in Fig. 23. In this system the output signals from the two masers are added, mixed with the 1400-MHz signal from the LO multiplier, amplified and phase-detected. The synthesizer frequency is adjusted to produce a convenient difference frequency at the output which is detected and recorded. The envelope modulation due to the difference frequency between the two masers is then the measure of frequency stability of the masers. A typical recording is shown in Fig. 24. A chart of the reduced data for approximately 1 month is shown in Fig. 25. While the extrema of this record would indicate a stability figure of 27×10^{-13} (peak-to-peak) for

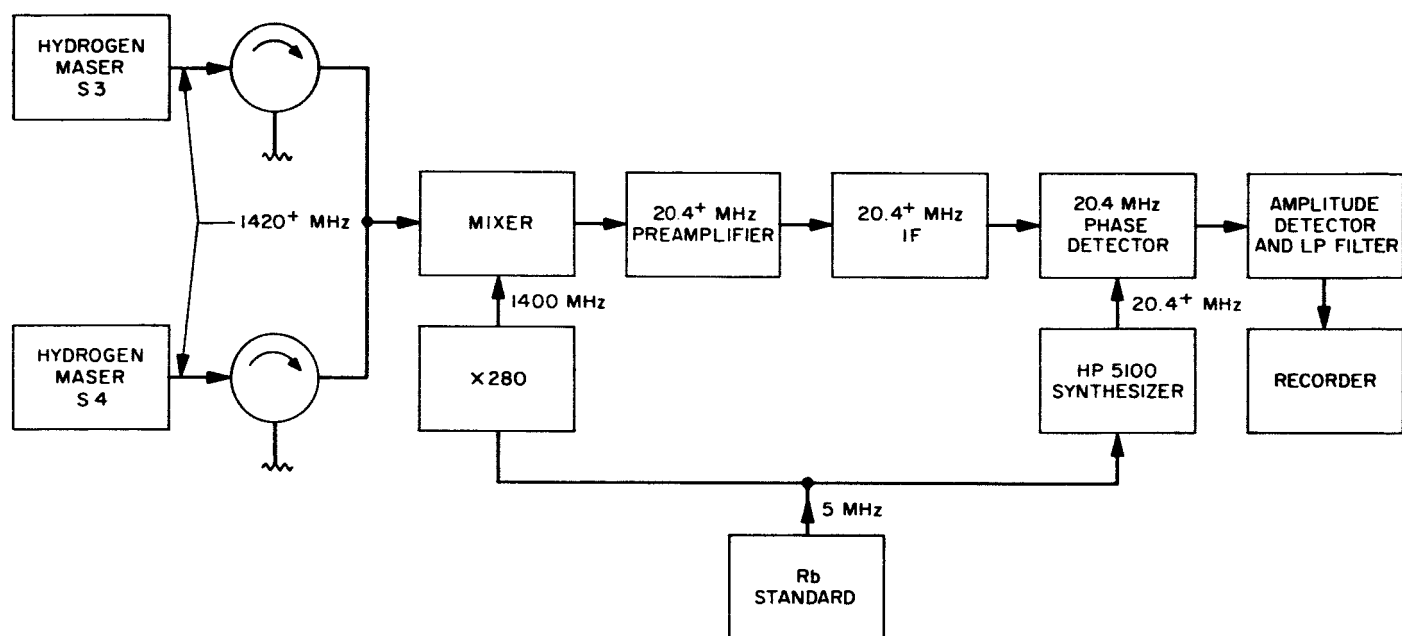


Fig. 23. Test system for monitoring hydrogen maser stability

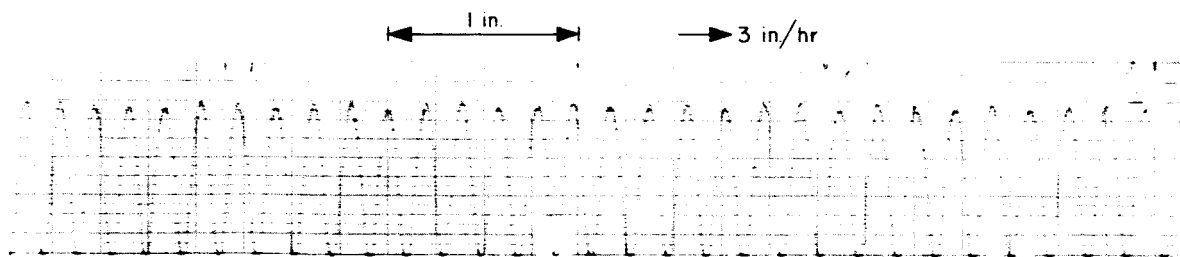


Fig. 24. Beat tone between two masers

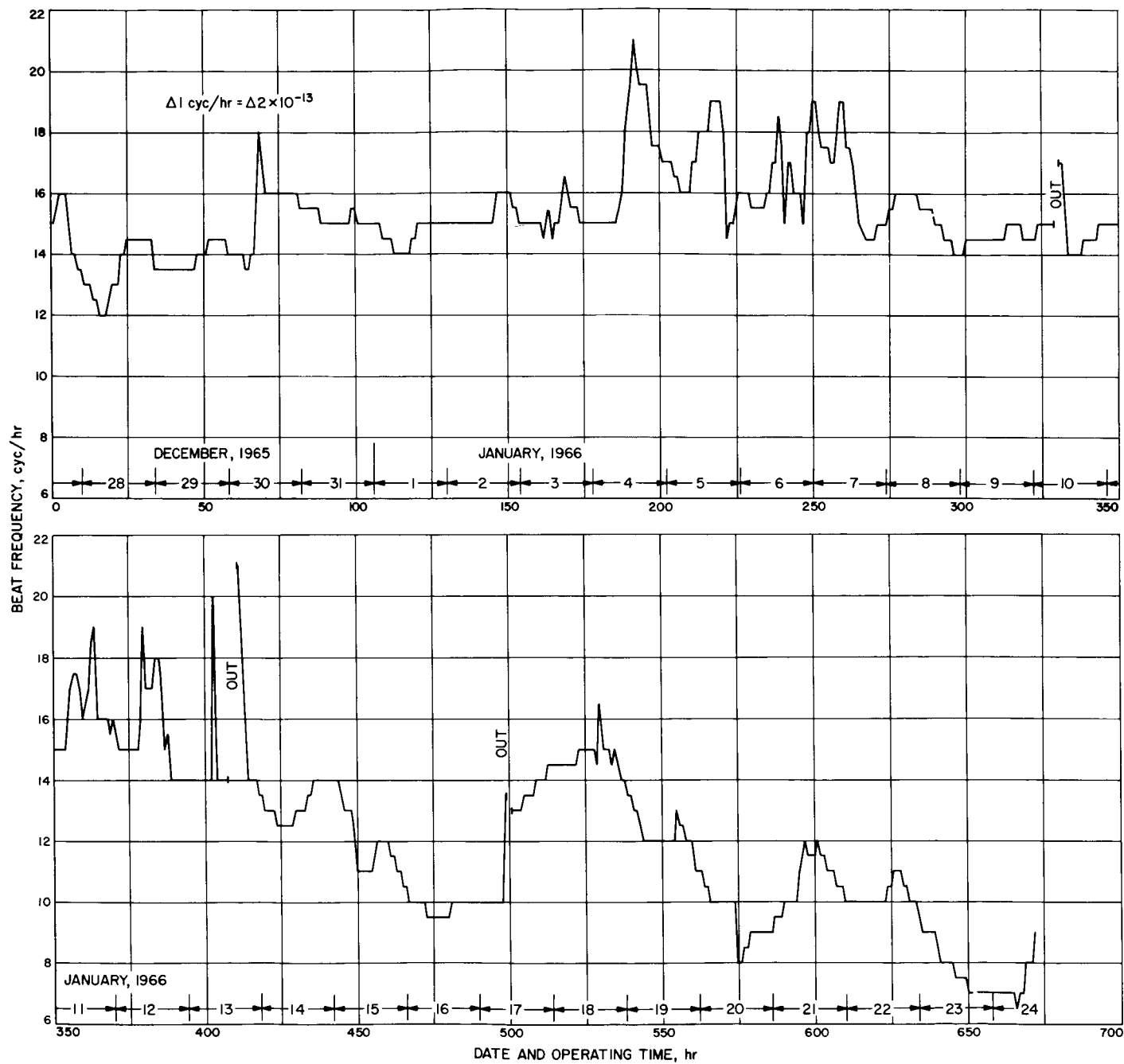


Fig. 25. Maser stability

N66 38555

the two masers (corresponding roughly to 4 to 5×10^{-13} RMS) a number of problems have arisen during this period. It is felt that upon solution of some of these difficulties the performance of the masers will be much better than this figure. Some indication of these problems may be seen on the record of Fig. 25. Three failures occurred during the period covered by this record. These failures (in every case preceded or followed by large variations in the frequency) are noted by "out" on the record, and were caused by stoppages of the RF discharge in maser number 4. Since the power out of the RF source was just large enough for the discharge, small perturbations in the power would cause the discharge to stop. By replacing the vacuum tubes in the RF source, the power was increased to well above the discharge threshold, thus eliminating the high failure rate due to this problem.

A number of failures have occurred in the temperature control, pressure control, voltage regulator, and high-voltage (Vac-Lon pump) circuits. In most cases these were due to poor packaging techniques and poor quality control (bad solder joints, broken wires, etc.). A few were due to faulty design and inadequate safety margins as evidenced by the large number of transistor failures (4 in one unit).

Because of the apparently poor reliability of the units and the need for better space utilization to permit the addition of the necessary synthesis equipment to the units, a complete repackaging of the units is planned. This repackaging and redesign of the electronics will be aimed at more reliable operation, increase ease of maintenance, and better space utilization.

The maser itself will not be changed in this redesign since it appears to be operating as expected, when the controllers and RF discharge are performing correctly. One failure in the maser itself was experienced during this period. The maser cavity and storage bulb were replaced by Varian when this failure occurred, and it was found that the original cavity had too low Q due to poor silver plating of the fused quartz and the original storage bulb had a defective layer of Teflon on the wall. Upon replacement of these parts the maser operated correctly again.

The preliminary design of the new packaging and modifications of the electronics are started. Most of the parts necessary for this work are on order. Development on a new receiver synthesizer has begun.

I. Frequency Generation and Control: Hydrogen Maser Frequency Standard

W. H. Higa

The assembly of the dual-channel traveling wave maser (TWM) for the hydrogen line frequency, 1420 MHz, is in progress. This TWM will permit an evaluation of the short-term fluctuations in the output of a hydrogen maser. A brief discussion is given here of the properties of a good atomic frequency standard.

The long-term stability of an oscillator is improved by using a low Q cavity since the well known frequency-pulling effect prevails. This effect is stated as

$$f_{osc} - f_{atom} = \frac{Q_{car}}{Q_{atom}} (f_{car} - f_{atom}) \quad (1)$$

where most of the terms are self-explanatory. f_{osc} is the oscillator output frequency and is seen to be a function of the cavity tuning f_{car} . A low cavity Q is seen to be desirable on the basis of Eq. (1); however, it is to be noted that for good short-term stability it is important to have high Q_{car} .

The cavity acts like a flywheel for the atoms and introduces a system time constant.

$$\tau = \frac{Q_{car}}{2\pi f_{atom}} \quad (2)$$

This time τ defines the order of magnitude of the minimum integration time required to specify the short-term characteristics of the oscillator. In other words, there is no need to be concerned about fluctuations occurring in shorter time than that specified by Eq. (2). For the atomic hydrogen maser with a loaded $Q_{car} \cong 10^4$, τ is around 1 μ sec.

On the basis of Eqs. (1) and (2) it is seen that a compromise is required for good oscillator design. A high Q_{car} is desirable for short-term stability provided the center frequency of the cavity, f_{car} , can be kept from drifting on a long-term basis. A high Q_{car} is also desirable in order to allow operation at reduced atomic beam intensity.

The effects of thermal noise on an oscillator have been studied by Edson (Ref. 11). The effect on amplitude fluctuation is negligible, but the effect on phase perturbation may be significant. Edson (Ref. 11) gives the rms

value of fractional phase deviation in a time t as

$$\frac{\phi_t}{\phi} (kT/2tPQ_{cav}^2)^{1/2}$$

where k is Boltzmann's constant, T is the cavity temperature in $^{\circ}\text{K}$, and P is the power generated by the oscillator. This result shows the importance of operating at high power levels in order to improve short-term stability.

The need for low-noise amplifiers is evident if stability measurements are to be made by comparing two hydrogen masers; the post detection time constant should not exceed about $1 \mu\text{sec}$ as stated above. With such a short integration time, it is necessary to use high-level signals at the detector.

J. Improved RF Calibration Techniques: DC Potentiometer Microwave Insertion Loss Test Set

C. T. Stelzried and D. Mullen

1. Summary

It is necessary to accurately measure the insertion loss of low-loss coaxial and waveguide components for the

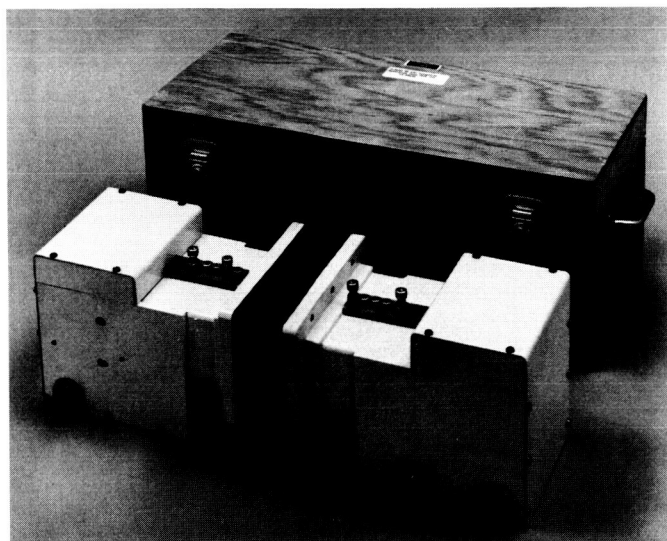


Fig. 26. Photograph of the WR 430 waveguide microwave calibration heads of insertion loss test set

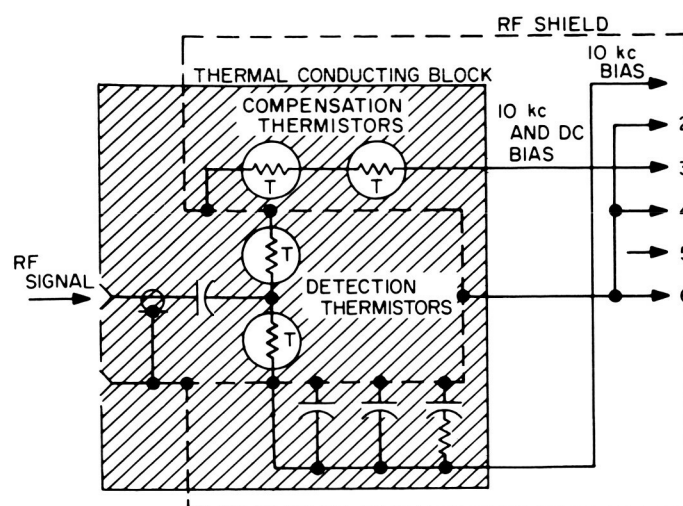


Fig. 27. Schematic of Hewlett Packard Model 478A coaxial thermistor mount

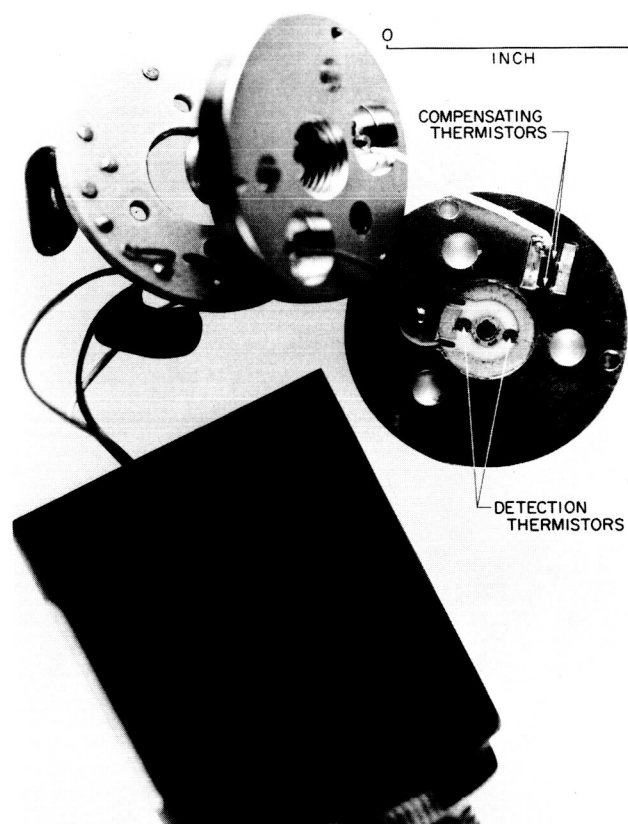


Fig. 28. Photograph of disassembled power meter thermistor mount

evaluation of low-noise receiving systems. A simple dual-channel insertion loss test set has been constructed, which

incorporates modified commercially available power meters with a DC nulling scheme (Ref. 12; see also SPS 37-30, Vol. IV, p. 234).

A description is given of an orientation problem with the Hewlett Packard power meter coaxial thermistor mounts Model 478A when used as an integral part of the DC insertion loss test set. An alternate method of thermal adjustment of the detection thermistor is illustrated to reduce this effect.

2. Power Meter Thermistor Orientation Effect

An insertion loss measurement is made by adjusting the read out potentiometer for a null with the calibration heads bolted together with and without the unknown connected. The difference in reading converted to dB is the insertion loss. It has recently been noted that some error in insertion loss occurs if the head (Fig. 26) orienta-

tion is different between the readings with and without the unknown. It is not always possible to arrange the unknown so that the insertion loss heads can retain the same orientation.

It has been noted that a 90 deg change in orientation of a standard Hewlett Packard Thermistor Mount Model 478A changes the zero by an amount equivalent to a power change of approximately 0.5 microwatt. This effect has been investigated and can be virtually eliminated for some orientations by changing the thermal matching adjustment technique of the compensation thermistors. Fig. 27 shows the thermistor mount schematic. Fig. 28 shows a photograph of the disassembled thermistor mounts. Figs. 29 and 30 show photographic enlargements of the thermistor mount compensating and detection thermistors. The scale can be determined by the approximate 0.075-in. distance between the mounting bars of Fig. 29. The longer leads of the compensating thermistors offer a higher thermal resistance.



Fig. 29. Photographic enlargement of disassembled thermistor mount showing the compensating thermistors

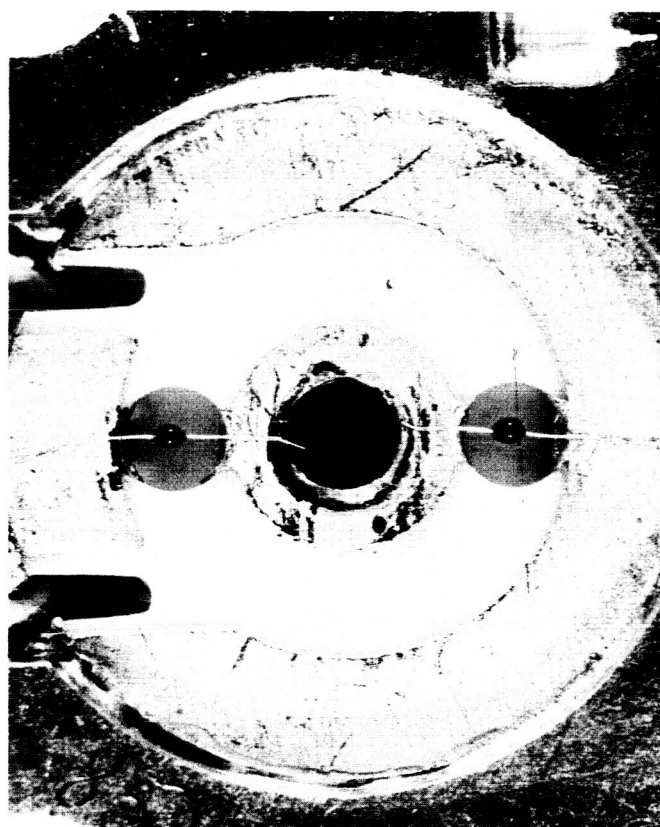


Fig. 30. Photographic enlargement of disassembled thermistor mount showing the detection thermistors

Fig. 31 shows the normal thermal adjustment technique used with the compensating thermistors. The screws are physically adjusted close to the thermistor until a zero is obtained on the power meter. For example, one particular set of thermistors has spacings of approximately 0.030 in. and 0.001 in. for the two thermistors, respectively. Unfortunately, changing the orientation of the mount changes the position of the thermistor relative

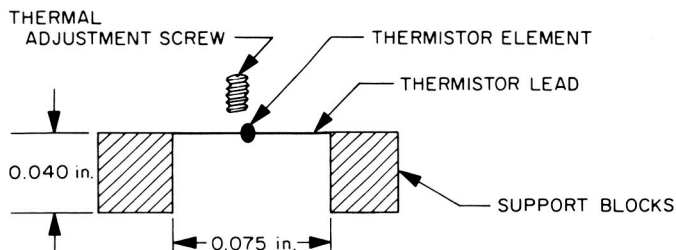


Fig. 31. Thermistor and thermal adjustment screw



Fig. 32. Photographic enlargement of thermistor mount showing the reference thermistors

to the adjustment screw due to sag in the thermistor leads and therefore affects the null. Another technique to obtain thermal adjustment is to apply a small amount of conductive epoxy on the thermistor leads (Fig. 32). This is done under a microscope while observing the power meter null. The required thermal path is now supplied through the thermistor leads reducing the orientation effect. Fig. 33 is a recording to show a comparison of the null stability of an unmodified and modified thermistor mount with position. The sensitivity is the same in each position of the reading. A base line is established with the mount in a vertical position. The mount is then tilted to a horizontal position and rotated through 360 deg. The modified unit has one horizontal position where the null is the same as when in the vertical position. This unit can now be used with an insertion loss test set if the rotation is maintained about the axis.

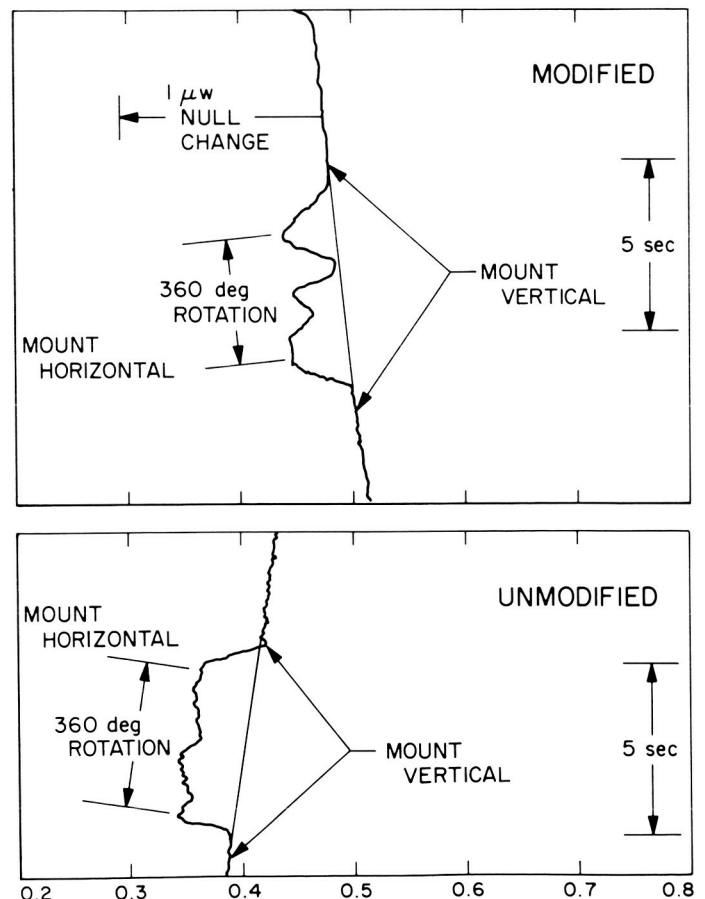


Fig. 33. Power meter coaxial thermistor mount model HP 478A stability tests (200 Ω negative SN 19319)

References

1. Cooley, J. W., and Tukey, J. W., "An Algorithm For Machine Calculation of Complex Fourier Series," *Mathematics of Computation*, Vol. 19: pp. 297-301, 1965.
2. Peterson, W. W., *Error Correcting Codes*, Chap. 9, pp. 173-175, MIT Press, Cambridge, Mass., 1961.
3. Pyle, J. R., *A Circular-to-Rectangular Waveguide Transition Maintaining a Constant Cutoff Wavelength*, Technical Note Pad 94, Australian Defense Scientific Service Weapons Research Establishment, Salisbury, S.A., September 1964.
4. Stuchly, S., and Kraszewski, A., "Wideband Rectangular to Circular Waveguide Mode and Impedance Transformer," *IEEE Transactions on Microwave Theory and Techniques*, pp. 379-380, May 1965.
5. Pyle, J. R., and Angley, R. J., "Cutoff Wavelengths of Waveguides with Unusual Cross Sections," *IEEE Transactions on Microwave Theory and Techniques*, pp. 556-557, September 1964.
6. Southworth, G. C., *Principles and Application of Waveguide Transmission*, D. Van Nostrand Co., Inc., Princeton, N.J., 1950, pp. 104-125. Note p. 104 typographical transpose of 754 to 574 ohms.
7. Young, L., "Tables for Cascaded Homogeneous Quarter-Wave Transformers," *IRE Transactions on Microwave Theory and Techniques*, pp. 233-237, April 1959; also—"Correction," L. Young, *IRE Transactions on Microwave Theory and Techniques*, pp. 243-244, March 1960.
8. Young, L., "Practical Design of a Wide-Band Quarter-Wave Transformer in Waveguide," *The Microwave Journal*, pp. 76-79, October 1963.
9. Milosevic, L. J., and Vauley, R., "Traveling Wave Resonators," *IRE Transactions PGMTT*, pp. 136-141, April 1958.
10. Miller, S. J., "The Traveling Wave Resonator and High-Power Microwave Testing," *Microwave Journal*, pp. 50-58, September 1960.
11. Edson, W. A., "Noise in Oscillators," *Proceedings of the IRE*, Vol. 48: pp. 1454-1466, 1960.
12. Stelzried, C. T., and Petty, S. M., "Microwave Insertion Loss Test Set," *IEEE Transactions on Microwave Theory and Techniques*, Vol. MTT-12 (No. 4): p. 128, July 1964.

N66 38557

III. Communications Development Engineering

A. Frequency Generation and Control: Comparison of Frequency Synthesizers

W. F. Gilmore, Jr.

1. Introduction

The modern frequency synthesizer is a versatile piece of equipment, as it can generate any of a wide range of sinusoidal signals. Frequency selection is usually made either in discrete steps by controls on the front panel or electrically from a remote control point.

Recently, frequency synthesizers have been used extensively as building blocks in larger systems. One or more of these units is becoming a standard part of every deep space or planetary radar tracking installation. Design of these systems requires a knowledge of many characteristics of the frequency synthesizer, such as range resolution, frequency stability, and phase stability. Some of these characteristics are readily available from the manufacturer's data sheets. This report describes a comparison

study which was made to supplement available information for several commercial units.

It was necessary at the outset to limit both the number of different frequency synthesizers tested, as well as the total number of tests run. Originally, remotely controlled frequency synthesizers covering the ranges 0 to 1 MHz and 30 to 40 MHz were needed. Consequently, this study is restricted to these units.

Two fundamental measurements were needed: the first to determine the spectrum of the phase noise of the output signal as a function of frequency, and the second to determine the amplitude distribution of this phase noise. These two statistical properties constitute a reasonable basis for the design of phase coherent systems which use frequency synthesizers as components.

2. Tests Performed

Three synthesizers were selected for the final comparison tests. These were units manufactured by General Radio (GR), Hewlett-Packard (HP), and Montronics. Although others are available, these were considered to be

the best ones available for the present systems. All of the units had the capability of being remotely controlled.

In the 0 to 1 MHz range either the GR or HP synthesizer can be used, but in the 30 to 40 MHz range either the HP or the Montronics synthesizer can be used. Although the synthesizers are operated in a fairly wide range around the nominal 500-kHz and 36-MHz frequencies, these exact frequencies were best for measurement purposes. Frequency division or multiplication from a 1-MHz standard gives a clean signal, independent of the frequency synthesizers, which can be used for comparison purposes. Furthermore, the outputs of the synthesizers at 500 kHz and 36 MHz are typical of their performance anywhere within the general range of frequencies which are of interest.

At 500 kHz, tests were run using an identical pair of frequency dividers. Similarly, at 36 MHz tests were run with an identical pair of frequency multipliers. Results from these tests help to establish the dividers and multipliers as standards of comparison for measurements on the frequency synthesizers.

For each of the synthesizers, as well as for the dividers and multipliers, three main tests were run. The first test measured the power spectral density of the phase noise. Useful results have been obtained from about $\frac{1}{4}$ through 1000 Hz. Power at frequencies above this is vanishingly small. There is a large amount of power at frequencies lower than $\frac{1}{4}$ Hz, however, which can cause the measurements to become lengthy and difficult to interpret. For this reason, a second test was devised to measure the variance of the phase noise as a function of time. Curves of this type show how far and how fast the phase can drift in any given length of time. The third test measured the amplitude distribution of the phase noise.

In the next section a complete description of the equipment used for the tests is given. Results and conclusions follow in the final sections.

3. Experimental Apparatus and Procedure

The basic test equipment which was used for all parts of this experiment is shown in Fig. 1. Each test consists of a direct comparison of one device (Unit A) against another (Unit B). Both devices are synchronized with a stable 1-MHz reference signal. Changes in phase between the two devices are detected with a phase detector. An amplified voltage proportional to this phase difference is the desired output.

There is always a certain fixed phase shift associated with any device to be tested. In the case of most frequency synthesizers the phase depends upon the exact instant of time at which the last output frequency was selected. Another factor affecting the phase is the length of the connecting cables. Since a large fixed phase shift degrades the linearity of the phase detector, it is necessary to have a compensating phase shifter following one of the devices.

At 500 kHz a lumped constant type of phase shifter was used, and at 36 MHz a coaxial line of adjustable length was used. In all cases the output voltage from the synthesizers was sufficient to drive both the phase shifter and phase detector. For the low level multipliers, however, it became necessary to insert a distribution amplifier ahead of the phase detector. The fixed phase shift in the amplifier was easily balanced out, and the overall increase in phase noise was almost negligible.

Fig. 2 shows the digital data-processing system. A long cable ran from the test equipment shown in Fig. 1 to the recording facility. It was necessary to use a special isolation amplifier at the end of the cable in order to completely eliminate ground loop problems.

At the recording facility a PDP4 computer was used to collect samples of digitized data and store them on magnetic tape. Later, after all of the data had been recorded, these tapes were processed on 7094 computers. Although the digital data-processing system appears to be relatively complicated, it was the best one to use because it was readily available.

A low-pass filter ahead of the analog-to-digital converter removed unwanted high-frequency components of phase noise. This prevented excessive folding from occurring in the computed spectra. The transfer function of the entire system is shown in Figs. 3 and 4. Fig. 3 was made with a filter cutoff of 1200 Hz, and Fig. 4 was made with a filter cutoff of 40 Hz. The first setting was used in short 5-sec runs with the sampling at a 3200 samples/sec rate, and the second was used in long 200-sec runs with the sampling at a 100 samples/sec rate.

Before the digital data can be interpreted properly, the entire system shown in Figs. 1 and 2 must be calibrated. This can be done very efficiently and accurately by using a newly developed method. First, Unit B in Fig. 1 is set to a frequency which differs by a small amount, such as 0.1 Hz, from the measurement frequency. Then a digital tape recording is made.

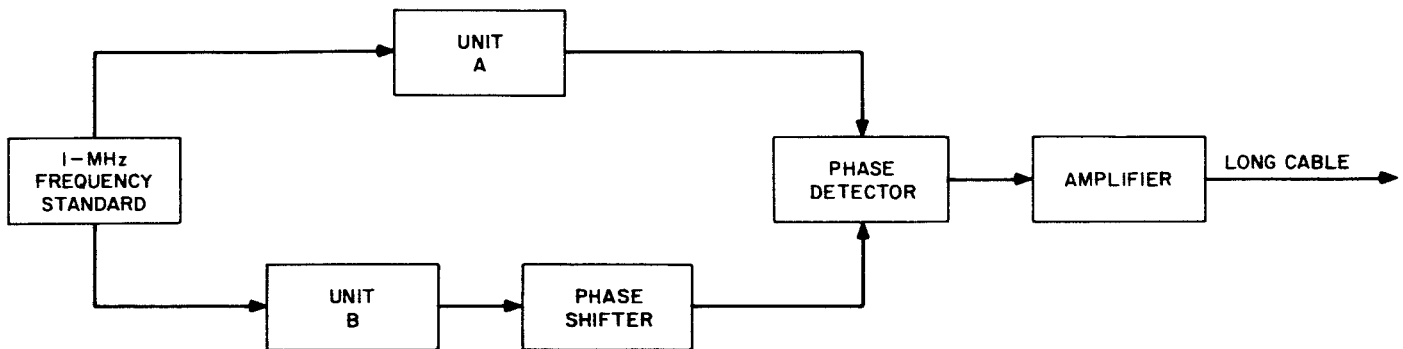


Fig. 1. Simplified block diagram of test equipment

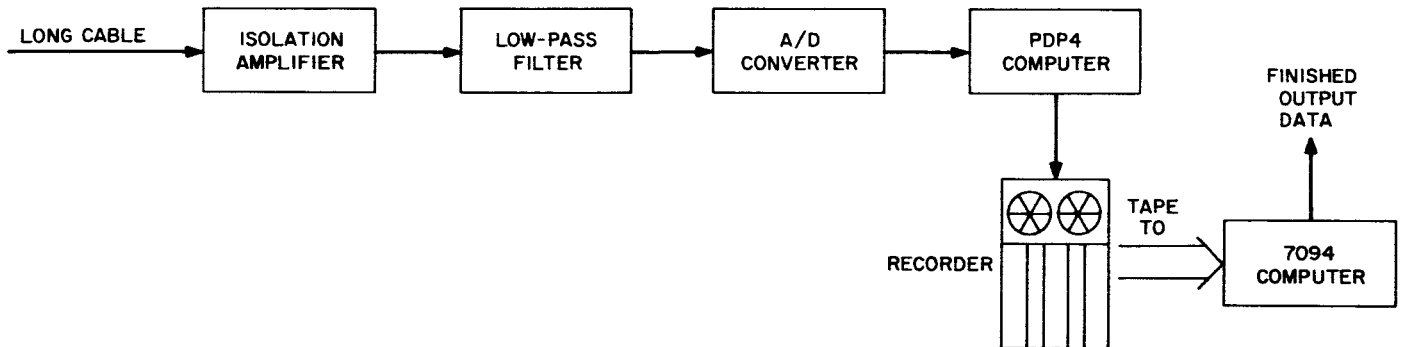


Fig. 2. Digital data-processing system

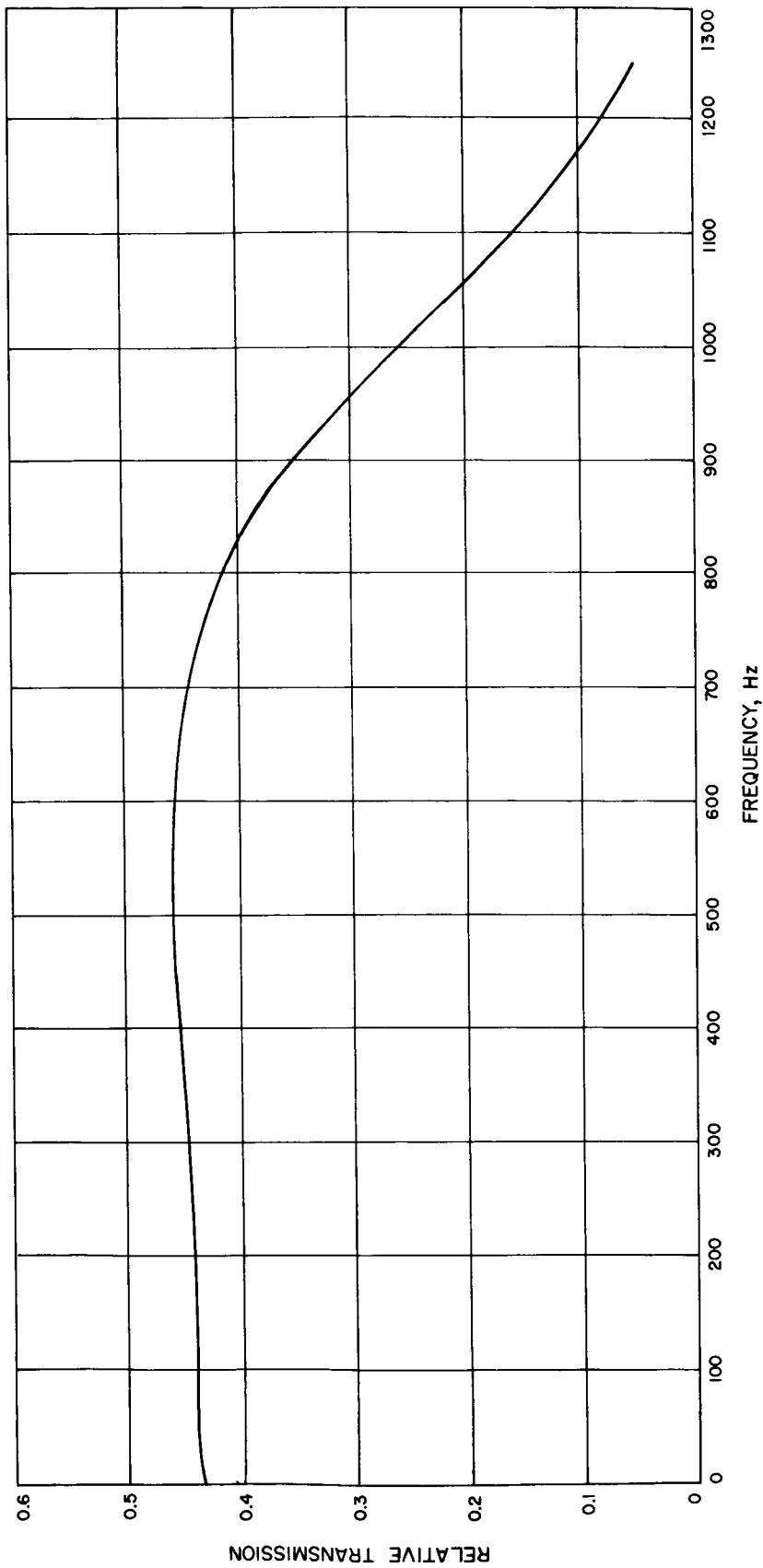


Fig. 3. Transfer function of digital data-processing system with filter set at 1200 Hz

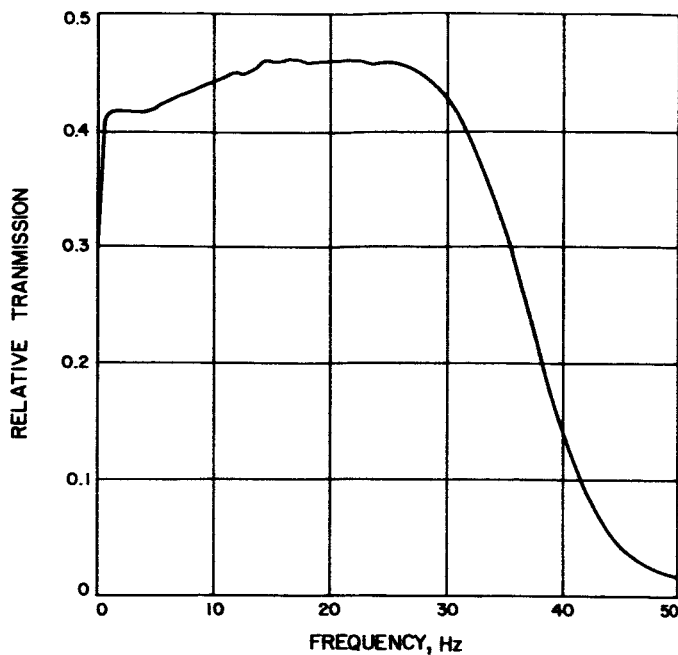


Fig. 4. Transfer function of digital data-processing system with filter set at 40 Hz

If the numbers on this calibration tape are plotted, they will lie approximately on a sine curve as shown in Fig. 5. This is the response of the system to a uniformly increasing phase difference. Since synthesizer phase noise is small, it is possible to keep the system within its linear range during the data runs.

Calibration of this system is complete when the slope of the curve in Fig. 5 is known over its linear range. The slope indicates the number of converter counts for each degree of phase angle. Although this slope can be found graphically, a better method has been developed. It utilizes a special calibration program which was written for the 7094 computer.

Basically, the computer program fits straight lines to the calibration data by the method of least squares. A separate line is determined from each contiguous set of sufficiently small samples. In one case, sample groups between -1024 and $+1024$ counts were used. In Fig. 5 these groups lie within 10 deg of the phase angles $0, \pm 180, \pm 360$, etc.

The computer program gave a dozen or so estimates of the slope for each calibration run. Half of the slopes were positive and half were negative, but they all agreed with each other in magnitude to within less than 1%. Inaccuracies in the calibration due to phase noise in the system are virtually eliminated by this least squares fitting process. Other programs for processing the synthesizer data

give results directly in terms of degrees when the proper calibration constants are used.

Curves showing the power spectral density of the phase noise were computed using standard techniques for sampled data (Ref. 1). The autocorrelation functions were computed as a sequence of points, and by transforming these, the final power spectra were found. Points for these computed curves consistently fell very close to the smooth curves of the following section.

Power spectral density curves are plotted for positive frequencies only. The total area under any curve gives the variance of the phase noise. Noise power between any two frequencies can be easily found from the curves with a planimeter. Its reading may be used directly without "doubling it to account for negative frequencies."

Two basic runs were made on each different unit to be tested. One run lasted 5 sec with a sampling rate of 3200 samples/sec, and the other lasted 200 sec with a sampling rate of 100 samples/sec. Later, when higher resolution was needed at the lower frequencies, this data was reprocessed, using every tenth data point. Effects of aliasing were small because of the small magnitude of the spectra at the higher frequencies. The resulting spectra had their frequency scales expanded by a factor of 10.

One of the most difficult things to show properly on the power spectral density curves is the amount of phase noise at very low frequencies. In any reasonable length data run this can show up only as a trend in the data, or as a very large amount of power concentrated at the lower frequencies. Normally one might expect the low-frequency behavior of phase noise in a short run to resemble the model of a random walk, whose variance is proportional to time. To check this model and see more clearly how the variance behaved, a curve of variance versus time has been plotted for each data run. The final variance at the end of the run is equal to the zero lag of the autocorrelation function and the area under the power spectrum for that particular run.

Another interesting property of phase noise data is its amplitude distribution. A few typical curves are given. In each case the data, which was grouped into fairly coarse boxes, appeared to lie close to a normal distribution with the same mean and variance. Only in those cases where a strong trend was present did this generalization break down. Probably even the most unsymmetrical curves would become normal as the run length increased. In the limit, physical considerations suggest that the variance

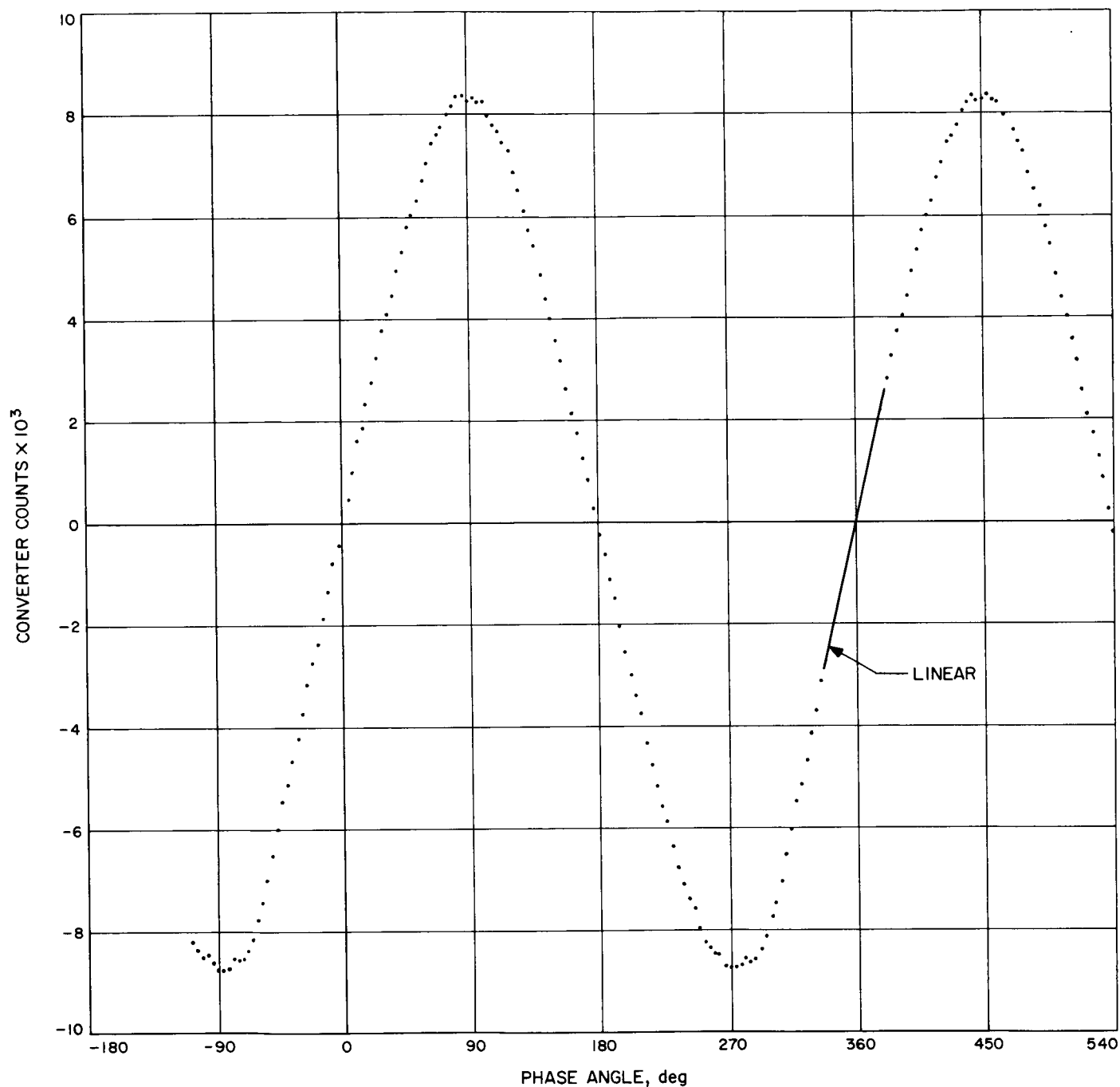


Fig. 5. Calibration run data

or width of the curve would increase somewhat but still remain bounded.

4. Results

Figs. 6 through 10 were made from 500-kHz data, and Figs. 11 to 20 were made from 36-MHz data. At each frequency there are separate curves for power spectral

density and variance of the phase noise. Typical curves in Fig. 21 show how closely the amplitude distribution of the phase noise approaches a normal probability density function.

For cases in which measurements were made over an extended range, several curves are given. All of the curves should be regarded as typical for a single measurement

and not as an ensemble average. Thus, a certain amount of variation can occur in overlapping ranges from one curve to the next when the data used is not from the same run.

5. Conclusions

All of the quantitative data from the synthesizer tests is given graphically in Sect. 4. During the tests a few qualitative observations were made also. These are summarized

Table 1. Qualitative comparison of three frequency synthesizers

Synthesizer	Estimated weight, lb	Mechanical stability	Long-term drift	Approximate price
General Radio	40	fair	fair	\$6,000.00
Hewlett-Packard	155	good	good	\$16,000.00
Montronics	35	poor	poor	\$12,000.00

in Table 1. This table gives a comparison of the price, size, and ruggedness of the three units.

In addition to the data shown on the curve, the Montronics synthesizer was often found to drift for several hours at a rate of 5 or 6 deg/min. When the drifting reversed direction, possibly because of temperature changes in the laboratory, it provided a brief opportunity to make a test before the drifting accelerated again. Thus, the table shows a poor long-term drift characteristic which is not especially noticeable on the previously given variance curves.

Some quite unexpected results were also obtained from these tests. At 36 MHz it was found that phase noise in the multipliers of the Hewlett-Packard driver was more than an order of magnitude lower than the phase noise in the previously used transistor multipliers. This made it

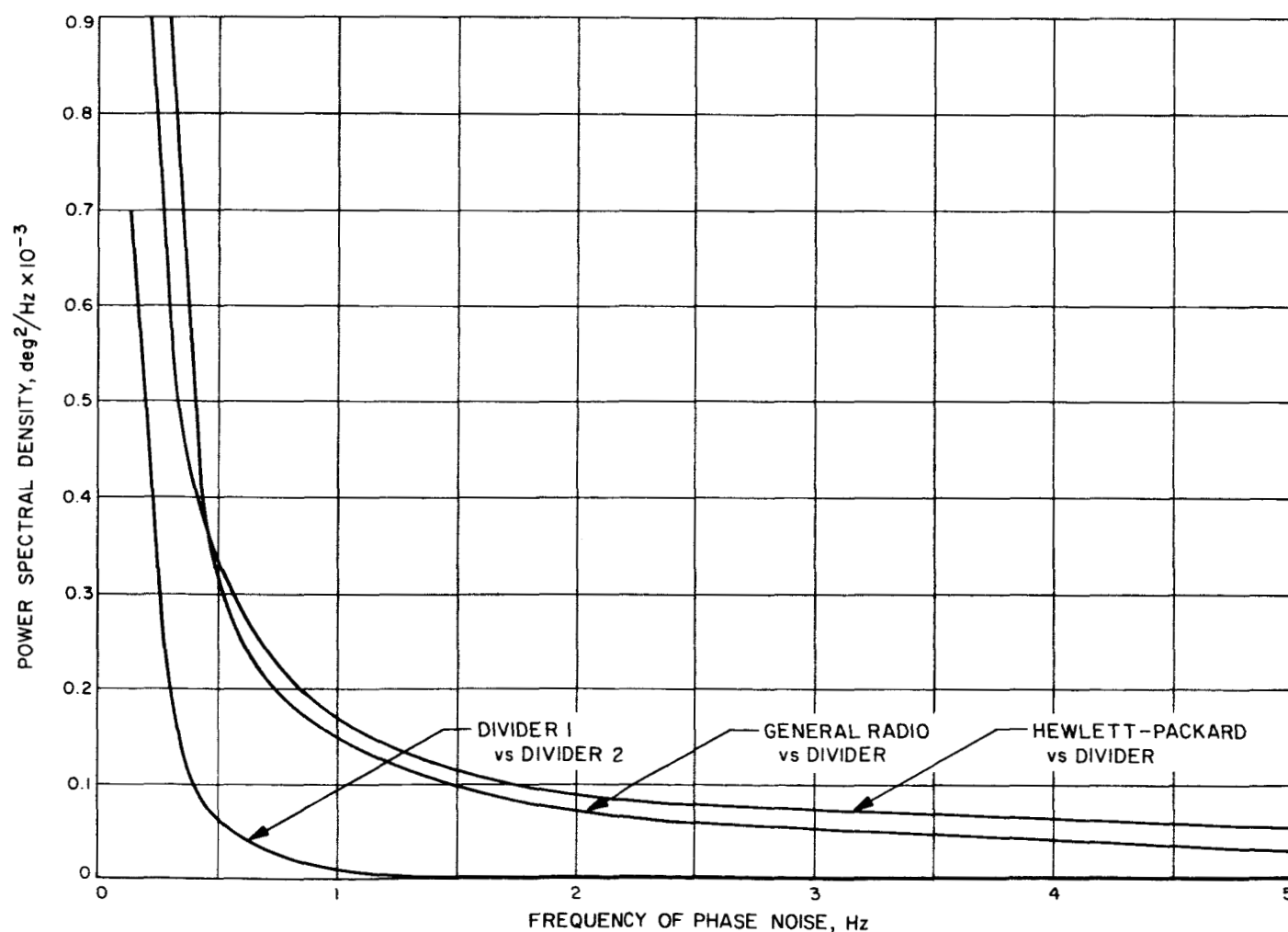


Fig. 6. Low-frequency spectra of phase noise measured at 500 kHz

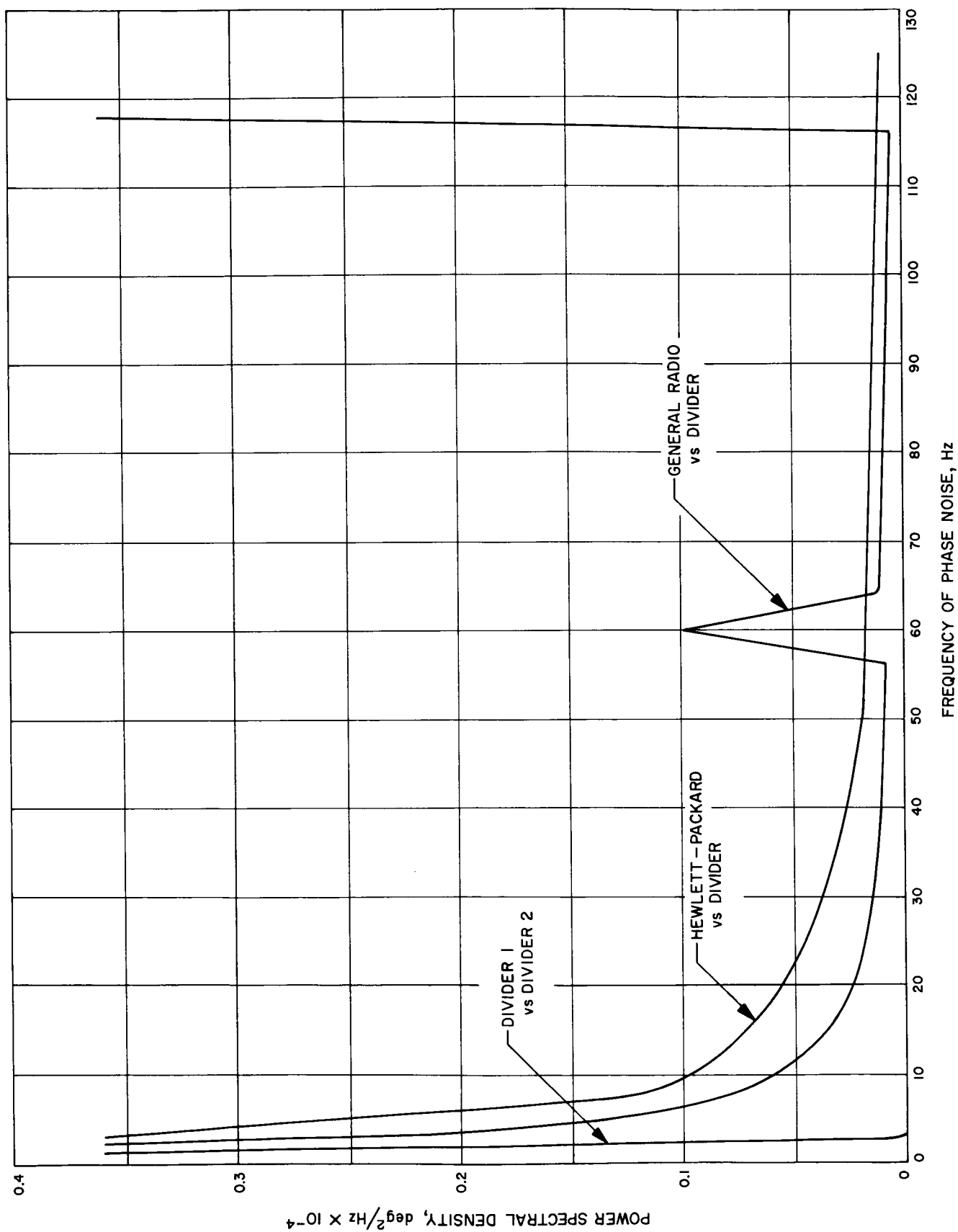


Fig. 7. Intermediate-frequency spectra of phase noise measured at 500 kHz

reasonable to use the driver as the basic standard for comparison. It also seemed unusual to find that the phase noise in the multiplier and divider curves decreased exponentially at increasingly high frequencies rather than remaining flat.

Experience shows that the high-frequency power spectral density curves are very repeatable. Even when different units of the same make are tested, they can produce curves lying within about $\pm 25\%$ of each other. This is remarkable consistency, considering how much effect tuning can have on the output. Drift and low-frequency

spectra vary considerably more, and it should be remembered that all curves were prepared from a single data run no more than 200 sec long.

In general, the complicated data system used here worked quite well. Better results might be obtained with a simpler computer system that gave results immediately in real-time, but such a system was not available. Hopefully, these tests will provide a basis for designing complex systems which use frequency synthesizers. If more detailed test information should become necessary later, this work may serve as a helpful guide.

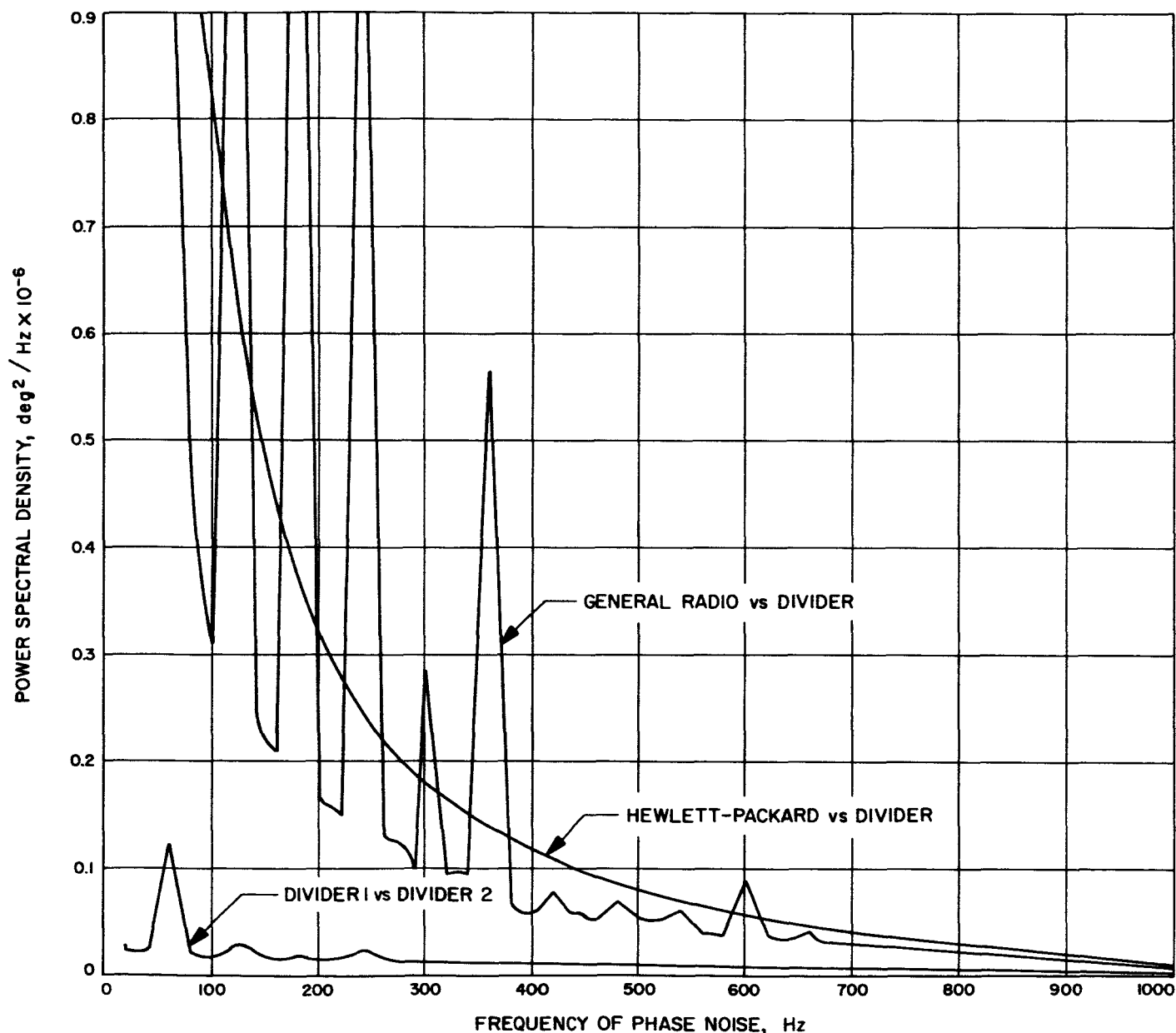


Fig. 8. High-frequency spectra of phase noise measured at 500 kHz

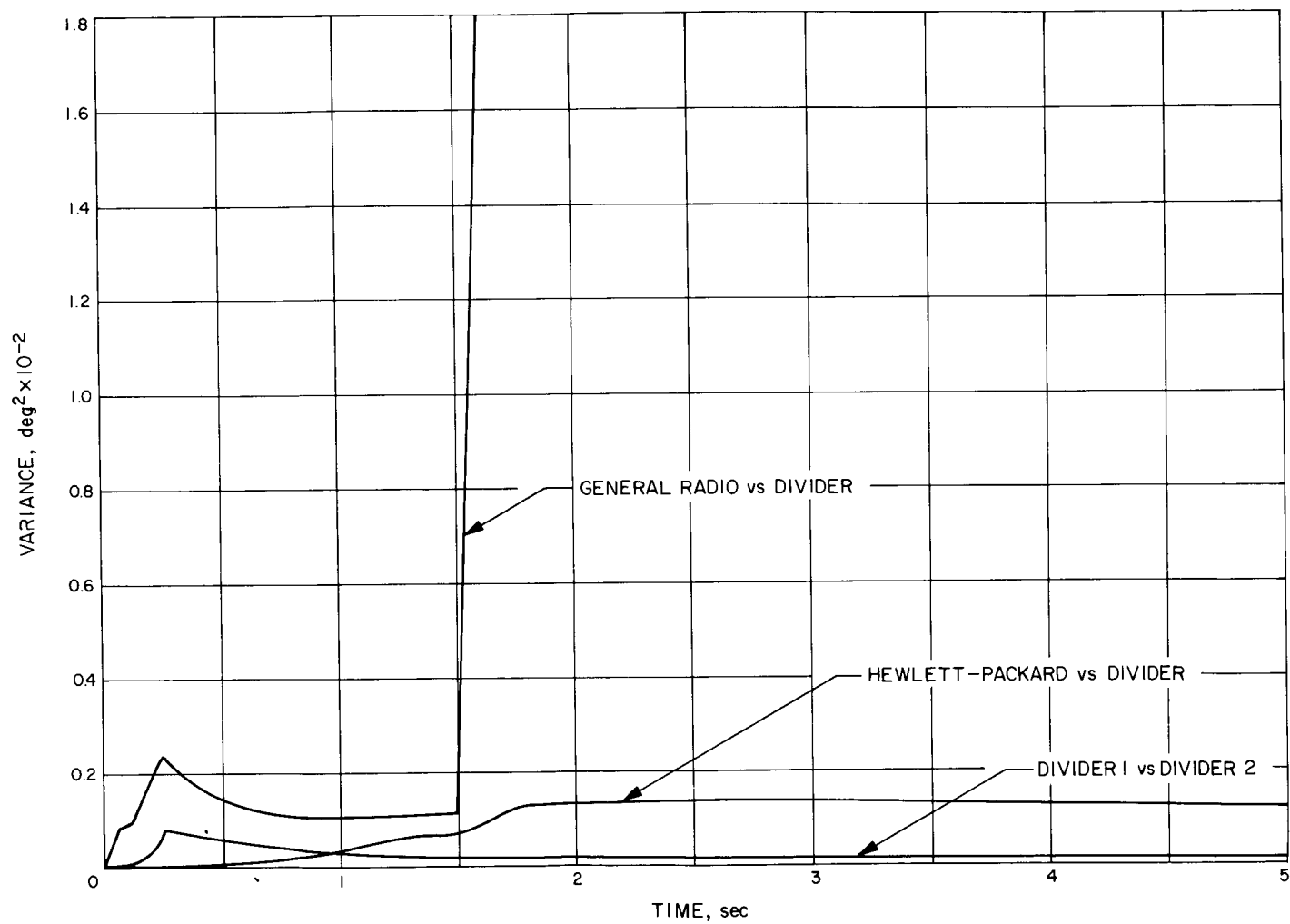


Fig. 9 Variance of phase noise as a function of time measured at 500 kHz in a short run

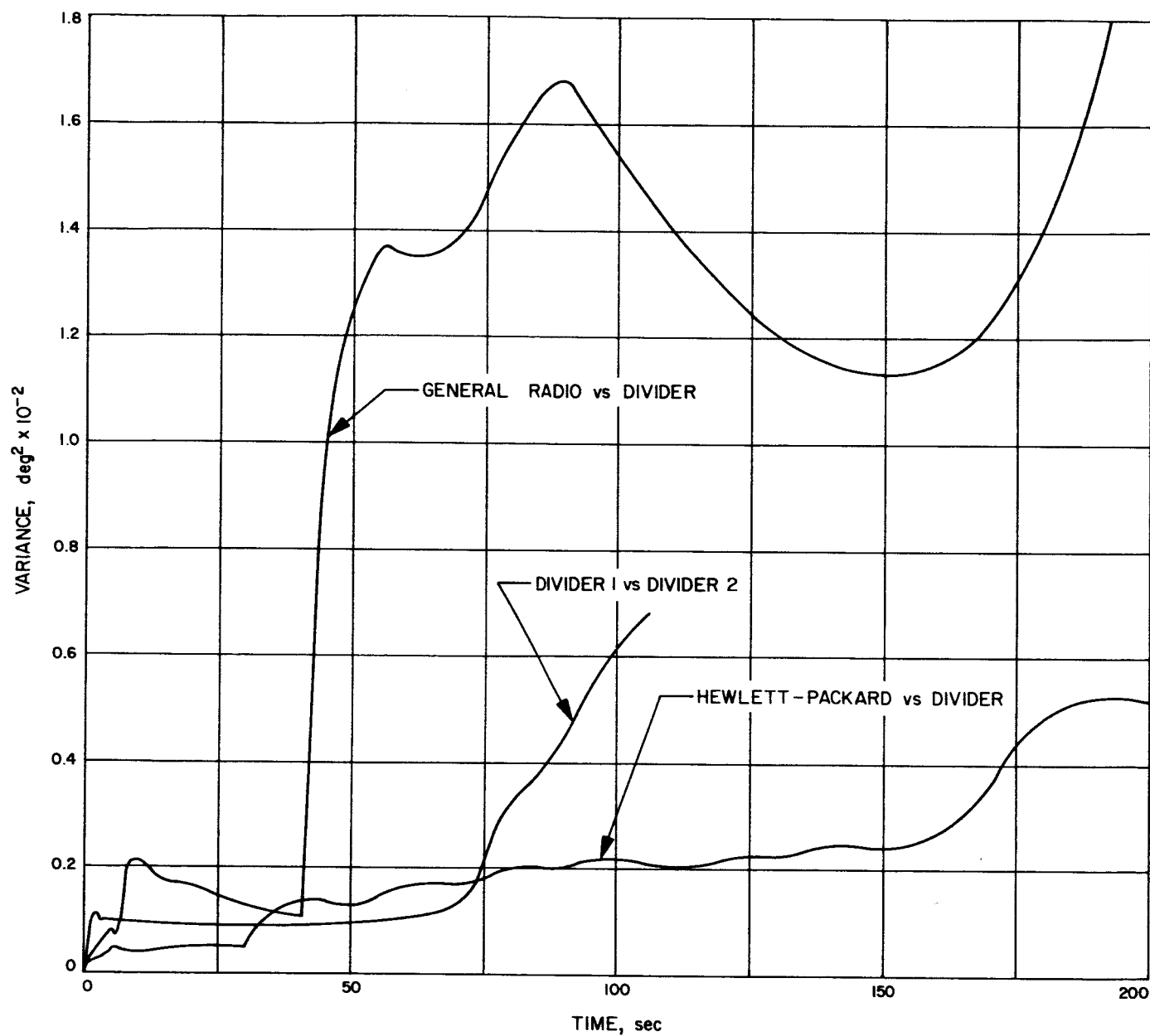


Fig. 10. Variance of phase noise as a function of time measured at 500 kHz in a long run

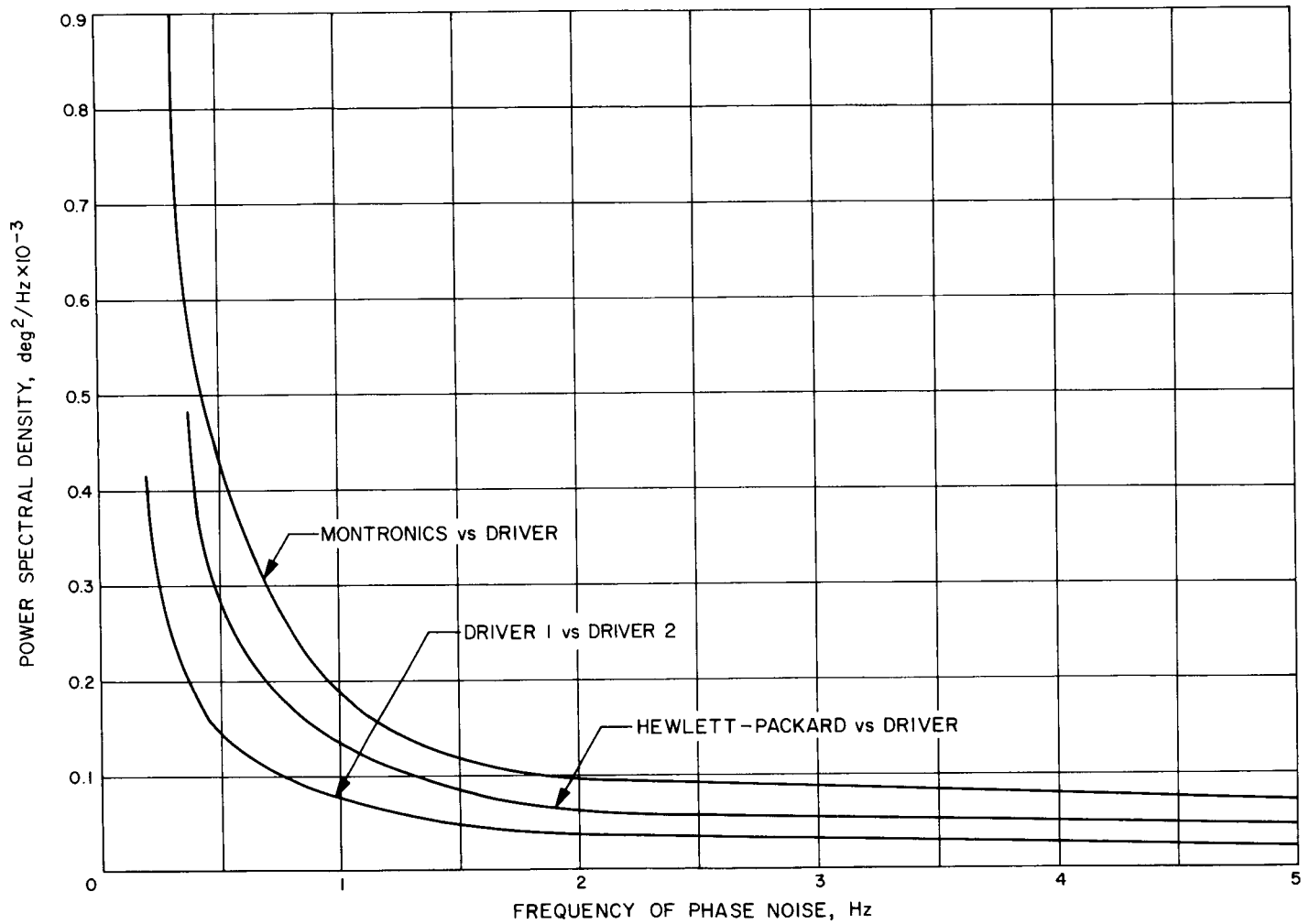


Fig. 11. Low-frequency spectra of phase noise measured at 36 MHz for Montronics and Hewlett-Packard synthesizers

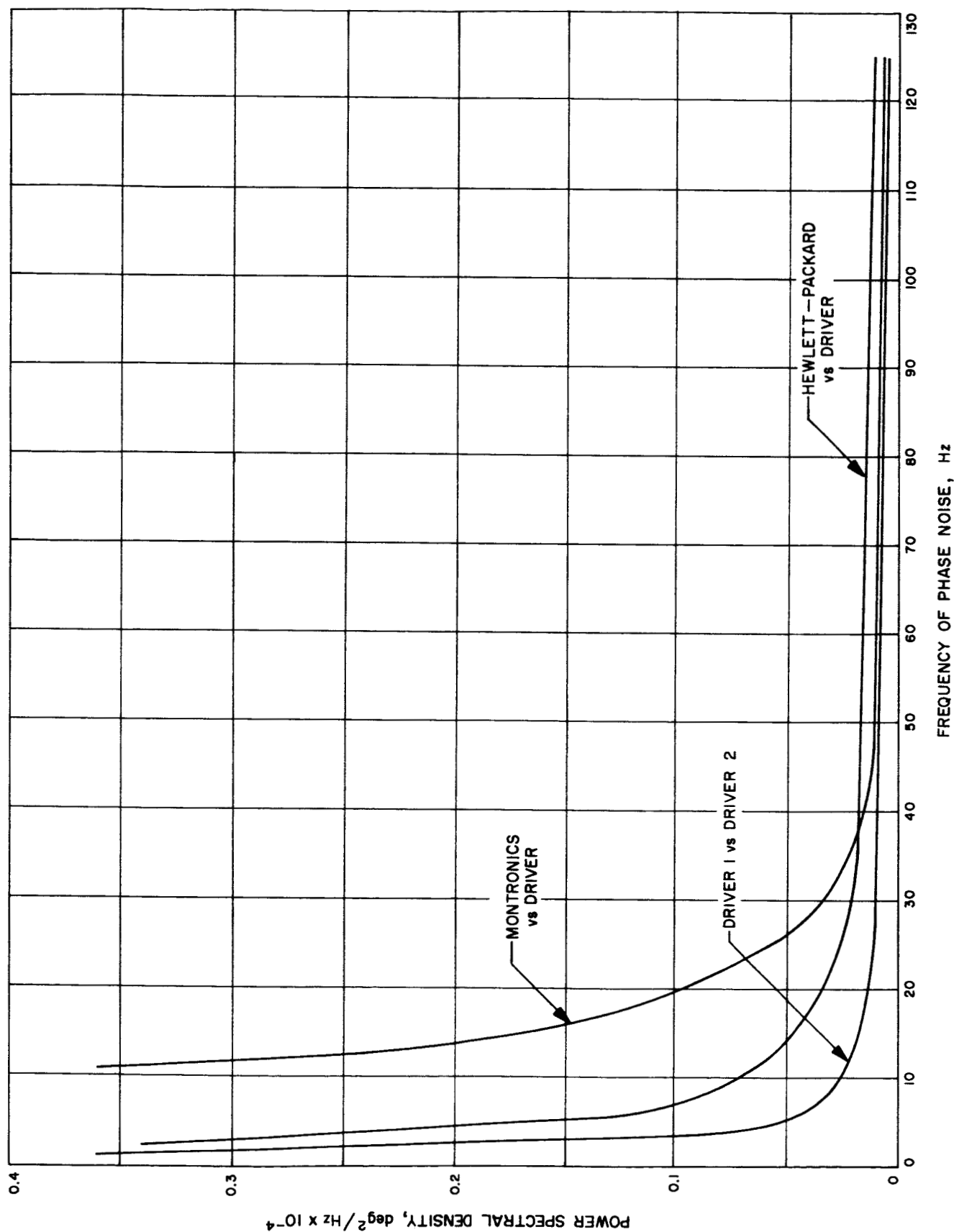


Fig. 12. Intermediate-frequency spectra of phase noise measured at 36 MHz for Montronics and Hewlett-Packard synthesizers

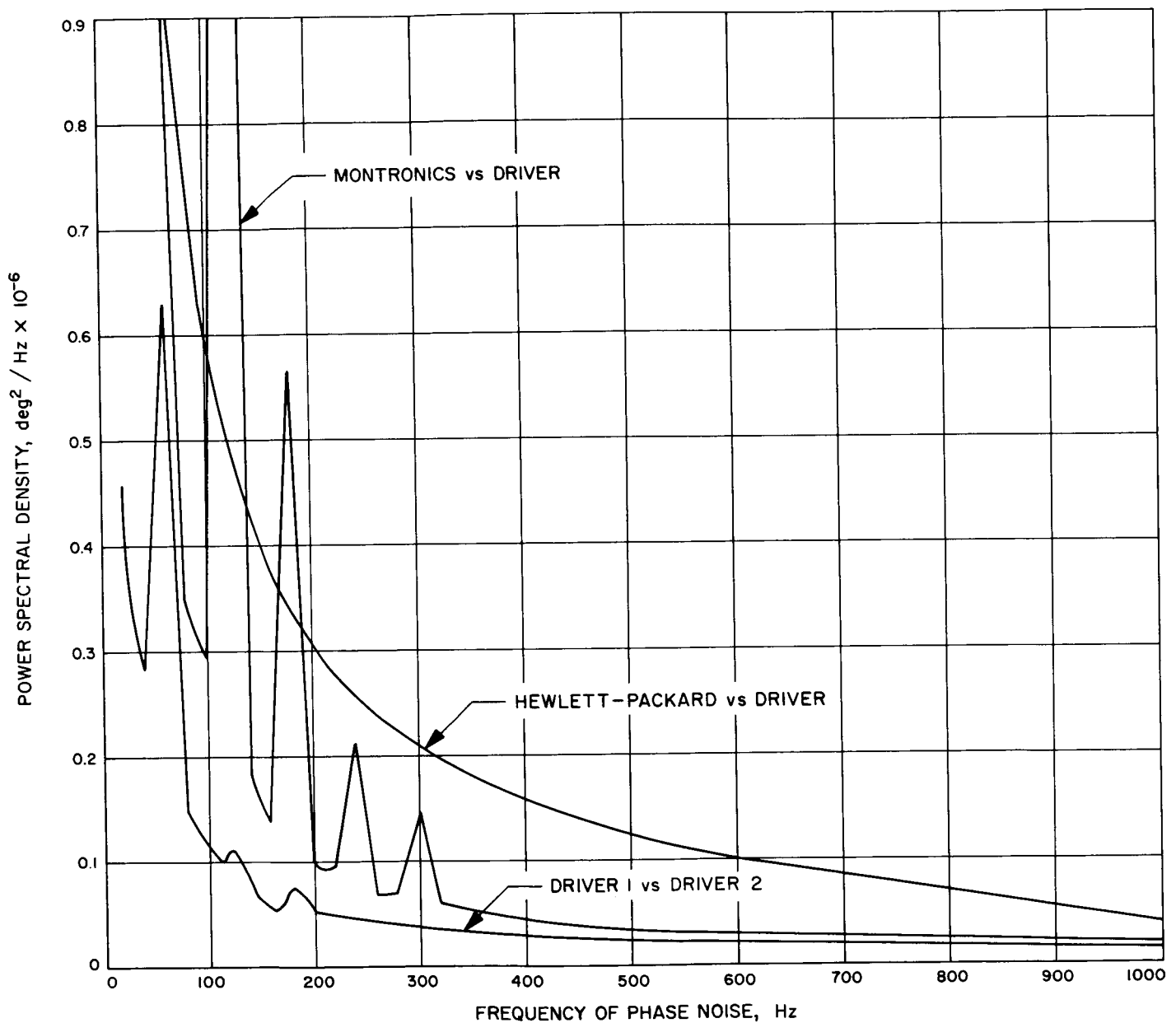


Fig. 13. High-frequency spectra of phase noise measured at 36 MHz for Montronics and Hewlett-Packard synthesizers

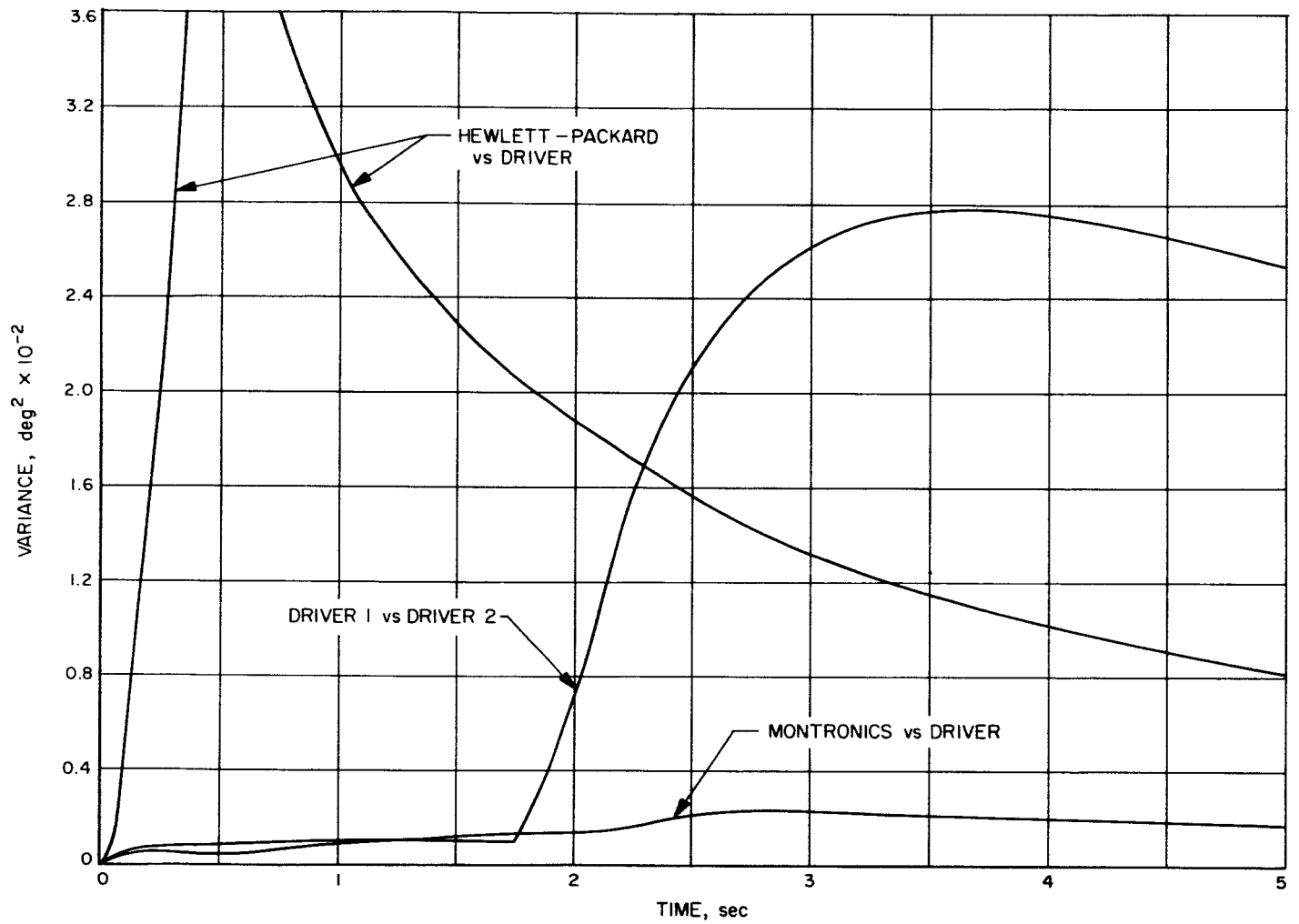


Fig. 14. Variance of phase noise as a function of time measured at 36 MHz in a short run for Montronics and Hewlett-Packard synthesizers

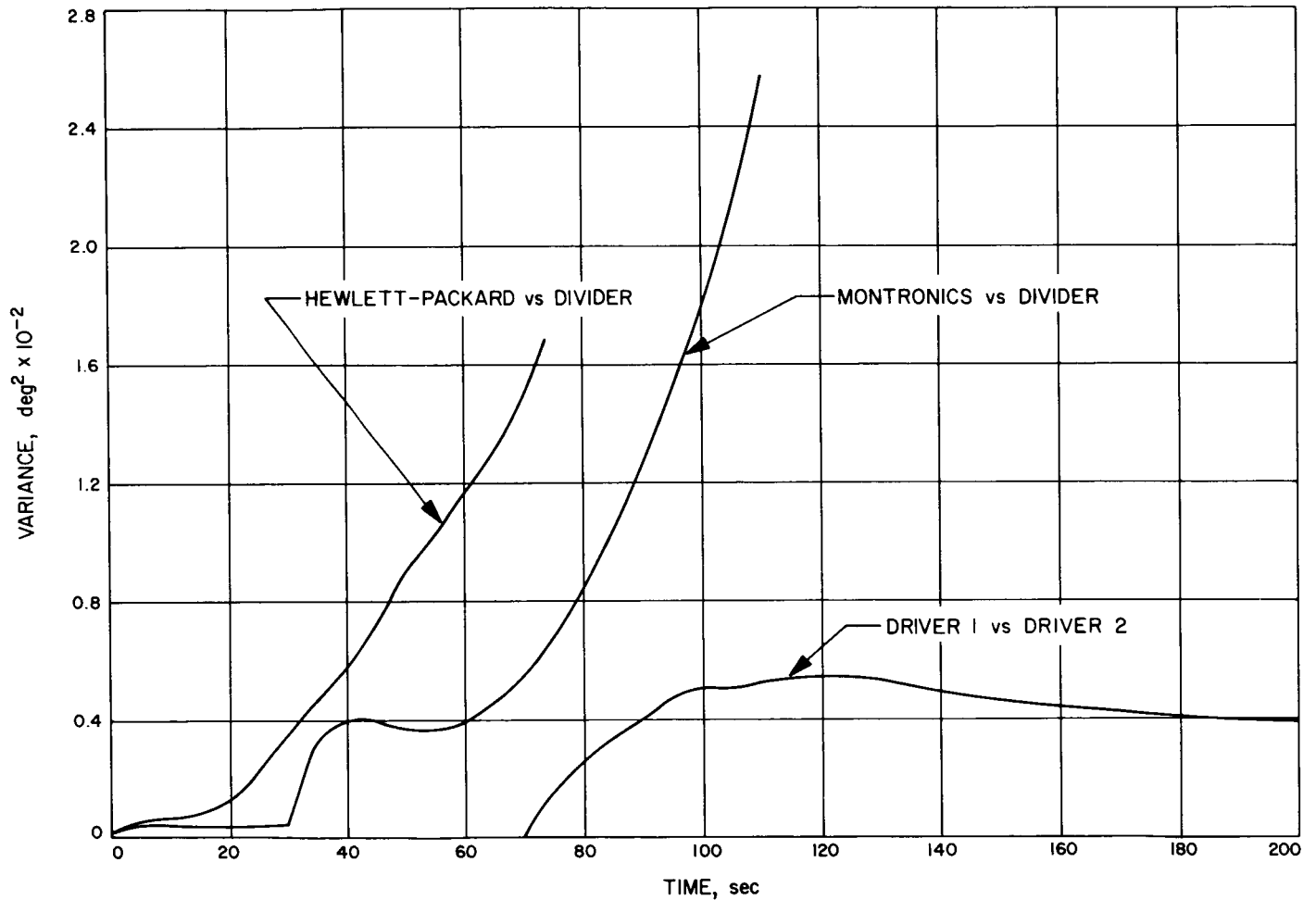


Fig. 15. Variance of phase noise as a function of time measured at 36 MHz in a long run for Montronics and Hewlett-Packard synthesizers

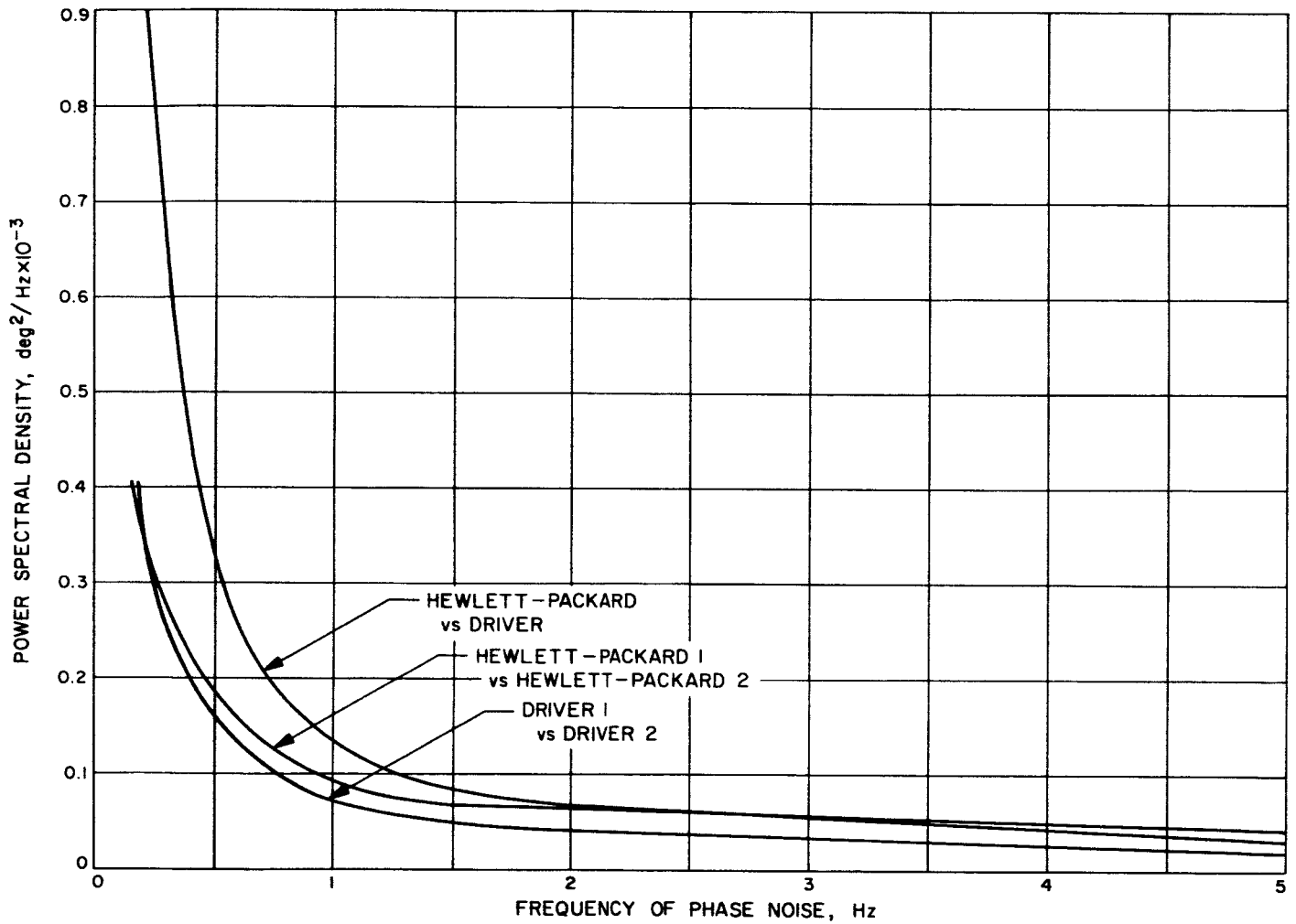


Fig. 16. Low-frequency spectra of phase noise measured at 36 MHz for Hewlett-Packard synthesizers

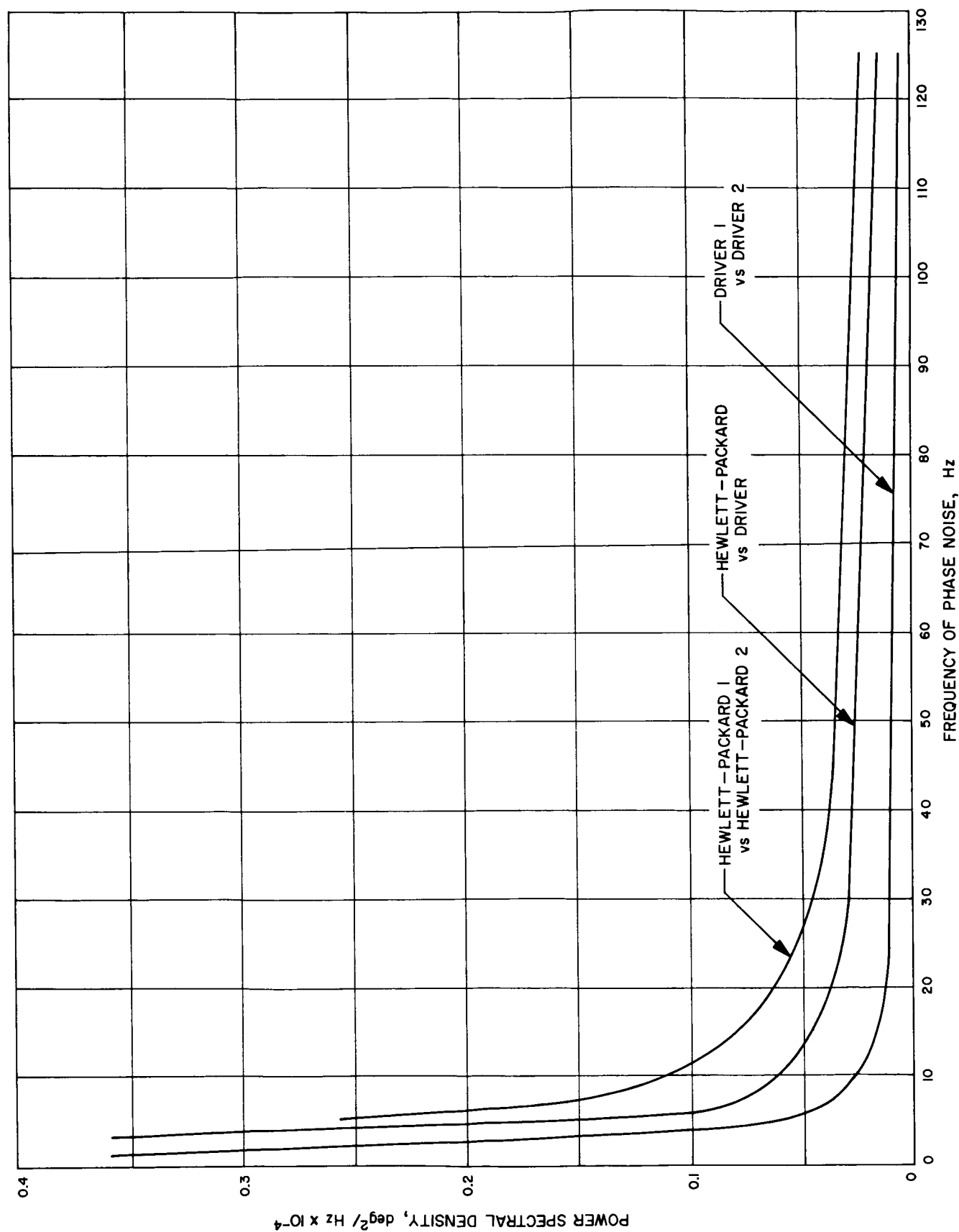


Fig. 17. Intermediate-frequency spectra of phase noise measured at 36 MHz for Hewlett-Packard synthesizers

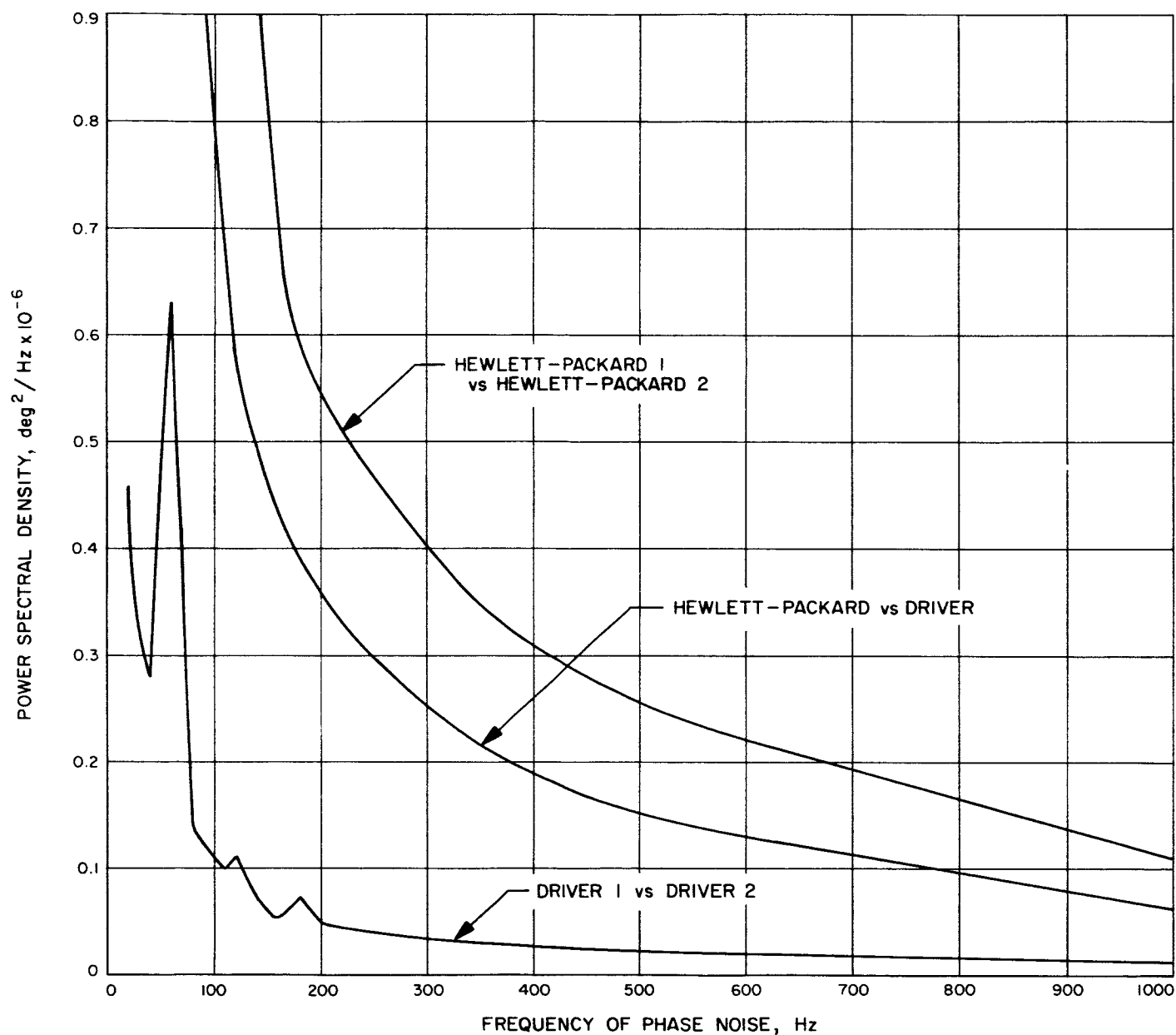


Fig. 18. High-frequency spectra of phase noise measured at 36 MHz for Hewlett-Packard synthesizers

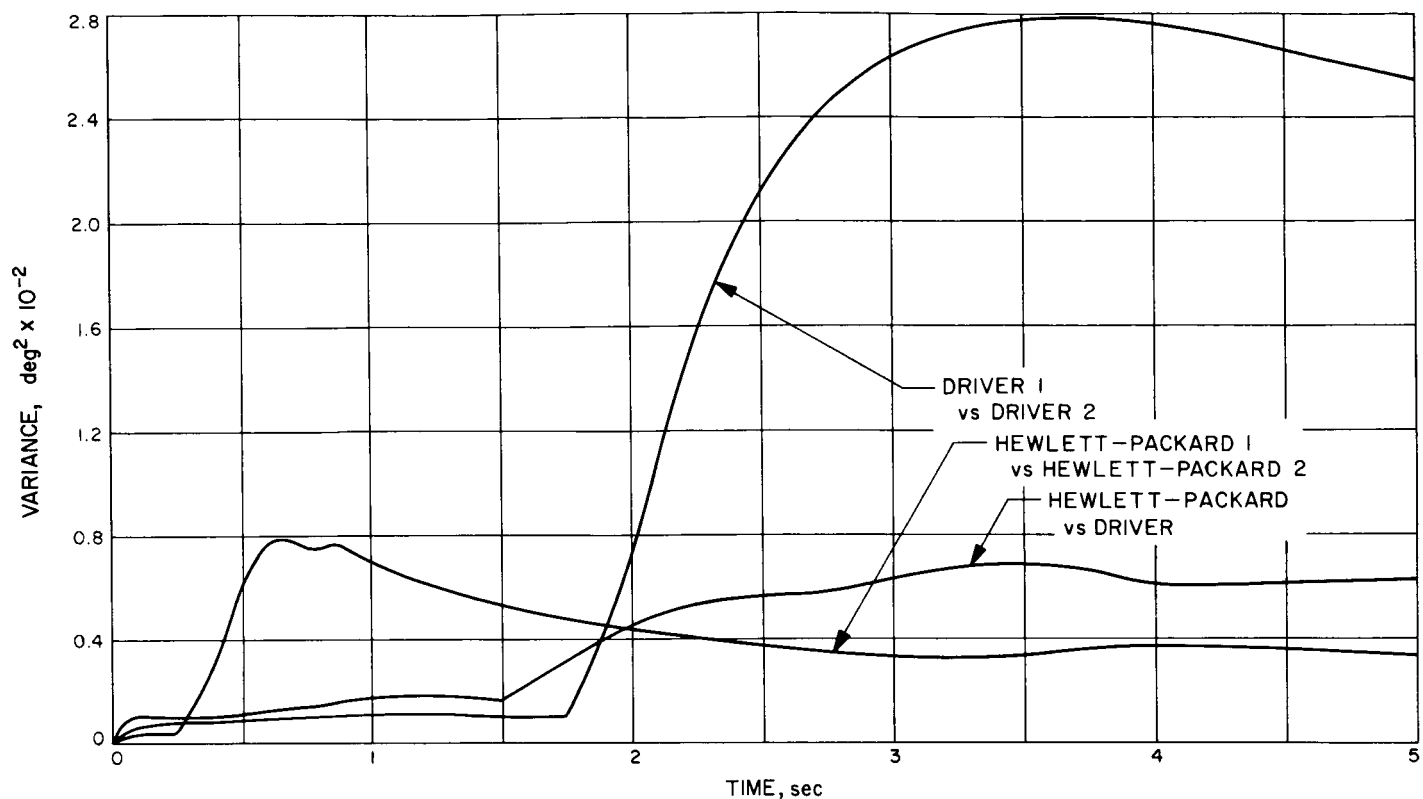


Fig. 19. Variance of phase noise as a function of time measured at 36 MHz in a short run for Hewlett-Packard synthesizers

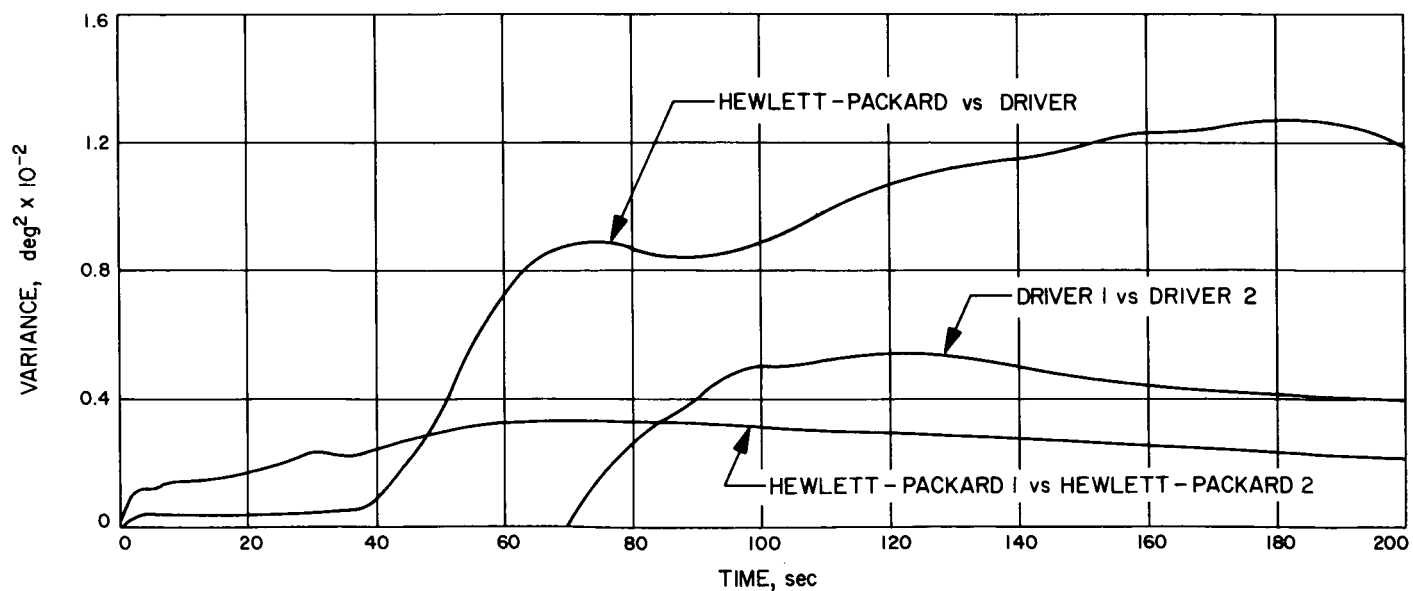


Fig. 20. Variance of phase noise as a function of time measured at 36 MHz in a long run for Hewlett-Packard synthesizers

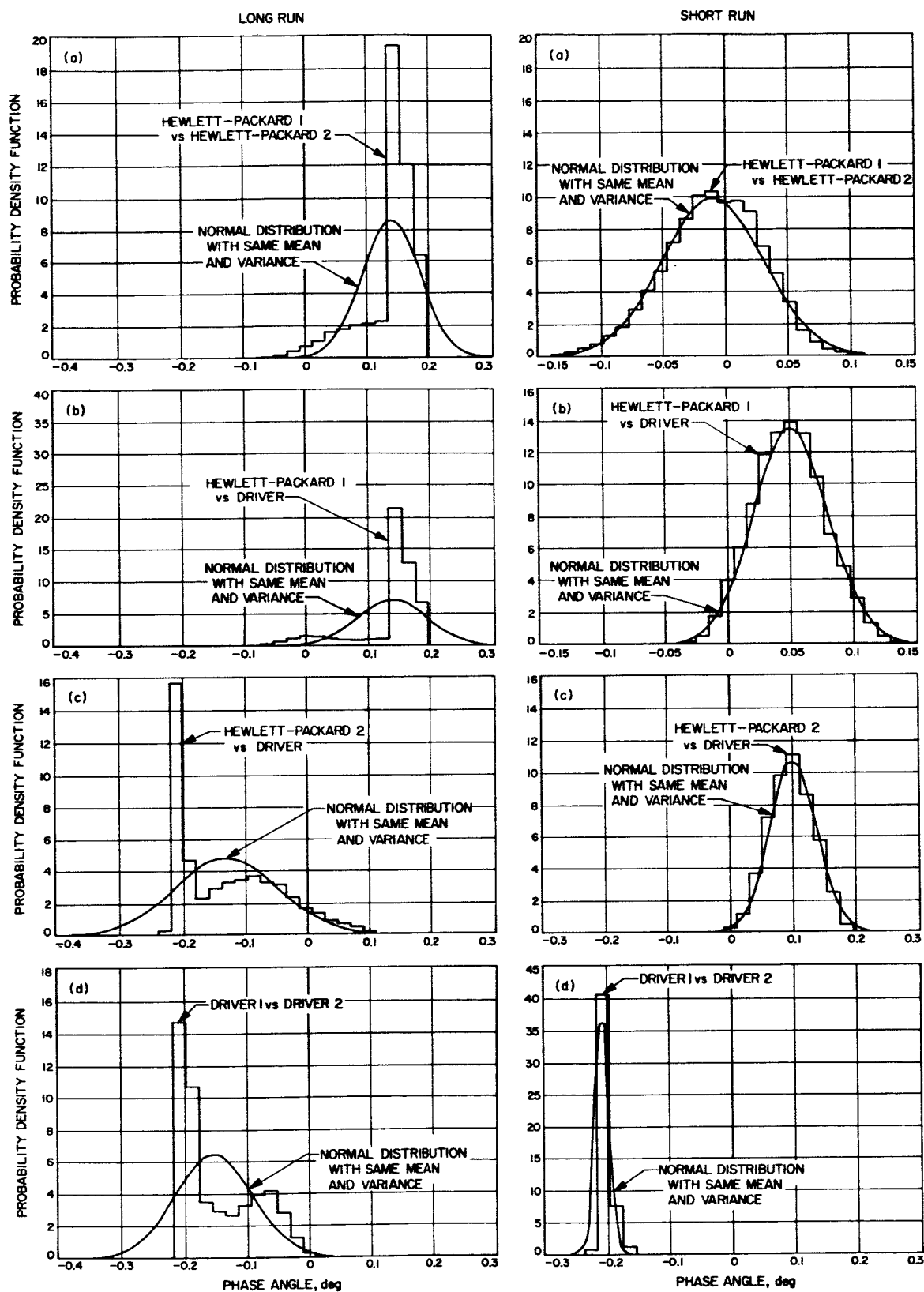


Fig. 21. Probability density function of phase noise measured at 36 MHz

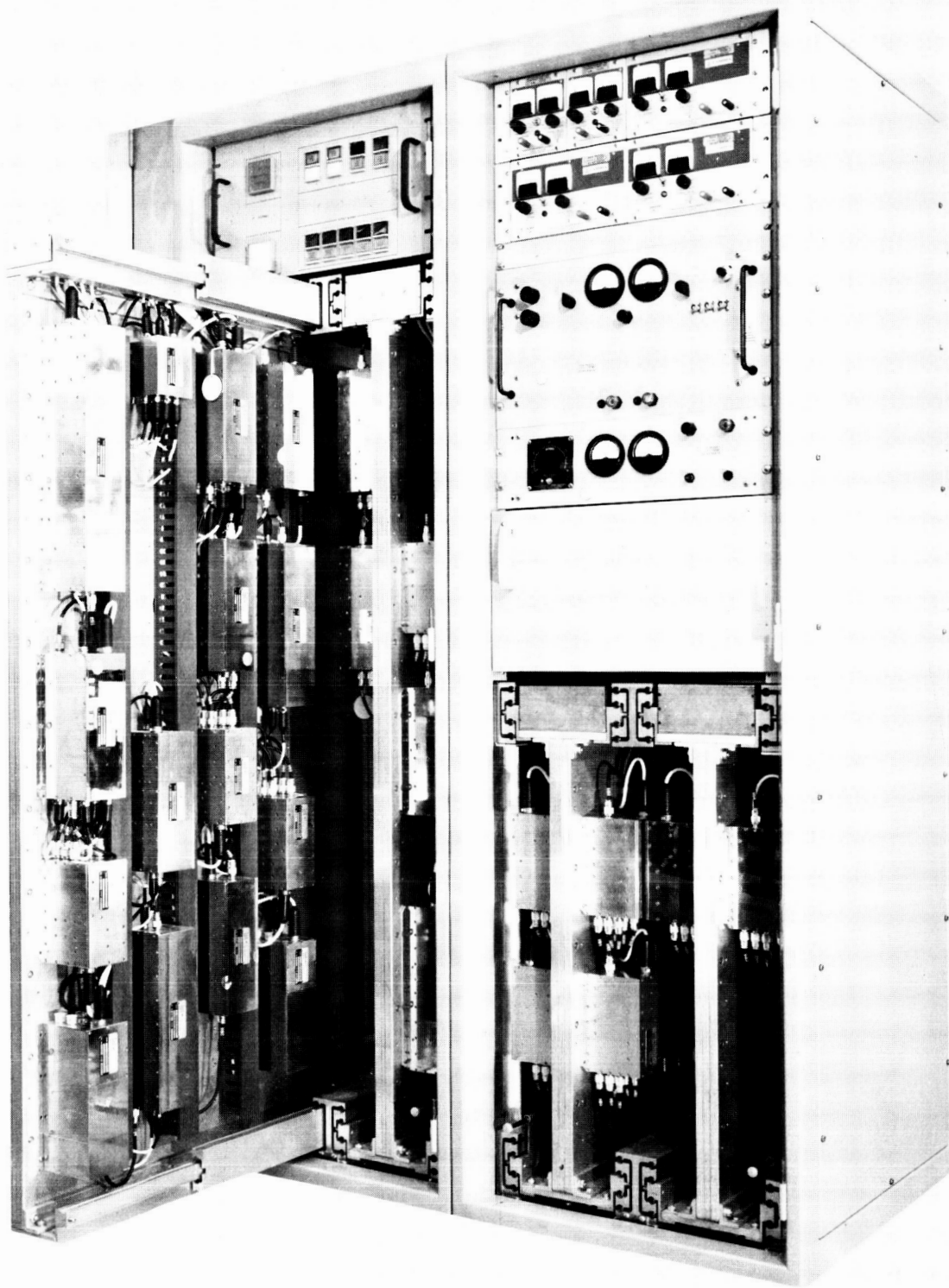


Fig. 22. Central frequency synthesizer

N66 38558

B. S- and X-Band Central Frequency Synthesizer at the Venus Deep Space Station

G. U. Barbani

The central frequency synthesizer (CFS) has completed final system tests, has been weighted, shipped, installed, and has been in operation at the Venus Deep Space Station, Barstow, California, since May 3, 1966.

1. Description

All RF modules are mounted on full or half-size cold plates, which can be water-cooled, if necessary. There is 30% additional space on the cold plate should the need arise. 500-lb sliders are provided to extend the cold plates for service. System power supplies and voltage vigilant unit (SPS 37-39, Vol. III, pp. 66-71) are mounted on light-weight sliders. The rubidium vapor frequency standard and its power supply are rigidly mounted. The internal hardware, such as cold plates, RETMA angles, and structural supports, have been cadmium-plated to eliminate grounding problems through painted surfaces. The cabinets are externally painted GSDS grey. Fig. 22 shows the

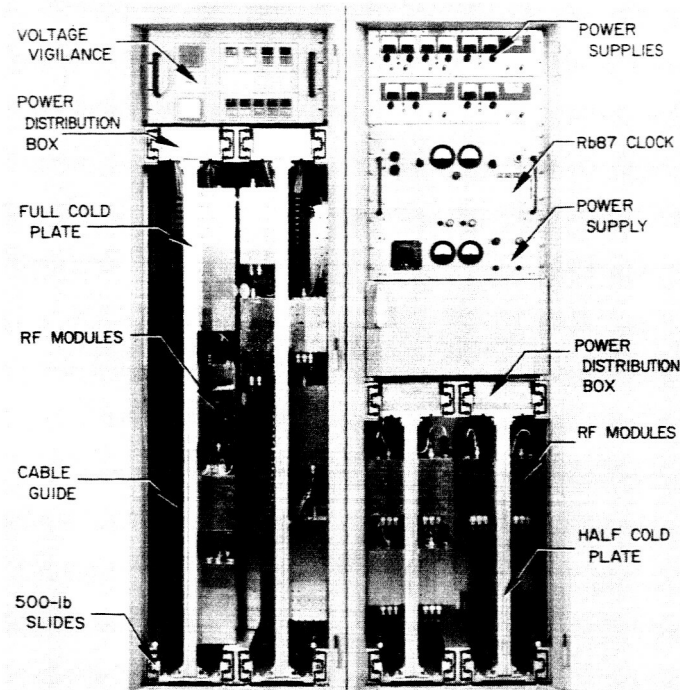


Fig. 23. Central frequency synthesizer, front view

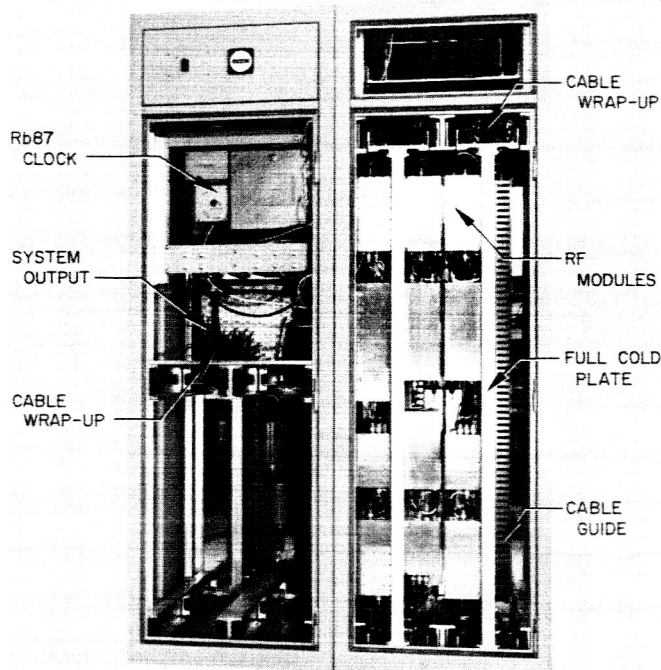


Fig. 24. Central frequency synthesizer, rear view

2-bay system with all doors removed. Refer to Figs. 23 and 24 for system details.

2. System Evaluation and Tests

DC power consumption for the CFS is measured at 92.4 w from a 309-w source rated at 50°C. Power reserve available can be seen on Table 2. Considering a 20% safety margin on all supplies, the available power for additional loads is shown in Table 2. Power consumption from the various supplies is given in Table 3.

Table 2. DC Power reserve for CFS

Power supply	+ 15 vdc	- 15 vdc	+ 30 vdc	- 30 vdc
Watts	23.3	22.8	24	103.2

Table 3. DC Power distribution

Power supply	+ 15 vdc	- 15 vdc	+ 30 vdc	- 30 vdc
Watts	3.9	4.5	51	33

All power supplies were checked for noise under full load, and none were found to be $> 400 \mu\text{V rms}$ (Table 4).

Table 4. DC Power supply noise

Power supply	+15 vdc	-15 vdc	+30 vdc	-30 vdc
Noise	295 μ v	275 μ v	365 μ v	395 μ v

Remote sensing lines were inspected and found to be satisfactory.

As system and subsystem testing continued at the Laboratory and at the Venus Deep Space Station, all RF module tuning was rechecked and locked. RF levels, noise, bandwidths, distortion and power drains were recorded. Phase jitter measurements were taken on each of the four phase-lock loops, with test results shown in Table 5. Fig. 25 depicts typical phase jitter in two of the phase-lock loops. The calibration in each case is 2 v/cm, 1.0 mm/sec paper speed and 10 mv/mm record scale. An S-curve calibration appears for the 35.2-MHz loop only, although

Table 5. Phase noise and measured bandwidth for all phase-locked loops in CFS

Phase noise		Bandwidth	
VCO frequency, MHz	Degrees, rms	Design $2\beta_L$, cps	Actual $2\beta_L$, cps
31.44	0.13	1.0	1.0
31.84	0.10	1.0	1.05
35.075	0.04	1.0	1.04
35.2	0.10	1.0	0.90

all other loops have been so calibrated. The character of the phase noise is somewhat different in each loop. This is due to the synthesized loop input signals. (See SPS 37-36, Vol. III, p. 68.) The 31.44-MHz loop input signal is derived from a 1.44-MHz synthesizer and a 400-kHz source, whereas the 35.2-MHz loop input signal is derived from a 35.2-MHz synthesizer and a 200-kHz source. The differences between the loops are the 31.44-MHz balanced mixer which does not allow all the high frequencies to pass through, and the synthesizer multiplication factor.

Comparison of 35.075-MHz versus 35.2-MHz phase jitter shows the latter to be 2.5 times greater. Again, the block diagram shows the generation of 35.075 MHz from a series of dividers and a balanced mixer, an arrangement where no multiplication or synthesizers are used. This low phase jitter is partly attributed to modifications made to the voltage-controlled oscillators. Refer to SPS 37-30, Vol. III, p. 66 for comparative phase-noise results.

The audio alarm circuit was connected to the CFS and tested (SPS 37-39, Vol. III, Fig. 24, p. 70). The external batteries were not connected to the rubidium vapor frequency standard because of a discharge test in process with the interim central frequency synthesizer (ICFS). Upon completion of this discharge test, the batteries will be connected to the CFS.

Bandwidth measurements ($|1 - H(s)|$) were taken on each of the four phase-lock loops to determine the accuracy of the tracking filter constants. The modulation

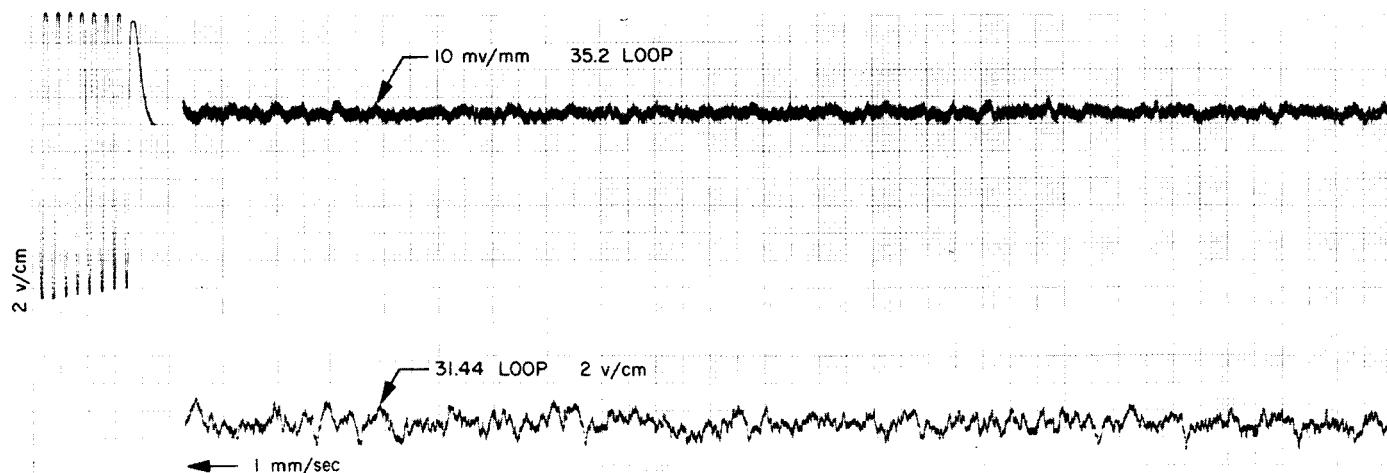


Fig. 25. Measured phase jitter for the 31.44- and 35.2-MHz phase-lock loop

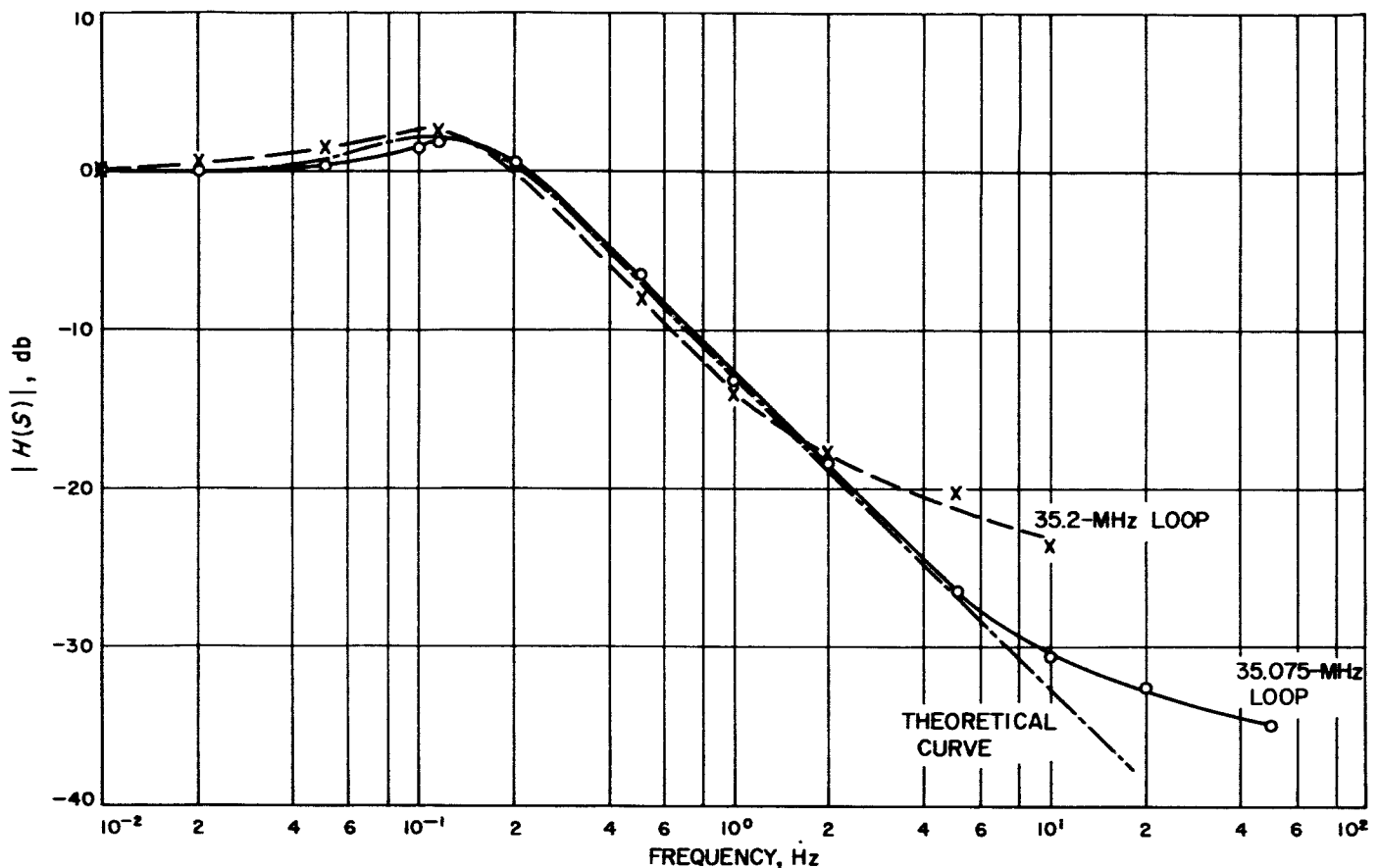


Fig. 26. The 35.075- and 35.2-MHz measured loop bandwidth

varied from 6 to 10 deg, depending upon the parameters of each phase-lock loop. Figs. 26 and 27 show the theoretical curve and two of the measured phase-lock loops in each figure. Table 5 shows the design bandwidth of $2\beta_L$ versus the actual measured bandwidth.

A temperature measurement was made throughout the CFS to locate any thermal buildup or hot spots. The +30 vdc power supply proved to be the hottest module with a +34°C temperature environment. This is well below the +50°C design figure. All other areas throughout the system remained at or near ambient.

3. Modifications

A $\times 4$ frequency multiplier (1 to 4 MHz) and a 4.0-MHz distribution amplifier are required to provide the programmed local oscillator with reference signals in conjunction with the 2295-MHz *Mariner IV* receiver. The $\times 4$ multiplier was removed from the ICFS, checked to meet RF module specifications and installed in the CFS.

A distribution amplifier tuned at 4.16 MHz was retuned to 4.0 MHz and installed in the CFS.

Modification of a voltage-controlled oscillator (VCO), provided the necessary data for the evaluation of all VCO's in the CFS. Phase noise measurements were made prior to and after modification (Table 6). The modification involved the removing of the AGC system, changing the transistors, selection of low leakage varicaps, bias, and crystal inductance change (Fig. 28).

Table 6. The effects of phase-noise versus VCO modification

VCO frequency, MHz	Phase noise prior to modification, deg, rms	Phase noise after modification, deg, rms
31.44	0.306	0.13
31.84	0.15	0.10
35.075	0.18	0.04
35.2	0.31	0.10

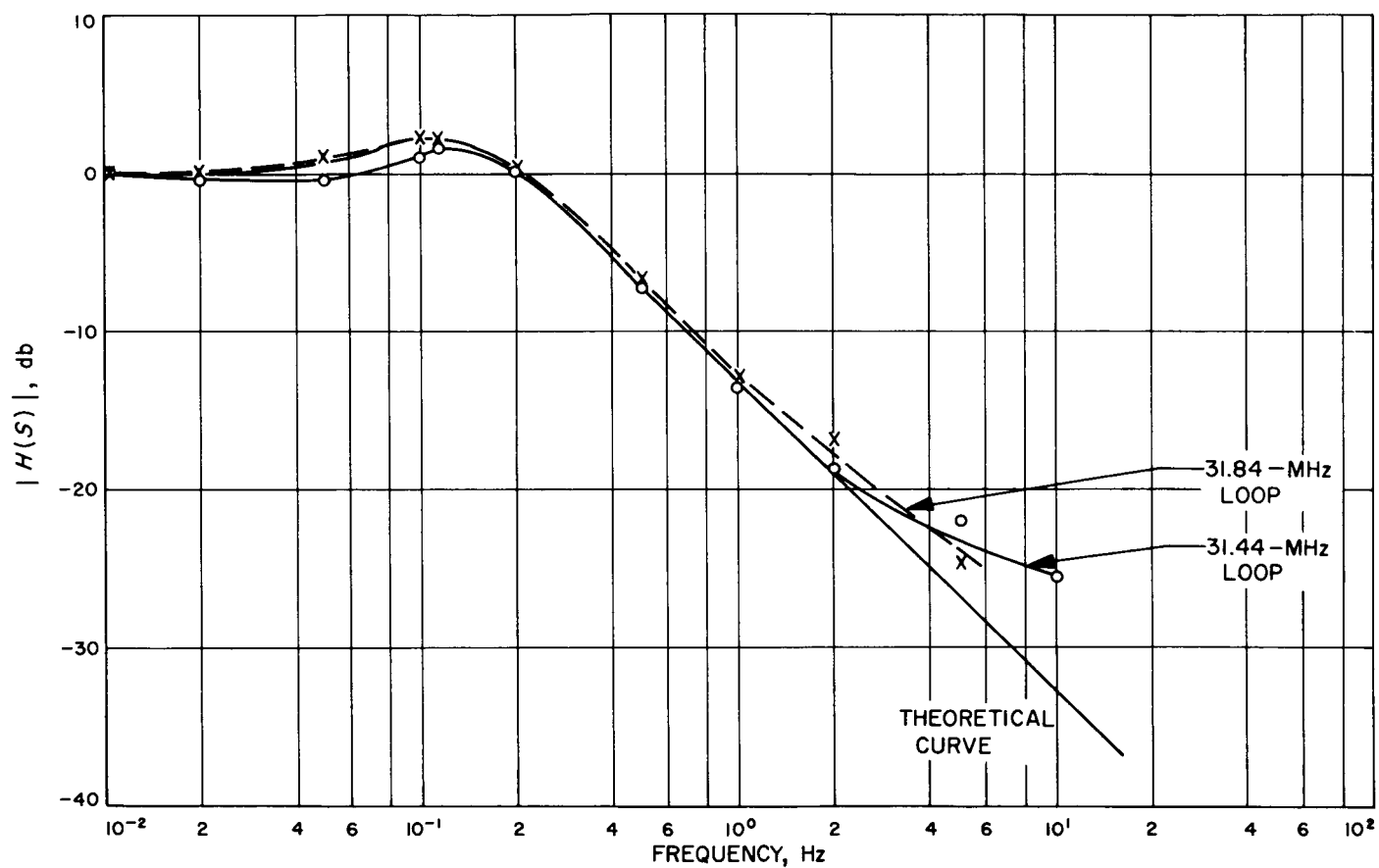


Fig. 27. The 31.44- and 31.84-MHz measured bandwidth

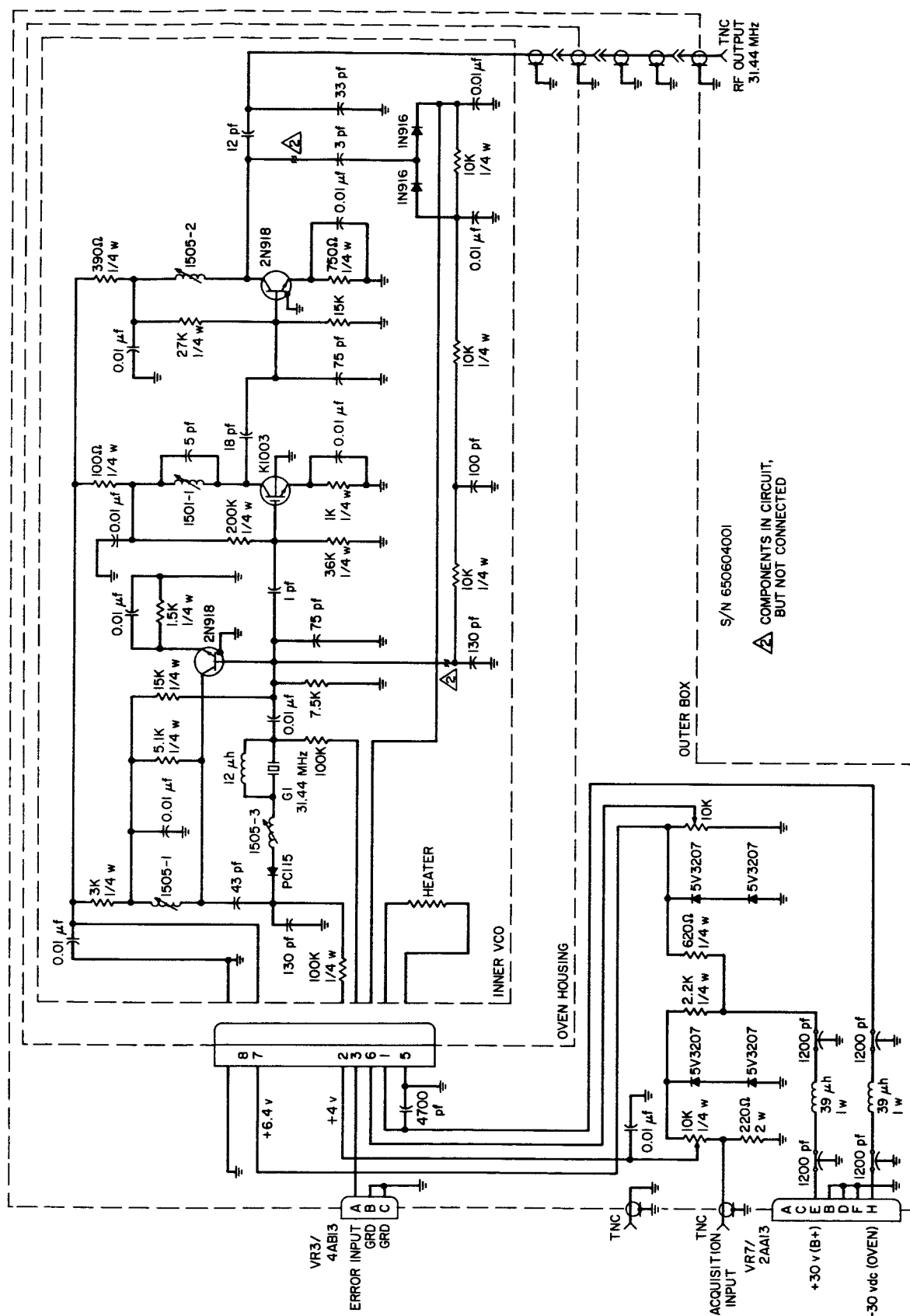


Fig. 28. Voltage-controlled oscillator schematic

C. Experimental S-Band Receiver at the Mars Deep Space Station

D. W. Brown

Initial planning for post-encounter tracking of *Mariner IV* at the Goldstone Mars Deep Space Station included modification of the GSDS receiver for use with a programmed local oscillator (PLO) for open-loop tuning and an autocorrelator for signal processing. These changes were to consist of:

- (1) Cabling to allow injection of 70-Mc PLO output into the standard $\times 32$ frequency multiplier;

- (2) Provision for a special $\times 12$ frequency multiplier to supply a stable 60-Mc second local oscillator (to be derived from the 5-Mc output of the frequency and timing subsystem); and
- (3) Addition of a stable third local oscillator (commercial synthesizer), balanced mixer, and special 10-Mc IF amplifier to provide an output centered at 1050 cps to the autocorrelator.

As it became apparent that site implementation schedule would not provide a standard receiver until late spring of 1966, an experimental receiver was provided. This receiver was implemented as shown in Figs. 29 and 30. The unshaded portion of the block diagram of Fig. 31 represents this configuration. In addition to the modifications described above, a 1-Mc cleanup loop and

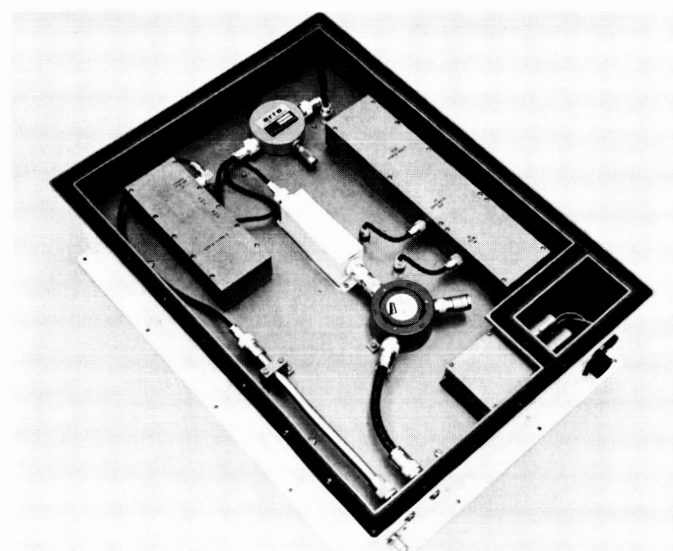
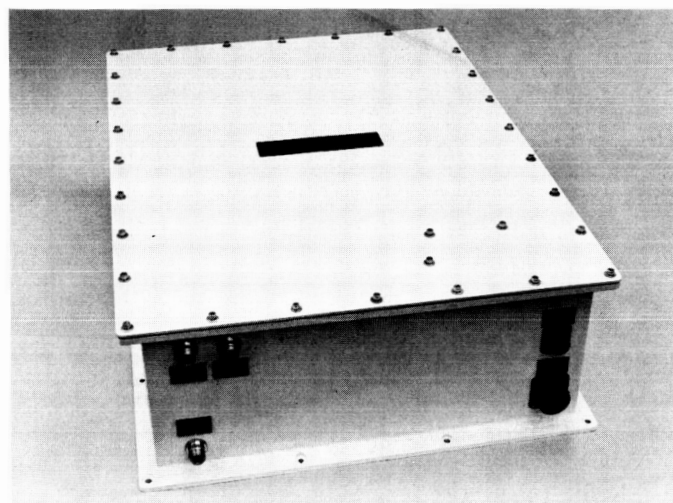


Fig. 29. 2295- to 50-Mc converter (a) outside (b) inside

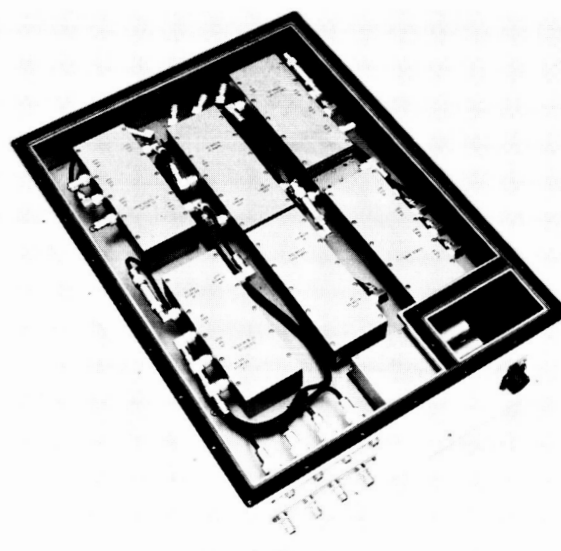
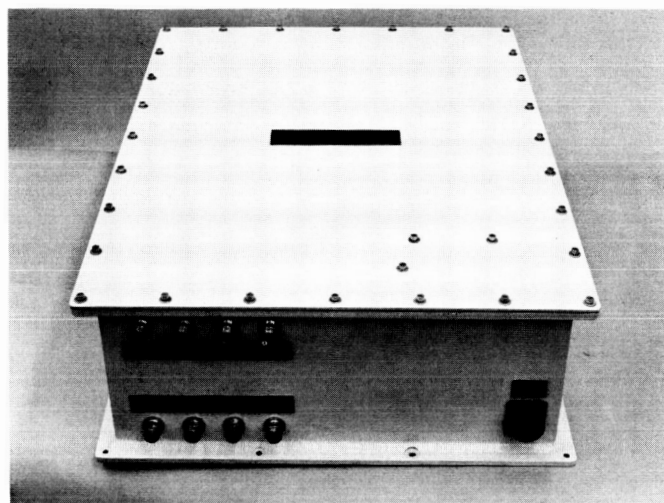


Fig. 30. 50- to 1050-cps converter (a) outside (b) inside

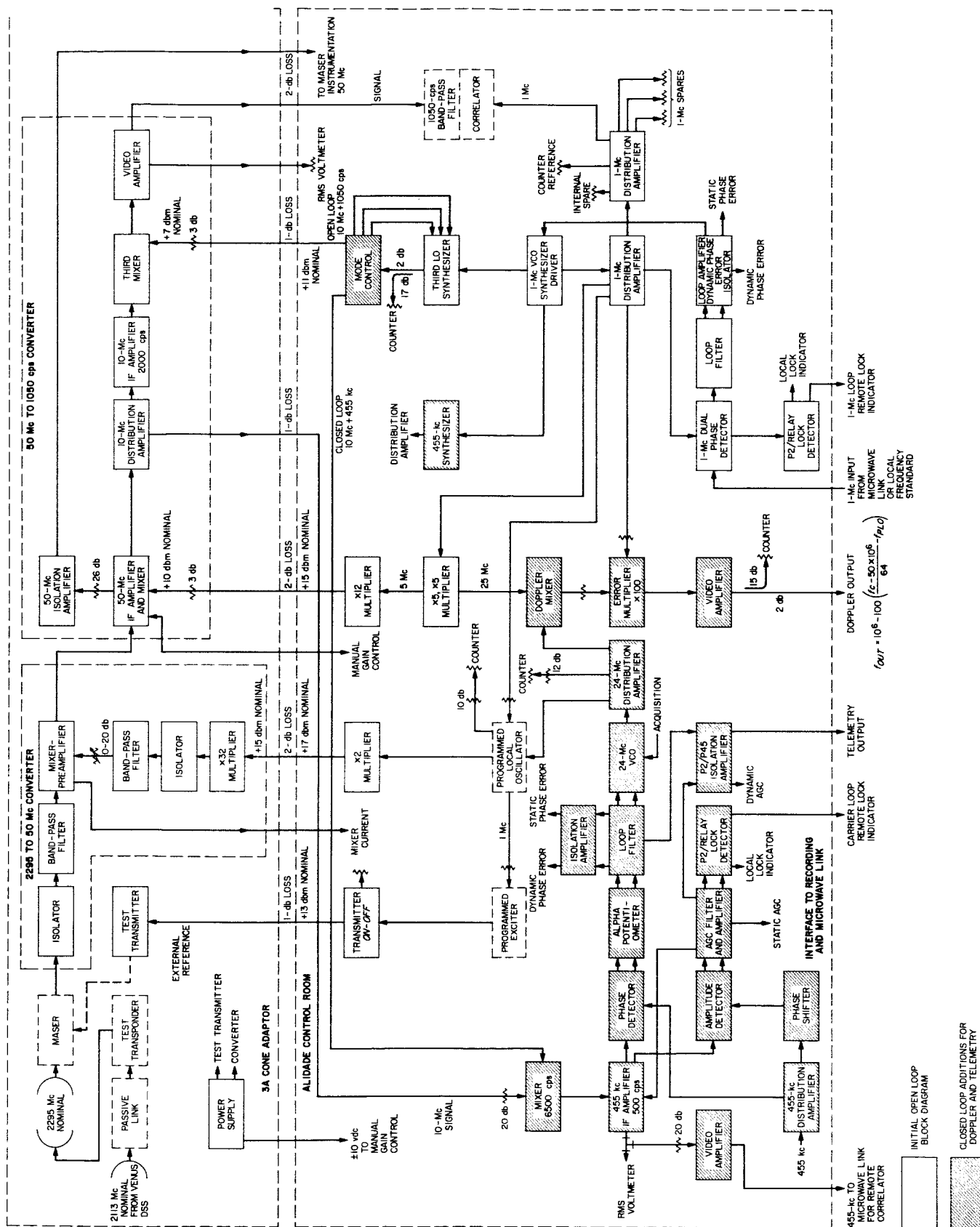


Fig. 31. S-Band experimental receiver, Mars DSS, block diagram

distribution system were utilized in connection with the microwave link from Venus Deep Space Station to establish a common frequency reference in two-way operation (SPS 37-39, Vol. III, pp. 106 to 108). The modifications under Item (3) were accomplished by installing a special six-pole crystal filter at 10 Mc to provide third image rejection in excess of 45 db with a nominal bandwidth of 2000 cps and by using appropriate standard telemetry modules as the third mixer and video amplifier. Manual

gain control (MGC) was provided in the usual manner through biasing of the "50-Mc IF amplifier and mixer" module. The resulting gain distribution is shown in Fig. 32.

When the postencoder tracking program was broadened to include the solar occultation experiment which was to begin in early March 1966 and continue through mid-April, it became desirable to provide a closed-loop

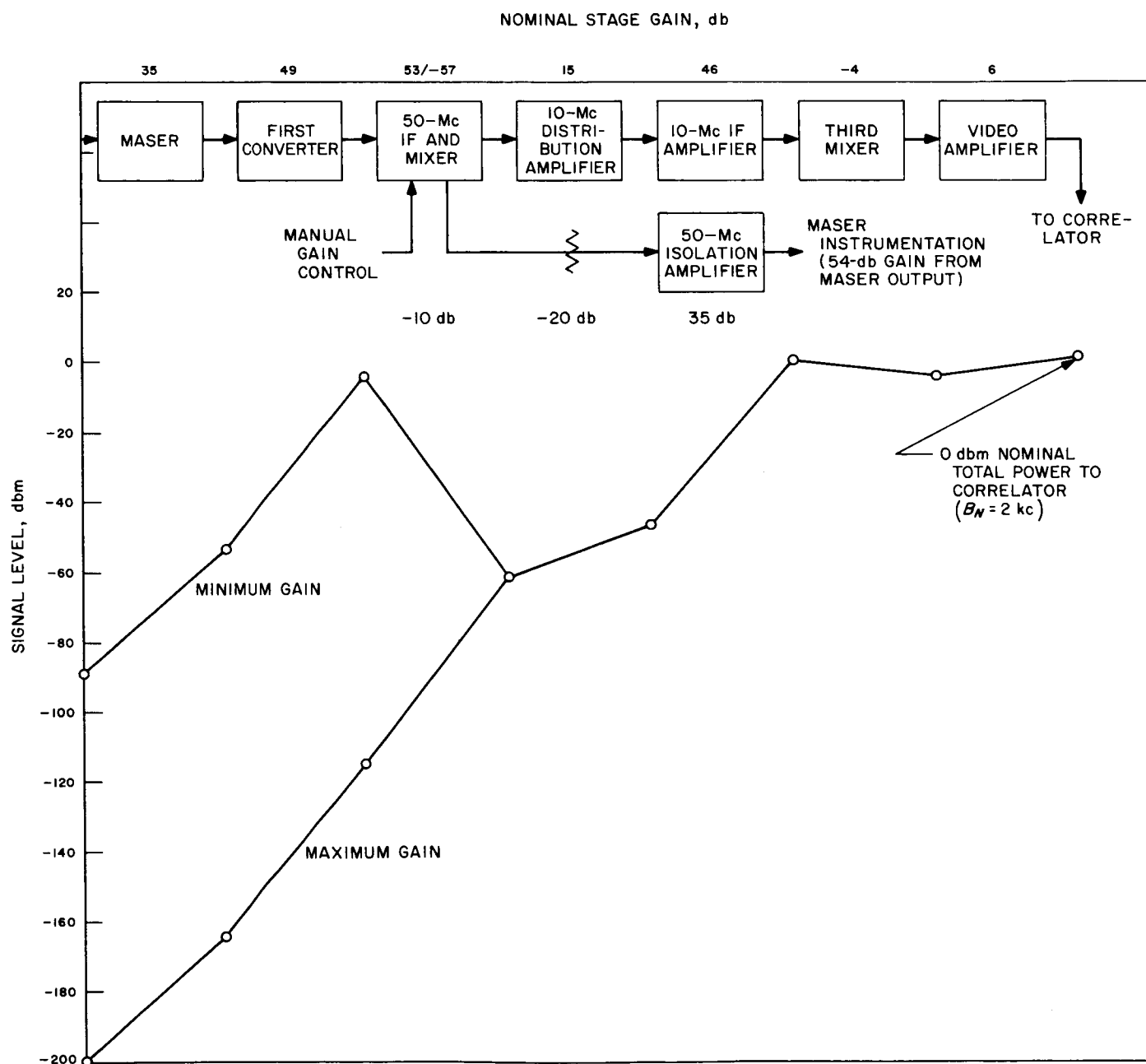


Fig. 32. Open-loop signal profile

capability for doppler extraction as an experimental flexibility in the event such factors as open-loop frequency prediction and tracking noise, solar noise temperature, and magnitude of frequency shift due to occultation would warrant this mode of operation. Fig. 31 in its entirety depicts the combined open-loop and closed-loop receiver. A two-month effort was undertaken to implement a two-bay subsystem consisting of the frequency synthesis equipment, the closed-loop additions, and operator instrumentation. Fig. 33 shows this equipment as installed in the alidade control room of the Mars Deep Space Station antenna. In anticipation of improved signal-to-noise ratios, provision was made for recording telemetry video for use at the earliest favorable time.¹ The implementation paralleled that for telemetry for *Mariner IV* at the Venus Deep Space Station in the spring of 1965 (SPS 37-35, Vol. III, p. 42) and, in fact, used some of the same hardware.

¹Although several recordings were made during the closed-loop operation in March, it was not until the postoccultation tracking on May 3 that the signal-to-noise ratio was adequate to re-establish demodulated telemetry from *Mariner IV*.

Of primary concern in this mode of operation was the selection of receiver loop bandwidth. Fortunately, as a part of the PLO activity, a compatible low-noise 24-Mc VCO had been made available. Previous results (SPS 37-38, Vol. III, Table 2, p. 66) indicated that the design goal of 3-deg RMS phase noise at S-band could be obtained with receiver loop bandwidths ($2B_{L_o}$) as narrow as 2 cps. Two other principal factors were minimization of signal-to-noise ratio of the doppler output and dynamic signal tracking capability. A design bandwidth of 3 cps ($2B_{L_o} = 3$ cps) was chosen which, with the anticipated carrier level of -170 dbm and system noise temperature of 29°K , yielded an expected doppler signal-to-noise ratio of approximately 7 db and could track the maximum expected doppler rate with a 5-deg rate error. The resulting internal phase noise was measured to be 2.0 and 3.3 deg rms for $\alpha/\alpha_0 = 4$ and 1, respectively.

In order to provide automatic gain control for the closed-loop mode, a preset bias was supplied to the 50-Mc IF MGC described above, and a conventional coherent AGC system as used in planetary radar systems was

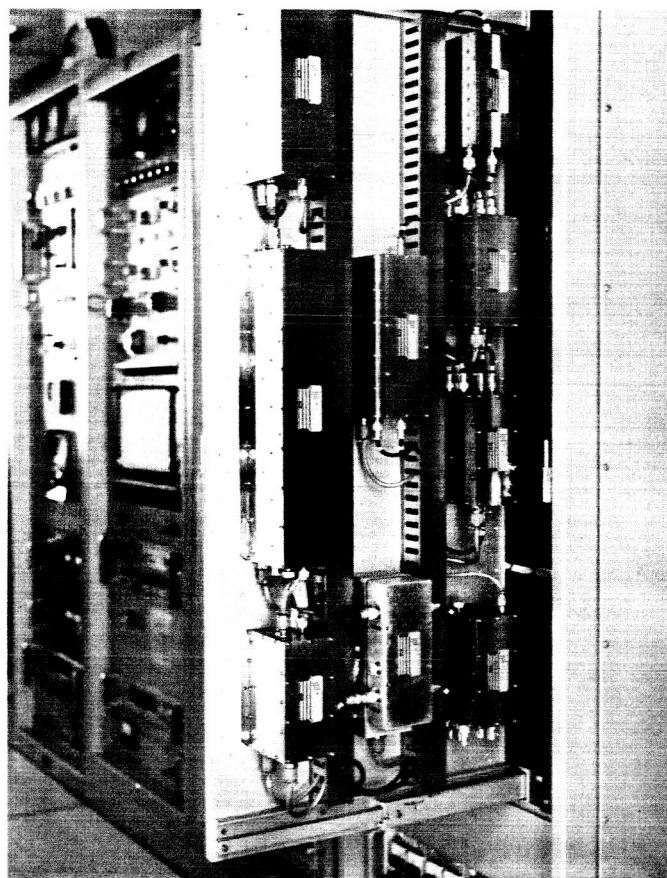
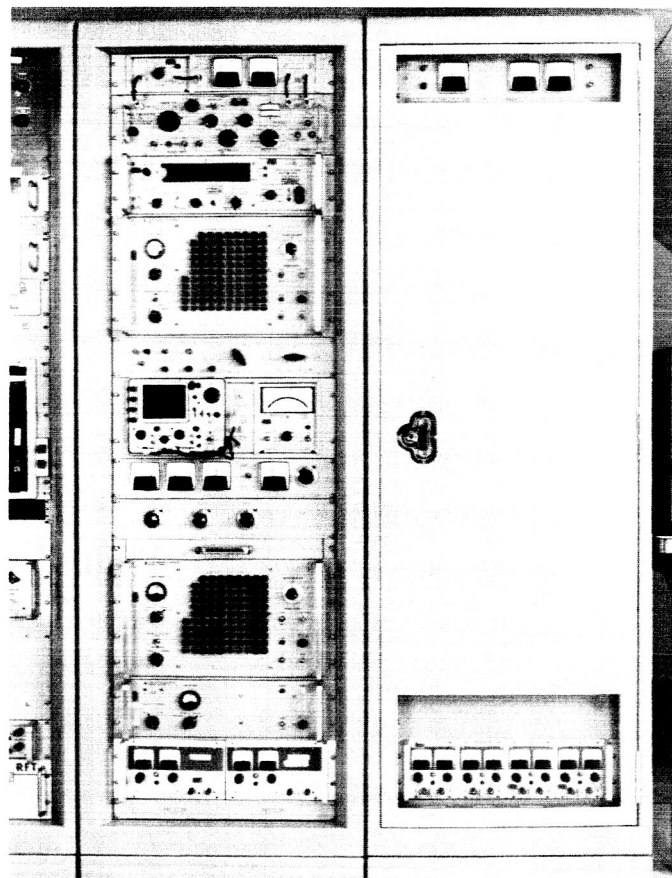


Fig. 33. S-Band experimental receiver (a) outside (b) inside

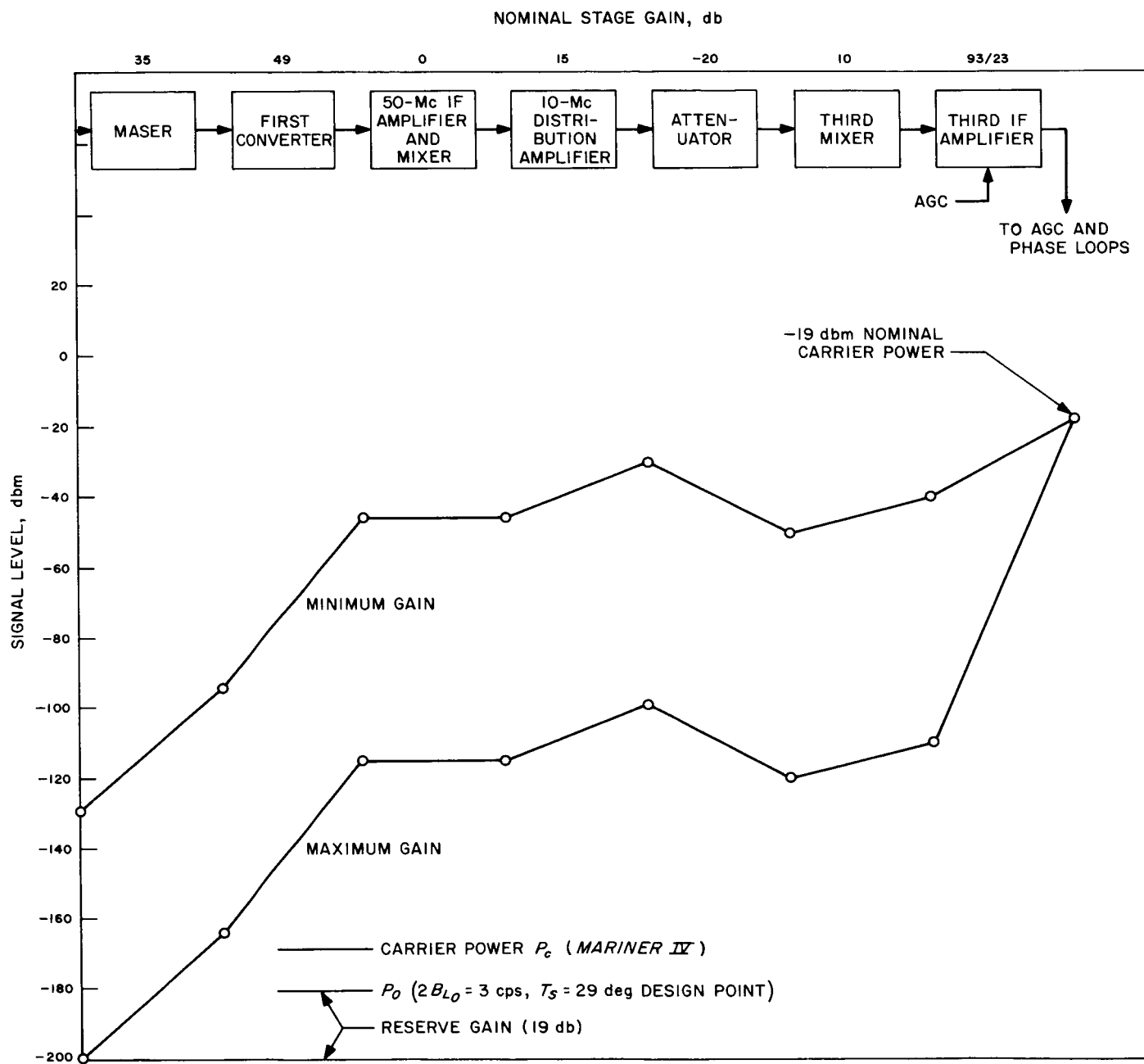


Fig. 34. Closed-loop signal profile

N66 38560

implemented at the third IF amplifier. The signal profile of the closed-loop mode is given in Fig. 34. The receiving system as described above was installed and initially tested in the "3A" cone adapter and alidade control room and was used in the antenna calibration and solar occultation activities commencing March 16, 1966. Of considerable effect upon operating mode and resulting data for the next two months was the increase of system noise temperature when the antenna tracked the *Mariner IV* spacecraft. A preliminary analysis of this partial result of the experiment follows in Sect. D.

D. Operational System Temperature at Mars Deep Space Station During Solar Occultation of *Mariner IV*

D. W. Brown

In contrast to the occultation effects upon the *Mariner IV* signal, the proximity of the Sun to the antenna beam (to within approximately 0.8 deg or 6 beamwidths) caused significant increases in system noise temperature. This temperature was monitored by the usual instrumentation techniques at roughly 1-hr intervals through the observation period (March 17 through April 12), both as a reference for autocorrelator signal-to-noise ratio data concurrently obtained and as independent data. It was also used during the experiment to influence the choice of operating time during a given day. (Much of the period was restricted to half-day operation due to other commitments of the antenna, then in final stages of completion and initial shakedown.) Typical plots of one-day data are given in Fig. 35.

Brief study of the entire set of data points (approximately 140) revealed that significant variations occurred not only on a day-to-day basis but also during a given day, as suggested above. Although difficult to interpret as first examined on a continuous linear time base plot, trends seemed to indicate that further data reduction might prove fruitful. The first step was to plot daily temperature minima as a function of operating date. This curve appears as Fig. 36. The fact that operating time during a given day did not always include a true mini-

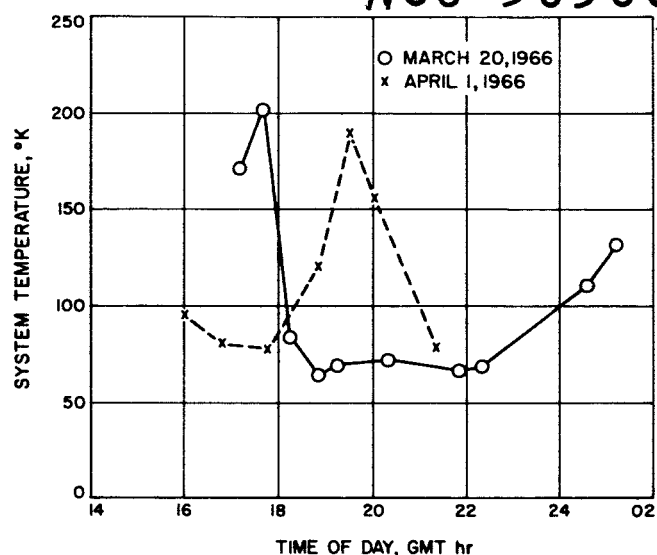


Fig. 35. Typical temperature calibrations

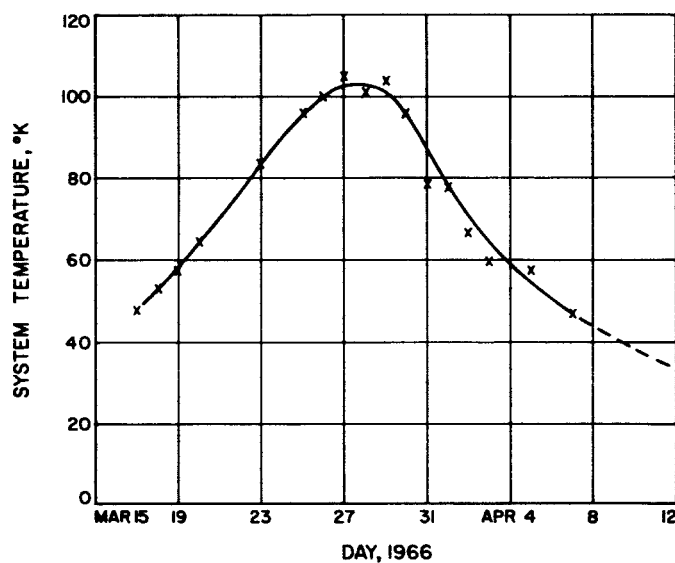


Fig. 36. System temperature daily minima

um is evident from the missing data points; however, enough were available to plot the smooth curve shown. When the time base of Fig. 36 is converted to the corresponding Sun-Earth-probe (SEP) angle, and the latter is interpreted as a radial deviation from the principal axis of the antenna beam, these daily minima correspond, in general, to predicted side lobe effects in a radial direction.

This SEP (radial) dependence of the data can be removed for further data analysis by a daily normalization.

This was accomplished by adding to each day's data the difference between the daily minimum and the maximum (midoccultation) minimum, from Fig. 36. The angular dependence of the data around the pointing axis of the antenna beam was established as follows: The spacecraft-to-Sun vector, as viewed from the antenna, rotates around the pointing axis with respect to the fixed reference of the azimuth-elevation (Az-El) mount. This angular variation is evidenced by the familiar movement of the quadripod shadow upon the face of the reflector. This angle γ is defined in Fig. 37.

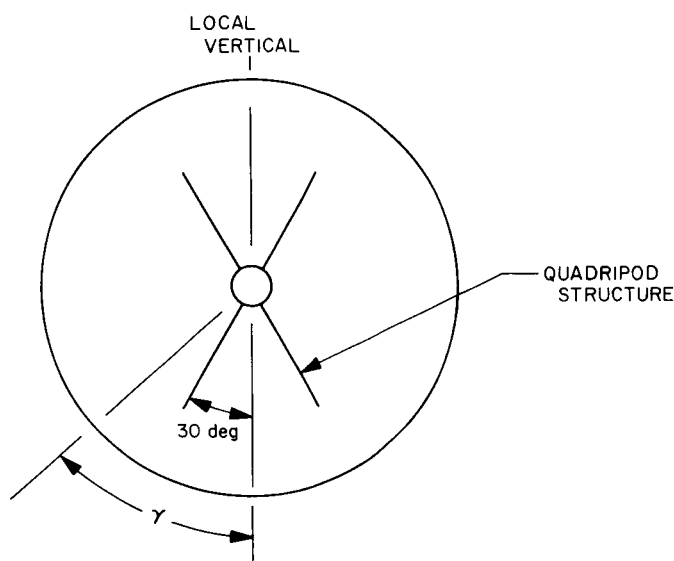


Fig. 37. Mars DSS reflector, face view

There are two principal effects contributing to the angle γ . The first is the relative motion of the spacecraft and the Sun. Fig. 38² presents the angle α of the apparent spacecraft-to-Sun vector with respect to the equatorial plane as a function of time. Secondly, a daily "spin" of the equatorial plane with respect to the Az-El coordinate system has been defined:

$$\beta = \cot^{-1} \left[\frac{\tan(\text{latitude})}{\sin(\text{hour angle})} - \frac{\tan(\text{declination})}{\tan(\text{hour angle})} \right]$$

The angle γ as defined in Fig. 37 is then given by:

$$\gamma = \alpha + \beta - 90 \text{ deg.}$$

An approximate conversion of time-of-day and date has been made for each data point yielding a value of γ for

²Derived from Fig. 1 in JPL IOM 312.4-443 by D. A. Tito.

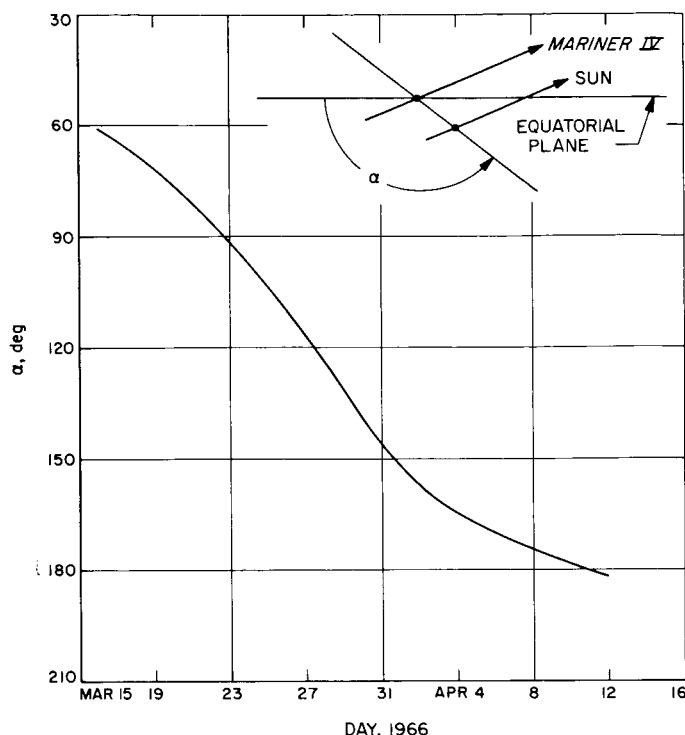


Fig. 38. Apparent angle of Mariner IV Sun vector from the equatorial plane

each. Although the value of α varies by as much as 8 deg in one day, each day's data points were adjusted by a single daily value. The differential error here is estimated to be of the order of 1 or 2 deg, since the observation period was generally less than 6 hr in duration. Time of day was converted to equivalent "spin" angle β , by assuming a one-to-one correspondence between time-of-day and hour angle with noon at the meridian transit and by assigning a fixed value of zero for the declination angle. In reality, the declination of the spacecraft varied between -0.2 and $+8.4$ deg in the observation period.³ Spot checking the error in β thus obtained reveals maximum error of approximately 6 deg on the last day. The majority of the data was obtained at hour angles and dates resulting in errors less than 4 deg.

Thus normalized with respect to both SEP (temperature correction) and total spin angle, the data is presented in Fig. 39. The three prominent peaks occurring at approximately -60 , $+60$, and $+120$ deg confirm first-order side lobes 90 deg removed from the quadripod legs (Fig. 37). The absence of a fourth symmetrical side lobe (at -120 deg) is due to the geometry of the spacecraft trajectory. It is interesting to note that the data peak at

³Tito, D. A., JPL IOM 312.4-443, Figs. 1 and 2.

N66 38561

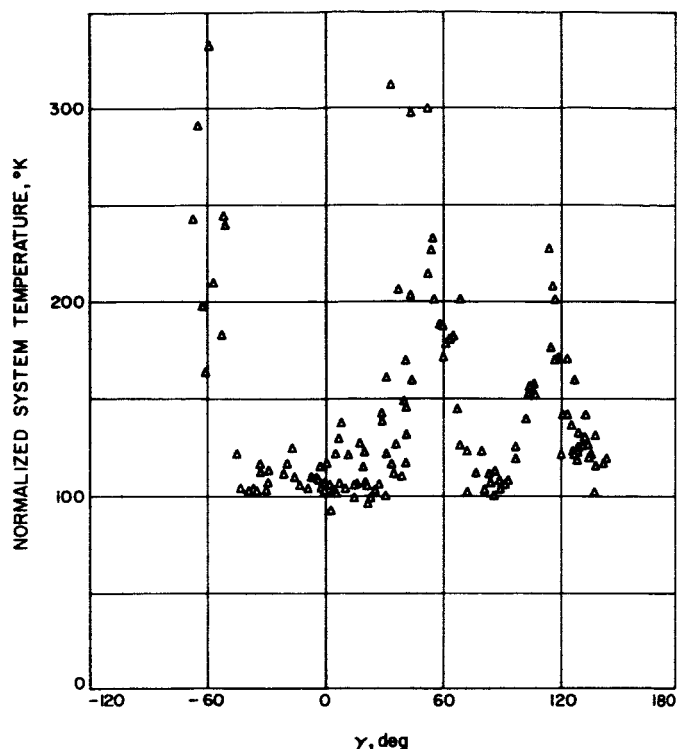


Fig. 39. Normalized system noise temperature on Mariner IV

-60 deg was recorded early in the experiment, when the declination passed through zero. Later, as the zero-declination approximation became less valid, the other two peaks were recorded, both of which would likely be better centered on +60 and +120 deg, respectively, and exhibit less spreading (narrower peaks) without the errors resulting both from step correction in α and from the declination approximation. Given Fig. 39, the data of Fig. 36 can now be better interpreted as a radial cut of the (unnormalized) pattern over the range of SEP experienced (1.6 to 0.8 to 1.8 deg)¹ taken at the γ minima of approximately 0 and +90 deg. Insufficient data were available to describe such a radial cut at the γ maxima of -60, +60, and +120 deg.

This normalized curve served to provide better reference temperatures in reducing the data obtained with the autocorrelator by allowing interpolation and extrapolation to points not recorded during the experiment. Further interpretation with respect to antenna pattern must include consideration of the narrow beamwidth (approximately 0.14 deg) and associated fine sidelobe

structure. That is, the solar diameter of approximately 0.53 deg results in an averaging effect over more than one sidelobe.

E. Equipment for RF Carrier Acquisition Using the MSFN S-Band Receiver/Exciter

M. H. Brockman and R. E. Weller

During critical phases of a mission, rapid acquisition of the RF carrier (within the frequency rate of change and tracking range capability of the phase-locked receiver) is required on both the up-link to the spacecraft and down-link to the Earth-based tracking station. A description of the new equipment required to accomplish rapid two-way RF carrier acquisition of the *Apollo* transponder with the MSFN receiver/exciter is presented herein. The design is relatively flexible so as to accommodate a wide range of acquisition conditions. The design is also applicable, in general, to the DSIF and to the programs to which the DSIF provides support. The MSFN receiver/exciter has been described in SPS 37-33, Vol. III, and in subsequent reports. The results of a Laboratory investigation of two-way RF carrier acquisition for a simulated Block II transponder was presented in SPS 37-36, Vol. III. A block diagram of the MSFN receiver/exciter is shown in Fig. 40, which updates the block diagram presented in SPS 37-33, Vol. III, Fig. 18, p. 41, to include the capability described in this report.

Fig. 41 illustrates RF acquisition during the Earth-orbital phase of the *Apollo* mission. A priori information is required to determine the path the spacecraft will travel in passing through the region of visibility for the tracking station (i.e., antenna position). Both the Block I and the Block II *Apollo* transponder designs require that frequency bias be applied to the Earth-based transmitter and receiver voltage-controlled oscillators (VCO's) during two-way RF acquisition. This frequency bias is required, in addition to the acquisition sweep waveform applied to the transmitter VCO, so as to maintain the phase error in the transponder and/or Earth-based receiver within a prescribed maximum value (± 20 deg) while still providing sufficient sweep frequency coverage (spacecraft transponder and Earth-based receiver) to accommodate transponder frequency uncertainty and the

¹Tito, D. A., JPL IOM 312.4-323, Fig. 2.

expected doppler shift. After two-way RF phase lock has been achieved, the triangular sweep waveform amplitude is reduced to zero, and the frequency biases are decayed to zero at a rate well within the frequency rate capabilities of both the transponder and the ground-based receiver phase-locked loops. Both the transmitter exciter and receiver VCO's have been adjusted (manually) to their "nominal" frequencies prior to acquisition, using the latest available information. The frequency synthesizer in the exciter is preset to the nominal exciter frequency so that, immediately following removal of the acquisition sweep and bias voltages, the synthesizer phase-locked loop can be activated to provide precision frequency control of the transmitter. Also illustrated in Fig. 41 is RF reacquisition, both prior to and following passage of the spacecraft through the station zenith plane. Note that the frequency bias applied to both the Earth-based transmitter and receiver must be reversed if RF reacquisition is required after passage of the spacecraft through the station zenith plane. In addition, the frequency bias (transmitter and receiver) is switched to zero if reacquisition is required during passage of the spacecraft through the zenith plane. Fig. 41 also illustrates operation for a second tracking station to accomplish either station hand-over or RF acquisition.

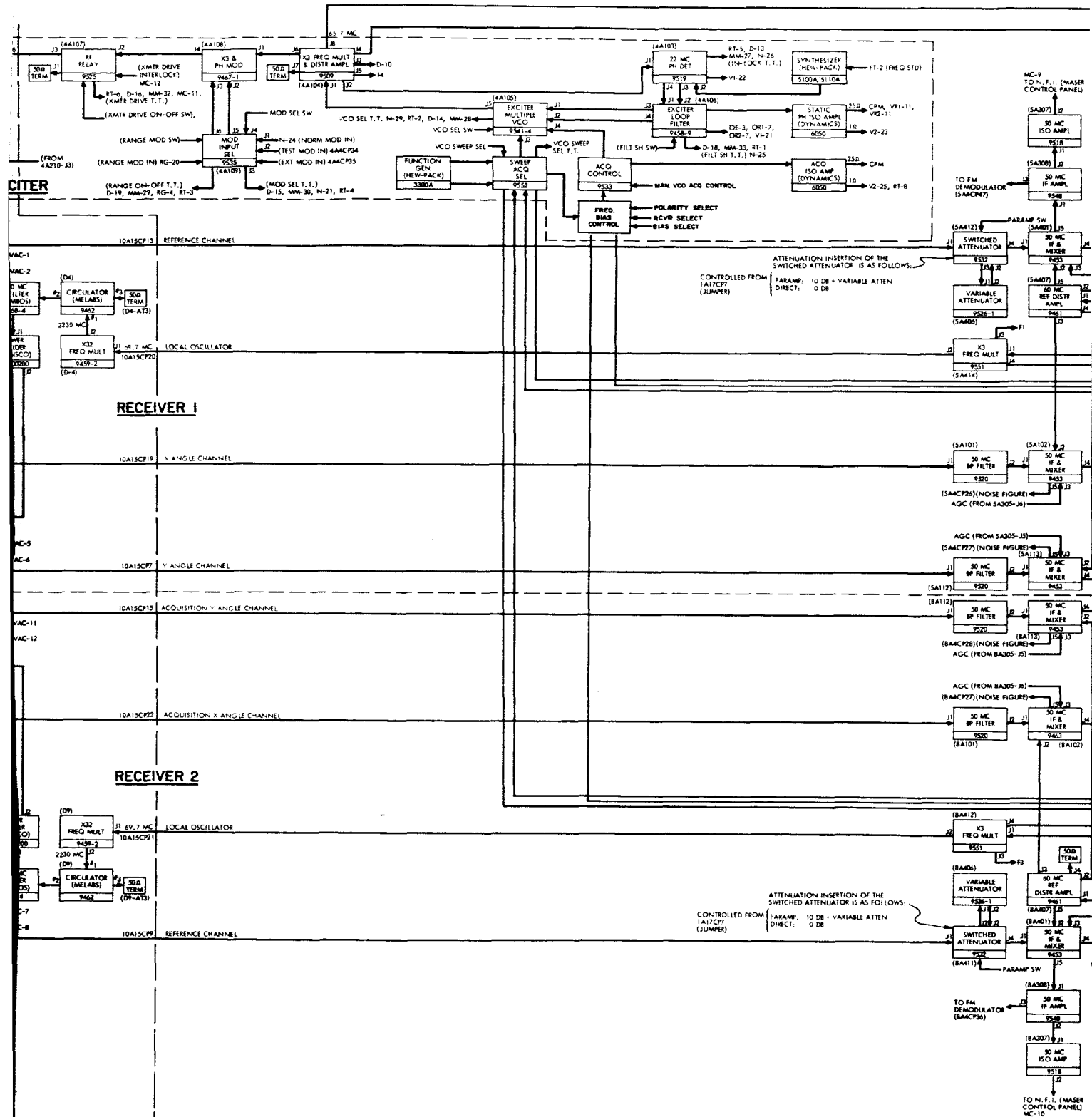
A photograph of receiver/exciter rack No. 1, which contains the exciter control panel as well as the acquisition equipment and the acquisition control panel, is shown in Fig. 42. Fig. 43 shows the acquisition control panel (new equipment) which is installed at the top of rack No. 1. Two controls (in addition to the manual acquisition control used to set nominal frequency) are used on the exciter control panel (Fig. 42) during RF acquisition (acquisition sweep control and sweep amplitude). Selection of *exciter* (acquisition sweep control) provides two-way RF acquisition capability with the receiver(s) selected (note that selection of *Receiver 1* or *2* provides one-way down-link acquisition capability for the receiver selected). The second control (*sweep amplitude*) incorporates an *off* position switch. Turning this control from its *off* position applies frequency bias voltages to both the exciter and receiver VCO's. Turning this control to its full clockwise position applies the acquisition sweep waveform to the exciter VCO at a preset sweep amplitude and sweep waveform frequency (sweep acquisition generator, Fig. 42). After two-way RF carrier acquisition has been achieved the sweep amplitude control is turned back to its zero amplitude position and then *off* to permit the frequency bias (receiver and exciter) to decay to zero. The rate of frequency bias decay is controlled by the *bias bandwidth* selector switch on the acquisition control panel

(Fig. 43). The *narrow*, *medium*, and *wide* designations on this selector switch permit time constant selection to correspond to the selected RF loop bandwidth in the receiver. The selector switches designated *Receiver 1* or *2*, *MSFN/DSN*, provide selection of frequency bias decay rate on either the *MSFN* or the *DSN* RF loop bandwidths. The decay time constants are:

<i>Bias bandwidth</i>	<i>MSFN</i>	<i>DSN</i>
Wide	2.5 sec	30 sec
Medium	25.0 sec	300 sec
Narrow	250.0 sec	750 sec

The selector switch (Fig. 43) designated *two-way acquisition* permits selection of two-way RF acquisition with *Receiver 1* or *Receiver 2* or both *Receivers 1* and *2*. The selector switch designated *spacecraft position bias* permits acquisition of the spacecraft from its ascent horizon (ASC) to zenith, at zenith (ZEN), or from zenith to its descent horizon (DESC). Ascent spacecraft position bias selection provides negative frequency bias to the transmitter exciter VCO and positive frequency bias to the receiver VCO. Descent spacecraft position bias selection reverses the polarity of both the exciter and receiver VCO biases (from ascent). Selection of zenith spacecraft position bias results in zero frequency bias for both the exciter and receiver VCO's. The remaining selector switch is designated *zone selector*, and it provides selection of one of six sets (exciter and receiver) of frequency biases designated 1, 2, 3, 4, 5, and 6 (Fig. 43). This permits the region of visibility for the tracking station (from overhead to horizon pass) to be divided into a maximum of six zones. Division of the region of visibility into six zones provides capability to accomplish two-way RF acquisition of both the Block I and Block II transponders within less than 10 sec during the Earth orbital phase. The zero position of the *zone selector* provides zero frequency bias to both the exciter and receiver VCO's.

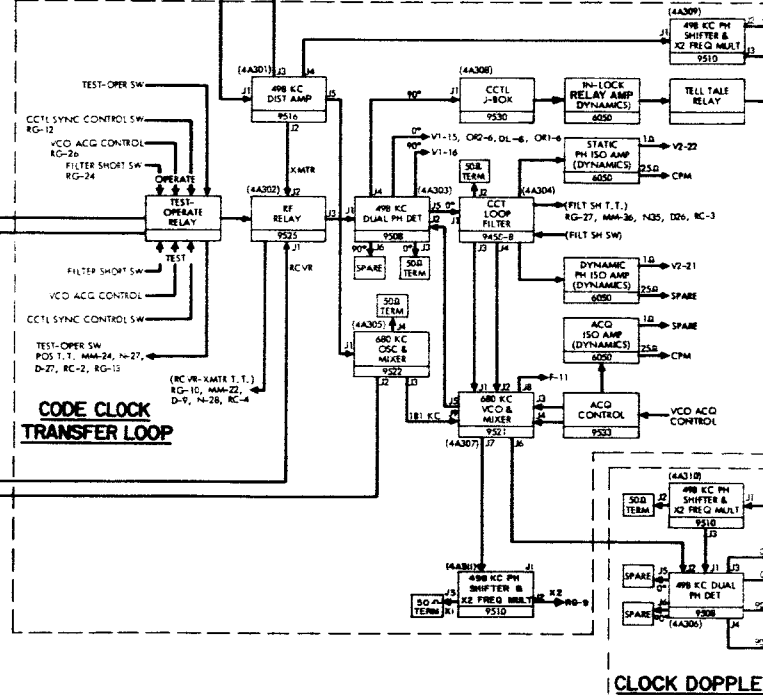
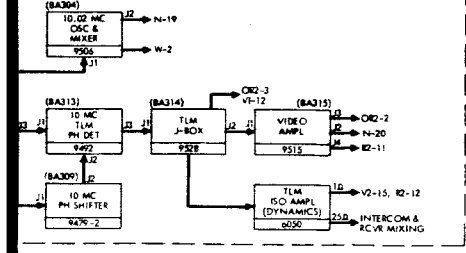
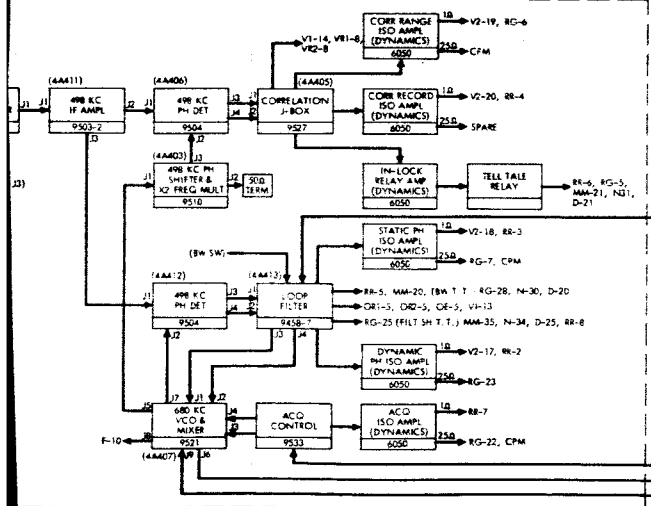
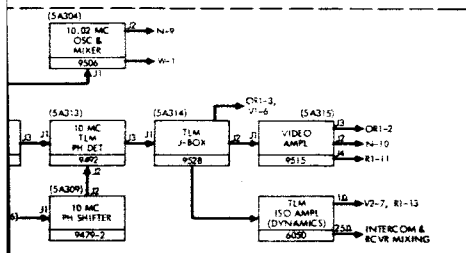
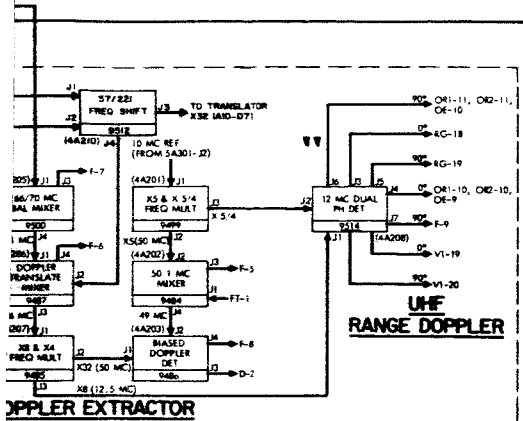
Adjustment of the six exciter frequency bias voltages is provided by potentiometers in the acquisition zone selector module which is mounted behind the transmitter exciter control panel. Similarly, adjustment of the receiver frequency bias voltages is provided in the acquisition zone selector module mounted behind *Receiver 1* control panel (Rack 2) and *Receiver 2* control panel (Rack 3). Range of frequency bias adjustment is provided from zero to the specified maximum tracking range of the VCO's. In addition, each acquisition zone selector module (exciter,





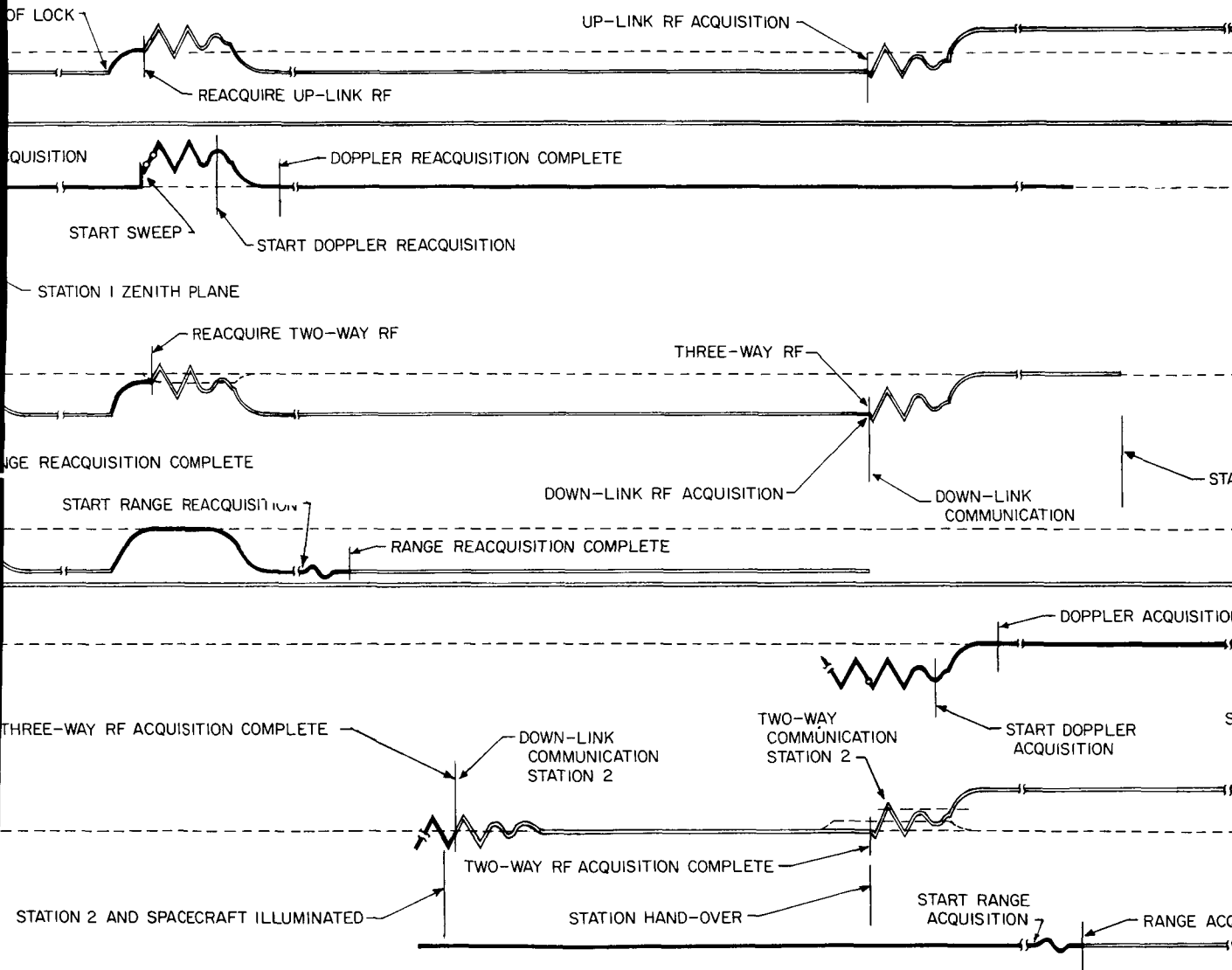
SUBSYSTEM SUBASSEMBLIES

SPEC NO.	SUBASSEMBLY TYPE	SCHEMATIC NO'S	ASSEMBLY NO'S	SPEC NO.	SUBASSEMBLY TYPE	SCHEMATIC NO'S
9451	X 1/2 FREQ MULT	9332156	9332147	9506	10.02 MC'S OSC & MIXER	9332073
9452-2	10 MC'S IF AMP	9332017	9332016	9507	10 MC'S BAL DET & 498 KC'S AMPL	9332074
9453	50 MC'S IF & MIXER	9332041	9332040	9508	498 KC'S DUAL PH DET	9332075
9455	10 MC'S PH DET	9330719	9330714	9509	X3 FREQ MULT & DISTR AMPL	9332076
9456-4	20 MC'S OSC & X3 FREQ MULT	9330823	9330810	9510	498 KC'S PH SHIFTER & X2 FREQ MULT	9332077
9457	5-BAND MIXER	9330670	9330602	9511	5/221 FREQ SHIFTER	9332078
9458-6	RECEIVER LOOP FILTER	9330019	9330018	9512	12.5 MC'S DUAL PH DET	9332079
9458-7	RANGING LOOP FILTER	9330021	9330020	9514	12.5 MC'S DUAL PH DET	9332080
9458-8	CCT LOOP FILTER	9330022	9330022	9515	VIDEO AMPL	9332081
9458-9	EXCITER LOOP FILTER	9330023	9330024	9516	498 KC'S DISTR AMPL	9332082
9459-2	X2 FREQ MULT	9330948	9330947	9518	37 MC'S ISO AMPL	9332083
9459-3	10 MC'S REF DISTR AMPL	9330948	9330947	9519	22 MC'S PH DET	9332084
9460	40 MC'S REF DISTR AMPL	9330711	9330711	9520	50 MC'S IF FILTER	9332085
9461	UNF PRE-SELECTOR	9330402	9330402	9521	498 KC'S VCO & MIXER	9332086
9462-1	10 MC'S IF DISTR AMPL	9330641	9330641	9522	498 KC OSC & MIXER	9332087
9462-2	X3 FREQ MULT & PH MOD	9330715	9330715	9523	RF RELAY	9332088
9463-4	LO PASS FILTER	9330725-2	9330725-2	9524	RF RELAY	9332089
9464-4	EXCITER HP FILTER	9331735-2	9331735-2	9525	VARIABLE ATTENUATOR (0-12 DB)	9332090
9471-2	AGC AMPL & FILTER	9330326	9330326	9526-2	VARIABLE ATTENUATOR (0-120 DB)	9332091
9472-2	UNF BUFFER AMPLIFIERS	9330327	9330327	9527	COBOLATION JUNCTION	9332092
9473-2	UNF BUFFER AMPLIFIERS	9330328	9330328	9528	TLM JUNCTION BOX	9332093
9479-2	10 MC'S PH SHIFTER	9330324	9330324	9529	ANGULAR ERROR JUNCTION BOX	9332094
9480	50/1 MC'S MIXER	9330320	9330320	9530	CCTL JUNCTION BOX	9332095
9481	12.5 MC FREQ MULT	9330523	9330523	9531	ALFID MONITOR AMP	9332096
9482	BIASED DOPPLER DET	9330756	9330756	9532	SWITCHED ATTENUATOR	9332097
9483	DOPPLER TRANSLATE MIXER	9330756	9330756	9533	ACQ CONTROL	9332098
9484	10 MC'S W8 TLM IF AMPL	9330756	9330756	9534	ACQ INFLU SELECTOR	9332099
9485	10 MC'S TLM IF AMPL	9330756	9330756	9535	RECEIVER MULTIPLE VCO	9332100
9486	TLM IF FILTER	9330756	9330756	9536-1	EXCITER MULTIPLE VCO	9332101
9487	10 MC'S TLM IF AMPL	9330756	9330756	9537	10 MC'S ANGLE CHANNEL IF AMPL	9332102
9488	10 MC'S TLM IF AMPL	9330756	9330756	9538	50 MC'S IF AMPL	9332103
9489	10 MC'S TLM IF AMPL	9330756	9330756	9539	10 MC'S IF AMPL	9332104
9490	10 MC'S TLM IF AMPL	9330756	9330756	9540	10 MC'S IF AMPL	9332105
9491	10 MC'S TLM IF AMPL	9330756	9330756	9541-4	10 MC'S IF AMPL	9332106
9492	10 MC'S TLM IF AMPL	9330756	9330756	9542	10 MC'S IF AMPL	9332107
9493	10 MC'S TLM IF AMPL	9330756	9330756	9543	10 MC'S IF AMPL	9332108
9494	10 MC'S TLM IF AMPL	9330756	9330756	9544	10 MC'S IF AMPL	9332109
9495	10 MC'S TLM IF AMPL	9330756	9330756	9545	10 MC'S IF AMPL	9332110
9496	10 MC'S TLM IF AMPL	9330756	9330756	9546	10 MC'S IF AMPL	9332111
9497	10 MC'S TLM IF AMPL	9330756	9330756	9547	10 MC'S IF AMPL	9332112
9498	10 MC'S TLM IF AMPL	9330756	9330756	9548	10 MC'S IF AMPL	9332113
9499	10 MC'S TLM IF AMPL	9330756	9330756	9549	10 MC'S IF AMPL	9332114
9500	10 MC'S TLM IF AMPL	9330756	9330756	9550	10 MC'S IF AMPL	9332115
9501	10 MC'S TLM IF AMPL	9330756	9330756	9551	10 MC'S IF AMPL	9332116
9502	10 MC'S TLM IF AMPL	9330756	9330756	9552	10 MC'S IF AMPL	9332117
9503-2	498 KC'S IF AMPL	9330331	9330331	9553	10 MC'S IF AMPL	9332118
9504	498 KC'S PH DET	9330331	9330331	9554	10 MC'S IF AMPL	9332119

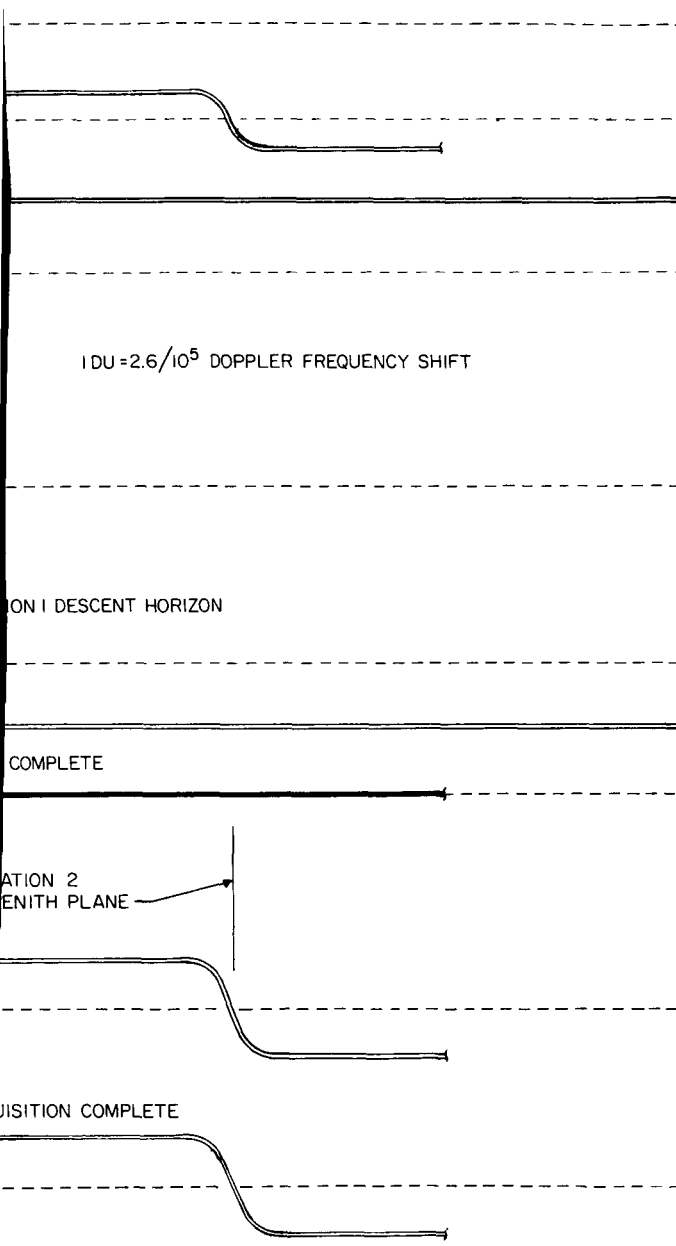


CLOCK DOPPLER

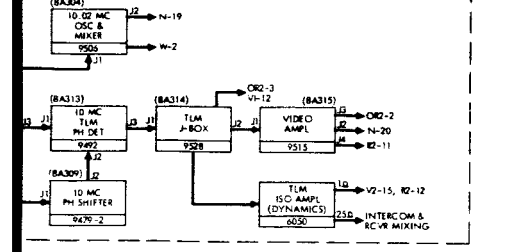
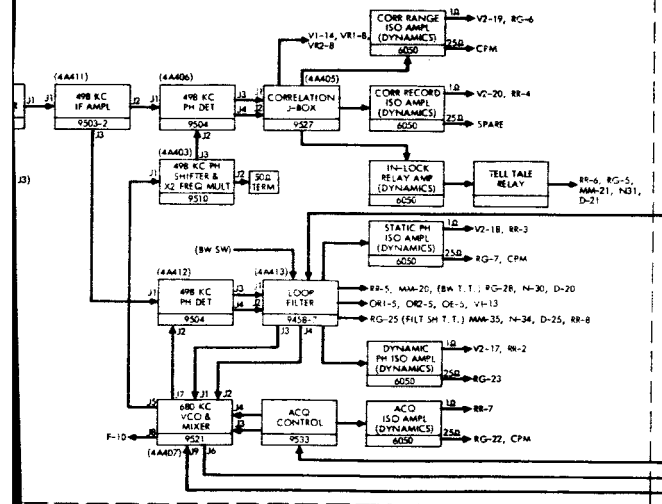
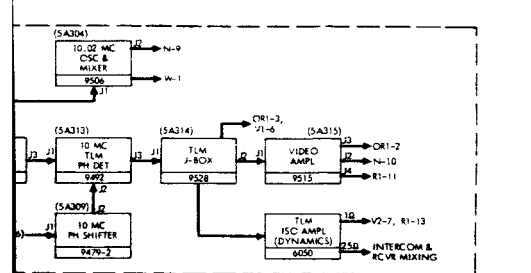
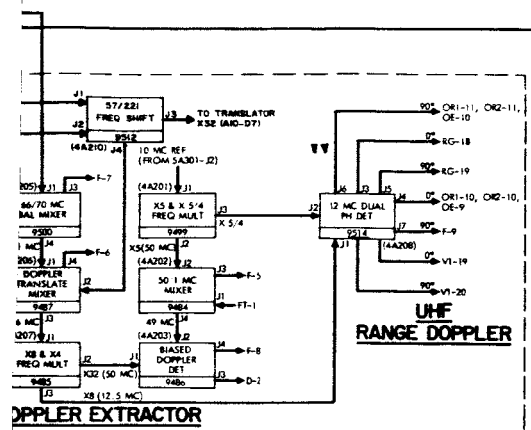
POSITION



72-112 3

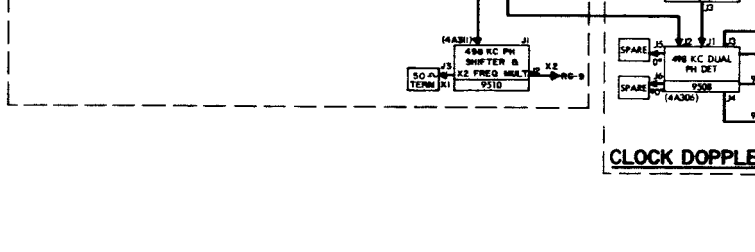
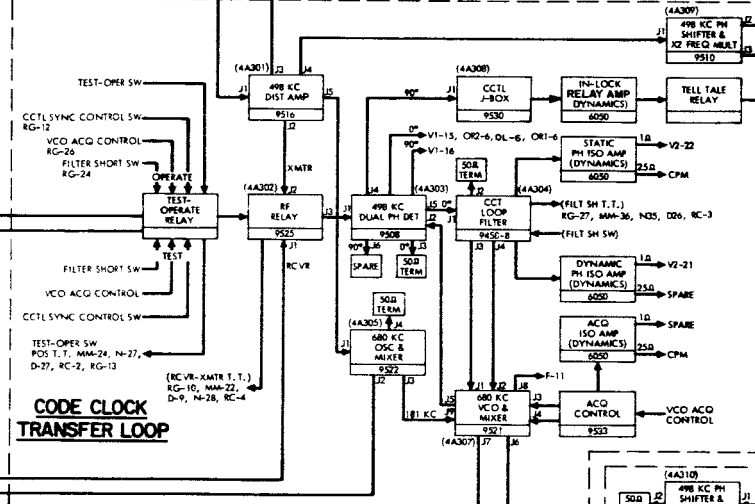


72-9 4



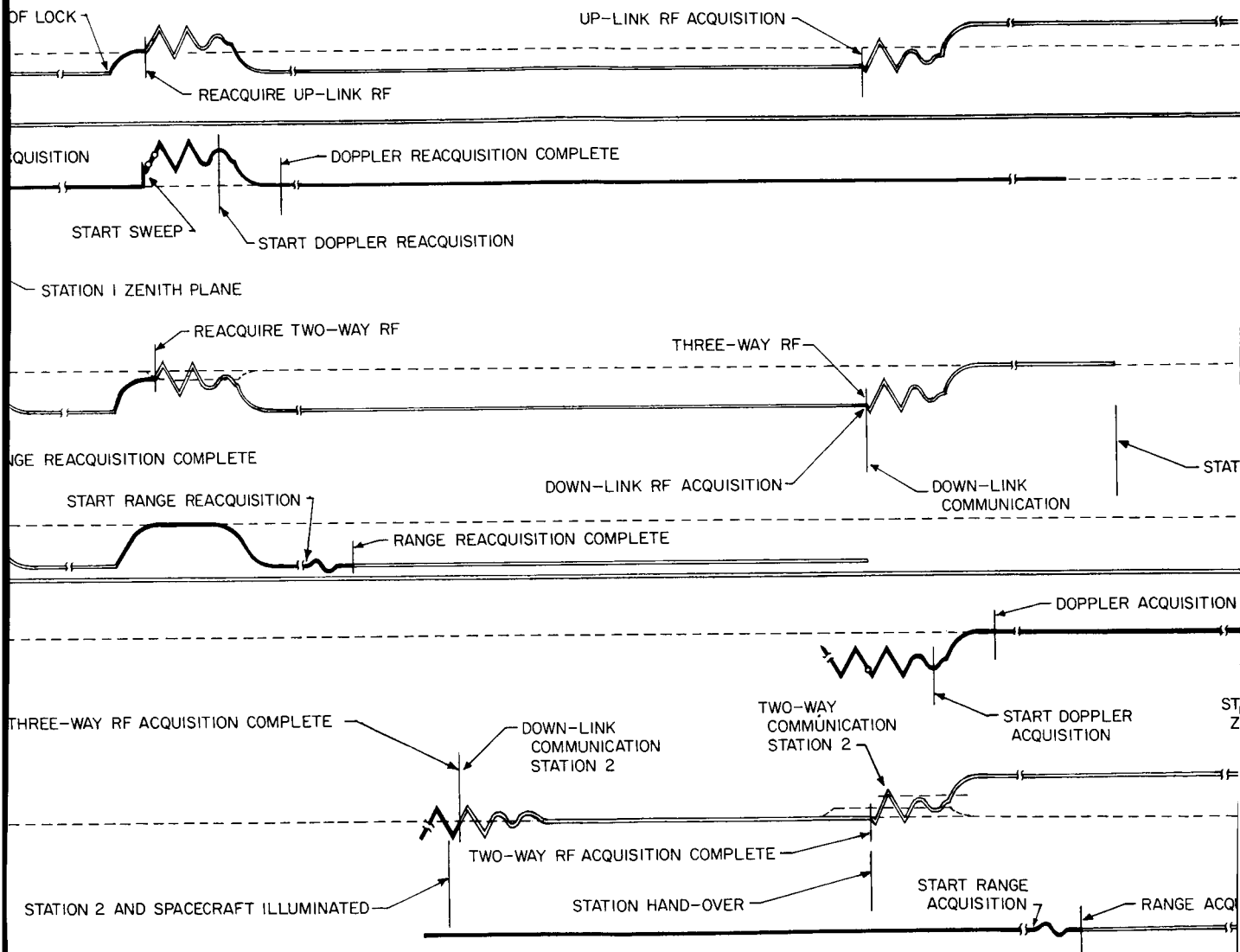
SUBSYSTEM SUBASSEMBLIES

SPEC NO.	SUBASSEMBLY TYPE	SCHEMATIC NO'S	ASSEMBLY NO'S	SPEC NO.	SUBASSEMBLY TYPE	SCHEMATIC NO'S
9451	X 1/2 FREQ MULT	9332156	9332147	9506	10.02 MC/5 OSC & MIXER	933097
9452-2	10 MC/5 IF AMP	9330167	9330166	9507	10 MC/5 BAL DET & 498 KC/5 AMPL	933094
9453	50 MC/5 IF & MIXER	9330168	9330167	9508	498 KC/5 DUAL PH DET	933097
9455	10 MC/5 PH DET	9330179	9330174	9509	X2 FREQ MULT & DISTR AMPL	933081
9456-4	20 MC/5 OSC & X2 FREQ MULT	9330183	9330180	9510	498 KC/5 PH SHIFTER & X2 FREQ MULT	933098
9457	S-BAND MIXER	9330190	9330182	9511	5/221 FREQ SHIFTER	933097
9458-6	RECEIVER LOOP FILTER	9330191	9330188	9512	12.5 MC/5 DUAL PH DET	933040
9458-7	RANGING LOOP FILTER	9330192	9330189	9514	12.5 MC/5 DUAL PH DET	933097
9458-8	CCT LOOP FILTER	9330193	9330190	9515	VIDEO AMPL	933087
9458-9	EXCITER LOOP FILTER	9330194	9330191	9516	498 KC/5 DISTR AMPL	933087
9459-1	X22 FREQ MULT	9330195	9330192	9518	30 MC/5 ISO AMPL	933101
9459-2	X22 FREQ MULT	9330196	9330193	9519	22 MC/5 PH DET	933101
9460	10 MC/5 REF DISTR AMPL	9330197	9330194	9520	50 MC/5 IF AMP	933110
9461	40 MC/5 REF DISTR AMPL	9330198	9330195	9521	498 KC/5 VCO & MIXER	943186
9463-2	UHF PRE-SELECTOR	9330199	9330196	9522	498 KC OSC & MIXER	943192
9465	10 MC/5 IF DISTR AMPL	9330200	9330197	9523	RF RELAY	933148
9467-1	X3 FREQ MULT & PH ACO	9330201	9330198	9524	VARIABLE ATTENUATOR (0-12 DB)	933124
9468-3	LO PASS FILTER	9330202	9330199	9525	VARIABLE ATTENUATOR (0-120 DB)	933124
9468-4	EXCITER IF FILTER	9330203	9330200	9526	CORRELATION JUNCTION	933148
9471-2	AGC AMPL & FILTER	9330204	9330201	9527	TLM JUNCTION BOX	933148
9477-2	UHF BUFFER AMPLIFIERS	9330205	9330202	9528	ANGLE ERROR JUNCTION BOX	933148
9479-2	10 MC/5 PH SHIFTER	9330206	9330203	9529	CCT JUNCTION BOX	933148
9484	50/1 MC/5 MIXER	9330207	9330204	9530	ALPHA MONITOR AMPL	933148
9485	X2 & X4 FREQ MULT	9330208	9330205	9531	SWITCHED ATTENUATOR	933148
9486	BIASED DOPPLER DET	9330209	9330206	9532	ACQ CONTROL	933148
9487	DOPPLER TRANSLATE MIXER	9330210	9330207	9533	ACQ INPUT SELECTOR	933148
9490	10 MC/5 WB TLM IF AMPL	9330211	9330208	9534	RECEIVER MULTIPLE VCO	933008
9492	10 MC/5 TLM PH DET	9330212	9330209	9535	10 MC/5 ANGLE CHANNEL IF AMPL	933175
9493	TLM IF FILTER	9330213	9330210	9536	20 MC/5 IF AMPL	943186
9497	10 MC/5 TLM IF AMPL	9330214	9330211	9537	EXCITER MULTIPLE VCO	933008
9499	X2 & X4 FREQ MULT	9330215	9330212	9538	STATIC PH ISO AMPL (DYNAMICS)	933148
9500	66/70 MC/5 BAL MIXER	9330216	9330213	9539	RECEIVER MULTIPLE VCO	933008
9502	10 MC/5 PH SWITCH	9330217	9330214	9540	FREQUENCY TRANSLATOR	943202
9503-2	498 KC/5 IF AMPL	9330218	9330215	9541	TRANSLATOR X2 FREQ MULT	943202
9504	498 KC/5 PH DET	9330219	9330216	9542	X2 FREQ MULT RCVR LO	943202
				9543	SWEEP ACQ SELECTOR	943202
				9544	TEST REC. REPENDER	918980
				9545	TEST TRANSMITTER	918980



CLOCK DOPPLER

POSITION



72-112 3

SUBSYSTEM MONITORING

TIC ASSEMBLY NO'S

9330538
9330539
9330540
9330541
9330542
9330543
9330544
9330545
9330546
9330547
9330548
9331014
9331015
9332015
9431900
9431901
9331168
9331218-1
9331218-2
9331219
9331220
9331221
9331216
9331222
9331166
9331186
9331482
9330300
9330302
9331746
9431980
9432000
9432020
9432042
9432046
9330119
9159021

13

2
13

RG-15
RG-14

RG-11
RG-13
RG-24

RG-16
VI-17, OE-7,
OE-8, OE-1-8
VI-18, OE-9,
OE-8, OE-1-9
RG-17

I DETECTOR

OSCILLOSCOPE

EXCITER (CONTROL PANEL SELECT - CABINET 1)

- OE-1 RCVR-1 DYN PH
- OE-2 RCVR-2 DYN PH
- OE-3 SYNTH 0 DEG DYN PH
- OE-4 COMD (DAISCP18)
- OE-5 RANGE DYN PH
- OE-6 CCTLO DEG DYN PH
- OE-7 CLOCK 0 DEG DOPP
- OE-8 CLOCK 90 DEG DOPP
- OE-9 UNF 0 DEG DOPP
- OE-10 UNF 90 DEG DOPP
- OE-11 (BLANK)
- OE-12 EXT (DAISCP20)
- OE-13 (BLANK)
- OE-14 (BLANK)
- OE-15 OPEN

RECEIVER-1 (CONTROL PANEL SELECT - CABINET 2)

- ORI-1 RCVR-1 TUM PH VIDEO
- ORI-2 RCVR-1 TUM PH NB
- ORI-3 RCVR-1 DYN AGC
- ORI-4 RANGE DYN PH
- ORI-5 CCTLO DEG DYN PH
- ORI-6 SYNTH 0 DEG DYN PH
- ORI-7 CLOCK 0 DEG DOPP
- ORI-8 CLOCK 90 DEG DOPP
- ORI-9 UNF 0 DEG DOPP
- ORI-10 UNF 90 DEG DOPP
- ORI-11 (BLANK)
- ORI-12 COMD (DAISCP18)
- ORI-13 EXT (DAISCP20)
- ORI-14 OPEN
- ORI-15 OPEN

RECEIVER-2 (CONTROL PANEL SELECT - CABINET 3)

- OQ-1 RCVR-2 DYN PH
- OQ-2 RCVR-2 TUM PH VIDEO
- OQ-3 RCVR-2 TUM PH NB
- OQ-4 RCVR-2 DYN AGC
- OQ-5 RANGE DYN PH
- OQ-6 CCTLO DEG DYN PH
- OQ-7 SYNTH 0 DEG DYN PH
- OQ-8 CLOCK 0 DEG DOPP
- OQ-9 CLOCK 90 DEG DOPP
- OQ-10 UNF 0 DEG DOPP
- OQ-11 UNF 90 DEG DOPP
- OQ-12 (BLANK)
- OQ-13 COMD (DAISCP18)
- OQ-14 EXT (DAISCP20)
- OQ-15 OPEN

COUNTER

(CONTROL PANEL SELECT - CABINETS 1, 2 & 3)

- F-1 RCVR-1 VCO
- F-2 REF OSC
- F-3 RCVR-2 VCO
- F-4 EXC VCO
- F-5 DOPP EXT, 4 MC/S
- F-6 DOPP EXT, 1.5 MC/S
- F-7 DOPP EXT, 4 MC/S
- F-8 BIASED DOPP
- F-9 RANGE DOPP
- F-10 RANGE RCVR VCO
- F-11 CCTLO VCO
- F-12 EXT (DAISCP20)
- F-13 EXT (DAISCP18)
- F-14 EXT (DAISCP20)
- F-15 OPEN

WAVE ANALYZER

(CONTROL PANEL SELECT - CABINET 4)

- W1 RCVR-1
- W2 RCVR-2

VTVM

RECEIVER-1 (CONTROL PANEL SELECT - CABINET 2)

- VR1-1 RCVR-1 AGC
- VR1-2 RCVR-1 DYN AGC
- VR1-3 RCVR-1 ST PH
- VR1-4 X ANGLE
- VR1-5 Y ANGLE
- VR1-6 ACO A X ANGLE
- VR1-7 ACO A Y ANGLE
- VR1-8 CORREL RANGE
- VR1-9 EXT (DAISCP12)
- VR1-10 NORM CSOS
- VR1-11 SYNTH ST PH
- VR1-12 (BLANK)
- VR1-13 (BLANK)
- VR1-14 OPEN
- VR1-15 SHORT

RECEIVER-2 (CONTROL PANEL SELECT - CABINET 3)

- VQ2-1 RCVR-2 AGC
- VQ2-2 RCVR-2 DYN AGC
- VQ2-3 RCVR-2 ST PH
- VQ2-4 X ANGLE
- VQ2-5 Y ANGLE
- VQ2-6 ACO A X ANGLE
- VQ2-7 ACO A Y ANGLE
- VQ2-8 CORREL RANGE
- VQ2-9 EXT (DAISCP12)
- VQ2-10 NORM CSOS
- VQ2-11 SYNTH ST PH
- VQ2-12 (BLANK)
- VQ2-13 (BLANK)
- VQ2-14 OPEN
- VQ2-15 SHORT

VTVM (CONTINUED)

RECEIVER OUTPUTS (CONTROL PANEL SELECT - CABINET 4)

- VI-1 X ANGLE
- VI-2 Y ANGLE
- VI-3 RCVR-1 DYN PH
- VI-4 RCVR-1 AGC
- VI-5 RCVR-1 DYN AGC
- VI-6 RCVR-1 TUM PH NB
- VI-7 ACO A X ANGLE
- VI-8 ACO A Y ANGLE
- VI-9 RCVR-2 DYN PH
- VI-10 RCVR-2 AGC
- VI-11 RCVR-2 DYN AGC
- VI-12 RCVR-2 TUM PH NB
- VI-13 RANGE DYN PH
- VI-14 CORREL RANGE
- VI-15 CCTLO DEG DYN PH
- VI-16 CCTLO DEG DYN PH
- VI-17 CLOCK 0 DEG DOPP
- VI-18 CLOCK 90 DEG DOPP
- VI-19 UNF 0 DEG DOPP
- VI-20 UNF 90 DEG DOPP
- VI-21 SYNTH 0 DEG DYN PH
- VI-22 SYNTH 0 DEG DYN PH
- VI-23 (BLANK)
- VI-24 (BLANK)
- VI-25 (BLANK)
- VI-26 XTAL MON SW PNL
- VI-27 POWER SUPPLY
- VI-28 OPEN
- VI-29 SHORT
- VI-30 SHORT

RECORDING ISO AMP OUTPUTS (CONTROL PANEL SELECT - CABINET 4)

- VZ-1 X ANGLE
- VZ-2 Y ANGLE
- VZ-3 RCVR-1 DYN PH
- VZ-4 RCVR-1 ST PH
- VZ-5 RCVR-1 AGC
- VZ-6 RCVR-1 DYN AGC
- VZ-7 RCVR-1 TUM PH NB
- VZ-8 RCVR-1 AGC
- VZ-9 ACO A X ANGLE
- VZ-10 ACO A Y ANGLE
- VZ-11 RCVR-2 DYN PH
- VZ-12 RCVR-2 ST PH
- VZ-13 RCVR-2 AGC
- VZ-14 RCVR-2 DYN AGC
- VZ-15 RCVR-2 TUM PH NB
- VZ-16 RCVR-2 AGC
- VZ-17 RANGE DYN PH
- VZ-18 CORREL RANGE
- VZ-19 CORREL RECORD
- VZ-20 CCTLO DEG DYN PH
- VZ-21 CCTLO DEG DYN PH
- VZ-22 SYNTH ST PH
- VZ-23 (BLANK)
- VZ-24 (BLANK)
- VZ-25 (BLANK)
- VZ-26 (BLANK)
- VZ-27 ZERO ISO AMP
- VZ-28 OPEN
- VZ-29 SHORT
- VZ-30 SHORT

CRYSTAL CURRENT (CONTROL PANEL SELECT - CABINET 4)

NOTE: MASTER CONTROL SW ON RECEIVER OUTPUT VTVM CONTROL PANEL

- VC-1 RCVR-1, XTAL 1
- VC-2 RCVR-1, XTAL 2
- VC-3 X ANGLE, XTAL 1
- VC-4 X ANGLE, XTAL 2
- VC-5 Y ANGLE, XTAL 1
- VC-6 Y ANGLE, XTAL 2
- VC-7 RCVR-2, XTAL 1
- VC-8 RCVR-2, XTAL 2
- VC-9 ACO A X XTAL 1
- VC-10 ACO A X XTAL 2
- VC-11 ACO A Y XTAL 1
- VC-12 ACO A Y XTAL 2

CRYSTAL CURRENT (ANTENNA CONTROL PANEL SELECT - CABINET 5)

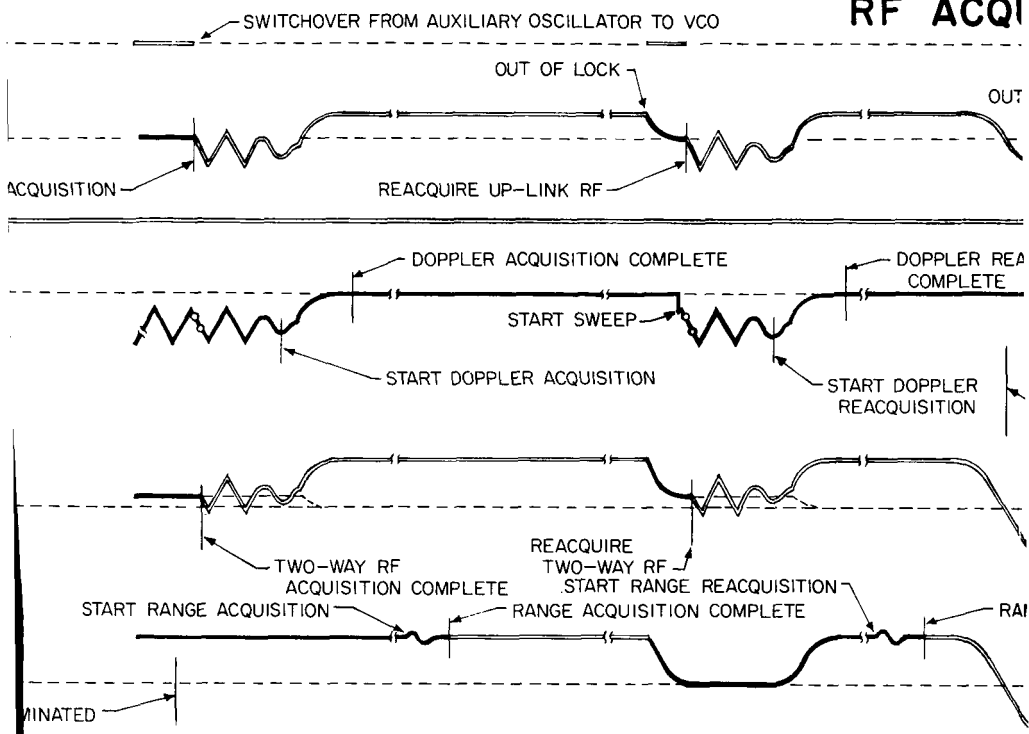
- VAC-1 RCVR-1, XTAL 1
- VAC-2 RCVR-1, XTAL 2
- VAC-3 X ANGLE, XTAL 1
- VAC-4 X ANGLE, XTAL 2
- VAC-5 Y ANGLE, XTAL 1
- VAC-6 Y ANGLE, XTAL 2
- VAC-7 RCVR-2, XTAL 1
- VAC-8 RCVR-2, XTAL 2
- VAC-9 ACO A X XTAL 1
- VAC-10 ACO A X XTAL 2
- VAC-11 ACO A Y XTAL 1
- VAC-12 ACO A Y XTAL 2
- VAC-13 ANT RCVR-15V
- VAC-14 ANT EXC -15V
- VAC-15 ANT EXC -28V
- VAC-16 ANT EXC -5V
- VAC-17 ANT EXC -350V
- VAC-18 ANT TB -28V
- VAC-19 ANT TB -28V
- VAC-20 RCVR-1 DYN AGC
- VAC-21 RCVR-2 DYN AGC
- VAC-30 SHORT

DIGITAL VM (CONTROL PANEL SELECT - CABINET 3)

- DV-1 RCVR-1 AGC
- DV-2 RCVR-2 AGC
- DV-3 RCVR-1 DBM
- DV-4 RCVR-2 DBM
- DV-5 POWER SUPPLY
- DV-6 EXT (DAISCP12)
- DV-7 OPEN (BLANK)
- DV-8 SPARE (BLANK)
- DV-9 SPARE (BLANK)
- DV-10 OPEN

71-5

RF ACQ



SUBSYSTEM INTERFACES

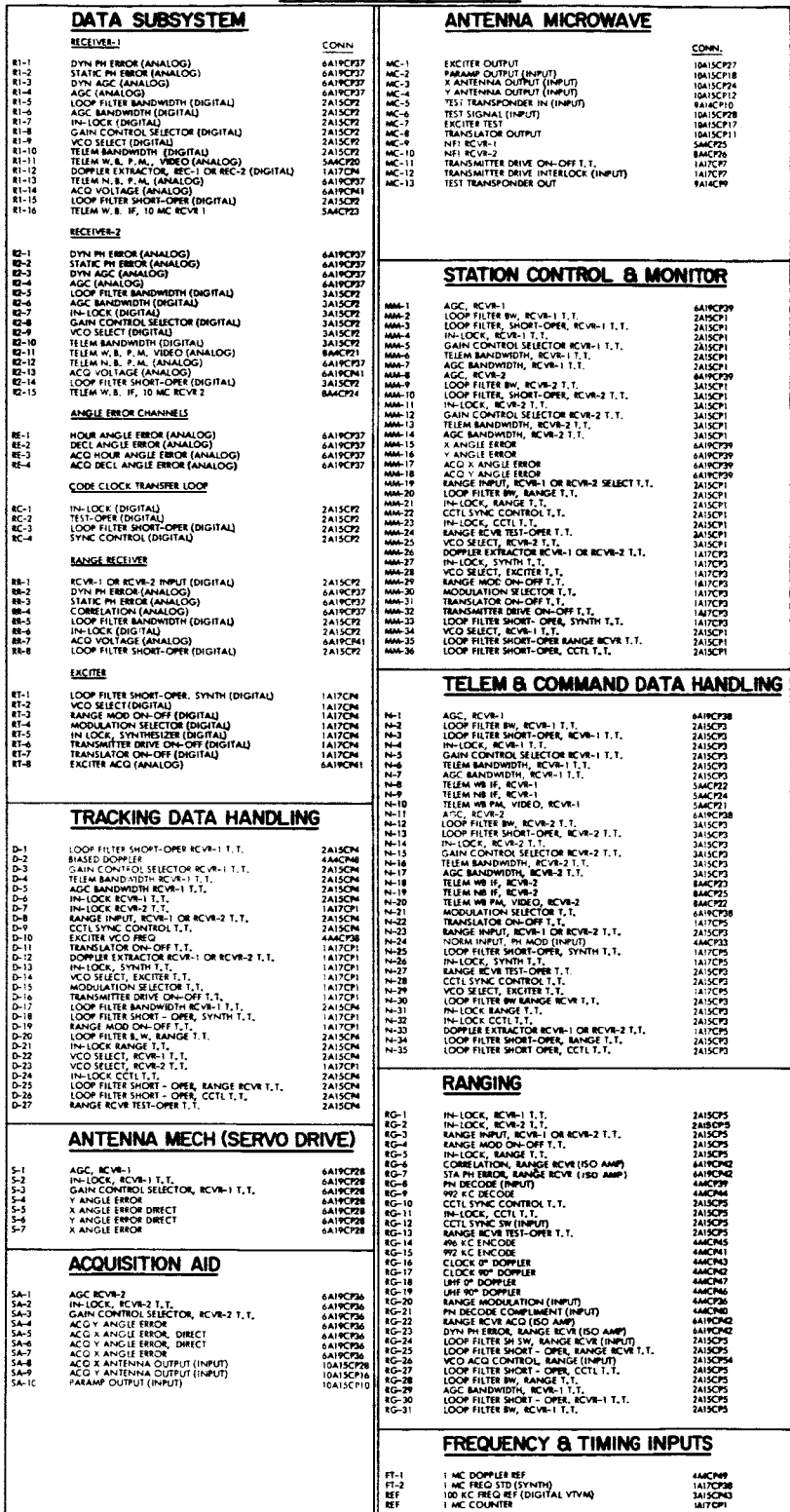


Fig. 40. MSFN unified S-band receiver/exciter subsystem block diagram

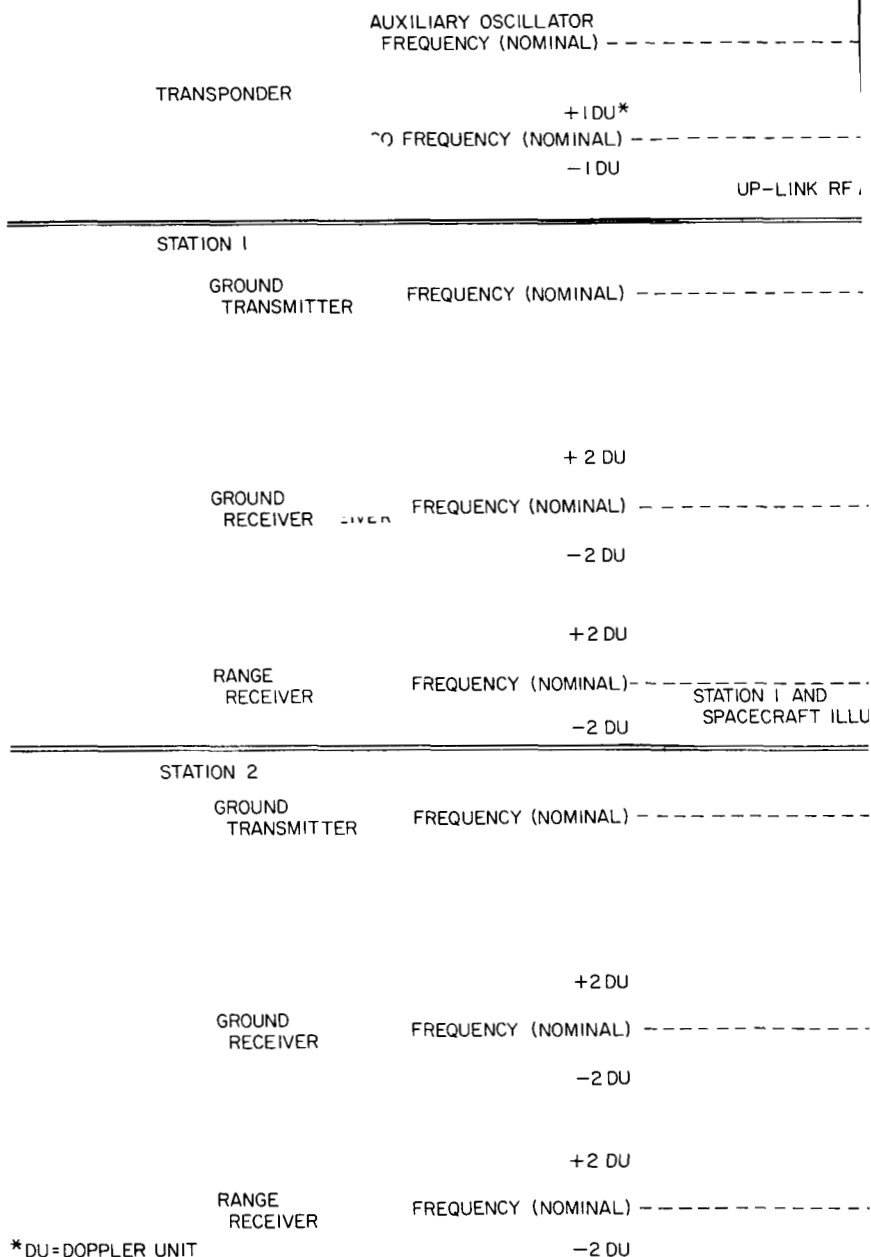


Fig. 41. RF acquisition

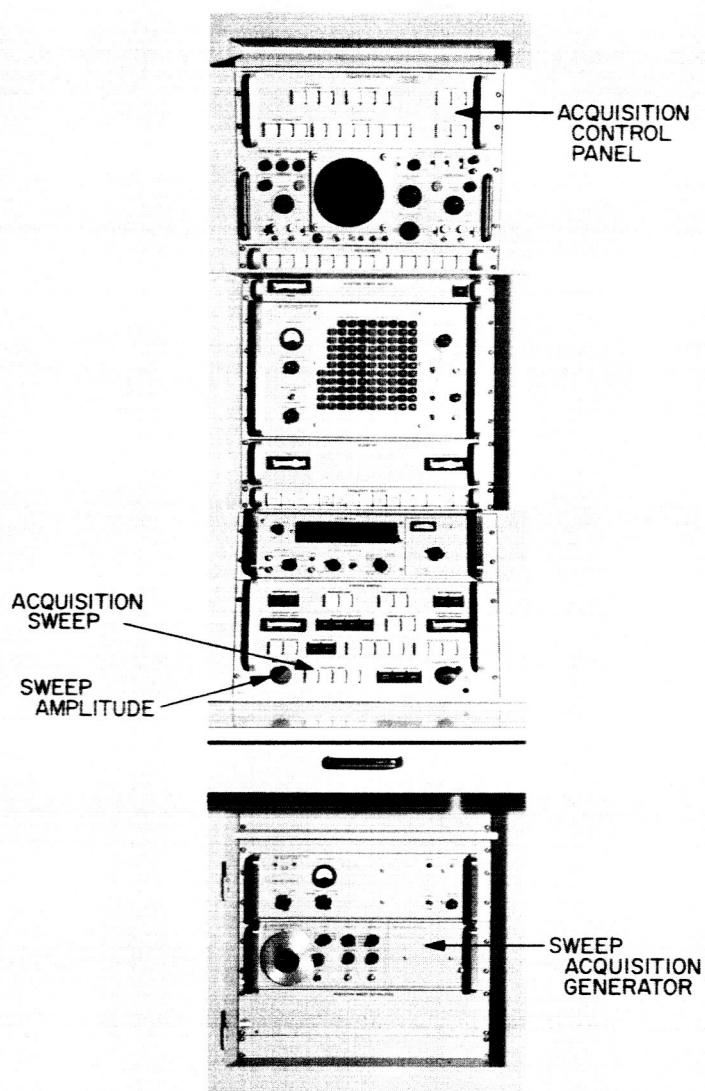


Fig. 42. Receiver/exciter rack 1

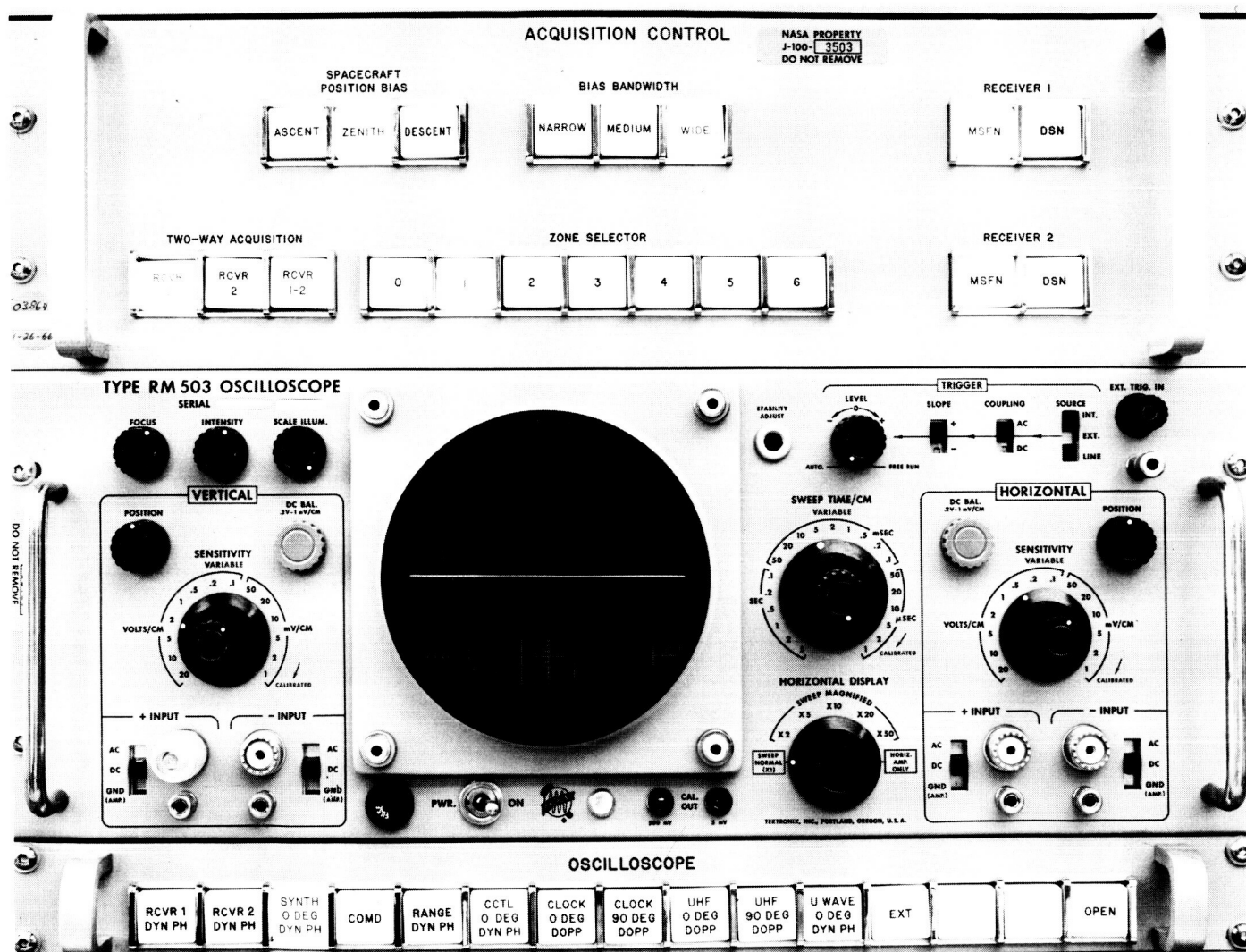


Fig. 43. Acquisition control panel

Receiver 1, and Receiver 2) includes provision for operation with remote bias. A switch and three coaxial connectors are mounted on the acquisition zone selector for the use of a remote bias control. Two of the coaxial connectors furnish a voltage to the remote bias control, and the third accepts the output bias voltage. It should be noted that the remote bias source must be "floating" to operate properly with the acquisition circuitry.

F. Efficient Antenna Systems: Advanced Antenna System Radiation Patterns Obtained Using the Surveyor I Spacecraft

D. Bathker

On the night of June 7, 1966, the *Surveyor I* spacecraft was operating in the low (+20 dbm) RF carrier power mode, and the Mars Deep Space Station was made available for tests. Thus, a unique far-field collimation facility was available to boresight, focus, and obtain radiation patterns of the recently completed Mars Deep Space Station 210-ft reflector. A receive-signal power of -108 dbm at the traveling wave maser preamplifier input when the spacecraft was operating on the high-gain planar array provided a useful dynamic range of approximately 62 db.

Fig. 44 shows the receiver automatic gain control (AGC) curve and polynomial fit used for subsequent data reduction. Two AGC calibrations were made for system temperatures of 303 and 29.2°K (ambient load and cold sky) to avoid the possibility that the lunar blackbody radiation would interfere with the calibrations. For receive-signal levels greater than -150 dbm, essentially no deviation exists. Threshold, for a 12-cycle reference loop bandwidth and a 10-sec AGC time constant, was approximately -160 dbm for the 300°K system and -170 dbm for the 29°K configuration. Because the main beam "sees" the cold sky for those portions of the antenna radiation patterns where receive signal power is of the order of -150 dbm, the 29°K system noise temperature AGC calibration may be used throughout the data reduction.

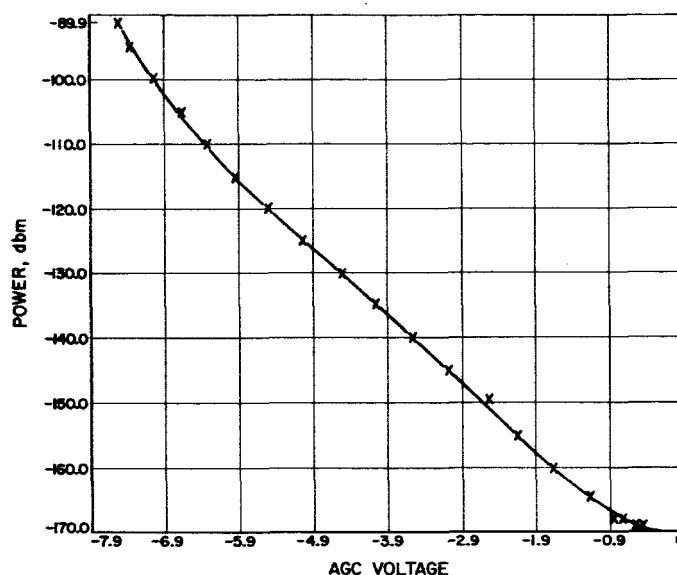


Fig. 44. Mars DSS receiver AGC calibration for antenna patterns, $T_s = 29.2^\circ\text{K}$

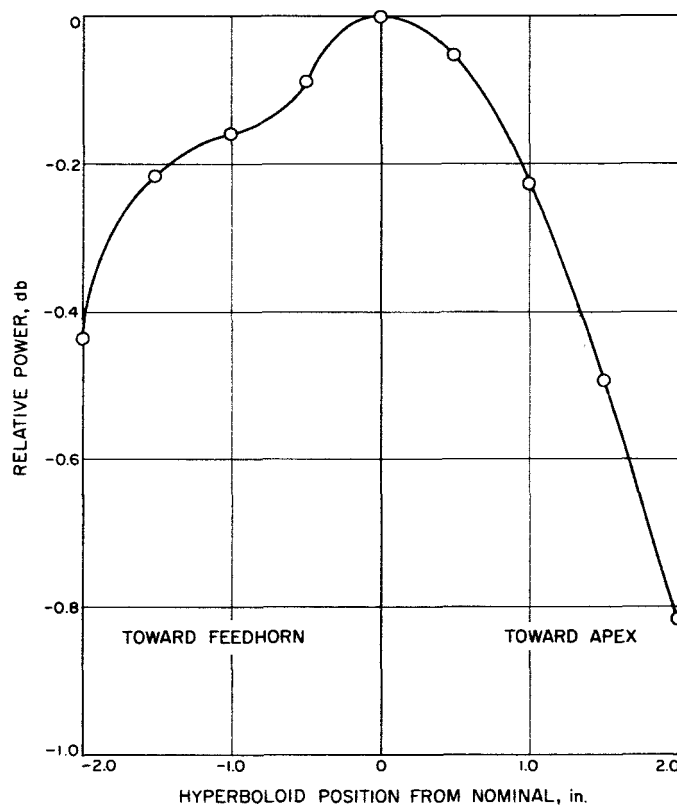


Fig. 45. Mars DSS 210-ft reflector focus curve

Throughout the pass, the antenna was open-loop pointed with the standard computer assisted command system. The antenna was boresighted at elevation angles of 10.0 and 32.5 deg; for both cases an elevation offset of +0.005 deg

was required. Azimuth boresighting was done at azimuth angles of 123 and 170 deg; again both cases were repeatable, and an azimuth offset of -0.080 deg was required, which indicated a possible bias error.

The hyperboloid focal adjustment was changed in 0.500-in steps, AGC voltages recorded, and later reduced to a db scale (Fig. 45). These data were obtained at an elevation angle of 14 deg. The nominal position in Fig. 45

was previously set up on the optical basis of a steel tape measurement from hyperboloid vertex to feedhorn aperture. While a tape measurement of this kind ignores the best-fit paraboloid vertex, the RF test confirms the setting well within an uncertainty of ± 0.25 in., or approximately 0.03 db.

For pattern taking, position offsets, in azimuth and/or elevation coordinates relative to the lunar motion, were manually inserted. Rate offsets of 0.002 to 0.008 deg/sec

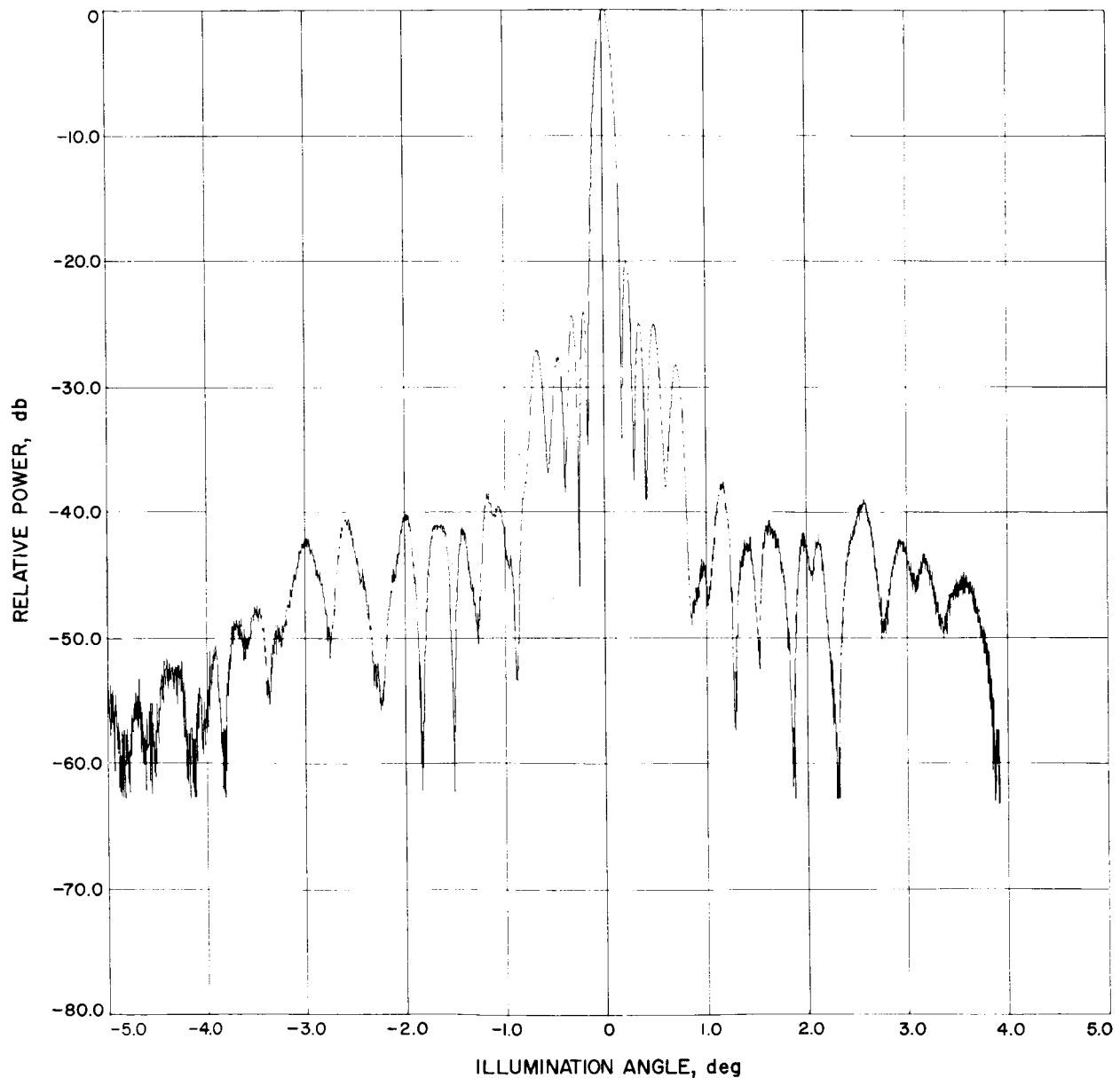


Fig. 46. Mars DSS azimuth radiation pattern

were automatically generated by the command system following a manual start. Zenith angle corrections for patterns having an azimuth motion component were used. AGC voltage was recorded at 1-sec intervals, and both rates provided excellent patterns. Data reduction was accomplished on two IBM 1620 programs, which converted recorded Universal Time (U.T.) to position offset and recorded AGC voltage to relative power. An antenna feed pattern program was modified to accommodate the small illumination angle and wide dynamic range. Figs. 46 and 47 show the azimuth and 45-deg plane patterns, and

Figs. 48 and 49 show elevation and 30-deg plane patterns. It is interesting to note the loss-of-lock at approximately ($-108 \text{ dbm} - 62 \text{ db} = -170 \text{ dbm}$), confirming the use of the 29°K system noise temperature AGC calibration. By coincidence, the loss-of-lock level is the predicted, and approximately verified ($\pm 0.5 \text{ db}$), isotropic level of the 210-ft system.

The pattern data are considered unique inasmuch as they are the only known data recorded using a large aperture at a high elevation angle, with a coherent source, long baseline, and large dynamic range.

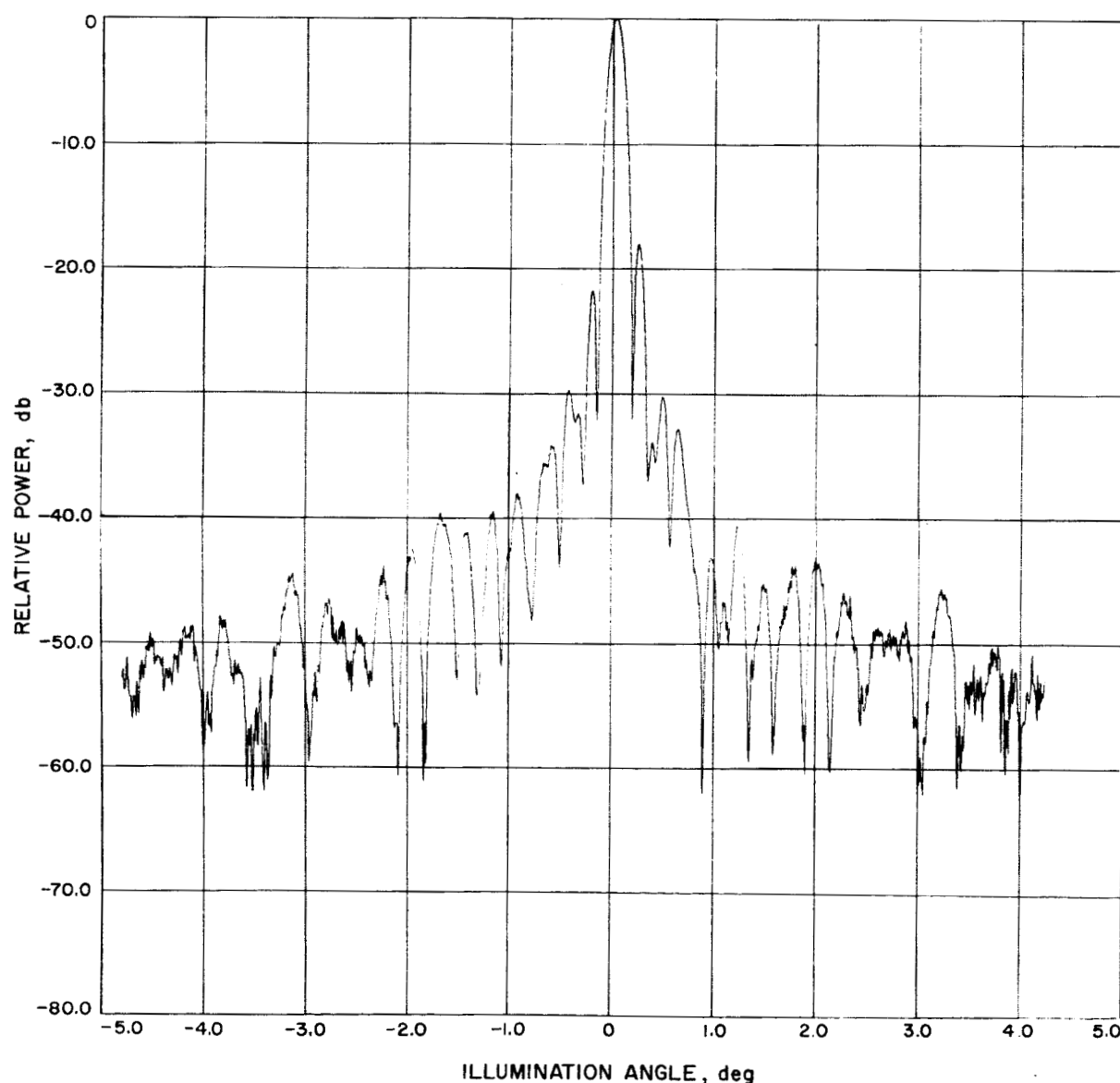


Fig. 47. Mars DSS 45-deg radiation pattern

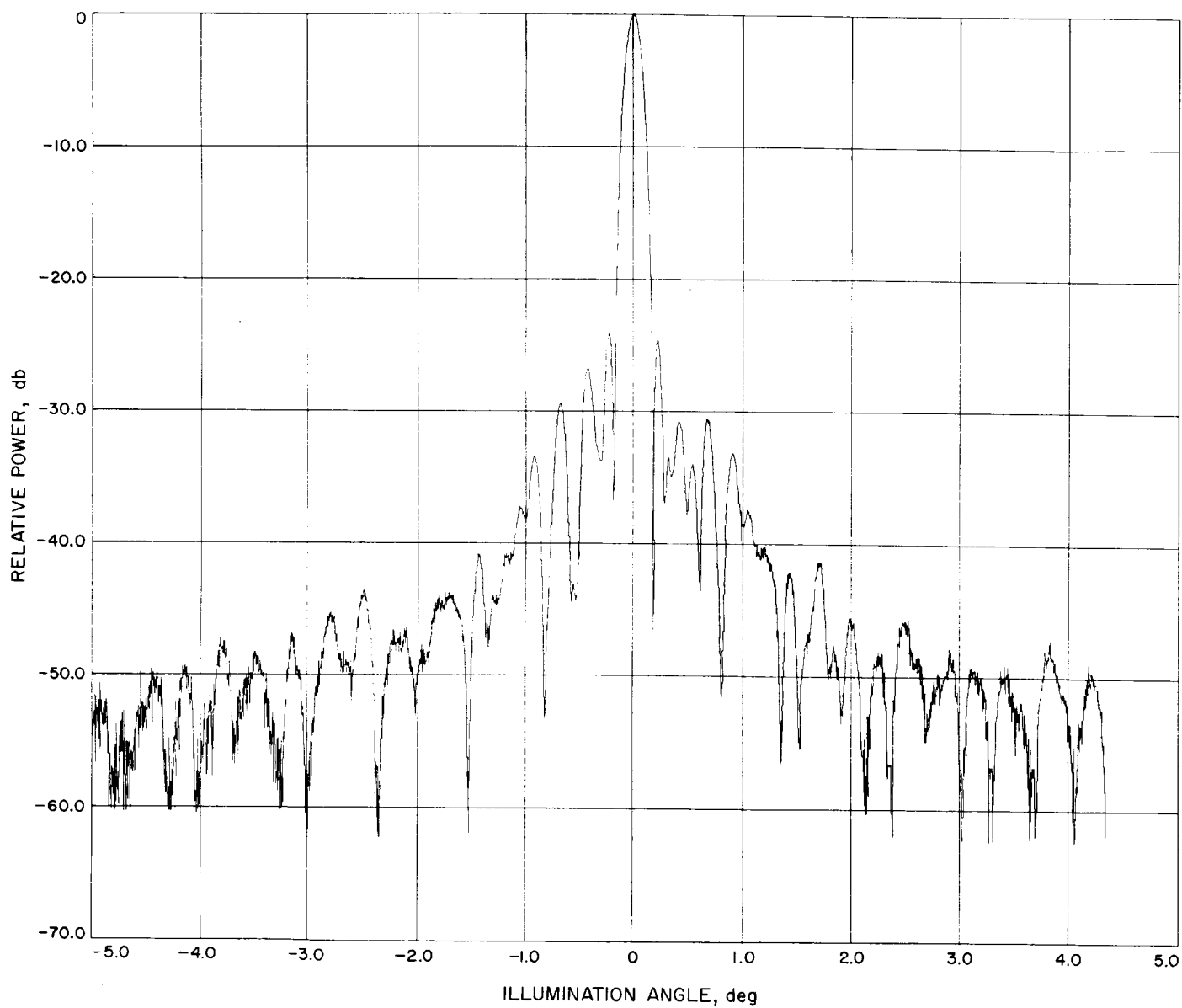


Fig. 48. Mars DSS elevation radiation pattern

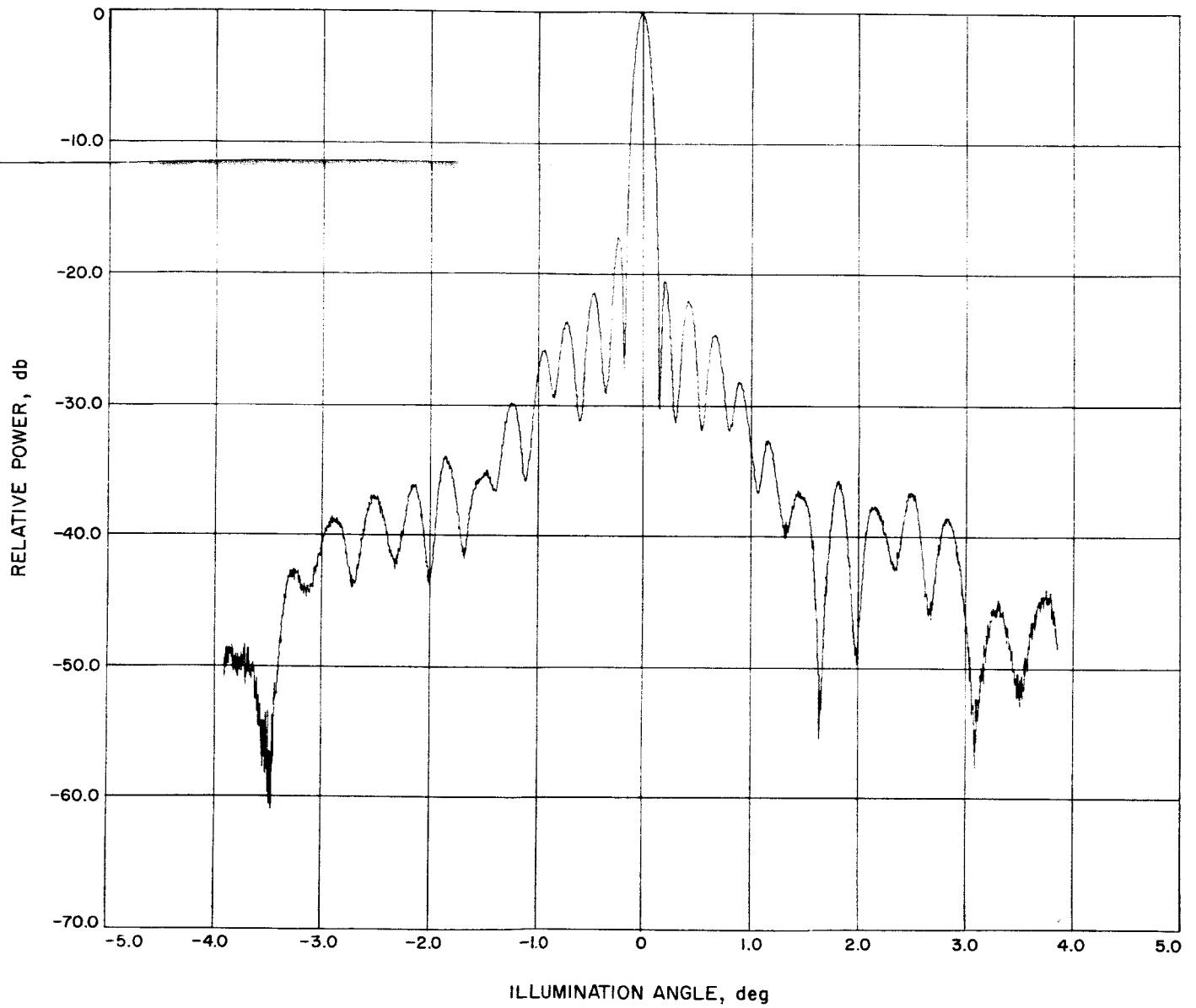


Fig. 49. Mars DSS 30-deg radiation pattern

G. Advanced Development of Microwave Antenna Subsystems

R. W. Hartop

Advanced development of the next-generation microwave antenna subsystem for the DSIF has been initiated in order to maintain state-of-the-art capability in diplexed antenna feed-system design. The goals of this advanced development are threefold:

- (1) To increase the transmitter power-handling capability of the feed, diplexer, transmitter noise filter, waveguide switches, and miscellaneous waveguide components to a minimum of 500-kw CW, with a design goal of 2000-kw CW;
- (2) To increase the antenna gain by extending present multimode techniques to the transmitter frequency band, in addition to the receiver band; and
- (3) To increase the antenna figure of merit over the receiver frequency band.

The above goals are stated in their order of importance; thus, the most immediate attention is being given to obtaining prototype megawatt microwave components. Procurements are being initiated for the most critical of these components which will, for the most part, be similar to the present GSDS designs except for the addition of water-cooling passages and reduction of insertion losses.

Concurrent with these procurements, high-power tests are being conducted at the antenna test site of the Venus DSS on present GSDS components in order to determine their limitations. A diplexer, transmitter filter, waveguide switch, and 90-deg E-plane mitered elbow have all been successfully tested at 100-kw CW with no water cooling. Although all these aluminum components became quite hot (up to 115°C in the case of the diplexer), the fact that no breakdowns occurred at these elevated temperatures indicates that these uncooled 10-kw designs are an excellent starting point for the advanced designs.

A resonant ring driven by a 20-kw CW klystron is now being placed in operation at the Echo DSS antenna test site (see R. B. Kolbly's report, "High Power CW S-Band Traveling Wave Resonator," on p. 24). As schedule time permits, the present GSDS components will be tested in this ring to power levels of 400 kw or higher.

It was reported in SPS 37-34, Vol. III, p. 45, that a complete S-band Cassegrain cone assembly was diplexed at a CW power level of 22 kw, more than twice its normal operating level. During the next reporting period, this work will be extended by attempting to diplex a complete cone assembly at power levels up to and including 100 kw CW without any water cooling. The cone will be fully instrumented to guard against irreversible damage; since most of the critical components have already been tested separately (with the notable exception of the multimode monopulse feed), it is felt that there is a good chance of reaching 100 kw without arcing.

N66 38564

H. High-Power Transmitter Development

E. J. Finnegan

1. Klystron Filament Monitor

a. Summary. Investigation of the accuracy of the klystron filament current and voltage remote-metering circuits was performed during this reporting period. Remote sensing is necessary because of the relative inaccessibility of the transmitter on the antenna. The current was monitored by an instrument (current) transformer on the primary side of the filament transformer. This technique was adequate and tracked the true current within 4% when the load resistance was varied. The voltage, monitored by a separate (tertiary) winding on the filament transformer, did not track the actual filament voltage during the critical warmup period.

b. Voltage monitoring. The voltage monitoring is accomplished by a tertiary winding on the klystron's filament transformer. This winding must be isolated from the filament winding due to the high voltage (55 kv) on the klystron cathode. Accurate measurement of the filament voltage is necessary to assure long tube life, particularly during warmup. The resistance of a cold filament is about one-ninth that of a hot filament; thus, as a tube warms up, it presents a changing load to the filament supply.

Three transformers which are in use at the Venus DSS tracking station were tested, and calibration curves were plotted. The current sensing circuits were accurate enough to use when either the input line voltage or the load varied;

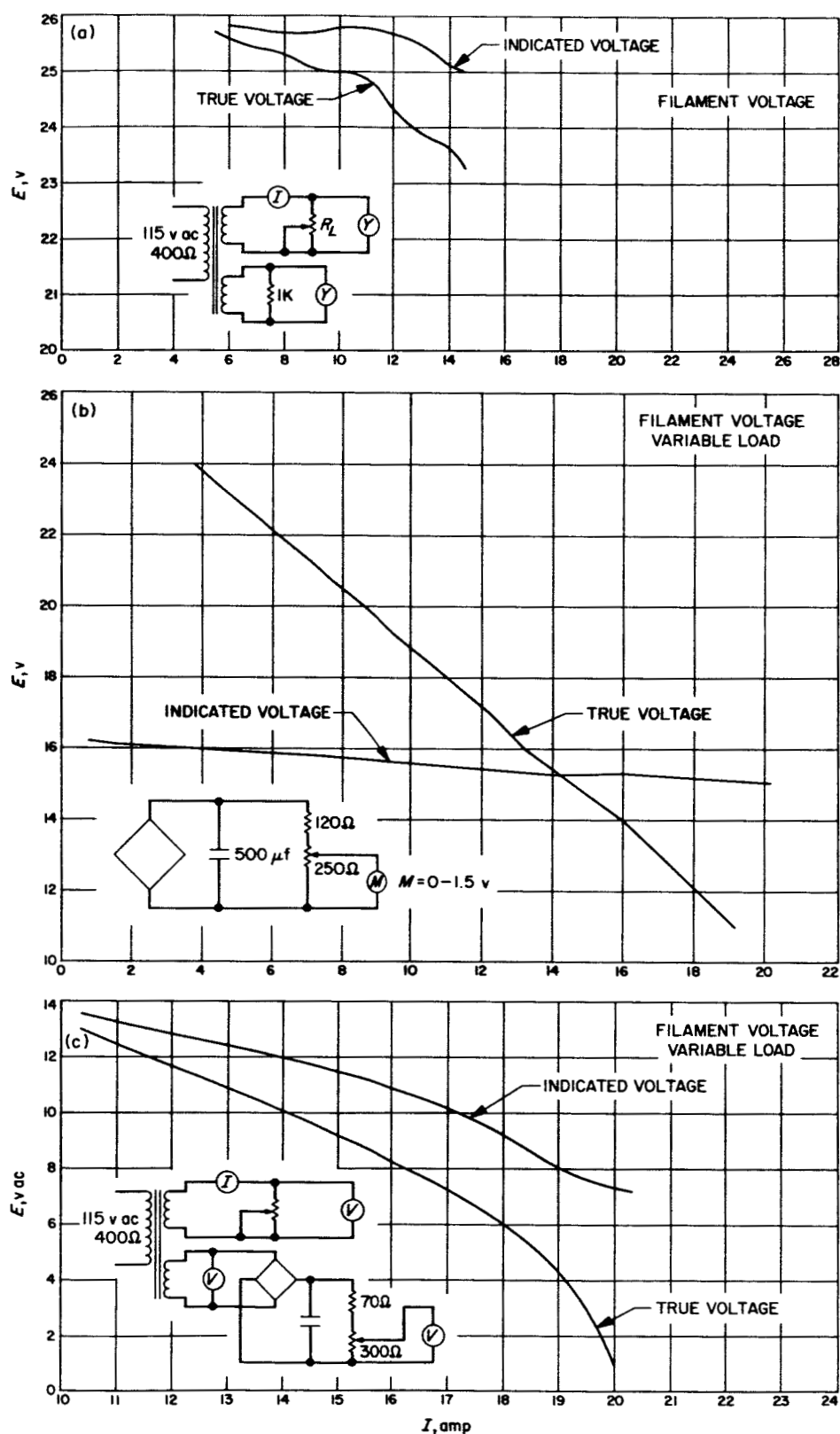


Fig. 50. Klystron filament transformer tracking voltage calibration, (a) transformer 1, (b) transformer 2, (c) low C transformer

however, the voltage sensing circuit did not track the true voltage when the load current varied. The voltage sensing circuit was adequate only when the line voltage varied.

Fig. 50(a), (b), and (c) show the curves for the three different transformers that were tested. As can be seen from the curves, the voltage did not track when a changing load occurred. The variation in results is probably due to a difference in coupling factors of the windings of the several transformers. The results using this method were not very satisfactory. A better method would be to use a feedback transformer insulated for 55 kv. This would give the correct voltage under all conditions. Future filament supplies now being manufactured will have this technique incorporated.

2. Silicon-Controlled Rectifier Firing Circuit

The development of a silicon-controlled rectifier (SCR) power supply is in process to investigate the response time required for use with a motor-generator set exciter (SPS 37-38, Vol. III, pp. 56-61). The purpose of this power supply is to replace the amplidyne, which uses vacuum tubes, with an SCR power supply which consists of all solid-state devices, thus increasing the overall reliability of the Venus transmitter. The present amplidyne has a very slow response time (≈ 0.5 sec). The turn-on time for the SCR's is in the microsecond region; however, the delay of the firing circuits is much greater. Therefore, it will be the only portion of the power supply considered here. A supply is being procured from a commercial source for operational use. The experimental supply discussed in this report will allow the investigation to continue without waiting several months for delivery of the commercial unit, which will be used upon receipt.

a. SCR firing circuit. The trigger circuit developed for this experiment was for a three-phase, 400-cycle power supply and was of the unijunction type. The triggers for all three phases are developed from a common oscillator. This circuit will control the power of the power supply over a range of approximately 75%.

Fig. 51 shows a block diagram for measuring the response time on a scope presentation. The bias supply varies the voltage to the base of a transistor which, in turn, acts as a variable resistor to change the RC time constant of the circuit. This causes the unijunction to trigger at different levels, thus changing the firing angle of the SCR's.

To measure the response of the power supply, the bias was changed by placing a step function on the base of the

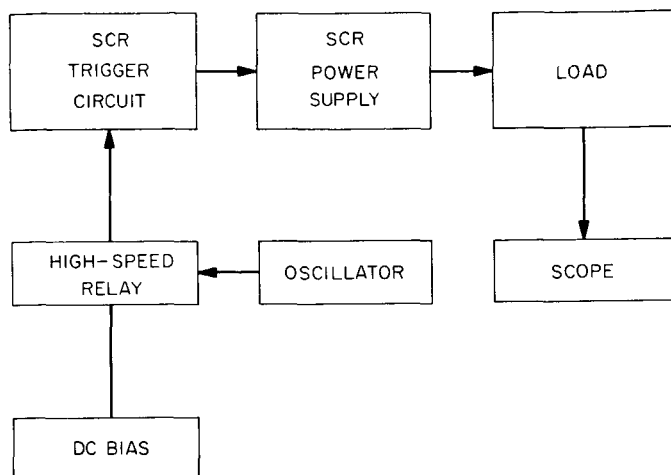


Fig. 51. SCR trigger response time

transistor and by observing the output of the power supply with a resistive load termination. Fig. 52 shows the voltage changing from 150 to 180 v at a load current of 3 amp. Fig. 53 shows a change from 150 to 220 v at a load current of 8 amp. The switching rate was approximately 2 cps.

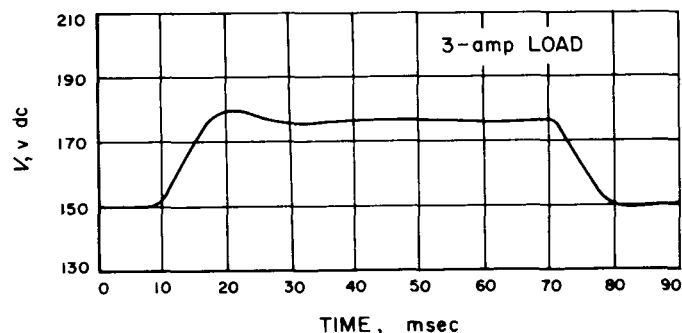


Fig. 52. Response time of SCR power supply (3-amp load)

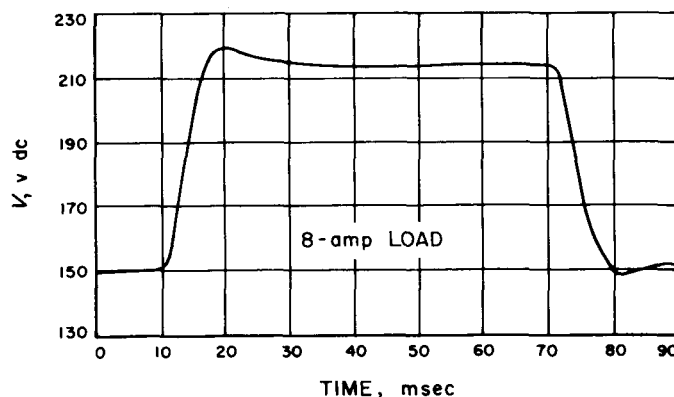


Fig. 53. Response time of SCR power supply (8-amp load)

The response time of approximately 8 msec is adequate for the motor-generator set.

b. Future plans. A second circuit has been developed, using separate triggers for each phase. The advantages of this circuit are smoother control and the capability of regulating the output voltage from zero to 100%. Response time of this circuit has not been measured.

3. Klystron Protective Device

Development of a crowbar for use in future DSN high-power transmitting systems is in process. A crowbar is a device used to protect the output tube in a high-powered transmitter in the event of an internal high-voltage arc by rapidly diverting the destructive high current through the crowbar and dissipating the stored energy while the over-current protective devices shut down the power supply. The characteristics of a lower voltage-triggered spark gap crowbar now in use are being measured. A crowbar utilizing a mercury pool ignitron is ready for evaluation.

a. Triggered spark gap. The 55-kv DC power supply at the high power test facility, Venus Deep Space Station,

includes a triggered spark gap crowbar. Briefly, this consists of two spark balls with an adjustable gap setting servoed by the high voltage. The gap is set higher than the breakdown voltage and triggered by an auxiliary spark gap fired by a sudden increase in klystron beam current. It may be possible to use this on higher voltages by increasing the gap spacing if breakdown does not occur.

An experiment was conducted to measure the response time of the crowbar. A block diagram showing how the response time was measured is shown in Fig. 54. Fig. 54 is a test setup for measuring the crowbar delay time. This is the elapsed time between the detection of an arc and the operation of the crowbar. The current probe and DC ammeter is one unit. The probe was necessary because the body current is measured as the differential between the high-voltage cathode current and the collector current. The battery B_1 , resistor R_1 , and switch S_1 combine to form a temporary circuit for inducing a simulated transient in the current probe. When S_1 is depressed, it excites a transient pulse in the current probe and initiates the trigger to fire the crowbar. S_1 also triggers the scope and starts the time base. When the crowbar fires, a pulse from

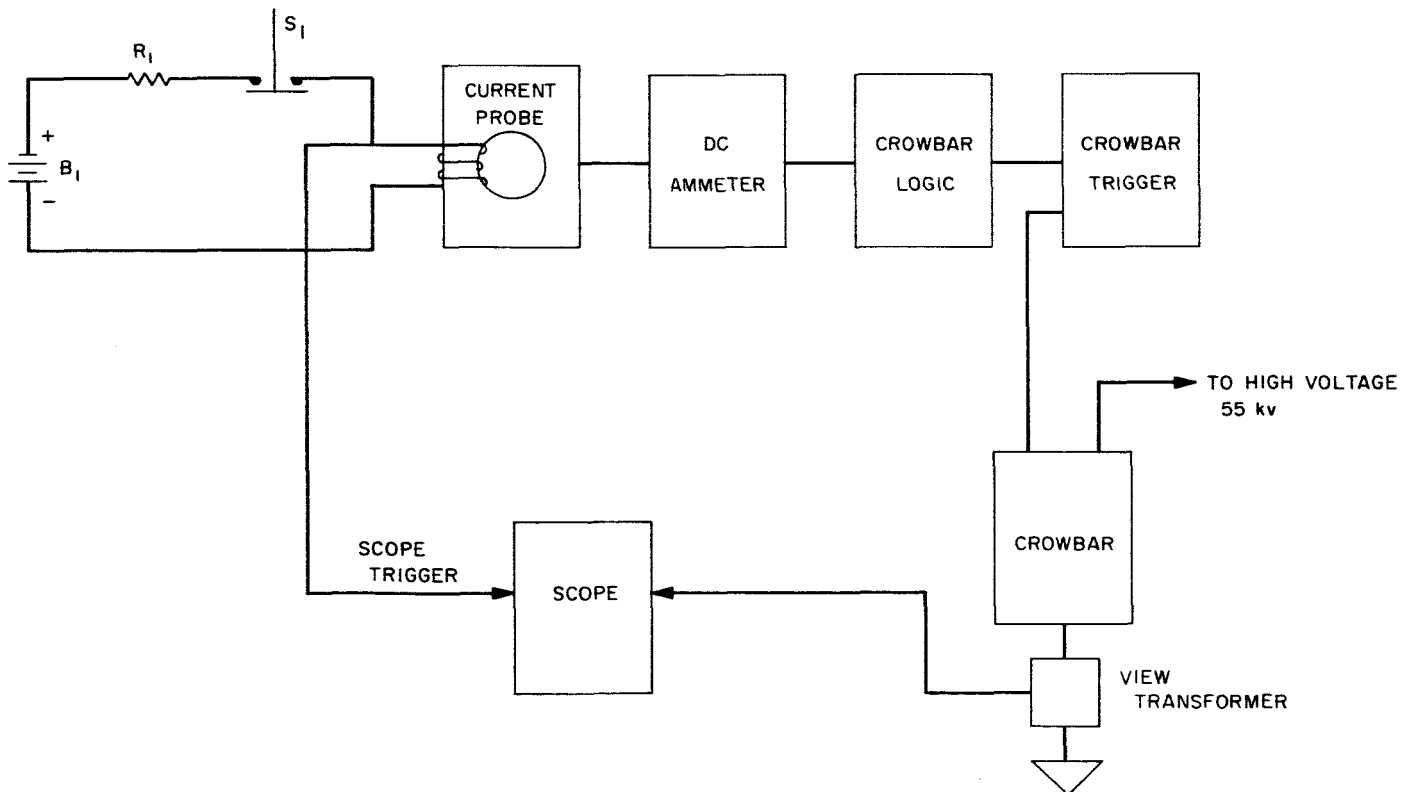


Fig. 54. Test setup for measuring crowbar delay

the viewing transformer is seen on the scope, thus establishing the overall delay. Figs. 55 and 56 show amplitude versus time; the amplitude has no significance except to establish the delay time. Measurements made at different voltages show no appreciable change in time due to voltage. The response time for the entire crowbar circuitry was approximately 2780 μsec . Most of the delay time is in the current probe. When the power supply voltage is raised to 70 kv, this slow response time may prove to be destructive to the klystron.

b. Future development. A new crowbar has been developed, using a mercury pool ignitron. This has the advantage of not requiring adjustment for changes in voltage, altitude, or humidity. The ignitron crowbar is ready for bench testing.

A new, high-speed current probe for sensing klystron arcs and for monitoring body current is also under development. With the new ignitron and current probe it is expected to bring the response time to 10 μsec or better, thus giving the klystron adequate protection.

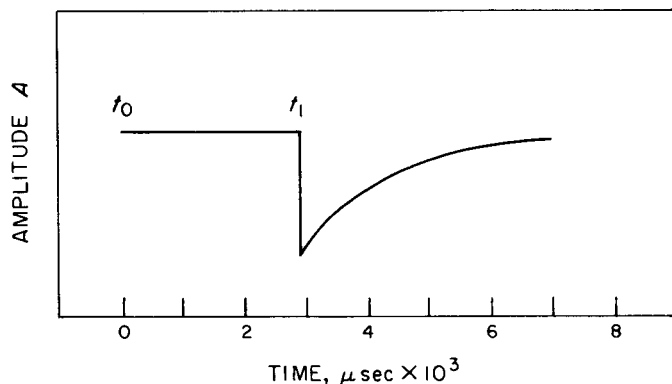


Fig. 55. Crowbar response time at 20 kv

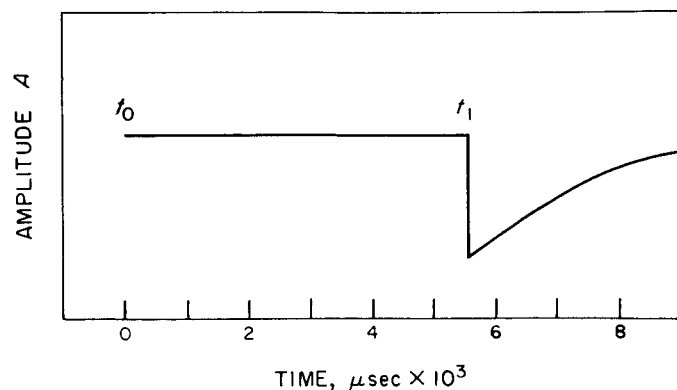


Fig. 56. Crowbar response time at 30 kv

I. A Manual Gain Control Remote-Control Subsystem for the Mars Deep Space Station Receiver

C. F. Foster

1. Introduction

The bistatic S-Band radar system (SPS 37-38, Vol. III, pp. 62-64) requires that all the operator controls of the Mars DSS receiver be located at the Venus DSS. With the use of a programmed exciter (SPS 37-36, Vol. III, pp. 54-63) at the Venus DSS, the Mars DSS receiver frequency will be fixed at 2388 Mc. This means that the only receiver function to be controlled by the operator is receiver gain.

The receiver will be mounted in the 3A-cone section of the Mars DSS antenna and will be unattended. The subsystem requirements for the remote gain control system are high reliability, freedom from maintenance, continuous control, with power requirements in the range of the existing receiver power supply's current and voltage capabilities; the system must be stable to the point that drift is negligible, and be packaged so that it can be mounted inside a standard antenna-mounted box. As no commercially available system meets all these requirements, a program to develop a remote-controlled gain subsystem was initiated.

2. Subsystem Description

A simplified block diagram of the subsystem is shown in Fig. 57. The manual gain control (MGC) remote-control

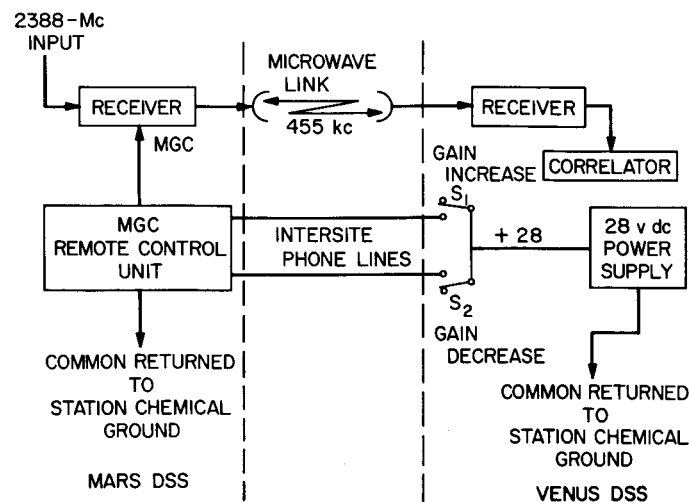
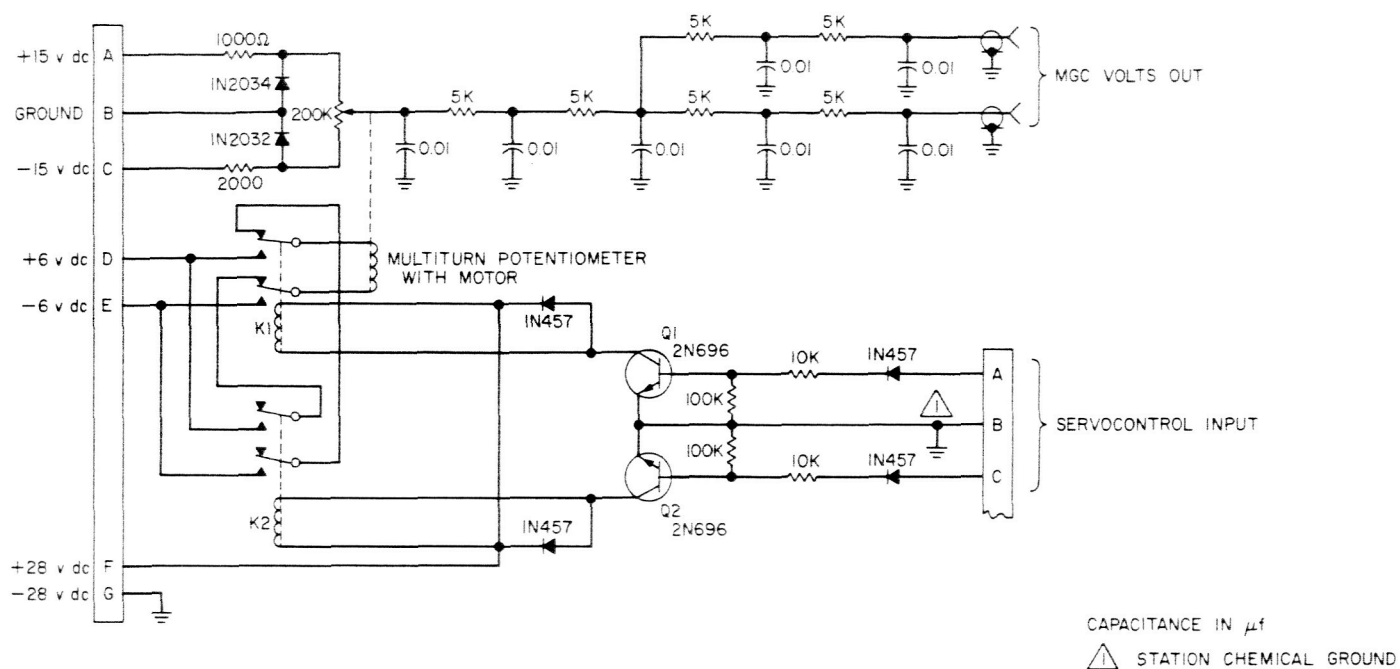


Fig. 57. MGC remote-control subsystem block diagram



unit (circuit is shown in Fig. 58), uses a motor-driven helipot connected across the output of two reference diodes (which are powered by a ± 15 v regulated power supply), to generate a stable DC voltage of -4.7 to $+6.8$ v dc. This voltage is used to bias a 30-Mc bandpass amplifier in the receiver. The output of the receiver is sent via the microwave link to the Venus DSS, where the level is monitored on a true root mean square meter at the correlator input.

This bias voltage is adjusted from the Venus DSS by switching the positive voltage of a 28 v dc power supply (which has its common tied to the Venus DSS chemical ground) into one wire of a pair of No. 20 wires (this pair is physically a part of the DSIF phone cable between the Mars and Venus Deep Space Stations). This voltage is then applied to the base of Q1 or Q2, depending on whether it is desired to increase or decrease the bias voltage of the MGC remote control unit located at the Mars DSS. The emitter of Q1 is returned to the Mars DSS chemical ground, and completes the control signal path,

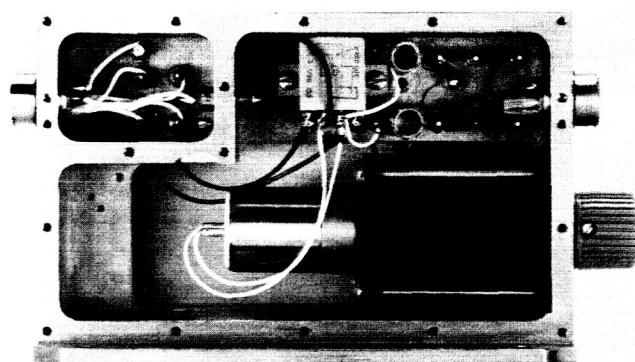
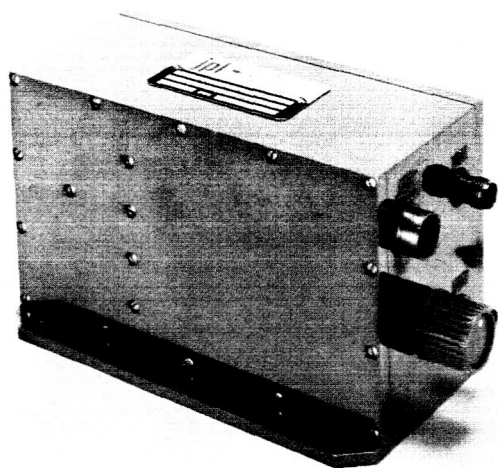


Fig. 59. Completed module (a) outer view (b) inside view

N66 38566

actuating Q1 and closing RL₁. This applies voltage to the motor-driven helipot, moving the arm of the potentiometer which selects a new bias voltage. RL₁ and RL₂ are interlocked so that, if a positive voltage is applied to Q1 and Q2 simultaneously, the system is protected. The helipot is protected against mechanical damage by means of a torque clutch. This clutch also allows the potentiometer to be changed manually at the Mars DSS.

3. System Performance

A prototype MGC remote-control unit was assembled at JPL and completely tested at both JPL and at the Mars and Venus Deep Space Stations. A photograph of the prototype MGC remote-control unit is shown in Fig. 59.

The voltage drift versus temperature change characteristic, with the potentiometer position fixed, is shown in Fig. 60. This represents a change over the entire temperature range of less than 0.01%, which, when compared with the volts-per-decibel characteristic of the receiver, amounts to a 0.3-db change in gain at this voltage setting. The slewing rate of the system is set by the gear ratio and by the voltage supplied to the driving motor; the limit-to-limit slewing time is 3 min.

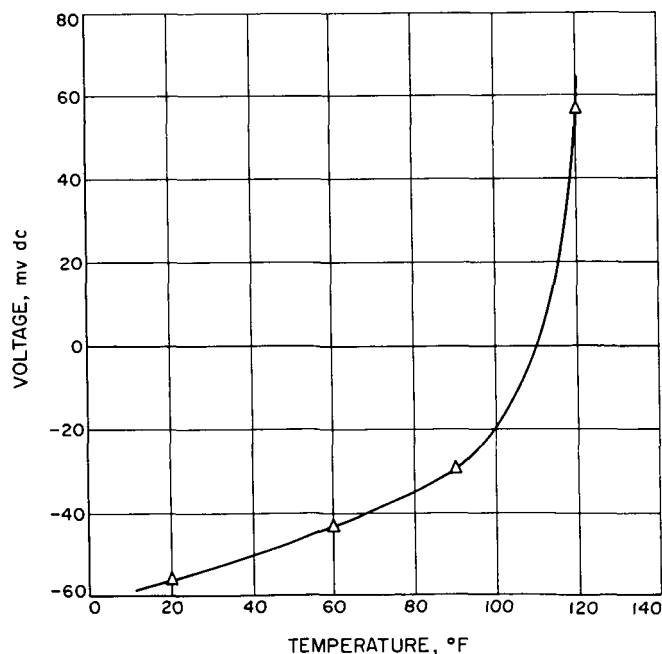


Fig. 60. Voltage vs temperature of MGC remote-control unit

The remote gain control has been installed and is now operating. Field service information will be recorded regarding system performance and reliability.

J. Redesign of Mod II and Mod III Stored Program Controllers

J. W. Newton

Mod II and Mod III stored program controllers (SPC's) are moderate-speed, moderate-memory-size, special-purpose computers built at JPL for use in extending the applications of pseudonoise (PN) coding. As generalized, expanded versions of the Mod I ranging controller, they are intended to be practical models of a Universal Turing Machine, with the particular characteristics for any given application specified by a stored program and effected through an input output interface of considerable size (Ref. 2).

Their development has progressed through the past five years. Mod II has been in use at JPL to control and evaluate ranging experiments in conjunction with helicopter transponders and JPL-based TRAC(E) receivers, and Mod III has been in use at the Venus DSS to control and evaluate ranging experiments involving Venus, Mercury, Mars, and the Moon. With research into coding techniques demanding greater operational speeds than those possessed by Mod II and Mod III, it has been decided to extend the life and usefulness of these machines by utilizing them as station-control computers, for which use they possess more than adequate speed.

Mod II has been moved to the Venus DSS where it and Mod III will be used to control the operation of the two service antennas; Mod II will serve the 30-ft and Mod III the 85-ft. Prior to splitting up the system in this manner, each computer is to be substantially reworked to increase its reliability and to make provision for future updating.

1. Evaluation

As they stand today, Mod II and Mod III are substantially identical and closely resemble small, general-purpose computers with rather extensive input-output capacity. By present-day standards their operating speed is slow, due primarily to the use of serial delay lines as main memory storage (an operating cycle can take 125 to 800 μ sec, compared to as little as 3 μ sec for contemporary

machines using core memories). On the other hand, the instruction list is long and sophisticated; Mod II and Mod III have available hard-wired commands possessed only by the largest commercial computers. For use as process-control devices, where cycle times of seconds and milliseconds are the rule, Mod II and Mod III will rank as fast machines for some time to come. Mod III has proved itself in such use during the past three years, and the addition of Mod II will permit considerable extension of automatic operations at the Venus DSS.

This experience with Mod III, however, has uncovered several mechanical weaknesses in the design, the greatest single weakness being susceptibility to overheating. SPS 37-31, Vol. III, p. 80 and SPS 37-34, Vol. III, p. 61 have reported quick-fix remedies necessary to keep Mod III operational under this handicap. Under-floor ventilation has been chilled to 50°F; the full bottom of

each rack has been removed to increase air flow; internal baffling and supports have been thinned out and 500-cfm fans installed in the top of each rack. Nevertheless, a rise in room ambient temperature of 2°F is sufficient to cause errors, the error rate rising with the temperature.

2. Redesign

This susceptibility is attributed primarily to the form-factor of the logic-card mounting-blocks employed in Mod II and Mod III. A new mounting block has been designed and is now in fabrication. Two views of the old and new approaches are shown in Figs. 61 and 62. The improvement in ventilation is obvious. The current drawn per card is quite low, and the original design would probably be satisfactory if the logic cards were not stacked so tightly and in such large numbers; unfortunately, this is the situation in Mod II and Mod III. Each rack contains

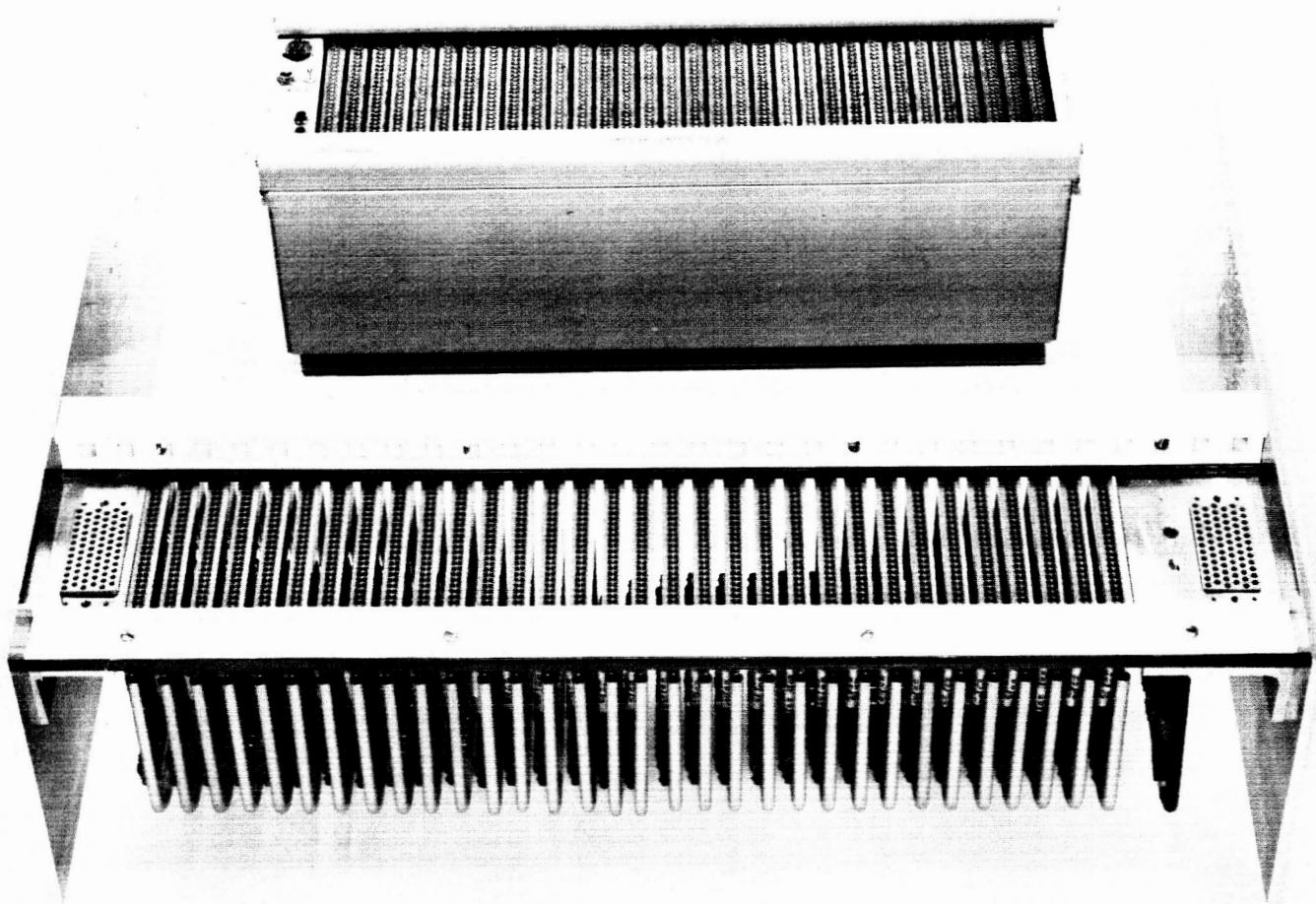


Fig. 61. Old and new logic mounting blocks, front

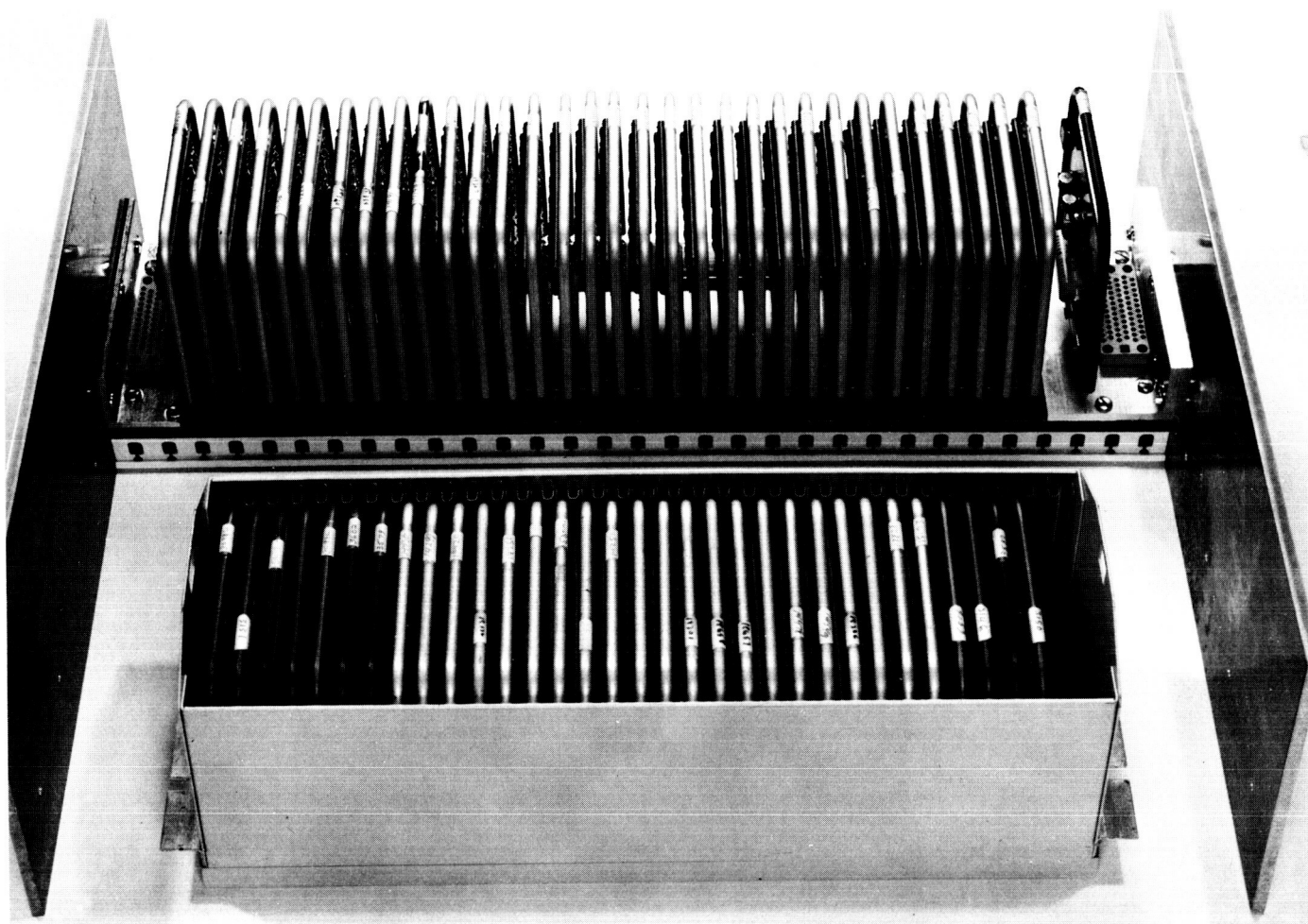


Fig. 62. Old and new logic mounting blocks, rear

22 logic blocks, and experience has proved the need of more effective air flow.

A proof-test model of the new block is shown in Figs. 63 and 64. The design emphasized the use of a minimum of parts and a minimum of labor in manufacture. Card/card spacing has been opened out to 0.600 in.; this approximates the industry standard of 0.625 in., at the same time easing fabrication difficulties. Though use of a skeleton frame mounting will provide the necessary increase in ventilation, increasing the card/card spacing by 0.100 in. has the corollary advantage of reducing air turbulence. Since Mod II and Mod III logic blocks are stacked to 6 ft in height, this means of providing laminar flow ensures that a reasonable amount of air will reach the topmost block direct from the underfloor plenum.

Several additional benefits have been incorporated into the new design. Two 75-pin Deutsch connectors, one in

each wing, provide a neat, controlled path for off-block connections; they also make possible the complete wiring of each block independent of the main frame, and the easy replacement and updating of blocks with a minimum of machine down-time.

3. Grounding

Less visible is an even more important improvement. Block supply voltages have been more heavily bussed together, using 0.032-in. copper strip, 0.175 in. wide. In addition to reducing common impedances somewhat, this makes possible the floating of the logic ground (Fig. 65). Previously, this had been strapped to the mounting block frame and thus tied circuit "common" in with power, AC, and system grounds. Second of Mod II and Mod III weaknesses has been susceptibility to power line and system "glitches" and to static discharge. It will now be possible to isolate these.

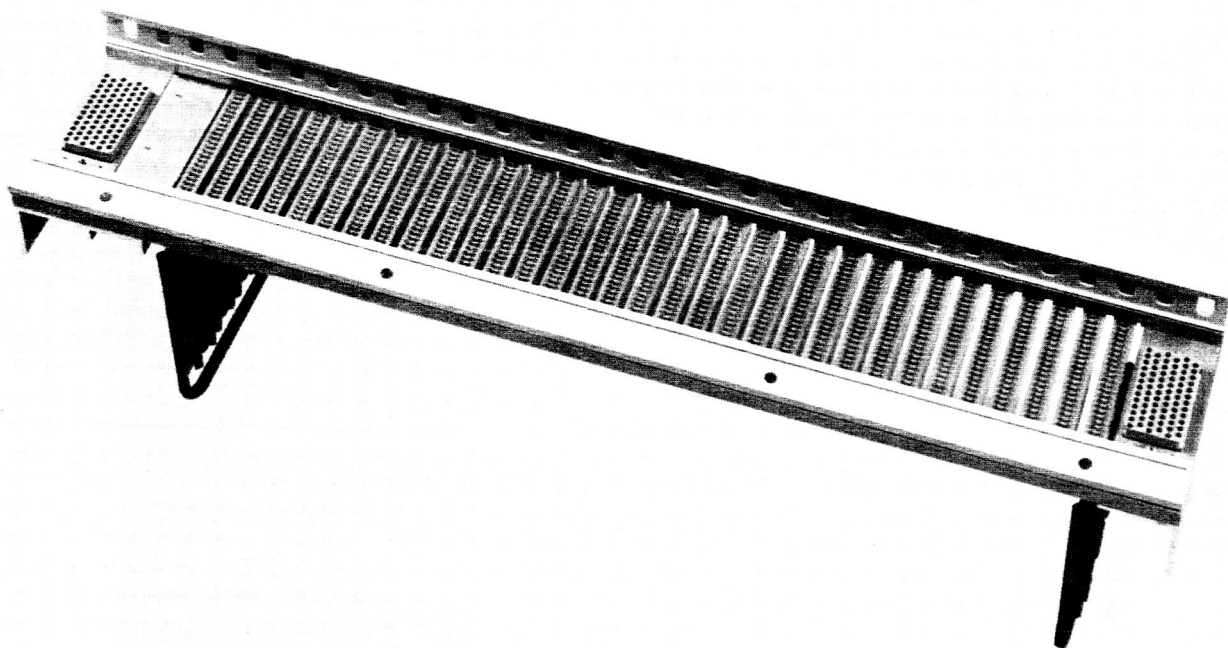


Fig. 63. Prototype mounting block, front

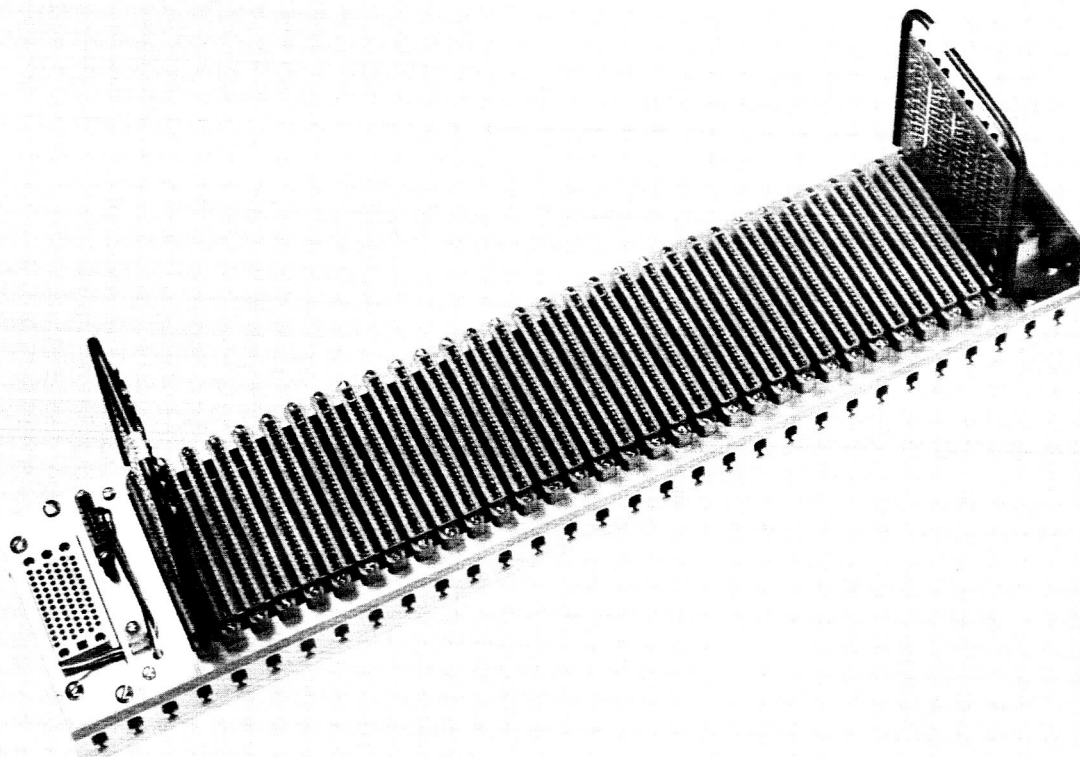


Fig. 64. Prototype mounting block, rear

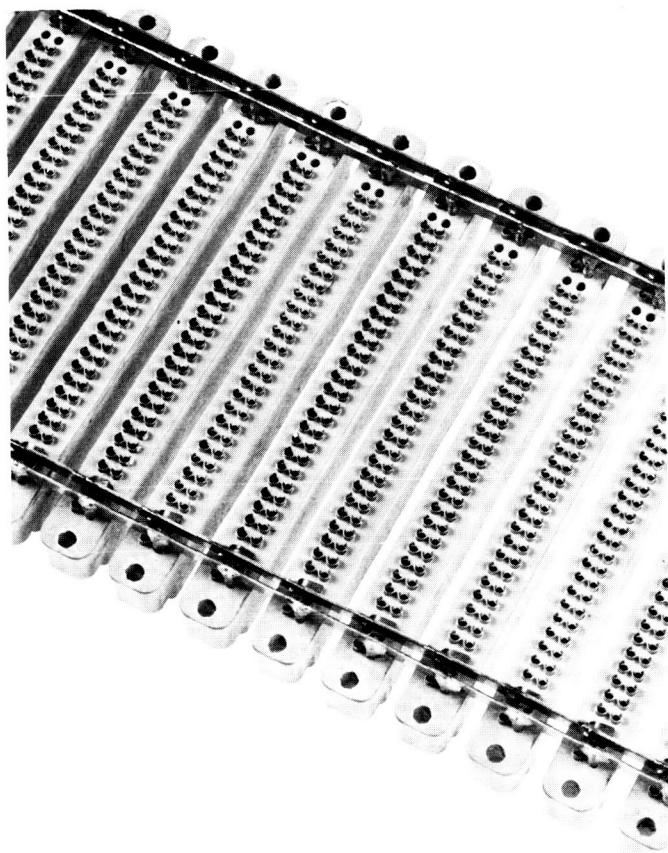


Fig. 65. Card connector bussing before assembly

The light, rigid construction of the new block will also permit a monocoque-type of construction in the rack mounting frame, in which a major portion of the frame strength and rigidity will be provided by the blocks themselves. Additional benefits of the new block will be described as the rework progresses.

K. Microwave Maser Development: Traveling Wave Maser for the Venus Deep Space Station

R. Clauss

1. Summary

A traveling-wave maser (TWM) has been completed for future use on the 85-ft antenna at the Venus DSS. Although the TWM is a copy of the amplifier previously

delivered to the Mars DSS (SPS 37-39, Vol. III, p. 83) slight changes in loading (SPS 37-38, Vol. III, pp. 51-53) have improved the forward loss characteristics. An "in-line quarter-wave thermal short" is used to cool the center conductor of the signal input transmission line. These changes have reduced the equivalent input noise temperature of the TWM (in comparison with previous TWM's). Calculated and measured values agree on a TWM noise temperature of 5°K at the waveguide interface.

2. Maser Performance Comparison

Performance characteristics of a TWM which describe amplifier quality are: net gain, forward loss, inversion ratio, and slowing factor. From these measured parameters we can predict the maser noise temperature (Ref. 3). A comparison of the Mars DSS TWM No. 1 and the Venus DSS TWM No. 2 is shown in Table 7. Fig. 75 shows the bandwidth of TWM No. 2 at 2388 Mc. In a uniform magnetic field with 38 db net gain the 1- and 3-db bandwidths are 7.7 and 13.6 Mc.

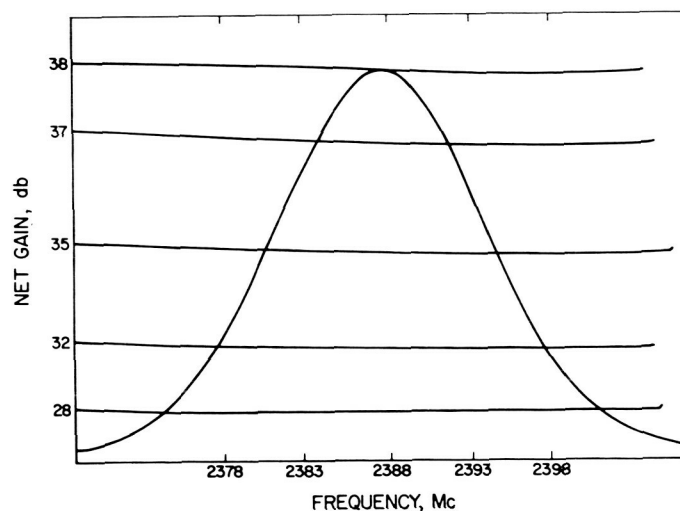


Fig. 66. TWM bandwidth at 2388 Mc

3. Noise

Noise added to the maser by the signal input transmission line has been reduced by cooling the center conductor. Previously this was accomplished by using refrigeration from the 4.4°K flange (SPS 37-39, Vol. III). A more efficient method, which transfers heat to the first stage of the refrigerator (at approximately 70°K), has been used in the Venus DSS maser assembly.

Fig. 67 shows the manner in which heat is transferred from the ambient vacuum seal, through the center con-

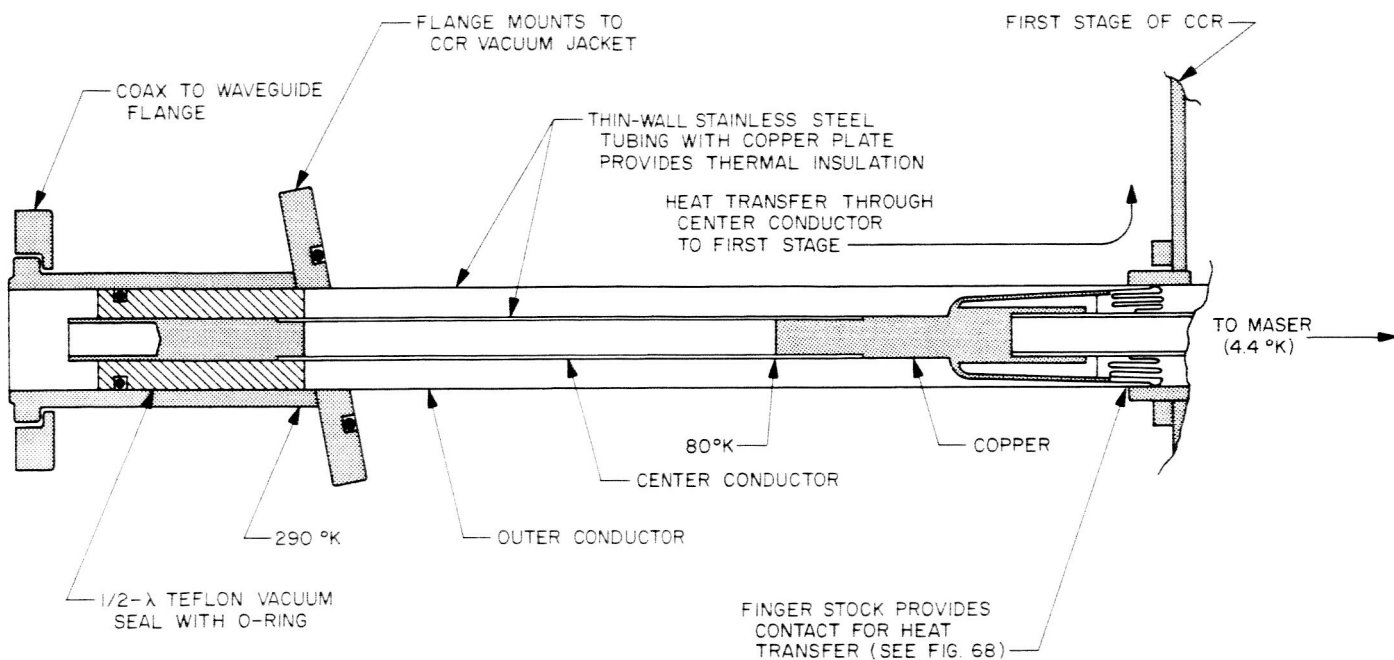


Fig. 67. Signal input coaxial line assembly

ductor into the closed-cycle refrigerator (CCR). Refrigeration at the first stage is sufficient to cool the center conductor from ambient to 80°K along a 4-in. length. This technique has two important advantages: the noise contribution of the coaxial line is reduced, and the heat leak through the center conductor to the maser at 4.4°K is reduced.

Fig. 68 is a photograph of the in-line quarter-wave thermal short which is used to transfer heat from the center conductor to the outer conductor of the coaxial line. Use of this device allows the removal of the center conductor (to replace the vacuum seal) in the field, without disassembly of the refrigerator.

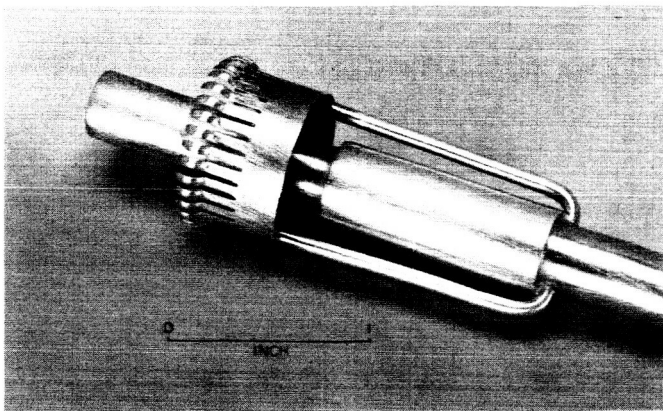


Fig. 68. In-line quarter-wave thermal short

Work on the thermal short has been concentrated in three areas: (1) low loss at the signal frequency, (2) low voltage standing wave ratio (VSWR) in the signal frequency range, and (3) sufficient thermal conductivity to transfer approximately 400 mw with a minimum temperature difference across the short. The use of 0.079-in. D copper rods has provided the necessary thermal path. The insertion loss of the short is 0.011 db. When cooled to 80°K this device contributes less than 0.1°K to the maser noise temperature. The measured VSWR from 2100 to 2800 Mc is shown in Fig. 69. Measurements of loss

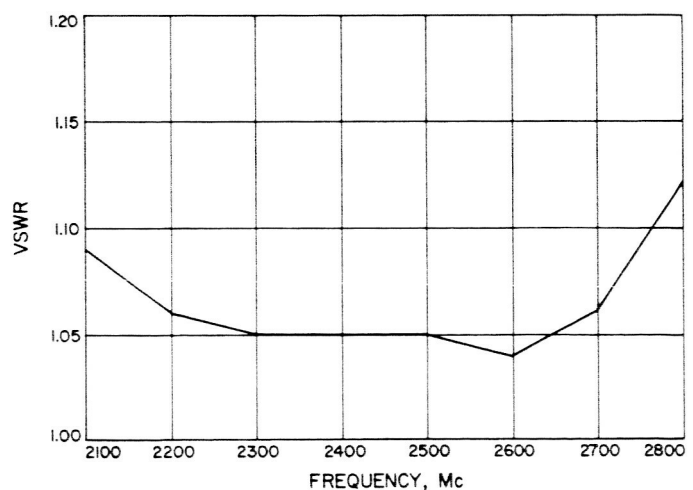


Fig. 69. VSWR versus frequency for thermal short

Table 7. TWM performance comparison

Frequency, Mc	Net Gain, db		Loss, db		Measured inversion ratio		Slowing factor		Calculated ^a noise temperature, °K	
	No. 1 ^b	No. 2 ^c	No. 1	No. 2	No. 1	No. 2	No. 1	No. 2	No. 1	No. 2
2265	—	45	—	—	—	—	—	105	—	—
2275	59	51	34	30	—	3.5	165	100	4.6	4.6
2285	62	52	27	22	3.4	3.4	125	100	3.8	3.7
2295	60	51	22	17	3.4	3.2	125	90	3.4	3.3
2305	58	50	19	14	3.4	3.2	125	85	3.2	3.0
2325	55	50	15	9½	3.4	3.0	115	85	2.9	2.6
2350	50	46	13	8½	3.5	3.1	110	85	2.7	2.5
2375	44	42	16	9½	3.6	3.1	110	85	3.3	2.7
2388	40	38½	18	10	3.6	3.0	110	85	3.7	3.0
2400	38	35	21	12	3.9	3.0	115	85	4.2	3.5
2415	34	32	25	14	3.9	—	125	85	5.1	4.0
2425	—	30	—	16	—	3.0	—	85	—	4.5

^aCalculated for TWM at 4.4°K CCR temperature. Does not include input line contribution.

^bTWM No. 1 for Mars DSS.

^cTWM No. 2 for Venus DSS.

and VSWR were made by comparing the loss and match of a standard 6-in. length of "rigid" coax to a coax with the thermal short.

The total noise contribution of the input line components is 2.1°K. This includes noise generated by losses in the waveguide to coaxial line transition, the vacuum seal, and the ⅞-in. D coaxial line feeding the maser (SPS 37-39, Vol. III, p. 83). The equivalent input noise temperature of the TWM is predicted by adding the maser noise temperature (based on Table 7) and the noise contributed by the input line components. Fig. 70 is a graph showing predicted and measured values for the Venus DSS TWM. Errors at 2325 and 2350 Mc are caused by input mismatch.

Laboratory evaluation of the TWM has made use of a WR 430 waveguide termination at liquid helium tem-

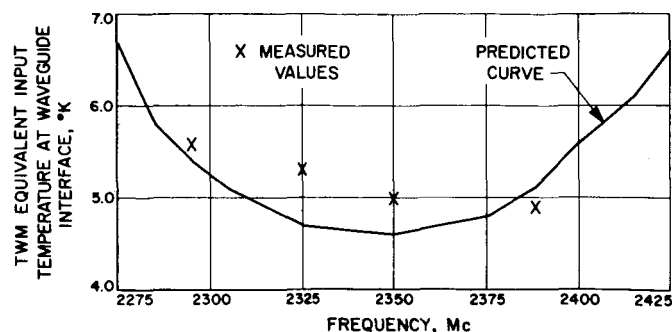


Fig. 70. TWM equivalent input temperature

perature (4.2°K). Fig. 71 is a sketch showing losses which result in a reference load temperature of 6.2°K at the ambient waveguide flange.⁵

⁵Stelzreid, C. T., private communication.

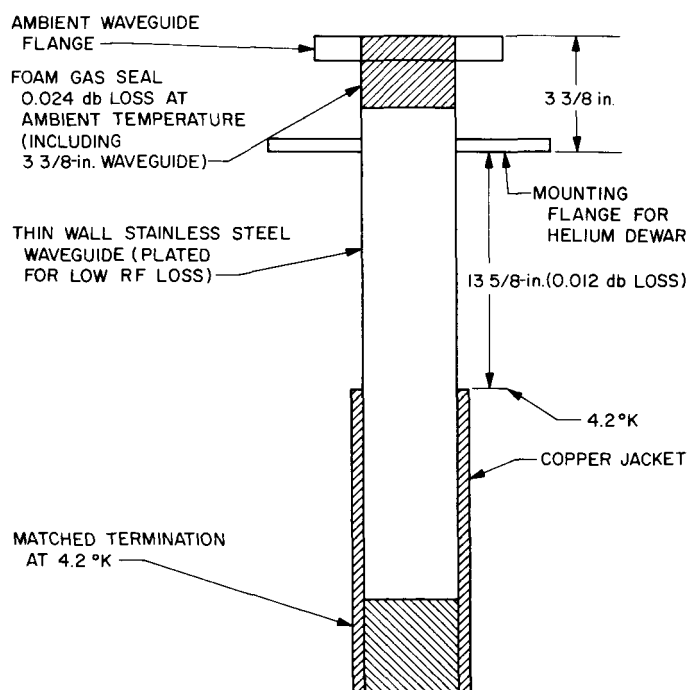


Fig. 71. Liquid-helium-cooled waveguide termination

A system block diagram for the temperature evaluation is shown in Fig. 72. Fig. 73 is a recording of total system noise power which shows the resolution obtained by hav-

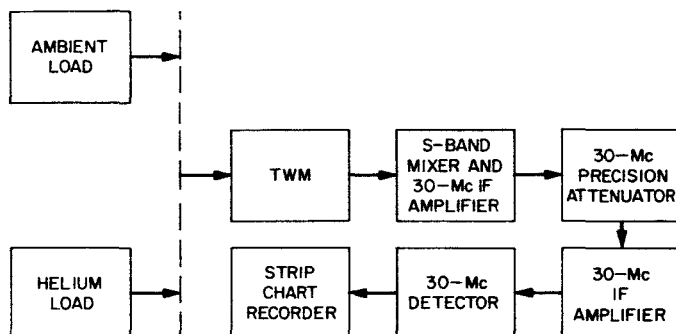


Fig. 72. System temperature evaluation block diagram

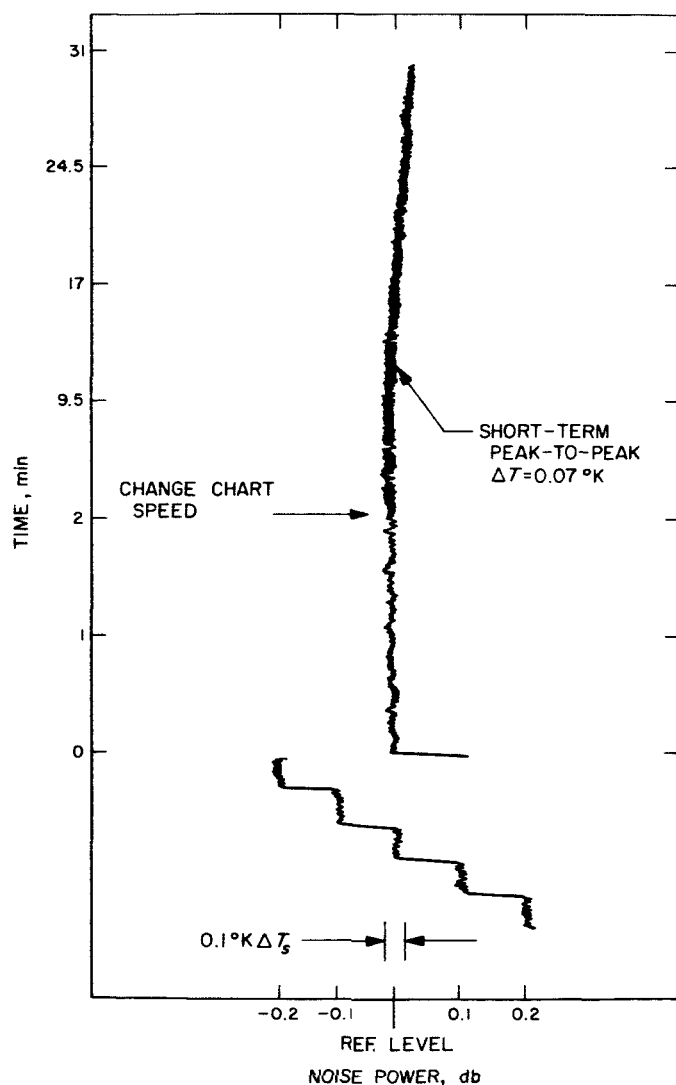


Fig. 73. Total system noise power

ing a very low system temperature and good short-term stability. A precision attenuator is used at the 30-Mc IF frequency to measure the change in system noise power when changing from an ambient load to the 6.2°K load. Table 7 shows contributions to the system temperature at 2388 Mc. The power change measured when switching loads was 14.08 db. This represents a total system noise temperature of 11.8°K.

Table 8. System temperature contributions

System	Temperature, °K
Liquid-helium-cooled termination	6.2
Waveguide connecting TWM to cooled termination	0.35
Receiver following TWM	0.35
TWM equivalent input temperature at waveguide interface	4.9
Total	11.8

L. Venus Deep Space Station R&D Cone Calibration

T. Otoshi and C. T. Stelzreid

For absolute antenna temperature calibrations by the Y-factor method, the total noise power received from the antenna is compared to the total noise powers received from two thermal noise standards. To accurately translate these noise powers (or effective noise temperatures) from one reference point in the measurement system to another, it is necessary that the transmission line loss between reference points be known. In addition, reflection coefficients of the transmission lines, noise sources, and receiver must be known in order to account for effects due to mismatch.

This report presents a description of changes made on the waveguide system for the Venus DSS R&D Cone and also results of insertion loss and reflection coefficient measurements made on the cone transmission lines during May, 1966. Results of similar measurements made during February, 1965 have been reported in SPS 37-33, Vol. III, pp. 65-67.

1. Cone RF Instrumentation

The RF instrumentation block diagram for the Venus DSS R&D Cone has been changed as shown in Fig. 74.

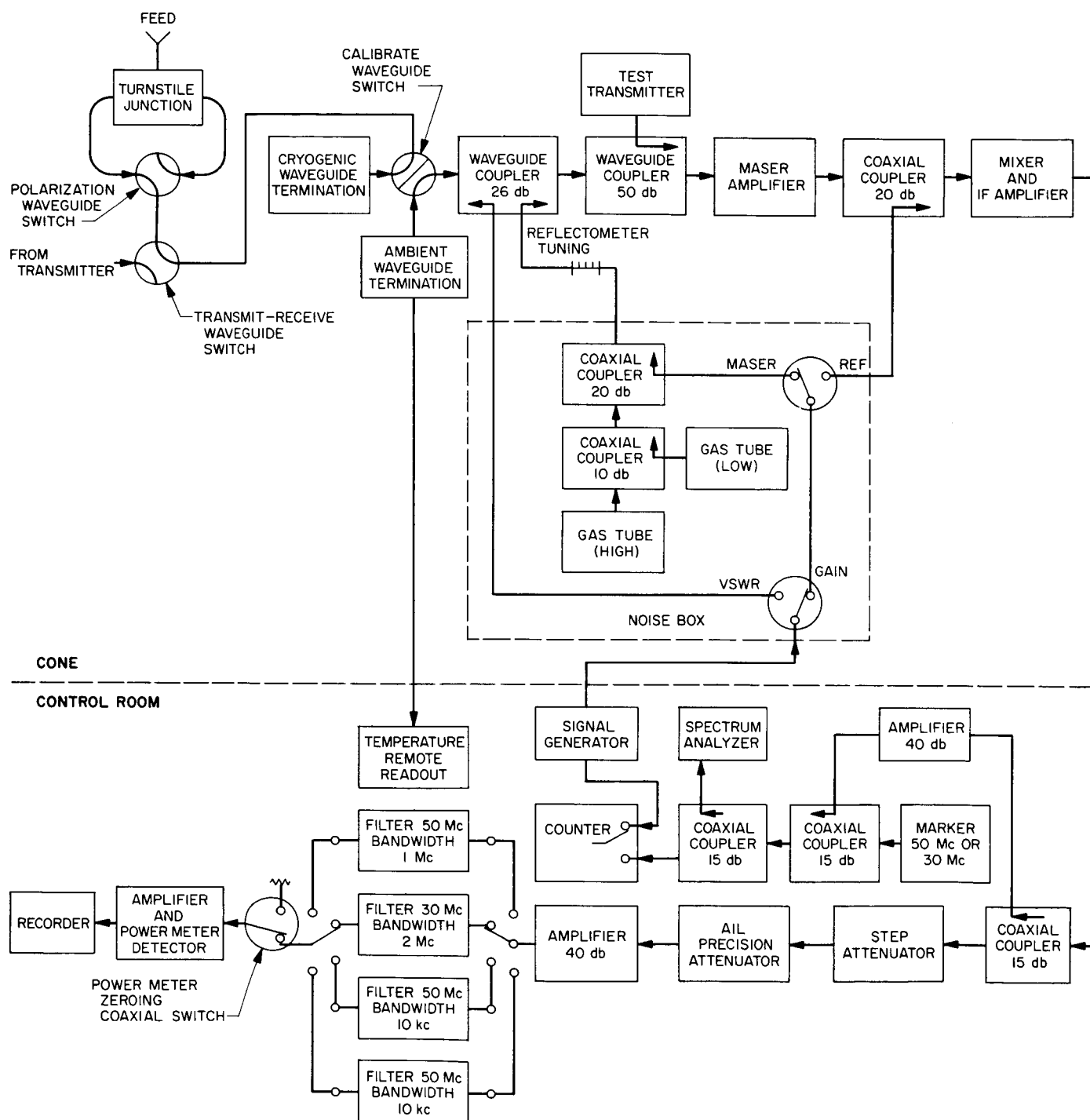


Fig. 74. Venus DSS R&D cone RF instrumentation block diagram

Fig. 75 is a photograph of the cone interior. The instrumentation provides for remote measurements of waveguide load reflection coefficients, system noise temperature measurements, and maser gain. It also provides calibration for AGC curves, radio sources, and antenna gain measurement.



Fig. 75. R&D cone waveguide system, partial view

The noise box is mounted on the cone wall instead of in the maser package so that the maser can be removed for servicing without disturbing the RF calibration system. The instrumentation is patterned after the Mars DSS listening cone (SPS 37-38, Vol. IV, p. 188). The cones are now directly interchangeable between the Mars and Venus Deep Space Stations for possible future experiments such as antenna gain measurements.

Fig. 76 is a block diagram of the RF calibration system for the Venus DSS R&D Cone. The transmission lines on which reflection coefficient and insertion loss measurements were made may be seen in this figure. The receiver input reference plane, defined to be the output flange of

the 26-db coupler, is one of the reference points to which noise temperatures will be referred. This reference plane was previously defined to be the input to the 26-db coupler in the SPS 37-33, Vol. III. The antenna output reference plane is defined as the input to the circular waveguide rotary joint preceding the turnstile junction (see Flange 2 in Fig. 76).

The ambient and cryogenic load noise sources are the thermal noise standards for this cone. The cryogenic noise source is a liquid-nitrogen-cooled termination assembly (Model SR 8135, SN004) fabricated by the Maury Microwave Corporation. Details of this load were described in SPS 37-31, Vol. III, pp. 283-284. The ambient load is a termination assembly which has: (1) good heat sinking of the termination element to the copper waveguide walls and (2) a digital ambient temperature readout from a thermometer imbedded in the copper heat sink. This waveguide assembly has been filled with polyfoam to prevent gas convections from creating possible temperature differentials in the termination assembly.

2. Reflection Coefficient Measurements

For noise temperature measurement mismatch error analysis, it is necessary to know the reflection coefficients of the transmission lines which connect antenna and microwave waveguide termination noise sources to the receiver input. It is also necessary to know the reflection coefficients of the antenna, termination noise sources, and the receiver measured (1) directly and (2) as seen through the transmission lines. These terms and transmission line reflection coefficients are defined as follows:

$\Gamma_A, \Gamma_B, \Gamma_C$ = voltage reflection coefficient of the antenna, ambient load, and cryogenic load, respectively, as measured directly at the respective reference planes (Fig. 76).

$\Gamma_{2A}, \Gamma_{2B}, \Gamma_{2C}$ = voltage reflection coefficient of the antenna, ambient load, and cryogenic load, respectively, as measured at the receiver reference plane (viewing through the respective transmission lines) (Fig. 76).

$\Gamma_{1A}, \Gamma_{1B}, \Gamma_{1C}$ = voltage reflection coefficients of the receiver as measured at the antenna, ambient load, and cryogenic load reference planes (viewing through the respective transmission lines) (Fig. 76).

Γ_R = voltage reflection coefficient of the receiver as measured at the receiver reference plane (Fig. 76).

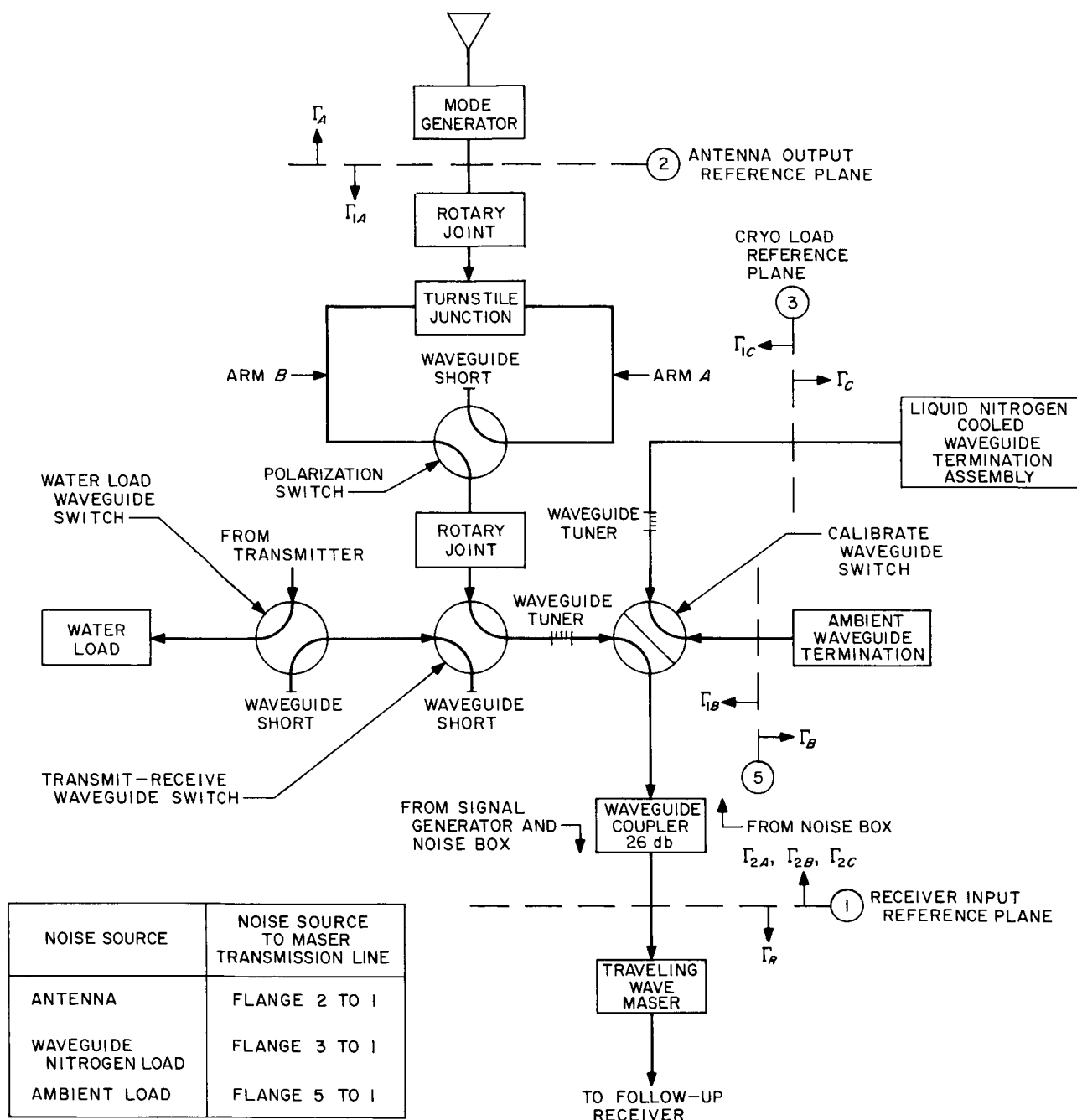


Fig. 76. Venus DSS R&D cone RF calibration system

- a_{11} = voltage reflection coefficient of the antenna transmission line as measured at the antenna reference plane with a matched load on the receiver reference plane flange.
- a_{22} = voltage reflection coefficient of the antenna transmission line as measured at the receiver reference plane with a matched load on the antenna reference plane flange.
- $(a_{22})_{IL}$ = voltage reflection coefficient of the antenna transmission line as measured at the receiver reference plane with a circular waveguide-to-WR 430 transition and matched WR 430 load assembly placed on the antenna reference plane flange (insertion loss measurement configuration).
- b_{11} = voltage reflection coefficient of the ambient load transmission line as measured at the ambient load reference plane with a matched load on the receiver reference plane flange.
- b_{22} = voltage reflection coefficient of the ambient load transmission line as measured at the receiver reference plane with a matched load on the ambient load reference plane flange.
- c_{11} = voltage reflection coefficient of the cryogenic load transmission line as measured at the cryogenic load reference plane with a matched load on the receiver reference plane flange.
- c_{22} = voltage reflection coefficient of the cryogenic load transmission line as measured at the receiver reference plane with a matched load on the cryogenic load reference plane flange.

If the physical temperature of the ambient load transmission line is the same as the effective noise temperature of the ambient load, then the Γ_{1B} , b_{11} , and b_{22} reflection coefficients do not have to be measured.

Table 9 presents a complete list of all reflection coefficients required for calculations of mismatch errors in antenna noise-temperature calibrations for the Venus Cone linear polarization (LP) and circular polarization (CP) configurations on the ground and also when mounted on the

85-ft paraboloid. Those reflection coefficient values which were measured at 2388 and 2295 Mc are presented in this table.⁶ The tolerances shown represent the accuracy limits of the measured reflection coefficients. A precision WR 430 waveguide reflectometer was used for the reflection coefficient measurements.

Reflection coefficient measurements for the antenna lines were limited to measurements looking into the transmission lines at the receiver reference plane. These reflection coefficients were measured with the antenna in both CP and LP configurations. Only the amplitudes of the reflection coefficients were measured.

For maximum accuracy in defining noise temperatures at the antenna reference plane for the various antenna noise-temperature measurement configurations, all of the reflection coefficients (both amplitude and phase) listed in Table 9 should be measured. However, in the time available, it was not considered profitable to measure reflection coefficients looking into the antenna transmission lines at the antenna reference plane. These measurements require special transitions which were not readily available and the employment of special measurement techniques which have not been fully analyzed at the present time.

It is possible to calculate some of the unmeasured reflection coefficients by assuming that for a low-loss transmission line $|a_{11}| \simeq |a_{22}|$. The maximum and minimum values of $|\Gamma_{1A}|$ can then be calculated from $|a_{11}|$ and $|\Gamma_R|$. If this assumption is made, the antenna noise temperature measurement uncertainty will be increased.

3. Insertion Loss Measurements

Insertion loss measurements for the antenna lines were restricted to the antenna line in the LP configuration due to the difficulty of making measurements of the antenna lines in the CP configuration. One method for making the latter measurements would have been to use a special CP-to-LP transition, such as an orthomode transducer or a turnstile junction on the input to the circular rotary joint (Flange 2). The effects of the losses and mismatch errors of the special transition would have to be analyzed for this measurement configuration.

At the present time, it is assumed that the total antenna line loss is the same for the CP configuration as for the

⁶R. Haag participated in the reflection coefficient and insertion loss measurements.

Table 9. Summary of reflection coefficient measurements for Venus DSS R&D cone noise temperature system

Antenna-related parameters							
Voltage reflection coefficient symbol	Input/load flanges (Fig. 76)	Load	Polarization (shorts)	Turnstile junction arm	Measured voltage reflection coefficient amplitude		Comments
					2295 Mc	2388 Mc	
α_{22}	①/②	Circular WG sliding load	CP	A	0.1050 ± 0.0050	0.0140 ± 0.0007	
α_{22}	①/②	Circular WG sliding load	CP	B	0.1179 ± 0.0050	0.0088 ± 0.0007	
α_{22}	①/②	Circular WG sliding load	LP	A	0.1087 ± 0.0050	0.0290 ± 0.0010	
α_{22}	①/②	Circular WG sliding load	LP	B	0.1178 ± 0.0050	0.0251 ± 0.0025	
$(\alpha_{22})_{IL}$	①/②	Circular WG-to-WR 430 transition and WR 430 sliding load	LP	A	0.0093 ± 0.0035	0.0282 ± 0.0025	Configuration for insertion loss measurements
$(\alpha_{22})_{IL}$	①/②	Circular WG-to-WR 430 transition and WR 430 sliding load	LP	B	0.0049 ± 0.0035	0.0309 ± 0.0026	Configuration for insertion loss measurements
α_{11}	②/①	WR 430 sliding load	CP	A			
α_{11}	②/①	WR 430 sliding load	CP	B			
α_{11}	②/①	WR 430 sliding load	LP	A			
α_{11}	②/①	WR 430 sliding load	LP	B			
Γ_{2A}	①/②	Mode generator-horn assembly and free space	CP	A	0.0841 ± 0.0040 0.0750 ± 0.0040 (See footnote a)	0.0122 ± 0.0010	Noise temperature measurement configuration for cone on the ground
Γ_{2A}	①/②	Mode generator-horn assembly and free space	CP	B	0.1059 ± 0.0045 0.0944 ± 0.0045 (See footnote a)	0.0075 ± 0.0005	Noise temperature measurement configuration for cone on the ground
Γ_{2A}	①/②	Mode generator-horn assembly and free space	LP	A	0.1585 ± 0.0050 0.1496 ± 0.0050 (See footnote a)	0.0339 ± 0.0010	Noise temperature measurement configuration for cone on the ground
Γ_{2A}	①/②	Mode generator-horn assembly and free space	LP	B	0.1778 ± 0.0055 0.1679 ± 0.0055 (See footnote a)	0.0299 ± 0.0010	Noise temperature configuration for cone on the ground
Γ_{2A}	①/②	Mode generator-horn assembly, subreflector and free space	CP	A			Noise temperature measurement configuration for cone on 85-ft dish
Γ_{2A}	①/②	Mode generator-horn assembly, subreflector and free space	CP	B			Noise temperature measurement configuration for cone on 85-ft dish
Γ_{2A}	①/②	Mode generator-horn assembly, subreflector, and free space	LP	A			Noise temperature measurement configuration for cone on 85-ft dish
Γ_{2A}	①/②	Mode generator-horn assembly, subreflector and free space	LP	B			Noise temperature measurement configuration for cone on 85-ft dish
Γ_{1A}	②/①	Maser assembly	CP	A			
Γ_{1A}	②/①	Maser assembly	CP	B			

*Assembly inside basket was rotated for maximum and minimum reflection coefficients.

*Assembly inside basket was rotated for maximum and minimum reflection coefficients.

Table 9. (Cont'd)

Antenna-related parameters (cont'd)							
Voltage reflection coefficient symbol	Input/load flanges (Fig. 76)	Load	Polarization (shorts)	Turnstile junction arm	Measured voltage reflection coefficient amplitude		Comments
					2295 Mc	2388 Mc	
Γ_{1A}	②/①	Maser assembly	LP	A			
Γ_{1A}	②/①	Maser assembly	LP	B			
Γ_A	②	Mode generator-horn assembly, and free space				0.030 ± 0.003	Data obtained from D. Bathker
Γ_A	②	Mode generator-horn assembly, subreflector, and free space				0.030 ± 0.008	Data obtained from D. Bathker
Cryogenic load related parameters							
ϵ_{22}	①/③	WR 430 sliding load			0.1116 ± 0.0050	0.0021 ± 0.0020	
ϵ_{11}	③/①	WR 430 sliding load			0.1122 ± 0.0045	0.0018 ± 0.0010	
Γ_{2C}	①/③	Cryogenic load					
Γ_{1C}	③/①	Maser assembly (maser on)				0.0188 ± 0.0010	
Γ_{1C}	③/①	Maser assembly (maser off)				0.0295 ± 0.0010	
Γ_C	③	Liquid nitrogen-cooled WR 430 termination (MMC SR 8135 SN 004)			0.0355 ± 0.0015	0.0100 ± 0.0030	
Ambient load related parameters							
Γ_{2B}	①/⑤	Ambient load			0.1496 ± 0.0050	less than 0.0032 ± 0.0020	
Maser assembly							
Γ_R	①	Maser assembly			0.079	0.045 ± 0.015	Measured by R. C. Clauss

LP configuration. This assumption is valid only if the matches and total losses of the turnstile junction were identical in either CP or LP configurations. It is felt that the error due to making the above assumption is less than the error which would result in a CP configuration line loss measurement.

The procedure used for insertion loss measurement for the antenna line in LP configuration is given as follows:

- (1) Remove the horn and mode generator assembly.
- (2) Place linear shorts on the turnstile junction.
- (3) Place a well-matched (less than 1.02 VSWR) circular waveguide-to-WR 430 transition on the input to the circular waveguide rotary joint (reference Flange 2). The diameters of the circular waveguides at the mating flanges must be identical.
- (4) Disengage the basket drive mechanism. (Basket supports the polarization switch and turnstile junction assembly.)
- (5) Operate the polarization switch for transmission through the antenna line via Arm A.
- (6) Terminate the circular-to-WR 430 transition with a WR 430 sliding load and place a WR 430 reflectometer assembly on the receiver input reference flange (Flange 1).
- (7) Rotate the assembly inside the basket until the best match is obtained. Record the reflection coefficient measured.
- (8) Remove reflectometer and sliding load assemblies. With the basket still aligned in the position obtained in Step 7, measure the insertion loss of the antenna line between Flange 1 and Flange 2 shown in Fig. 74.

- (9) Operate the polarization switch for transmission through the antenna line via Arm B and repeat steps 6 to 8.

Attenuation is the insertion loss which would be measured if the input and output waveguide heads of the insertion loss measurement system were perfectly matched. The attenuation of the antenna line is obtained by subtracting the attenuation of the circular waveguide-to-WR 430 transition from the total measured attenuation.

Attenuations for the antenna line via Arms A and B are summarized in Table 10. The dissipative attenuation values shown in the table were obtained by subtracting out the reflective attenuation component from the at-

tenuation value. Each attenuation value listed on the Table 10 represents the average of a minimum of 10 measurements. A total probable-error (pe) analysis has not been made for these attenuation values at this time. However, the total probable error is estimated to be of the order of ± 0.002 db at 2388 Mc and ± 0.004 db at 2295 Mc.

A comparison of the 2388-Mc attenuation values with those measured during February 1965, indicates that recently measured attenuation values are higher. This increase in attenuation can be partially attributed to the change in location of the receiver reference plane to the output of the 26-db coupler instead of the coupler input.

Table 10. Summary of attenuation values for Venus DSS R&D cone noise temperature system

Transmission line	Input/output flange (Fig. 76)	Polarization (shorts)	Turnstile junction arm	2295 Mc			2388 Mc		
				Transmission line voltage reflection coefficient	Attenuation, db	Dissipative attenuation, db	Transmission line voltage reflection coefficient	Attenuation, db	Dissipative attenuation, db
Antenna	①/②	LP	A	0.1087			0.0290	0.1297	0.1261
Antenna	①/②	LP	B	0.1178	0.1554	0.0947	0.0251	0.1244	0.1217
Cryogenic load	①/③			0.1116	0.0901	0.0351	0.0021	0.0497	0.0497

The transmission line voltage reflection coefficient values were obtained from Table 9.
 The attenuation for the antenna line case was obtained by subtracting the loss of the circular waveguide-to-WR 430 transition from the total measured insertion loss.
 All insertion loss measurements were made with the AC ratio transformer system.

References

1. Blackman, R. B., and Tukey, J. W., *The Measurement of Power Spectra*, Dover Publications, Inc., New York, N.Y., 1958.
2. Baugh, H. W., "Mod II Ranging Equipment," Technical Report 32-337, Jet Propulsion Laboratory, Pasadena, California, September 15, 1962. See also SPS 37-11, Vol. III and succeeding issues.
3. W. H. Higa, "Noise Performance of Traveling Wave Masers," Technical Report No. 32-506, Jet Propulsion Laboratory, Pasadena, California, January, 1964.

N66 38569

IV. Deep Space Station Engineering and Operations

A. Flight Project Support

J. Orbison

1. Surveyor I Project

Prior to the successful launch of *Surveyor I* on May 30, 1966, personnel at the Pioneer Deep Space Station (DSS), in cooperation with Hughes Aircraft personnel, had engaged in intensive preparation (SPS 37-27, Vol. III, through SPS 37-39, Vol. III). In the fall of 1965, the S-band system was relocated from the annex building used during the *Mariner IV* mission to the permanent location in the east wing of the control building. Comprehensive tests and personnel training continued until the countdown for launch standby. The *Surveyor* T-21 test model was delivered to Goldstone twice, the second time remaining until June 7, 1966, and was used to test all ground operations, including the Space Flight Operations Facility in Pasadena.

Surveyor I landed on the Moon at 23:17:37 PDT, June 1, and was under continuous surveillance and con-

trol (Fig. 1) by the Pioneer DSS. During passes one, two, and three, the Echo DSS tracked the spacecraft as backup command transmission, while the Mars 210-ft antenna tracked as a backup receive function. Microwave circuits integrated the three stations into a single unit. Following the successful soft landing, the Pioneer DSS participated in postlanding picture-taking and experiments. During the first seven postlanding passes, the Pioneer DSS commanded and received data on the following:

- (1) Transmission of the first ten 200-line TV pictures
- (2) Transmission of approximately 4000 600-line pictures
- (3) The gas jet surface dust experiment
- (4) The TV pictures of the star Sirius
- (5) The lunar surface color picture experiment

A total of over 10,000 pictures was received at the Pioneer DSS before the end of the lunar day on June 16.



Fig. 1. Surveyor ground operations equipment control room

2. Pioneer VI Project

The *Pioneer VI* spacecraft, which was launched on December 16, 1965, continues to be tracked by the Echo DSS. During the second pass, a Type II orientation was performed to position the spacecraft antenna relative to the Earth. Additional Type II orientations were performed in June. After the thirtieth pass, tracking has been on a three-to-five-day week basis. Late in May, daily tracking was reduced to approximately eight hours because of the increased noise factor and parity error rates prevalent during the near-horizon attitudes.

The Mars DSS has tracked the *Pioneer VI* spacecraft for system tests and pointing accuracy of the antenna. Initially, all tracking was performed with the R&D receiver. The reported use of a Goldstone duplicate

standard (GSDS) maser with the R&D receiver (SPS 37-38, Vol. III, p. 86) was in error. The maser used at that time — and currently in use — was a JPL development model, tuneable between 2295 to 2388 MHz, operating in a helium cryogenic closed-cycle refrigeration system at a temperature of 4.4°K (SPS 37-39, Vol. III, p. 79). Late in June, the *Pioneer VI* spacecraft was tracked by Mars DSS with the GSDS receiver; transmission and command support was provided by the Echo DDS.

3. Lunar Orbiter Project

Final preparations for the *Lunar Orbiter* July launch and tracking were in progress at the Echo DSS during the last week of June. Culminating months of integrated system testing concurrent with the *Pioneer VI* mission (SPS 37-35, Vol. III through SPS 37-39, Vol. III),

all Echo DSS operations personnel participated in a series of comprehensive training exercises. Three major areas were covered: the 3.2 and 3.3 series, including DSS mission procedural exercises; the 4.4 series of DSS simulation exercises, followed by a series of practice long countdown procedures; and the 5.1 series of operational readiness tests.

The multiple mission support area (MMSA) equipment is in the process of installation at the Echo Station for full, simultaneous support to the *Lunar Orbiter* and *Pioneer* missions. This equipment will provide duplicate analog instrumentation and associated multichannel tape recording subsystems, and will allow two stations to track different spacecraft simultaneously, while permitting one station to record the received data from both.

4. Mariner IV Mission

The Mars 210-ft antenna, currently using JPL R&D receiving equipment, became operational as a receiving antenna in March 1966, and, in conjunction with the Venus DSS, has successfully continued the tracking of the *Mariner IV* spacecraft. Venus DSS provided the up-link command capability through use of its 100-kw transmitter, and the necessary signal integration for receiving, at below and near threshold levels, Mars-tracked *Mariner IV* during the Sun occultation experiment and subsequent tracking.

Mars DSS personnel, using the station digital instrumentation subsystem, assisted with the operation of the antenna servo drive and tracking predictions. On Sunday, June 5, commands were transmitted to and received by the spacecraft, thus establishing two-way lock resulting in two-way doppler. Additionally, telemetry and spectrograms were received from *Mariner IV*, approximately 188 million miles distant, and were forwarded to JPL for analysis.

B. Facility Construction and Equipment Installation

J. Orbison

1. Mars Deep Space Station

Installation of the S-band system in the second-floor control room of the antenna pedestal is progressing.

Currently installed are the antenna servo, digital instrumentation, analog instrumentation, frequency and timing, recording, and system monitor console subsystems (Fig. 2). These subsystems were used with the JPL R&D maser for backup tracking of the *Surveyor I* passes and postlanding. All recorded data were forwarded to JPL for analysis. Also installed are the system junction module, the maser/parametric amplifier ground controls, and the microwave switching units. Full operational testing of these units will be performed during complete system testing. The transmitter installation is nearing completion and partial testing is in progress.

The master equatorial antenna pointing subsystem arrived at the Mars DSS just prior to the dedication ceremonies on April 29, and was thoroughly checked before installation in the room atop the instrument tower.

2. Echo Deep Space Station

The intersite microwave link between the Mars DSS and the Echo DSS is complete and in operation. Installation of the telephone microwave by the California Interstate Telephone Company is progressing and is scheduled for a fall completion.

The S-band system microwave control racks were relocated early in June in preparation for the installation of the multiple mission support area (MMSA) equipment in the Echo DSS control room.

Two FR-1400 seven-channel magnetic tape recorders were received in May and are currently undergoing operational tests.

3. Pioneer Deep Space Station

The Cebreros DSS equipment has been shipped from the Pioneer DSS to Spain, where further assembly and testing will be accomplished. Most of the Cebreros DSS personnel had also left Goldstone by the end of June.

Remodeling of the generator building continues, with reinstallation of two 150-kw generators and switchboards in progress (Fig. 3). The 300-kw diesel generator mounted outside the generator building (SPS 37-39, Vol. III, p. 85) was used as the "U" bus prime power during the *Surveyor I* mission, with commercial power backup.



Fig. 2. Mars antenna S-band system control room

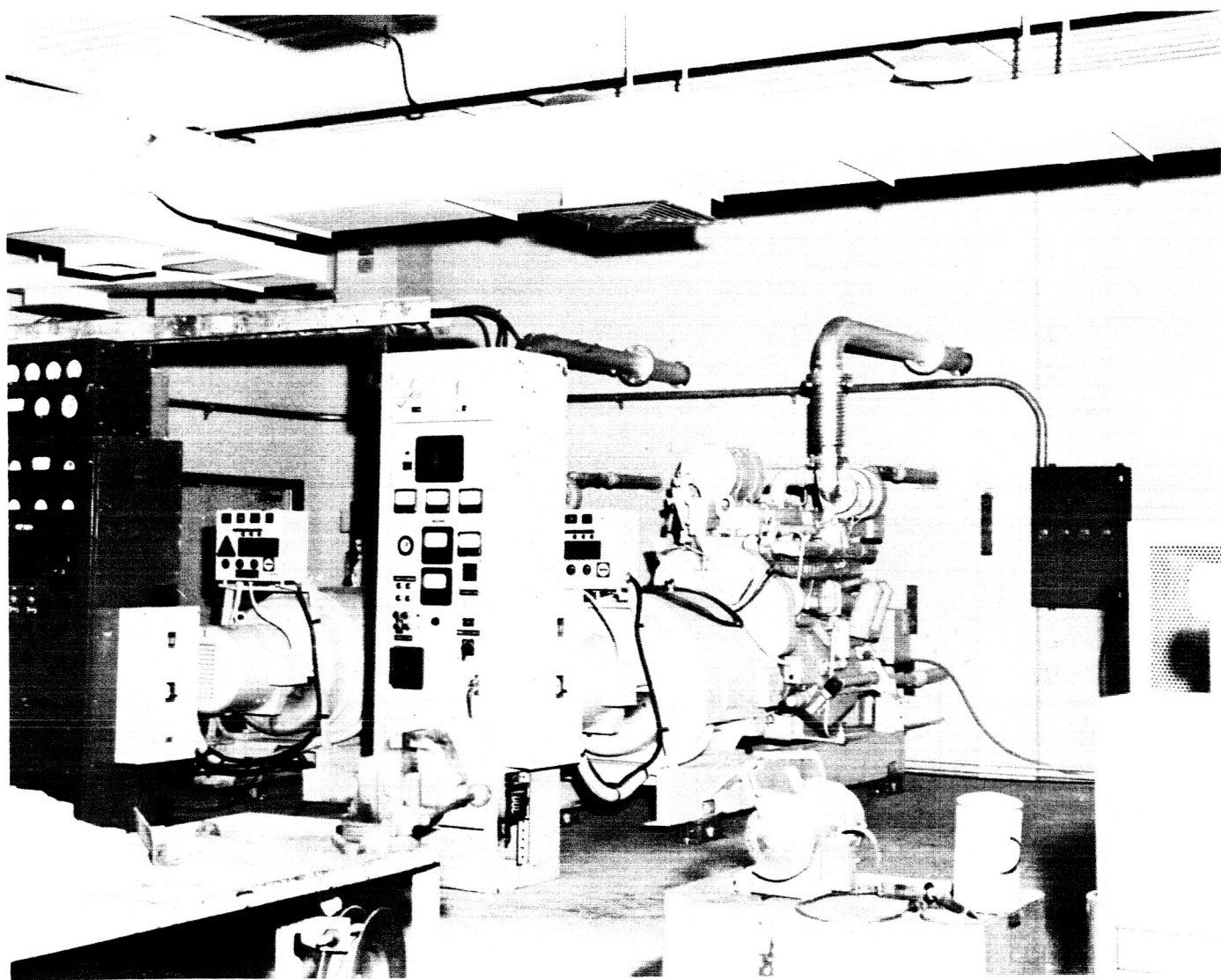


Fig. 3. Pioneer Deep Space Station generator building interior

4. Venus Deep Space Station

During the last week in June, construction of G-60, the laboratory and office building, was begun.

C. Venus DSS Operations

E. B. Jackson, M. A. Gregg, A. L. Price, and R. M. Gosline

1. Experimental Activities, E. B. Jackson

The only experiments conducted at the Venus Deep Space Station (DSS) during the period of April 14–June 13, 1966 were those involving reception of the *Mariner IV* spacecraft in cooperation with the Mars DSS. Maintenance, modifications, upgrading, and cleanup were performed, with the station operating on a regular day-shift basis. Activities are summarized in Table 1.

Table 1. Summary of Venus DSS activity
(April 14–June 13, 1966)

Activity	Hours	Percent
Mariner experiments		
Transmission, reception, and testing	55	3.76
Testing, calibration, construction, and scheduled maintenance	1385	94.61
Holidays and scheduled nonoperating time	24	1.63
Total	1464	100.00

The cooperative tracking of *Mariner IV* took place on May 3, May 21, and June 5, 1966. On each occasion, telemetry was recorded on magnetic tape at the Mars DSS, and spectrograms were taken at the Venus DSS. A specially adjusted telemetry decom unit at JPL was successful in recovering telemetry data from each of the above tracks, working from the magnetic tape recordings.

Various changes made in the equipment configuration at the Venus DSS during this period are detailed in the following paragraphs.

2. Subsystem Operation, M. A. Gregg and A. L. Price

a. 100-kw transmitter. The R&D cone was not on the antenna during this time, and no tests were run in the cone storage area. The klystron was removed from the R&D transmitter so that the cone could be shipped to JPL for tests (see p. 93).

b. Mariner 100-kw transmitter. The *Mariner* cone was on the antenna and was used for testing, checkout, and transmitting to the spacecraft. The *Mariner* transmitter amplifier No. 2 has accumulated a total of 286.9 filament hours and 106.6 beam hours with no failures in either the amplifier or the system.

c. Receiving systems. The only scheduled receiver operation was that of the monthly *Mariner* spacecraft track. This was accomplished by feeding the 455-kHz signal from the Mars *Mariner* receiver, via microwave, into the AM channel of the Venus S-band receiver. Throughout the remainder of this period, all receiving systems were shut down for overhaul and system improvement. During this shut-down period, several equipment failures occurred. Failures in the digital local oscillator subsystem power-on function and in a digital card in the clock display block have been repaired, and operation is now normal. One module failure and one power supply failure occurred in the S-band receiver. Both units were returned to JPL for repair or modifications.

3. System Improvements and Modifications

M. A. Gregg, A. L. Price, and R. M. Gosline

a. 100-kw transmitters. During most of this period, the systems were shut down for maintenance and modifications. The following major modifications were performed at this time:

- (1) To accommodate the 400-kw klystron tube under construction, the water system of the 85-ft antenna was modified to provide a flow capability of 400 gal/min. To meet this requirement, new pumps were installed, both at the heat exchanger and on the antenna, thus allowing the original pumps to be used to greater advantage for the rectifier and the transformer and the dc water load.
- (2) The water rotary joint was removed and cleaned, and all O-ring seals and carbon-face seals were replaced.
- (3) A new water filter was installed on the antenna to protect the rotary joint from foreign matter in the return water line from the cone.
- (4) Wiring of the auxiliary motor generator and the 1-Mw synchronous motor was modified to enable both units to be run independently of the transmitter system controls and water pumps. The synchronous motor can thus remain synchronized

to the incoming power line, with all safety circuits still active, eliminating some of the frequent starts to which the synchronous motor had been subjected in the past.

- (5) The coupling coolant controls were modified so that, if the cooling system is not already on, the cooling for the coupling begins automatically whenever the synchronous motor is started.
- (6) The Limit-Amp annunciators for the rectifier vault were removed from the lock-out circuits of the synchronous motor and installed in the high-voltage circuit only.

b. Receiving systems. An overall receiver cabling clean-up was conducted. This included the removal of numerous unused cables, as well as the addition of four long-run cables from the control room to the antenna cone. This addition provides complete separation between the 2388-MHz receiver and the *Mariner* receiver. No cable used on one system is needed in the other.

(1) *S-band receiver.* The S-band receiver was modified for use in bistatic radar experiments as well as the usual monostatic experiments. Selection is made with a push-button on the receiver control panel. In the bistatic configuration, 455 kHz from a double-conversion, open-loop S-band receiver (2388 MHz) at the Mars DSS is fed into the reference channel and the AM channel of the Venus DSS S-band receiver. Remote monitoring of the Mars receiver local oscillator drive level and power supply voltage has been provided on the Venus S-band receiver. Remote control of the Mars receiver gain has also been provided.

All the Venus S-band (2388-MHz) cone-mounted equipment has been returned to JPL for repair or modification.

(2) *Mariner receiver.* All modifications to the *Mariner* receiver have been completed. These include the addition and relocation of modules and the recabling of the receiver signal and power paths. In its present configuration, the *Mariner* receiver provides one open-loop channel. The 2295- to 30-MHz converter power supply was also modified, eliminating the need for remote control of the on-off function.

(3) *X-band receiver.* The X-band signal generator has been returned to JPL for testing and modification. As a

safety precaution, the 8448- to 30-MHz converter was removed from the 30-ft antenna to prevent possible damage during the forthcoming antenna overhaul. It is planned to use the converter in a test setup to check out the X-band maser during this time.

(4) *Central frequency synthesizer (CFS).* A new CFS has been received and installed at the Venus DSS (p. 57). This unit, which will replace the interim CFS as soon as system checkout has been completed, provides 17 different reference frequency outputs. All the outputs, including the 455 kHz, are synthesized from the rubidium frequency standard. The rubidium frequency standard standby battery life test has been completed. It was found that the battery will supply power for proper operation of the frequency standard for approximately 90 hr.

(5) *Programmed local oscillator (PLO).* Other than external cabling changes, no modifications were made to the PLO.

c. Digital section. A number of improvements were made during the station shutdown period. The most important was the underfloor cable cleanup and inter-rack cabling in the data system. All unused data cables were removed and remaining cables rerouted and securely clamped, greatly improving the system appearance and reliability. Cables to the Datex readout rack in the 85-ft pedestal were also rerouted.

Other improvements to the data system included the addition of relay contacts in series with the BRPE punch solenoids to provide burnout protection when the logic power is turned off. Additional output connectors were provided for the binary-coded decimal (BCD) time output, and cables supplying BCD time were run to the Scientific Data Systems (SDS) 930 computer and to the angle tape processor. Low impedance line drivers capable of furnishing 50 ma of current into 2000 pf line capacitance were provided. A doppler coax patch panel was installed, enabling either doppler counter to be switched at the doppler selector panel to the output of the patch panel, which, in turn, selects one of the six incoming coax lines (two from the S-band receiver, two from the X-band receiver, one from the PLO, and one from the CFS).

Following the re-installation of the azimuth-angle transmitting resolvers, the readouts were adjusted by optically positioning the antenna, using the boresight telescope in the TV package on the Tiefert mountain

collimation tower. The readouts were then adjusted by slipping the repeating resolver until the readouts agreed with previously recorded data corrected for parallax due to the displacement of the telescope from the centerline of the antenna. The resolver was checked to assure that it had been correctly adjusted to the null position. Alignment was then verified by RF and optical comparisons on the near-Venus collimation tower.

The angle tape processor/digital differencing junction (ATP/DDJ) system is being modified to allow use of the same drive tape format as used by the SDS 910 angle positioning system. Because the teletype (TTY) format is difficult for the operator to read directly, a BCD display will be added for time, azimuth, and elevation, as read from tape. All logic modules were removed and tested under controlled temperature conditions.

Several hardware additions were made to the SDS 930. The IBM 1622 card reader/punch and buffer previously located in the computer facility at the Echo DSS was installed, allowing polynomial cards to be processed at the Venus DSS. A full duplex communications buffer was installed providing communication from the Venus SDS 930 to the JPL SDS 930 over the TTY network. Other equipment added included a nine-bit digital-to-analog converter (D/AC) and a Moseley Autograf plotter. The parallel output-parallel input (POT-PIN) chassis was expanded with patch cards, more than doubling the previous capability. Two manual interrupt controls were also provided. Both the SDS 930 and SDS 910 were given a complete checkout and put through a preventive-maintenance program.

Considerable expansion of the software was performed. A card-reproduce program was written to be used with the IBM 1622. The angle-prediction program was modified to allow generation of limited prediction for other antenna locations. A test and troubleshooting program was written to detect and record transient errors in the BCD time output of the data system suspected of causing the spurious tape pulls when tracking with the SDS 910. As a result of this program, at least one trouble with BCD time was located and corrected.

The polynomial-drive tape program was modified to output TTY format for the ATP/DDJ. A utility program was written for the Mod III which samples the output of its A/DC and counts the number of samples falling in each of 40 pre-assigned ranges. The program will be used for statistical analysis of phase-locked loop response and other applications.

D. On-Site Prediction Generation at DSS 72, DSS 61, and DSS 42 During the *Atlas/Centaur 8* Mission

A. L. Berman

1. Desirability of On-Site Prediction Capability

It has always been the prevailing philosophy that real-time spacecraft predictions should generate from the JPL Space Flight Operations Facility (SFOF) and be transmitted via teletype to the DSIF stations. However, past experience has disclosed certain weaknesses in this operation. The most telling of these inadequacies is that, during certain types of launch passes over DSS 72 and DSS 51, it is impossible for SFOF-generated predictions to reach the station before spacecraft rise. Communications frequently become marginal, causing errors in the predictions; in severe cases, predictions failed to reach the station at all, or arrived in totally unusable condition. Since this present system of supplying predictions to the DSIF stations is both cumbersome and costly, alternative methods (such as on-site predictions) were considered.

Subsequently, the decision was made to allow DSS 72 and DSS 61 to generate on-site predictions during the *Atlas/Centaur 8* (A/C 8) mission. (The program was sent to DSS 42 at a later date on an unofficial basis as a possible backup measure.) The A/C 8 appeared to be almost ideally suited for this attempt because:

- (1) SFOF predictions before spacecraft rise would be impossible for the type of launch pass produced over DSS 72 by A/C 8.
- (2) Both DSS 61 and DSS 72 were participating, but on an uncommitted basis.
- (3) The mission had a relatively low priority.

A small Fortran/machine-language prediction program (WTRAJB), suitable for use on the Scientific Data Systems (SDS) 920 computer, was available within the Systems Data Analysis (SDA) group and required only a minimum of modification for use at DSS 72, DSS 61, and DSS 42. The program was designed to accept injection conditions from (1) the Air Force Eastern Test Range (AFETR) in the interranger vector (IRV) format via "torn" paper teletype tape, or (2) either AFETR or JPL via the typewriter. It was planned that AFETR send the parking orbit IRV directly to DSS 72 and the

transfer orbit IRV to the SFOF at JPL; from there it would be automatically rerouted to DSS 42 and DSS 61.

2. Implementation of the WTRAJB Program

During the week of February 21 to 25, the WTRAJB program was checked at DSS 71 for compatibility with the AFETR IRV and with the SDS 920 computer at DSS 71. It was discovered at this time that changes in the AFETR IRV made it totally incompatible with the WTRAJB program. The WTRAJB was reprogrammed at DSS 71 to accept the newly formatted IRV, and the compatibility tests proved successful.

From February 28 to March 4 the program operation was certified at DSS 61, and two digital instrumentation system (DIS) operators and the station analyst were thoroughly trained. During this week, an IRV message was generated at the AFETR and sent to DSS 61 via JPL, and was successfully accepted by the WTRAJB program at DSS 61.

From March 21 to April 8 the WTRAJB program was checked at Ascension Island, and the DIS operator was thoroughly trained. A/C 8 operational readiness tests successfully demonstrated (1) the direct teletype lines from AFETR, (2) the efficiency of DIS operator, (3) the WTRAJB program operation, and (4) the procedures provided by the SDA group concerned with the use of the WTRAJB program at DSS 72 during the A/C 8 mission.

3. WTRAJB Program Results During the A/C 8 Mission

Although the WTRAJB program was used at DSS 72, DSS 61, and DSS 42, the most critical need for the program was at DSS 72. Therefore, a detailed examination of the operations at DSS 72 will yield the most significant information.

a. Operations at DSS 72. The A/C 8 launching from Cape Kennedy was scheduled for April 7, 1966, at 01:00:00 GMT. The preflight nominal trajectory indicated that DSS 72 would have a view period of the parking orbit from 1:20:29 to 1:26:37 GMT, a period of 6.27 min. The nominal injection into parking orbit was to be at 1:11:13.851 GMT; AFETR had indicated that, on the basis of this injection time, DSS 72 could expect the IRV at 1:17:00 GMT and a set of predictions at approximately 1:21:00 GMT, or shortly after rise at DSS 72.

Preparations for use of the WTRAJB began with loading the program on the SDS 920 computer approximately 1 hr before launch. At 00:10:00 GMT, the latest spacecraft frequencies were received from JPL. The nominal injection conditions were already at hand, and at 00:21:00 GMT the program was initialized to generate preflight nominal predictions for the first (parking orbit) and second (transfer orbit) passes over DSS 72. These were completed at 00:50:00 GMT, and the program was deemed to be fully checked and ready for operation. The launch occurred at 01:00:02 GMT, almost exactly on schedule. Similarly, the injection into parking orbit occurred at 01:11:16 GMT, very close to the nominal time. The parking orbit IRV was received at 01:13:00 GMT, and the teletype tape was immediately fed into the computer, which accepted the first message. (The IRV message comes in bursts of three, and the computer will not accept a message unless it is perfect as indicated by the error coding built into the IRV.)

The first lines of predictions were released by 01:15:00 GMT, and the predictions were completed by 01:17:00 GMT. Copies were immediately distributed to the servo and RF operators. On the basis of these predictions, acquisition occurred in a rapid and orderly fashion. The first line of AFETR predictions arrived at 01:20:00 GMT. Although there was a time differential of only 5 min between the WTRAJB predictions and the AFETR prediction, this represents a crucial advantage in attempting to acquire a spacecraft with extremely high angle and doppler rates, such as DSS 72 will frequently encounter. Since the A/C 8 parking orbit was almost nominal, this advantage was minimized. However, had the trajectory been nonstandard, the additional 5 min for the operators to become familiar with the new prediction data could easily have meant the difference between acquiring and not acquiring. The WTRAJB parking orbit predictions appear in Fig. 4, and the AFETR parking orbit predictions are given in Fig. 5. A comparison of these two sets of predictions at 01:23:39 GMT shows the following differences: $\Delta EL = 0.19^\circ$, $\Delta AZ = 1.19^\circ$, $\Delta D1^1 = -960$ cps, $\Delta D2 = 1831$ cps, and $\Delta XA = 9$ cps. These values are well within the accuracies necessary for acquisition.

At 01:45:00 GMT, the transfer orbit IRV was received and entered into the computer. At 01:47:00 GMT, a single line of predictions was output at a (predicted) time of 02:58:42 GMT. Since nominal rise of the transfer orbit was expected at 08:06:31 GMT, A/C 8 was thought to be in Earth orbit. Shortly thereafter, an announcement of an

¹The one-way doppler value D1 depends on the reference ground transmitter frequency (SYNFRQ) used. When the two values of D1 are adjusted to the same SYNFRQ, then $\Delta D1 \approx 915$ cps.

DSIF = 72 DAY = 98 TINJ = 11116.000
 FT = 2295000950. FRQ = 22013658. FK1 = 0.
 X = 1.14800510E 07 Y = -1.66009640E 07 Z = 7.30759000E 06
 DX = 2.00737800E 04 DY = 9.55174000E 03 DZ = -9.81643000E 03
 X = -5.71735838E 03 Y = 2.27137344E 03 Z = 2.22735789E 03
 DX = -3.64380605E 00 DY = -6.23193635E 00 DZ = -2.99205385E 00
 GMT EL AZ D1 D2 XA
 12037 0.01 317.10 944237 893267 22.013146
 12047 0.66 317.88 944430 893653 22.013148
 12057 1.34 318.74 944663 894120 22.013150
 12107 2.05 319.69 944945 894683 22.013153
 12117 2.81 320.76 945285 895364 22.013156
 12127 3.61 321.95 945697 896188 22.013160
 12137 4.47 323.31 946199 897191 22.013165
 12147 5.40 324.85 946813 898420 22.013171
 12157 6.41 326.62 947572 899938 22.013178

Fig. 4. WTRAJB parking orbit predictions

ACNSION

ETR PREDICTS FROM PARKING ORBIT
 ETR PREDICTS 01 FOR DSIF 72 S BAND AC08
 XPONDER FREQ 2295.000950 XMITTER REF FREQ 22.013653
 DRIFT 00.000 STEP SIZE 0500 SYNFRQ 000.000000
 THREE WAY FROM DSIF

CHANGE XMITTER VCO FREQ TO 22.013640 AT 012037
 PRED 01, DSIF 72, 08 APR 66, DAY 098, RT, 00M 00.0S, AC08

H M S	AZ	EL	D1	D2	XA
012037	317112	-000000	9423401	8932252	3145.9
012039	317322	000177	9423919	8933287	3146.4
012059	319012	001520	9428504	8942456	3150.8
012119	321103	003018	9435125	8955700	3157.1
012139	323751	004725	9444853	8975154	3166.4
012159	327202	006714	9459529	9004507	3180.5

Fig. 5. AFETR parking orbit predictions

engine failure confirmed this probability, and the input parameters in the WTRAJB were changed to accommodate near-Earth predictions, which were then run. By 02:00:00 GMT, DSS 72 had a detailed set of predictions for a second pass, beginning at 02:55:32 GMT and ending at 03:01:02 GMT. Preparations for this pass began immediately, and the station was able to successfully acquire with these predictions (Fig. 6). The AFETR predictions (Fig. 7) for this pass began to arrive at 03:00:00 GMT, or approximately 1 min before the end of track! The differences between these two sets of predictions at 02:58:00 GMT are: $\Delta EL = 0.11^\circ$, $\Delta AZ = 0.39^\circ$,

$\Delta D1^2 = -4735$ cps, $\Delta D2 = -761$ cps, and $\Delta XA = -4$ cps. Once again, these differences lie within the accuracies needed for acquisition. The speed with which DSS 72 was able to react to this nonstandard trajectory should be underscored. Within 10 min after injection into transfer orbit, DSS 72 was able to predict a pass within 1 hr (instead of 8 hr), and 13 min later had a detailed set of predictions for this pass. It should be noted that this information would have been available from JPL only at a much later time, and the fact that

*The adjusted (as in Footnote 1) value of $\Delta D1 \approx -380$ cps.

DSIF = 72 DAY= 98 TINJ= 13841.900
 FT = 2295000950. FRQ = 22013658. FK1 = 0.
 X = 1.37290590E 07 Y = 1.28901050E 07 Z = -1.04137830E 07
 DX = -1.80133800E 04 DY = 1.58507600E 04 DZ = -4.31347080E 33
 X = -6.25915893E 02 Y = -5.70575751E 03 Z = -3.17412741E 03
 DX = 7.72884577E 00 DY = -1.47885987E 01 DZ = -1.31474829E 00
 GMT EL AZ D1 D2 XA
 25532 0.08 261.76 953637 912068 22.013236
 25537 0.33 260.92 954109 913012 22.013241
 25542 0.58 260.05 954610 914014 22.013246
 25547 0.84 259.14 955142 915078 22.013251
 25552 1.09 258.21 955706 916206 22.013256
 25557 1.35 257.23 956305 917403 22.013262
 25602 1.61 256.22 956940 918674 22.013268
 25607 1.87 255.17 957614 920022 22.013274
 25612 2.13 254.08 958329 921452 22.013281
 25617 2.39 252.94 958088 922969 22.013289
 25622 2.65 251.76 959892 924578 22.013296
 25627 2.91 250.54 960745 926285 22.013304
 25632 3.17 249.27 961650 928093 22.013313
 25637 3.43 247.94 962608 930010 22.013322
 25642 3.69 246.57 963623 932039 22.013332
 25647 3.94 245.15 964696 934186 22.013342
 25652 4.20 243.67 965831 936456 22.013353
 25657 4.44 242.14 967030 938854 22.013365
 25702 4.69 240.55 968295 941383 22.013377

Fig. 6. WTRAJB transfer orbit predictions

ACNSION

ETR PREDICTS FROM TRANSFER ORBIT

ETR PREDICTS 02 FOR DSIF 72 S BAND

AC08

XPONDER FREQ 2295.000950 XMITTER REF FREQ 22.013658

DGIFT 00.000 STEP SIZE 0500 SYNFRQ 000.000000

THREE WAY FROM DSIF

CHANGE XMITTER VCO FREQ TO 22.013620 AT 025530

PRED 02, DSF 72, 08 APR 66, DAY 098, RT, 00M 00.0S, AC08

H M S	AZ	EL	D1	D2	XA
025530	262170	000030	9494496	9116143	3234.1
025545	259695	000763	9508625	9144400	3247.6
025600	256835	001537	9526010	9179170	3264.3
025615	253630	002322	9546765	9220679	3284.2
025630	250035	003111	9571530	9270209	3307.9
025645	246004	003893	9601001	9329150	3336.2
025700	241498	004652	9635868	9398886	3369.7

Fig. 7. AFETR transfer orbit predictions

DSS 72 was self-sufficient allowed JPL to concentrate on getting predictions to the other stations.

b. Operations at DSS 61. The WTRAJB operations were a complete success at DSS 61. All inputs were received according to schedule, and no difficulties were encountered in the operation of the program. In essence, DSS 61 received the AFETR IRV at 1:44:00 GMT, ran the WTRAJB, did not obtain a view period (and therefore correctly concluded that A/C 8 was in an Earth orbit), made the necessary corrections to the semi-fixed inputs, and then successfully ran predictions showing a pass beginning at 15:44:42 GMT.

c. Operations at DSS 42. As of this time, a complete report of WTRAJB operations at DSS 42 has not been received. However, examination of the actual predictions that were run at DSS 42 and sent back in their data package indicates that no difficulties were encountered in

operating the WTRAJB program and that predictions were successfully generated before the first spacecraft rise.

4. Summary

The WTRAJB on-site prediction program was successfully run by station personnel at DSS 72, DSS 61, and DSS 42, and no difficulties were encountered. Operation of the program at DSS 72 showed that an on-site prediction program could handle both standard and non-standard launch-type passes in a far more responsive and successful manner than could JPL-generated predictions, at the same time allowing JPL to concentrate its efforts on other stations. Finally, the successful WTRAJB operations at DSS 61 and DSS 42 further strengthened the argument that predictions can be successfully generated on site in a relatively routine manner, at least in the non-critical portions of a mission.